Investigations on Liquid Crystal Reconfigurable Unit Cells for mm- Wave Reflectarrays

Vom Fachbereich 18 Elektrotechnik und Informationstechnik
der Technischen Universität Darmstadt
zur Erlangung der Würde eines Doktor-Ingenieurs (Dr.-Ing.) genehmigte

Dissertation

von

Dipl.-Ing.
Radu Marin
Geboren am 27.01.1979
in Bukarest, Rumänien

Referent	:	Prof. Dr.-Ing. Rolf Jakoby
Korreferent	:	Prof. Dr.-Ing. José Antonio Encinar

Tag der Einreichung	:	11.12.2007
Tag der mündlichen Prüfung	:	08.02.2008

D17
Darmstädter Dissertation

Darmstadt, 2008

Danksagung

Die vorliegende Dissertation entstand in Rahmen meiner Tätigkeit im Fachgebiet Funkkommunikation am Institut für Hochfrequenztechnik der Technischen Universität Darmstadt, als Stipendiat des Graduirtenkollegs "Physik und Technik von Beschleunigern" und als wissenschaftlicher Mitarbeiter. Ich bin vielen Menschen, die diese Arbeit möglich gemacht haben, zu Dank verpflichtet.
Zuerst möchte ich mich bei meinem Doktorvater, Herrn Prof. Dr.-Ing. Rolf Jakoby bedanken, dafür, dass er mir die Möglichkeit gegeben hat diese Arbeit zu schreiben, für das in mir gesetzte Vertrauen und für die kontinuierliche Unterstützung während der Promotion.
Herrn Prof. Dr.-Ing. Jose Antonio Encinar von der "Universidad Politecnica de Madrid" möchte ich für die Übernahme des Korreferats und für mehrere anregende Diskussionen danken.
Herrn Prof. Dr.-Ing. George Lojewski von der "Politehnica" Universität in Bukarest möchte ich für die Betreuung meiner ersten Schritte im Gebiet der Hochfrequenztechnik, sowie für die Ermunterung zur Annahme der Doktorandenstelle danken.
Bei Herrn Dr.-Ing. Jens Freese möchte ich mich herzlich bedanken, sowohl für die "Initialzündung", als auch für die unzähligen fruchtbaren Diskussionen.
Herr Dr.-Ing. Stefan Müller hat mir immer mit Rat und Tat geholfen, sei es wenn es um die Eigenschaften der Flüßigkristalle, um Messungen an dem Vektor Netzwerk Analysator oder um Hinweise zur Ausarbeitung ging. Ebenso hilfsbereit war auch sein Zimmerkollege, Herr Dr.-Ing. Patrick Scheele, bei den beiden habe ich in all den Jahren stets eine offene Tür und ein offenes Ohr gefunden.
Herr Dr.-Ing. Martin Schüßler fand neben nützliche fachliche Hinweise auch sonst ermunternde Worte. Allen Kollegen, insbesondere aber der Mitglieder unserer Arbeitsgruppe Funkkommunikation (Dr.-Ing. Steffen Bug, Dr.-Ing. Georg Bauer, Christian Damm, Alexander Gäbler, Andre Giere, Felix Gölden, Markus Köberle, Yuri Kryvoschapka, Holger Maune, Alexei Nazarov, Andreas Penirschke, Yuliang Zheng) möchte ich für die Hilfsbereitschaft in diverse Situationen, für die spontanen (Fach-)Diskussionen in der Kafferunde und für die angenehme Arbeitsklima danken. Den "Optikern" und anderen Fußballfreunde bin ich dankbar für die wöchentliche Entspannung auf dem Fußballfeld.
Meiner ersten Zimmerkollegin, Frau Dr.-Ing. Kira Kastell, mochte ich für die Geduld

die sie hatte, mir zahlreiche Fragen zu beantworten und mir viele Sachen zu erklären in meinen ersten Monaten am Institut, sowie für die Tanzstunden in Darmstadt und Hemsbach, danken.
Besonders möchte ich mich bei Alexander Mössinger bedanken, mit dem ich viele Jahre das Zimmer und das Forschungsgebiet geteilt habe. Unsere Zusammenarbeit war reibungslos, aus unseren Diskussionen sind viele Ideen hervorgekommen, er hat mich oft motiviert und immer unterstützt.
Herrn Peter Kießlich danke ich für die Herstellung und Vorbereitung vieler Aufbauten und für seine kompetente Beratung in feinmechanischen und aufbautechnischen Angelegenheiten. Ebenso möchte ich mich bei allen anderen nicht wissenschaftlichen Mitarbeitern für die Unterstützung bedanken.
Meinen Freunden aus Darmstadt, die mir das Aufenthalt hier um vieles bereichert haben und es zu einer der schönsten Abschnitte meines Lebens gemacht haben, will ich ebenfalls bedanken: Tudi und Ilina Murgan, Monika und Eike, Ileana und Jaro, Judith und Alex "Fuché", Gusti, Dana, Paul, Adina und Matei Demetrescu, Gabi und Lef von Borck.
Meiner Verlobten Alina, die mich durch die Dissertationszeit unterstützt hat, mir in den schwierigen sowie in den schönsten Zeiten beigestanden hat, insbesondere für die Geduld während dieses langen letzten Jahres, möchte ich herzlich danken. Meinem Bruder Alex, für Ermunterung und die spätnächtliche Diskussionen danke ich auch.
Schließlich möchte ich noch zwei Leuten danken: meinen beiden Eltern Elena und Dumitru Marin, für ihre Liebe und Hingabe.

Acknowledgement

This thesis is the result of my activity at the Department of Wireless Communications, Fachbereich ETIT at the Darmstadt University of Technology, as recipient of a scholarship in the Graduate School "Physics and Technics of Particle Accelerators" and as employee of the Institut for High Frequency. There are many people to which I am indebted for making this thesis possible.
First of all I would like to thank my advisor, Prof. Rolf Jakoby, for giving me the possibility to write this thesis, for the confidence shown in me and for the continuous support during the dissertation.
To Prof. Dr.-Ing. Jose Antonio Encinar from "Universidad Politecnica de Madrid" I am thankful for accepting to be the co-referent of the thesis and for several interesting discussions.
Prof. George Lojewski from the Politehnica University in Bucharest I would like to thank for making Microwave Engineering an attractive subject, thus giving me the first insights into this wonderful field. Further, I thank him for encouraging me to accept the challenge of starting this thesis.
A special thanks goes to Dr.-Ing. Jens Freese, for providing the "initial spark", and for the numerous times he indulged into revealing to me some of the secrets of the microwave engineering, and into searching together for the unrevealed ones.
Dr.-Ing. Stefan Müller was always ready to help, whether the topic was the properties of liquid crystals, measurements at the Vector Network Analyser or tips for the writing of the thesis. The same availability showed his room mate Dr.-Ing. Patrick Scheele, both have kept in all the years an open door for me and my questions.
Dr.-Ing. Martin Schüßler, apart from useful hints for my research found always encouraging words. To all the colleagues, but especially the members of our research group Wireless Communication Lab (Dr.-Ing. Steffen Bug, Dr.-Ing. Georg Bauer, Christian Damm, Alexander Gäbler, Andre Giere, Felix Gölden, Markus Köberle, Yuri Kryvoschapka, Holger Maune, Alexei Nazarov, Andreas Penirschke, Yuliang Zheng) for their readiness to help in various situations, for all the spontaneous discussions in the coffee break and for the very friendly atmosphere in the group, a big "thank you". To the "Optiker" and other footbal friends I am thankful for the weekly relaxation on the football field.
For her patience from the first months here at the Institute, answering a lot of questions

and explaining me a lot of things and for the dancing lessons in Darmstadt and Hemsbach I would like to thank my first room mate, Frau Dr.-Ing. Kira Kastell.
I would like to express special gratitude to Alexander Mössinger, with whom I have shared a room and a research area for quite some time. We had a good collaboration, with many discussions that lead to interesting ideas; he has often motivated and always supported me.
To Peter Kießlich I want to thank for the manufacturing and preparation of many samples and for his competent advice in technological issues. I would also like to thank all other members of the administrative staff for their support.
To my friends in Darmstadt, who have enriched my stay in Germany and made it one of the nicest periods of my life, I am also indebted: Tudi and Ilina Murgan, Monika and Eike, Ileana and Jaro, Judith and Alex "Fuché", Gusti, Dana, Paul, Adina and Matei Demetrescu, Gabi and Lef von Borck.
I thank my fiancée Alina, who has supported me during the dissertation in the difficult as well as in the beautiful times, especially for the patience during the last long year. To my brother Alex I am thankful for encouragements and late night discussions.
Finally, I want to express my gratitude to two people to whom I owe a lot: my parents Elena and Dumitru Marin, for their love and support.

Summary

In order to meet the increasing need for cost effective antennas with pattern reconfiguration capabilities (beam steering, beam shaping), a novel approach has been investigated in this thesis. It consists in integrating a thin liquid crystal substrate with electrically tunable permittivity with a class of highly directive, planer antennas - the microstrip reflectarrays.

Preliminary investigations have been conducted with fixed-beam reflectarrays, in which different feeding structures have been tested with the purpose of achieving compact and mechanically stable reflectarrays. Besides the widely used offset feed, reflectarrays with retro-directive feed and slotted waveguide array line-feed have been realized and investigated so far.

To assess the phase shifting capabilities of liquid crystal reflectarray elements, in a first phase diverse unit cell configurations have been designed, investigated via electromagnetic simulations and characterized in waveguide simulators. First worldwide realizations of liquid crystal tunable microstrip reflectarray unit cells have thus been demonstrated at 35 and 77 GHz.

It has been shown that it is possible to achieve adjustable phase ranges of up to 300° with simple microstrip configurations, like single printed patch or stacked patches. While the tunable phase range would be enough for the realization of large arrays, the reflection losses of the elements are still too high for many applications, primarily owing to the high dielectric losses of the employed liquid crystals.

To fully validate the concept, after successfully testing the tunable unit cells, full scale reflectarrays with beam steering capability have been for the first time demonstrated at 35 GHz. Despite the high losses, distinct beam collimation and beam steering with large steering angles have been demonstrated. To reduce the complexity of control circuitry reflectarrays have been realized with electronic steering in one plane only. The extension to two dimensional reconfiguration has been technologically implemented, but not verified owing to prohibitive calibration times.

The investigations in this thesis indicate clearly that reconfigurable liquid crystal reflectarrays are promising, easy to build, robust and cost efficient solutions for electronically reconfigurable, high-gain antennas in the mm and sub-mm wave bands. However, in order to fully exploit their application potential, liquid crystal mixtures with improved dielectric properties in the microwave region and further unit cell structures with reduced losses will have to be developed in future research.

Zusammenfassung

Um dem ansteigenden Bedarf an kosteneffektiven Antennen mit rekonfigurierbarem Richtdiagramm nachzukommen, wird in dieser Arbeit ein neuartiger Ansatz untersucht. Er besteht in der Integration eines dünnen Flüssigkristallsubstrates mit einer Klasse von hochdirektiven, planaren Antennen: den gedruckten planaren Reflektoren (*reflectarrays*).

Voruntersuchungen wurden mit Reflectarrays mit festem Hauptstrahl vorgenommen, indem unterschiedliche Speisestrukturen getestet wurden, mit dem Zweck Kompaktheit und mechanische Stabilität von Reflectarrays zu erreichen. Neben dem weit verbreiteten versetzten Speisehorn (*offset feed*) wurden Reflectarrays mit retrodirektiver Speiseantenne und mit linearer Schlitzhohlleiter-Gruppenantenne realisiert und untersucht.

Um das Phasenverschiebungspotenzial von Flüßigkristall-Reflectarrayelementen zu bewerten, wurden in einer ersten Phase unterschiedliche Elementarzellenkonfigurationen mittels elektromagnetischer Simulationen untersucht und in einem Hohlleiteraufbau charakterisiert. Weltweit wurden die erste Realisierungen und Charakterisierungen von steuerbaren Reflectarray-Elementarzellen auf Basis von Flüßigkristallen bei 35 GHz und 77 GHz demonstriert.

Es wurde gezeigt, dass die Möglichkeit besteht, die Phase der reflektierten Welle in einem Intervall von bis zu 300° mit einfachen Mikrostreifenstrukturen, wie z.B. einzelnen oder gestapelten Patches, einzustellen. Dieses Steuerintervall wäre ausreichend für die Realisierung großer Reflectarrays. Allerdings sind die hohen Reflexionsverluste der Elementarzellen, die hauptsächlich auf dielektrische Verluste der benutzten Flüßigkristalle zurückzuführen sind, noch kritisch für viele Anwendungen.

Nach erfolgreichem Testen der Elementarzellen wurden zur Validierung des Konzepts weltweit erstmals Reflectarrays mit elektronischer Strahlschwenkung basierend auf Flüßigkristallen bei 35 GHz demonstriert. Trotz der hohen Verluste der Elementarzellen, wurde gezeigt, dass es möglich ist den Hauptstrahl zu fokussieren und in einem großen Winkelbereich zu schwenken. Zur Reduzierung der Komplexität der Steuerschaltung wurden nur Reflectarrays mit Strahlschwenkung in einer Ebene realisiert. Die Ausweitung auf Hauptstrahlsteuerung in zwei Dimensionen wurde zwar technologisch implementiert, aber nicht verifiziert aufgrund der zur Zeit noch unvertretbar langen Messzeiten.

Die in dieser Arbeit durchgeführten Untersuchungen zeigen, dass Flüßigkristallreflectarrays eine einfache, robuste und kosteneffektive Lösung für elektronisch rekonfigurierbare, hochdirektive Antennen im Millimeter- und Mikrometerwellenbereich darstellen. Allerdings müssen weitere Verbesserungen der dielektrischen Eigenschaften der Flüßigkristallmischungen im Mikrowellenbereich erzielt und geeignete Elementarzellenstrukturen entwickelt werden um das ganze Anwendungspotential für steuerbare Reflectarrays auszuschöpfen.

Contents

Chapter 1

Introduction

1.1 Motivation

Announced by the advent of the mobile communication era, a new trend is becoming more and more obvious: communication, radar or sensor systems are becoming increasingly flexible at reasonable cost. The availability of tunable components in the RF-Frontend, like filters, diplexers or antennas, is a premise for higher flexibility. Among these components, steerable/reconfigurable antennas are key components for future radar-sensing and communications systems.

In communication systems there are numerous potential applications for reconfigurable antennas. SDMA, used in collaboration with other multiplex schemes (TDMA, FDMA, CDMA), offers the possibility to increase the number of users in a network by spatial separation achieved by the narrow main beam of the antenna. Selective noise suppression (*nulling*) is also possible with an antenna with reconfigurable pattern. In a cellular base station for instance, a sector antenna is needed, in order to provide nearly omnidirectional coverage in azimuth. An electronically steerable antenna would enable the scanning of a narrow beam over the desired sector. A narrow beam being equivalent to a higher directivity and thus presumably higher gain, the power and amplification requirements are reduced, as well as interference and multipath effects.

In automotive radar systems like the Long Range Radar for Adaptive Cruise Control (ACC) [Wen05], there is a need for high-directivity, narrow beam antennas. Most automotive radars presently on the market or under development provide at least three beams [Har02, Sch02] to enable a supervision of adjacent lanes or to "see" forthcoming bends. For future applications, such as anti-collision radar, even more beams are considered necessary to do some kind of imaging of the scene in front of the vehicle. Switching between several antennas or feeds, mechanical scanning, or frequency scan-

ning have been considered or, as an alternative, monopulse antennas are employed. An antenna with electronic beam scanning capacity would greatly enhance system reliability and potentially reduce cost.

The key components in a phased array system are without any doubt the phase shifters. They drive the costs of the system very high, and are also a main source of performance limitation. For the realization of electronic phase shifters there are a number of established technologies, which have their advantages and disadvantages. For analog phase shifters - providing a continuous phase shift with the control voltage - varactor diodes [Qur07] or ferroelectric film capacitors [Sch04, Hu07b] can be used. Digital phase shifters - providing only a limited number of phase states - are essentially based on switches, which can be realized in semiconductor (PIN diodes) or MEMS technology [Reb03].

None of the listed technologies meets all the requirements at the same time, like low attenuation, high tunable phase range of the RF signal, low DC-power consumption and low operation voltage, high linearity, low complexity, to name a few [Ji04]. Recently, promising phase shifting devices have been demonstrated with a novel technology: the use of liquid crystals as materials with electronically tunable permittivity at microwaves [Mue04, Mue05a, Mue06].

The Microstrip Reflectarray

Aperture antennas fall mostly in one of the two categories: those based on array theory, where a desired pattern is achieved by amplitude and phase control (phased arrays) and those based on geometrical optics, where the phase control is provided by the shaping of one or more surfaces in a certain manner (reflectors and lenses). A class of antennas introduced in [Ber63] are the reflectarrays. They combine the versatility of the arrays - the possibility of variable radiation pattern with the same aperture - with the simplicity of reflectors - where the complex and lossy corporate feeding network is not required.

Generally speaking a reflectarray consists of an aperture of elementary antennas placed on a grid and illuminated by a feed. The elementary antennas can be of various types; however, due to manufacturing simplicity, low-weight and low-profile, microstrip antennas have established themselves as the dominant type of element in reflectarrays. Microstrip reflectarrays have thus been intensively studied in the past 15 years.

Microstrip reflectarrays have found applications in diverse areas, and they are a serious candidate for others. For microwave communications in space missions, lightweight reflectarrays have been developed by NASA's Jet Propulsion Laboratory, based on the concept of a thin membrane that is stretched flat by attaching it to an inflatable frame [Hua99, Hua00, Hua01b]. Apart from the lightweight, the compact size of the stowed

antenna before inflating is also an advantage. Antennas of this type are meant to serve as alternative to conventional antennas with rigid reflector structures or mechanically deployed mesh reflectors [Hua01a]. Inflatable reflectarrays could also be used in terrestrial low-power, lightweight microwave systems.

Polarization twisting reflectarrays combined with a polarization grid in front of the reflector allowing for a considerable size-reduction have been developed for automotive applications (Long Range Radar for Collision Avoidance). The main beam can be scanned by mechanical tilting of the reflector [Men99], or multiple beams can be created by using a corresponding number of feeding horns [Men03].

Shaped beam reflectarrays mounted on satellites can provide selective coverage of desired areas [Poz99, Zor03a, Enc04]. The desired shape of the beam is obtained for instance by printing elements with appropriate sizes, which is far more cost effective than custom moulding of a metallic reflector. Reflectarrays are also a good alternative for shaped multiple-beam antennas in terrestrial communications, to be used for instance in the central station of Local Multipoint Distribution Systems (LMDS) [Arr06].

Other possible applications of reflectarrays include flush mounting on airplane tops to provide satellite link in the *Ku* Band for in-flight entertainment, or conformal mounting on building walls for high-data rate wireless links in the 60 GHz or 120 GHz bands.

Nematic Liquid Crystals

Nematic liquid crystals (LCs) are well known for their applications in the field of optics, especially for TFT-Displays, but also as optical switches or amplitude modulators. In these applications, the effect of the anisotropy of the refraction index is used. Apart from this optical anisotropy, LCs also feature a dielectric anisotropy at microwaves, caused by different orientations of the LC molecules relative to a reference axis. Thus, a liquid crystal serving as propagation medium for a RF field, will exhibit different relative permittivities ε_r for different molecular orientations. The LC orientation can be achieved by applying a static (or low-frequent) electric or magnetic field. It is thus interesting to study the properties of LCs in the microwave region and to investigate the possibility of designing and realizing novel tunable components based on them. In [Wei03a, Mue05a, Mue07] tunable LC phase shifter in various technologies have been successfully demonstrated.

Recent publications [Mue05b] covering the characterization of liquid crystals in the microwave region, suggest the possibility, that the properties of LCs (dielectric anisotropy $\Delta\varepsilon_r$ and losses $\tan\delta$) do not degrade at higher frequencies and even show a slight improvement, a rather uncommon behavior for most materials. Thus, liquid crystals could

prove a very promising alternative to semiconductor devices (diodes, FETs) or to MEMS for use in tunable devices in a large frequency range reaching up into the sub millimeter wave band.

The planarity of the microstrip reflectarrays as well as the arrangement of the elements in a regular grid bears a resemblance to an LC display, with each microstrip element being the equivalent of a "pixel". Having this comparison in mind, the idea of using the liquid crystal to tune the reflectarray elements pixel-wise suggests itself.

1.2 Scientific Objectives of the Thesis

The goal of this thesis was to investigate the possibility of integrating liquid crystal as a tunable material in microstrip reflectarrays, in order to enhance their functionality towards a pattern reconfiguration capability.

In the second chapter, first a brief theoretical introduction on reflectarrays is given, to understand how reflectarrays work, followed by the presentation of a lumped element equivalent circuit for reflectarray unit cells. Next, an overview of the mechanisms for phase adjustment in non-reconfigurable reflectarrays is given, with examples from the reflectarray literature. The chapter closes with a review of existing technologies used in electronically reconfigurable reflectarrays.

In the following chapter, a few non-reconfigurable reflectarrays are investigated. Several feeding structures are presented, aiming to simplify the mechanical construction of the reflectarrays. A bandwidth optimization employing stacked patch elements is also proposed.

Chapter four introduces the nematic liquid crystals, starting with a short theoretical background. It continues with the presentation of the microwave properties of liquid crystals employed in this work. Finally, some existing applications of liquid crystals as tunable materials at microwaves are presented.

Chapter five demonstrates the integration of liquid crystals in reflection type phase shifting elements (reflectarray unit cells). The design, measurement technique, as well as the obtained results with the worldwide first tunable reflectarray unit cells based on nematic liquid crystals are highlighted.

In chapter six full scale reconfigurable reflectarrays are presented. Their design, construction, and measured performance are in the focus. These are as well worldwide first realizations of 35 GHz LC-steerable full scale reflectarrays. The thesis closes with a final chapter, where the main contributions and results are reviewed, and directions for future research are outlined.

Chapter 2

Microstrip Reflectarrays

In this chapter, first some basic theoretical aspects concerning reflectarrays are exposed. Next, a lumped element equivalent circuit for reflectarray elementary cells is introduced and discussed. Different mechanisms used to adjust the reflection phase at each element of the reflectarray are highlighted, allowing an overview of existing reflectarray types from the literature. The last subchapter presents existing types of electronically steerable / reconfigurable reflectarrays.

2.1 Fundamentals of Reflectarray Theory

In its basic design, a microstrip reflectarray consists of an array of microstrip antennas, printed on a grounded substrate. This array is illuminated by a feed, usually a horn antenna. The electromagnetic energy is received by the microstrip elements and then it is reradiated. Thereby, the phase of the reflected wave is being adjusted locally, i.e. at each microstrip element, by using different methods. It is thus possible to obtain a cophasal wave in a desired direction (see Fig 2.1).

Considering an array with $M \times N$ elements, arranged in the XY-Plane like in Fig. 2.2, the total pattern of the array equals the *array factor* times the *element factor*. The element factor of a microstrip element (mostly a microstrip patch) has a relative low directivity, which means that the total pattern is dominated by the array factor. The array factor can be written:

$$F_a(\theta,\phi) = \sum_{m=0}^{M-1}\sum_{n=0}^{N-1} \underline{I}_{mn} \cdot e^{j\,k\,(m\,d_x \sin\theta\cos\phi + n\,d_y \sin\theta\sin\phi)}\,, \tag{2.1}$$

where $\underline{I}_{mn}$ is the complex current of the mn-th element. If the distribution of the exciting

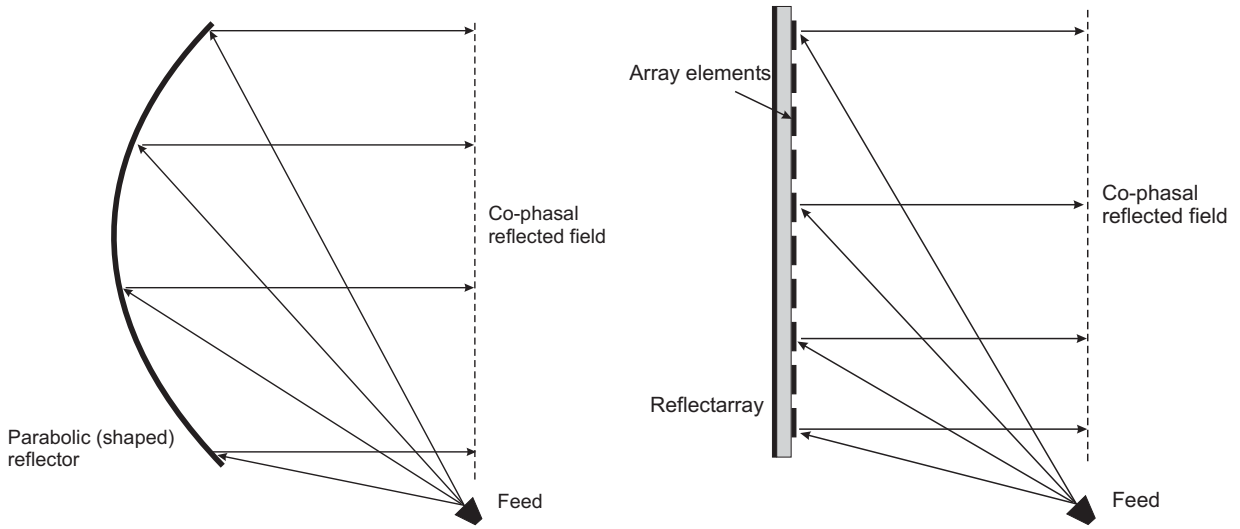

(a) Parabolic (shaped) reflector antenna (b) Reflectarray antenna

Figure 2.1: Parabolic reflector as compared to generic microstrip reflectarray: in a reflectarray the phase adjustment of different "rays" is done through the array elements instead of geometrical shape of the reflector.

currents has a constant phase progression in the x direction $\Delta\varphi_x$, or in the y direction $\Delta\varphi_y$, respectively, then the array factor is:

$$F_a(\theta,\phi) = \sum_{m=0}^{M-1}\sum_{n=0}^{N-1} I_{mn}\cdot e^{j\,(k\,m\,d_x\sin\theta\cos\phi+m\Delta\varphi_x)}\cdot e^{j\,(k\,n\,d_y\sin\theta\sin\phi+n\Delta\varphi_y)}\,. \tag{2.2}$$

Assuming the spacing between the elements to be the same in the x and y directions (i.e. $d_x = d_y = d$), a condition that is always fulfilled by the arrays considered in this work, the array factor can be written:

$$F_a(\theta,\phi) = \sum_{m=0}^{M-1}\sum_{n=0}^{N-1} I_{mn}\cdot e^{j\,k\,d\,m(\sin\theta\cos\phi+\beta_x)}\cdot e^{j\,k\,d\,n(\sin\theta\sin\phi+\beta_y)}\,, \tag{2.3}$$

with $\Delta\phi_x = k\,d\,\beta_x$ and $\Delta\phi_y = k\,d\,\beta_y$.

With a further assumption, that the magnitude of the element excitations is equal for all elements ($I_{mn} = I_0$ for all m, n), it follows for the array factor:

$$F_a(\theta,\phi) = I_0\cdot\sum_{m=0}^{M-1} e^{j\,k\,d\,m(\sin\theta\cos\phi+\beta_x)}\cdot\sum_{n=0}^{N-1} e^{j\,k\,d\,n(\sin\theta\sin\phi+\beta_y)}\,. \tag{2.4}$$

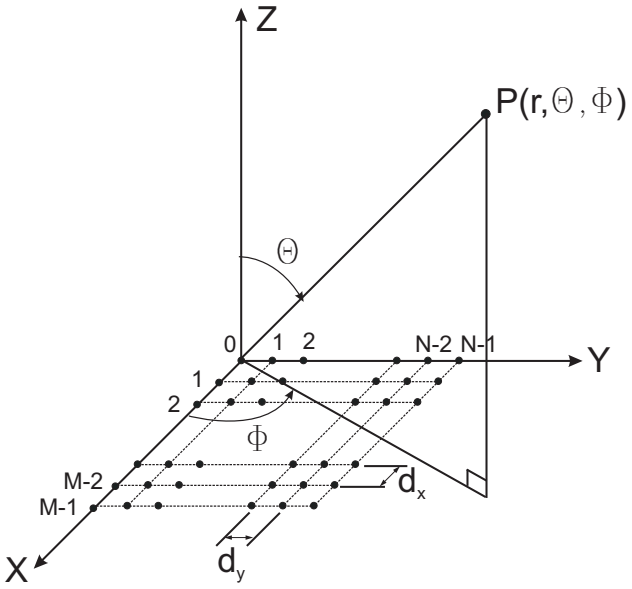

Figure 2.2: Planar array with uniformly spaced elements.

The summation of the geometrical series gives:

$$F_a(\theta,\phi) = I_0 \left(\frac{e^{j\,k\,d\,M\,(\sin\theta\cos\phi+\beta_x)} - 1}{e^{j\,k\,d\,(\sin\theta\cos\phi+\beta_x)} - 1} \right) \left(\frac{e^{j\,k\,d\,N\,(\sin\theta\cos\phi+\beta_x)} - 1}{e^{j\,k\,d\,(\sin\theta\cos\phi+\beta_x)} - 1} \right) \tag{2.5}$$

$$= I_0 \left(\frac{e^{j\,M\,\varphi_y} - 1}{e^{j\,\varphi_y} - 1} \right) \left(\frac{e^{j\,N\,\varphi_x} - 1}{e^{j\,\varphi_x} - 1} \right), \tag{2.6}$$

with $\varphi_x = kd\sin\theta\cos\phi + \beta_x$ and $\varphi_y = kd\sin\theta\sin\phi + \beta_y$. Further we obtain:

$$F_a(\theta,\phi) = I_0\, e^{j\,(M-1)\frac{\varphi_x}{2}} e^{j\,(N-1)\frac{\varphi_y}{2}} \frac{\sin\left(M\frac{\varphi_x}{2}\right)}{\sin\left(\frac{\varphi_x}{2}\right)} \frac{\sin\left(N\frac{\varphi_y}{2}\right)}{\sin\left(\frac{\varphi_y}{2}\right)} \,. \tag{2.7}$$

The magnitude of the array factor then amounts to:

$$|F_a(\theta,\phi)| = I_0 \cdot \frac{\sin\left(M\frac{\varphi_x}{2}\right)}{\sin\left(\frac{\varphi_x}{2}\right)} \frac{\sin\left(N\frac{\varphi_y}{2}\right)}{\sin\left(\frac{\varphi_y}{2}\right)} \,. \tag{2.8}$$

This function has a maximum for $\varphi_x = 0$ and $\varphi_y = 0$, which represents the main beam of the power pattern. It follows, that for:

$$\beta_x = -kd\sin\theta_0\cos\phi_0 \quad \text{and} \quad \beta_y = -kd\sin\theta_0\sin\phi_0 \,, \tag{2.9}$$

the array factor has its maximum in $|F_a(\theta_0,\phi_0)|$, and the main beam is pointing toward the (θ_0,ϕ_0)-direction. If one were able to reconfigure dynamically the phase distribution

of the excitation currents in eq. 2.9, β_x and β_y, this would render possible steering of the main beam to different pointing directions.

In case of the reflectarrays, the current distribution on the array elements is imposed by the incident electric field radiated from the feed. Assuming an infinite array with identical elements, an incident electric field from the direction (θ_i, ϕ_i) can be written [Poz97]:

$$\vec{E}_i = \vec{E}_0 \cdot e^{j\,k(x\sin\theta_i\cos\phi_i + y\sin\theta_i\sin\phi_i + z\cos\theta_i)}\,, \tag{2.10}$$

with $\vec{E}_0 = E_{0\theta}\hat{\theta} + E_{0\phi}\hat{\phi}$. The reflected field is a superposition of the field reflected by the grounded dielectric with the field scattered by the microstrip patches. In the absence of the patches, the field reflected from the ground plane can be expressed as [Poz97]:

$$\vec{E}_g = \mathbf{G} \cdot \vec{E}_0 \cdot e^{j\,k(x\sin\theta_i\cos\phi_i + y\sin\theta_i\sin\phi_i - z\cos\theta_i)}\,, \tag{2.11}$$

with $\mathbf{G} = \left(\begin{smallmatrix} G_{\theta\theta} & 0 \\ 0 & G_{\phi\phi} \end{smallmatrix}\right)$ a matrix describing the reflection of a plane wave on a grounded substrate.

The field scattered when only the patches are present can be expressed as:

$$\vec{E}_s = \mathbf{S} \cdot \vec{E}_0 \cdot e^{j\,k(x\sin\theta_i\cos\phi_i + y\sin\theta_i\sin\phi_i - z\cos\theta_i)}\,, \tag{2.12}$$

with $\mathbf{S} = \left(\begin{smallmatrix} S_{\theta\theta} & S_{\theta\phi} \\ S_{\phi\theta} & S_{\phi\phi} \end{smallmatrix}\right)$ the scatering matrix. The total field reflected from the reflectarray thus amounts to:

$$\vec{E}_r = (\mathbf{G} + \mathbf{S}) \cdot \vec{E}_0 \cdot e^{j\,k(x\sin\theta_i\cos\phi_i + y\sin\theta_i\sin\phi_i - z\cos\theta_i)} \tag{2.13}$$

$$= \mathbf{R} \cdot \vec{E}_0 \cdot e^{j\,k(x\sin\theta_i\cos\phi_i + y\sin\theta_i\sin\phi_i - z\cos\theta_i)}, \tag{2.14}$$

with $\mathbf{R} = \mathbf{G} + \mathbf{S} = \left(\begin{smallmatrix} G_{\theta\theta}+S_{\theta\theta} & S_{\theta\phi} \\ S_{\phi\theta} & G_{\phi\phi}+S_{\phi\phi} \end{smallmatrix}\right)$ an overall reflection matrix.

Once the total field reflected from the infinite array with identical elements is known, the central equation to the design of every reflectarray can be written as:

$$k_0(R_n + \vec{r}_n\hat{r_0}) - \varphi_n = 2\pi N\,, \tag{2.15}$$

where k_0 is the free space wave number, N={0,1,2...} is an integer, R_n, r_n and r_0 are shown in Fig. 2.3, and

$$\varphi_n = arg(\vec{E}_{r,n}) \tag{2.16}$$

is the phase of the total field reflected at the n-th array element.

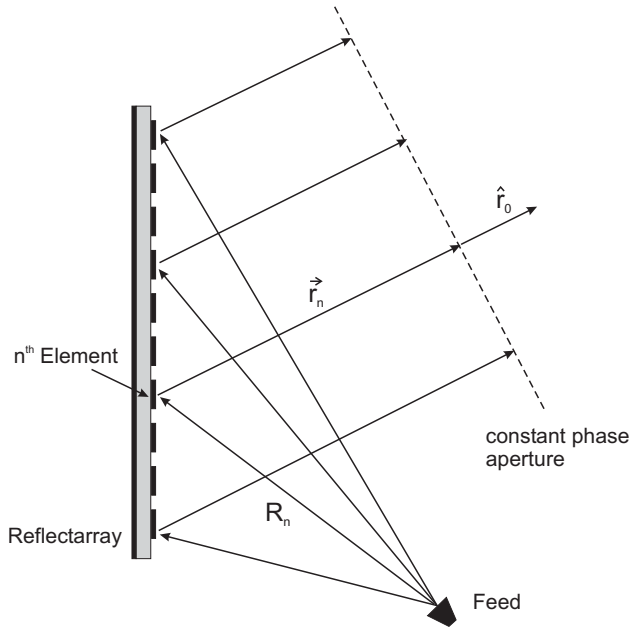

Figure 2.3: The phase equation (2.15) states that the phase difference from the feed to an aperture plane in front of the array should be the same for all reflectarray elements.

This equation states that the total phase from the feed to an aperture in front of the reflectarray should be constant for all elements. The main beam will point in the direction perpendicular to the considered aperture.

In this work, the phase of the total field reflected from an infinite array with identical elements is computed using *CST Microwave Studio* [cst07]. A unit cell, or elementary cell, is the building block of an infinite array with identical elements, consisting of the element itself (the printed microstrip structure) and the part of the substrate and ground plane assigned to it, as determined by the grid dimension. A single unit cell can be simulated using suitably chosen boundary conditions: two E-walls and two H-walls, i.e. perfect electric conductor and perfect magnetic conductor respectively, as shown in Fig. 2.4. According to image theory, this arrangement is equivalent to an infinite array with identical elements. Moreover, the boundary conditions allow the propagation of a TEM mode. Thus, the simulation of an elementary cell with the boundary conditions described above is equivalent with the simulation of a plane wave normally incident on an infinite array with identical elements.

The reflection coefficient resulted from such a simulation is:

$$\Gamma = \frac{\vec{E}_{inc}}{\vec{E}_{refl}} \, . \tag{2.17}$$

By setting $\vec{E}_{inc} = E_{0,i}$ (the phase of the incident wave is taken as reference and set to

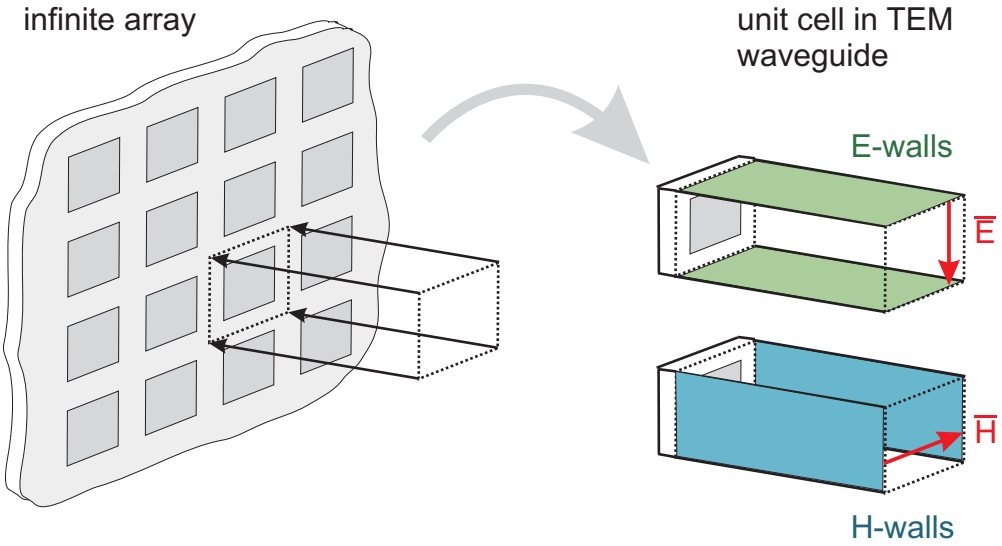

Figure 2.4: A single unit cell enclosed in a waveguide with appropriate boundary conditions is equivalent to an infinite array with identical elements. A plane wave at normal incidence is impinging on the array surface.

zero) and $\vec{E}_{refl} = E_{0,r}\, e^{j\varphi}$ the above relation becomes without loss of generality:

$$\Gamma = \frac{E_{0,i}}{E_{0,r}} \cdot e^{-j\varphi} = |\Gamma| \cdot e^{-j\varphi} \,. \tag{2.18}$$

Hence, the phase needed in Eq. (2.15) can be retrieved from the simulation results, albeit only for normal incidence. It has been however shown [Tar94], that the reflected phase does not change significantly as long as the incidence angle stays below about 40°. Thus, results at normal incidence can be successfully employed in reflectarray design.

If the infinite array with identical elements is to be regarded as a surface with an intrinsic surface impedance $\underline{Z}$, the expression for the reflection coefficient can also be written:

$$\Gamma = \frac{\underline{Z} - \eta_0}{\underline{Z} + \eta_0} \,, \tag{2.19}$$

with $\eta_0 = \sqrt{E_0 / H_0} = \sqrt{\mu_0 / \varepsilon_0}$ the wave impedance of free space.

Of course, the treatment of the infinite array with identical elements as a "homogeneous" surface is forced, since the element spacing is not considerably smaller than the wavelength. Nevertheless, this point of view can also be used to explain or better understand some phenomena.

Directivity, Efficiency, Gain

Aperture antennas can have a maximum directivity according to the well-known formula [Poz05]:

$$D_{max} = \frac{4\,\pi\,A}{\lambda^2}\,, \tag{2.20}$$

with A the physical aperture surface.

However, the actual value of the directivity is lower than this maximal attainable value, due to a series of factors [Bal97, Poz05]: energy from the feed radiated past the reflectarray surface (spillover efficiency, ϵ_s), nonuniform amplitude distribution over the reflectarray aperture (taper efficiency, ϵ_t), phase errors in the aperture plane (ϵ_p), feed blockage (ϵ_b) or cross polarization (ϵ_x). All this contributions yield the *aperture efficiency*:

$$\epsilon_a = \epsilon_s\,\epsilon_t\,\epsilon_p\,\epsilon_b\,\epsilon_x\,. \tag{2.21}$$

The *effective aperture* of an antenna is then derived as:

$$A_e = \epsilon_a\,A\,, \tag{2.22}$$

and is intuitively the part of the aperture effectively capturing power from an incoming plane wave.

The directivity is thus related to the aperture efficiency by:

$$D = \frac{4\,\pi\,A_e}{\lambda^2} = \epsilon_a\,D_{max}\,. \tag{2.23}$$

For reflectarrays the first three mechanisms (spillover, taper and phase errors) seem to be the most important. Of course, loss of efficiency by feed blockage is also possible, but usually care is taken in the design to avoid an unfavorable position of the feed.

There is a trade-off between spillover efficiency and taper efficiency. To illustrate this, feeds with a rotationally symmetric pattern given by:

$$G_f(\theta') = \begin{cases} (2\,n+1)\,\cos^n(\theta') & 0 \leq \theta' \leq \pi/2 \\ 0 & \pi/2 \leq \theta' \leq \pi \end{cases} \tag{2.24}$$

are considered (θ' is the azimuth angle in the coordinate system centered at the feed, $n = 1, 2, 3\ldots$ is a parameter influencing the directivity of the feed pattern, the higher n, the more directive the feed). These pattern represent quite accurately a major part of the main lobe for many practical feed antennas. Now the spillover, taper and aperture

efficiencies can be calculated with the formulas in [Bal97]:

$$\epsilon_s = \frac{\int_0^{\theta_0} G_f(\theta')\,\sin(\theta')\,d\theta'}{\int_0^{\pi} G_f(\theta')\,\sin(\theta')\,d\theta'}\,, \tag{2.25}$$

$$\epsilon_t = 2\,\cot^2\left(\frac{\theta_0}{2}\right)\frac{\left|\int_0^{\theta_0}\sqrt{G_f(\theta')}\tan\left(\frac{\theta'}{2}\right)d\theta'\right|^2}{\int_0^{\theta_0} G_f(\theta')\,\sin(\theta')\,d\theta'}\,, \tag{2.26}$$

$$\epsilon_a = \cot^2\left(\frac{\theta_0}{2}\right)\left|\int_0^{\theta_0}\sqrt{G_f(\theta')}\tan\left(\frac{\theta'}{2}\right)d\theta'\right|^2. \tag{2.27}$$

Using these formulas, the plots in Fig. 2.5 are obtained, which illustrates the trade-off between taper and spillover efficiency in reflector antennas. This trade-off holds for reflectarrays just as well. It can be seen that, the more directive the feed (higher n), the better the spillover efficiency and the lower the taper efficiency. For all considered feed

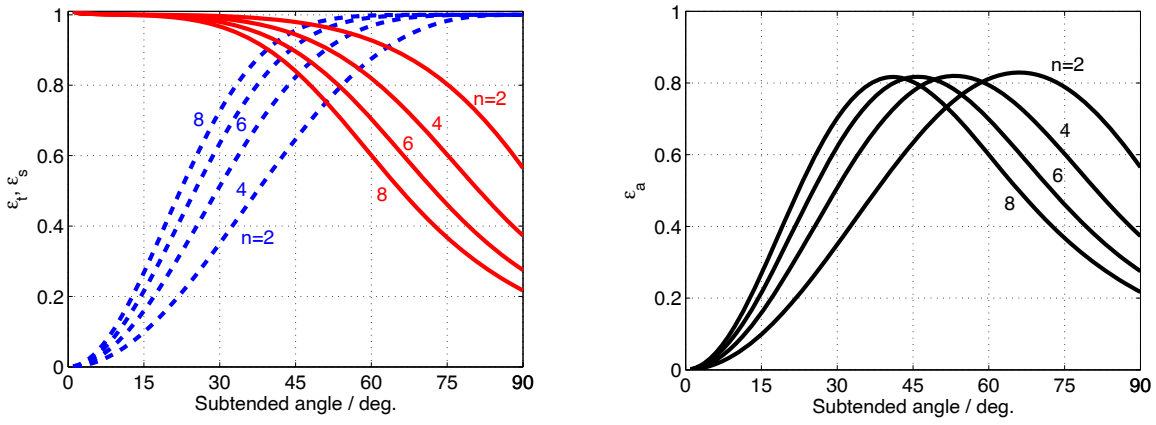

(a) Taper (–) and spillover (- -) efficiency.

(b) Aperture efficiency.

Figure 2.5: Taper, aperture and spillover efficiencies for a reflector antenna, as function of the subtended angle, for different feed pattern shapes.

patterns there is an aperture efficiency optimum at different subtended angles, which however does not exceed about 0.83% in any case.

The gain is related to the directivity by the formula [Bal97]:

$$G(\theta, \phi) = e_c \, e_d \, D(\theta, \phi) \, , \tag{2.28}$$

with e_c conduction efficiency and e_d dielectric efficiency. Thus, the gain is like the directivity a measure of the antenna's ability to collimate power in a certain direction, but additionally takes into account the power loss in conductor and dielectric.

A loss factor not accounted for in the gain is the mismatch loss between the antenna and the transmission line. This is accounted for by the reflection efficiency e_r [Bal97]. In case of a reflectarray this would represent the power that is lost due to mismatch of the feed antenna. Since the feed is usually a horn antenna, with very good matching in a broad band, this is mostly not a problem in the case of the reflectarrays, and the $e_c \, e_d$ term is dominant.

The overall efficiency can therefore be expressed as:

$$e_o = e_c \, e_d \, e_r \, . \tag{2.29}$$

2.2 Unit Cell Equivalent Circuit

Since the reflectarray elementary cell is a resonant structure, a resonant circuit suggests itself as lumped element model. The derivation of the lumped elements values from the geometry of the reflectarray elementary cell is however not trivial. Contrary to the artificial impedance surfaces, who consist of elementary cells much smaller than the wavelength and for which basic equivalent circuit models exist [Sie99, Sie03], in reflectarrays the elementary cells are about $\lambda/2$ apart. This is why, assigning to an infinite reflectarray with identical elements a surface impedance requires a different method to calculate the circuit model parameters compared to the impedance surface approach [Hum05b]. This might also be the reason, why very few publications on reflectarrays address the topic of unit cell equivalent circuit.

An equivalent circuit has been proposed in [Hum07] for a tunable reflectarray unit cell consisting of two patch halves connected by diodes (details in section 2.5). The two patch halves are modeled by microstrip line sections terminated at both ends with radiating resistances, the gap discontinuity and the fringing fields at patch edges are modeled by capacitances, and the inserted varactor diodes by a combination of inductances and capacitances. The values for these lumped elements are either calculated or extracted

from electromagnetic simulations.

In [Boz04a, Boz04b] the authors propose a lumped element model for a reflectarray unit cell as in Fig. 2.6. The propagation of the (plane) wave toward the unit cell is represented by the transmission line with characteristic impedance equal to the free space impedance $\eta_0 = 377\,\Omega$. The unit cell is represented by a LC parallel circuit, with a resistance R introduced in series with the capacitance to account for the losses.

The values of the lumped elements are given according to [Boz04a, Boz04b], under the hypothesis of low losses, by:

$$R = \frac{1-\Gamma_0}{1+\Gamma_0} \cdot \frac{16\,\eta_0}{f_0^2\,\sigma_0^2}\,, \tag{2.30}$$

$$L = \frac{2\,\eta_0}{\pi\,f_0^2\,\sigma_0} \quad \text{and} \quad C = \frac{\sigma_0}{8\,\pi\,\eta_0}\,. \tag{2.31}$$

where f_0 is the frequency where the phase of the reflection coefficient vanishes, Γ_0 is the magnitude of the reflection coefficient at f_0 and

$$\sigma_0 = -\left.\frac{\partial(arg(\Gamma))}{\partial f}\right|_{f_0}\,. \tag{2.32}$$

The values of the lumped elements L, C and R can thus be calculated with an electromagnetic analysis in few frequency points (in f_0 and in its proximity for the calculation of σ_0).

The results obtained with this RLC-model show good agreement with results obtained with electromagnetic simulations. However, the model has the drawback that it does not offer enough insight in the physics of the reflectarray unit cell: there is no separation between the contribution of the dielectric and metallic losses to the overall losses and the values of the lumped elements are not directly related to the physical properties of the unit cell (geometry, loss tangent, permittivity etc.), but only indirectly, by means of the full wave simulation.

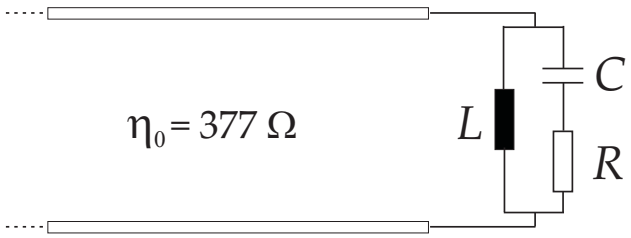

Figure 2.6: Lumped element model of the elementary unit cell of a microstrip reflectarray as proposed in [Boz04a, Boz04b]

In this work, an alternative lumped element model according to Fig. 2.7 is proposed. C is the capacitance formed between the microstrip structure printed on the substrate and the ground. In parallel to this capacitance is a resistance R_C, accounting for the losses in the dielectric substrate (alternatively, a conductance G can be used, for a more symmetrical notation). The currents flowing in the microstrip element and in the ground plane cause the inductance L and at the same time generate losses due to the finite conductivity of the metal, accounted for by the resistance R_L.

The complex impedance of the unit cell is designed $\underline{Z}_{cell}$ and can be readily calculated:

$$\underline{Z}_{cell} = \frac{R_L + j\,\omega\,L}{1 + (R_L + j\,\omega\,L)\,(1/R_C + j\,\omega\,C)}\,. \tag{2.33}$$

The resonance frequency of this circuit, given by the condition $\Im\,(\underline{Z}_{cell}) = 0$, amounts to:

$$\omega_r = \sqrt{\frac{1}{LC} - \left(\frac{R_L}{L}\right)^2}\,. \tag{2.34}$$

However, due to the very low values for R_L (for common metal conductivity values in the range of $10^{6\ldots7}\,\mathrm{S/m}$ yields R_L values in the order of $10^{-2\ldots-1}$) the term $(R_L/L)^2$ can be neglected compared to $1/(LC)$, so that practically one can use the value of the resonance frequency for the lossless case:

$$\omega_r \approx \sqrt{\frac{1}{LC}}\,. \tag{2.35}$$

Only in case of a metal with very low conductivity (lower than $10^4\,\mathrm{S/m}$), the metallic losses have an appreciable impact on the value of the resonance frequency.

The complex reflection coefficient Γ can be calculated with the well-known formula:

$$\Gamma = \frac{\underline{Z}_{cell} - \eta_0}{\underline{Z}_{cell} + \eta_0}\,, \tag{2.36}$$

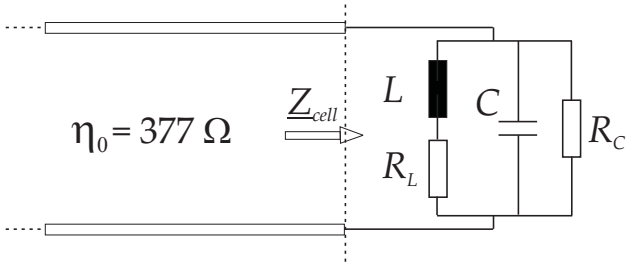

Figure 2.7: Proposed lumped element model of the elementary unit cell of a microstrip reflectarray

from which then the phase characteristic $arg\,(\Gamma)$ and the magnitude characteristic $|\Gamma|$ can be extracted.

Calculating the capacitance and inductance values (C and L respectively) with analytical methods is very difficult. There are available formulas which model capacitance of a microstrip patch, however the microstrip patch is not in an infinite array environment, as it is assumed for the unit cell and its associated equivalent model. There is significant difference between analytical calculations for C and L and the values extracted from electromagnetic simulations.
However, the model is suitable for assessing losses in the reflectarray unit cell, as well as their origin: dielectric or metallic. The dielectric losses are governed by the relation:

$$Q_d = \frac{1}{\tan\delta} = \omega_r C\, R_C\ , \tag{2.37}$$

with Q_d the dielectric quality factor and $\tan\delta$ the loss angle of the substrate. By knowing the loss angle of the substrate, resonant frequency and the capacitance of the equivalent circuit one can thus extract R_C.
The metallic losses are a more complicated function of the surface resistance

$$R_S(f) = \sqrt{\frac{\pi\, f\, \mu_0}{\sigma}}\ , \tag{2.38}$$

with f the frequency, μ_0 the permeability of vacuum and σ metallic conductivity, and of the substrate height h. The calculation of R_L is based on formulas found in [Sch01], and given in Appendix A1.

For conventional reflectarrays up to the K-Band, printed on RF-substrates with relatively low loss angle ($\tan\delta \approx 0.001$) the losses are not critical. However, liquid crystals, which we intend to use as substrate to achieve reconfigurability, have higher substrate losses ($\tan\delta \approx 0.01...0.02$). Additionally, metallic losses increase with the frequency according to the skin effect (Eq. (2.38)), and also increase as a consequence of thin layers of LC. Both loss mechanisms together can cause significant reflection losses in the reflectarray unit cell, as it will be shown in section 5.1. For this reason, a model for understanding and quickly assessing losses as well as their origin is important.

To illustrate the use of the model, let us consider a more or less arbitrary unit cell configuration, consisting of a microstrip square patch with a size $\ell_{patch} = 2.5\,\text{mm}$, printed on a substrate with $h = 0.3\,\text{mm}$ and $\varepsilon_r = 2.5$. From the electromagnetic simulation of the unit cell, without considering losses ($\tan\delta$=0 and $\sigma \to \infty$), the values for C, L and ω_r can be extracted. Based on these values, one is able to calculate instantly R_C and R_L for various values of $\tan\delta$ and σ, and obtain with Eq. (2.36) the phase and magnitude characteristics of the unit cell as well.

Table 2.1 summarizes the values of the lumped element equivalent circuit components for a few chosen cases. The first row represents the lossless case, which is used to extract the values of C and L with the aid of a *CST Microwave Studio* simulation. Then, the conductivity of the metal, the loss angle of the substrate, and finally the relative permittivity of the substrate are varied each at a time, and the values for R_C and R_L are computed in each case.

Table 2.1: Values of extracted (C, L) and calculated (R_C, R_L) components of the lumped element unit cell equivalent circuit, for different variations in substrate permittivity ε_r, loss angle $\tan\delta$ and metallic conductivity σ.

Substrate		Metallization	C [pF]	L [nH]	R_C [Ω]	R_L [Ω]
ε_r=2.5	$\tan\delta$=0	$\sigma=\infty$	0.1584	0.1336	∞	0
ε_r=2.5	$\tan\delta$=0	$\sigma=10^6$	0.1584	0.1336	∞	0.2735
		$\sigma=10^7$				0.0865
		$\sigma=10^8$				0.0273
ε_r=2.5	$\tan\delta=0.005$	$\sigma=\infty$	0.1584	0.1336	6387	0
	$\tan\delta=0.01$				3194	
	$\tan\delta=0.02$				1597	
ε_r=2.2	$\tan\delta$=0.015	$\sigma=10^7$	0.1417	0.1336	2316	0.0889
ε_r=2.5			0.1584		2162	
ε_r=2.8			0.1758		2035	

Fig. 2.8 shows a comparison between full wave simulations and results obtained with the equivalent circuit for three different values of the electric conductivity σ of the patch metalization. The phase characteristic is only very slightly influenced by variations in electric conductivity, but the magnitude characteristic is heavily affected, especially at the resonance frequency.

In Fig. 2.9 a similar comparison is shown, this time with lossless metal and different values for the substrate loss angle $\tan\delta$. In both cases the predictions made with the equivalent circuit are quite close to the results obtained with the full wave simulation. However, the computations using the equivalent circuit are more or less instantaneous, while a full wave simulation can be quite time consuming, especially when fine meshing is required for accurate calculation of metal layers and very thin dielectric layers.

Apart from prediction of the losses, the lumped element equivalent circuit can also be used to asses changes in the phase and magnitude characteristic of a unit cell when the

permittivity of the substrate is varied. This is shown in Fig. 2.10, where full wave simulations are compared to the results computed with the equivalent circuit for different values of the substrate relative permittivity. The figure suggests that reflexion losses are dependent not only on substrate and metalization properties, they can also vary when the relative permittivity of the substrate is changed.

Noteworthy is also, that only the capacitance value for ε_r=2.5 is extracted from electromagnetic simulation, the other two values (corresponding to ε_r=2.2 and ε_r=2.8) can be quickly calculated based on the equivalent circuit.

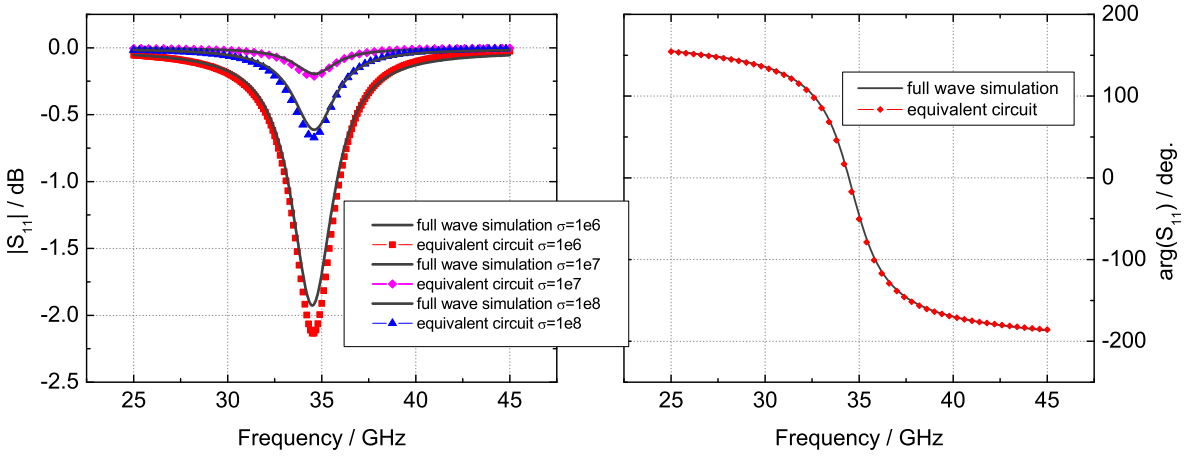

Figure 2.8: Comparison between full wave simulations and equivalent circuit simulations for a reflectarray unit cell with no losses in the substrate and three different values for electric conductivity σ of the patch metalization.

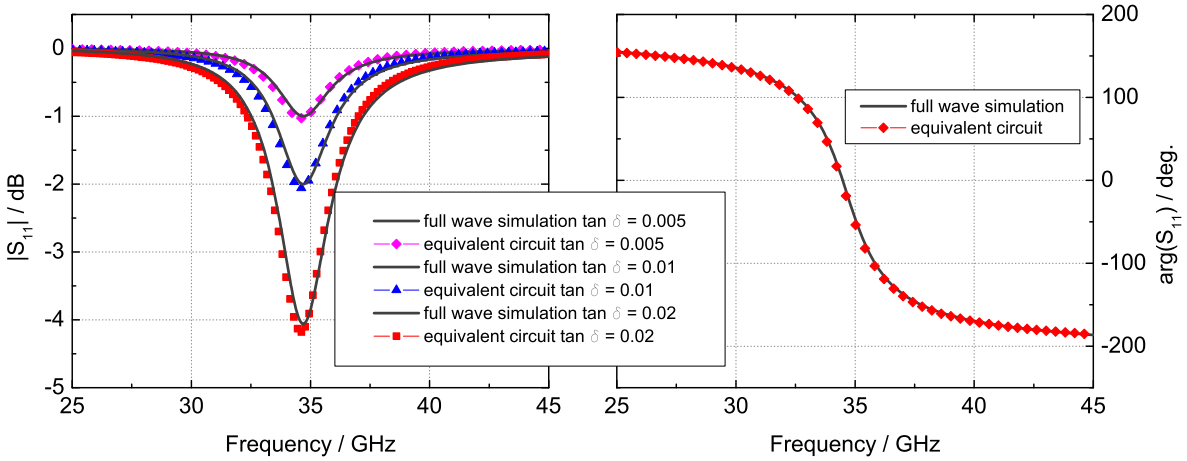

Figure 2.9: Comparison between full wave simulations and equivalent circuit simulations for a reflectarray unit cell with no metalic losses and three different values for the loss angle $\tan\delta$ of the substrate, emulating LC tunability.

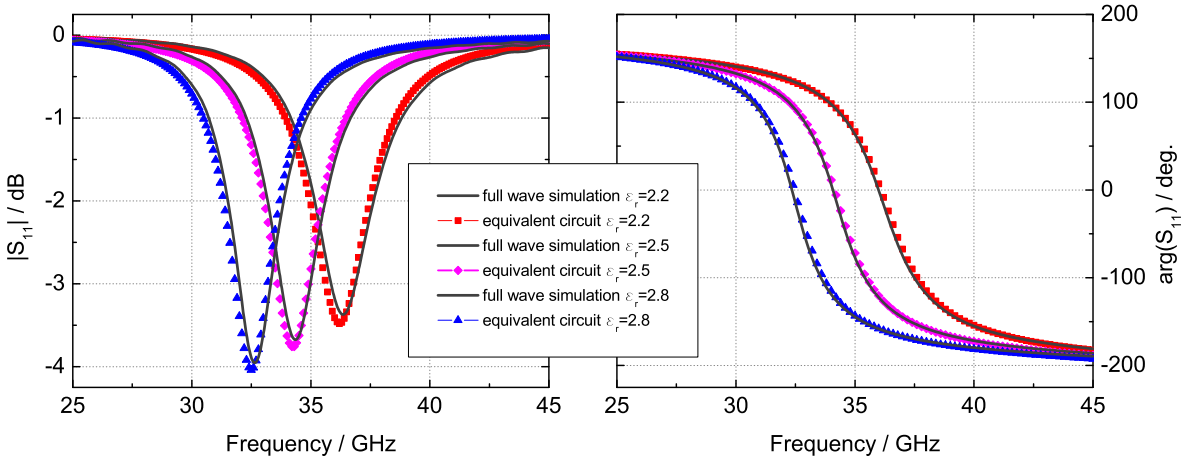

Figure 2.10: Comparison between full wave simulations and equivalent circuit simulations for a reflectarray unit cell with metallic losses (σ=1e7 S/m), substrate with dielectric losses ($\tan\delta$=0.015) and three different values for the relative permittivity of the substrate.

2.3 Overview of Phase Adjustment Mechanisms

In section 2.1 was shown, that the function of a reflectarray is assured by the adjustment of a certain phase distribution on the array elements. This section presents the most important mechanisms for phase control for fixed beam (non reconfigurable) reflectarrays. All methods are based, in principle, on shifting the resonant frequency of a unit-cell of the reflectarray, which in a generic case consists of a microstrip element (mostly microstrip patch) printed on a grounded dielectric substrate.

Elements with Variable Length Stubs

Employing stubs of variable length to control the phase was, historically speaking, the first technique. At each of the microstrip elements of the array, a line stub is attached, playing the role of a fixed phase shifting element (see Fig. 2.11). The energy received by the element as an electromagnetic wave is transmitted over the stub line, reflected at the open end, and then re-radiated by the element. The line stub thus causes a phase shift twice its electrical length.

$$\Delta\varphi = 2 \cdot \beta \cdot \ell = 2 \cdot \frac{2 \cdot \pi}{\lambda} \cdot \ell \,, \tag{2.39}$$

where $\Delta\varphi$ is the phase shift, β and λ are the substrate phase constant and the substrate wavelength respectively, ℓ is the length of the line stub. From Eq. (2.39) is obvious, that the phase shift is directly proportional to the physical length of the line stub. By

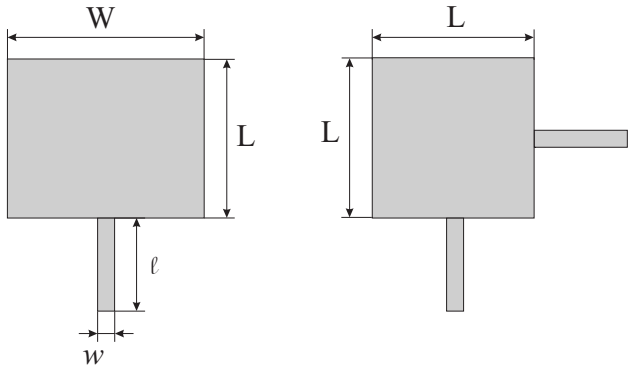

Figure 2.11: Microstrip patch with line stub.

appropriate choice of the line stub lengths, one can thus locally adjust the phase of the reflected wave and obtain a desired phase distribution. The idea to realize such a reflecting element originates in the microstrip antenna fed by a microstrip line. The element is actually a microstrip antenna, operating simultaneously as a receiving and transmitting antenna. The patch length must be therefore, according to patch antenna theory, about $\lambda/2$. Exact formulas for the resonance behavior of a microstrip patch antenna, are given by [Bal97]:

$$f_{res} = \frac{c_0}{2\sqrt{\varepsilon_e}(L + 2\Delta\ell)}\,, \tag{2.40}$$

where

$$\varepsilon_{eff} = \frac{\varepsilon_r + 1}{2} + \frac{\varepsilon_r - 1}{2}\frac{1}{\sqrt{1 + 12t/W}} \tag{2.41}$$

and

$$\Delta\ell = 0.412 \cdot t\frac{\varepsilon_e + 0.3}{\varepsilon_e - 0.258}\frac{(W/t) + 0.264}{(W/t) + 0.8}\,, \tag{2.42}$$

with ε_r the relative permittivity of the substrate, ε_{eff} the effective relative permittivity, L, W and t the patch length, width and thickness respectively, and c_0 the light velocity in vacuum. $\Delta\ell$ is a length extension given by the contribution of fringing fields.

This element works only when the electric field vector $\vec{E}$ is polarized parallel to the line stub, thus exciting the edge to which the stub is attached and allowing energy to couple to the stub. If a circular polarized antenna is desired, the element must be square and it must have two stubs, attached to perpendicular sides of the patch. In all cases, the characteristic impedance of the line stubs must be matched to the radiation resistance of the elements.

A reflectarray with such an element type was first investigated by Huang in [Hua91]. A

realization is reported in [Cha92]: it consists of 32 different elements, used to change the phase in 32 discrete steps (5 bit quantization). The array is 75 cm in diameter, has 2828 elements and was designed to work at 12 GHz. A side-lobe level (SLL) better than 23 dB and 48% efficiency were achieved.

In [Jav95] two 3x4 reflectarrays are presented, working at 10 GHz. The first one is linearly polarized, the second one works in dual polarization. For the linearly polarized one a beam-switching concept is presented and verified: the concept is based on using PIN-diodes connected an different positions between the stubs and the ground.

There are however some difficulties related to the presence of the stubs: the high impedance of the patch (usually more than 200 Ω) has to be matched to the line impedance, leading to very narrow lines at *Ka* band and above. This causes high losses and can pose serious manufacturing problems. Moreover, in order to achieve the desired phase values, some lines will have to be bent, in order to be accommodated in the grid. The bends cause spurious radiation and degradation of the cross polarization.

Elements of Variable Size

A straightforward alternative to the line stubs, is to control the phase simply by varying the dimension of the (square or rectangular) patch. In this case, the phase shifting mechanism is not so explicit like in the case of the line stub patches. The phase required at each element is now adjusted by detuning the patch, i.e. changing its resonant frequency. In terms of the lumped element equivalent circuit presented in section 2.2, a variation of the patch dimension corresponds to a change in both the capacitance C as well as the inductance L, which shifts the phase characteristic, and thus the resonance frequency.

In Fig. 2.12 the phase variation of the reflection coefficient versus the length of a square microstrip patch is exemplary presented for different substrate thicknesses, using RT-Duroid 5880 substrate with $\varepsilon_r = 2.2$, at f=35 GHz.

From the figure some interesting observations can be derived. In order for a reflectarray to function properly, the entire phase range from 0° to 360° must be covered, or as close to that as possible. The diagram shows nevertheless, that the attainable phase range is inversely proportional with the substrate thickness. According to [Tsa03a], the attainable phase range dependency of the substrate thickness is:

$$2\,\pi - 2\,k\,h = 2\,\pi\,\left(1 - \frac{2\,h}{\lambda}\right) = 2\,\pi\,\left(1 - \frac{k\,h}{\pi}\right) \tag{2.43}$$

where k is the wavenumber in the substrate, λ the substrate wavelength and h is the

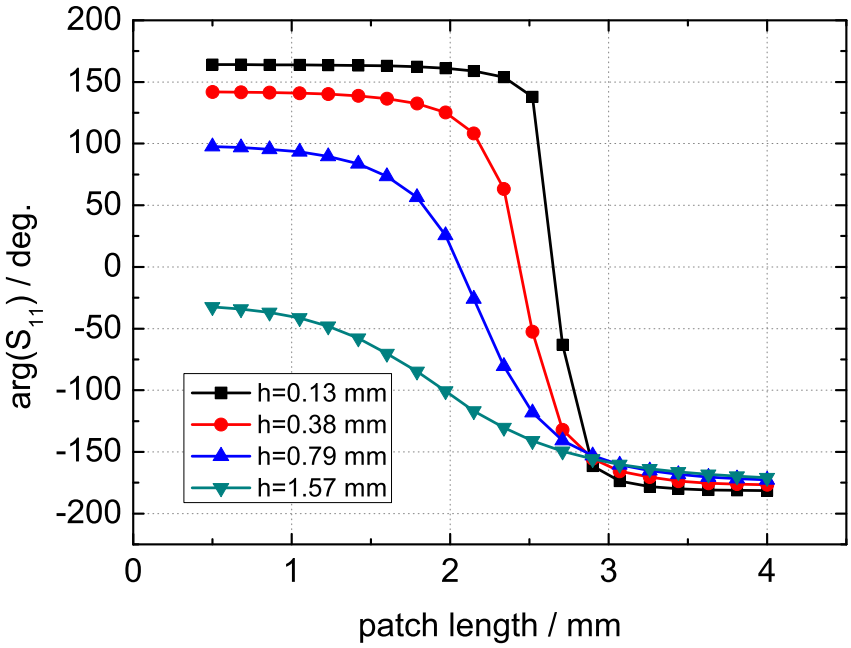

Figure 2.12: Phase of the reflection coefficient for patches with variable sizes (RTDuroid substrate with different thicknesses, f=35 GHz) simulation with *CST Microwave Studio*

substrate thickness. This relation is easy to explain intuitively: when the patch dimension is very small, the incident wave is reflected almost entirely from the ground plane; whereas when the patch dimension is very large, the wave is reflected primarily from the patch. The path difference $2h$ corresponds to a phase difference of $2kh$. The results derived from this equation agree well with results obtained with simulations, as shown in Fig 2.13.

In consequence, when a single substrate is used, there will always be an unattainable phase range, proportional with the substrate thickness. This is an argument in favor of using a substrate as thin as possible, in order to maximize the attainable phase range and minimize the phase errors.

Another interesting feature that can be observed in Fig. 2.12 is the different slope of the curves. The thinner the substrate, the steeper the slope of the curve. The slope is tightly related to the bandwidth of the antenna [Poz97], namely the steeper the curve, the smaller the bandwidth, i.e. a thicker substrate would contribute to a higher bandwidth [Poz03], [Sze99b]. Hence, a compromise has to be made between attainable phase range and bandwidth and the most suitable substrate thickness has to be chosen depending on the targeted performance and application.

The reflectarray using variable sized patches for phase control was introduced by Pozar

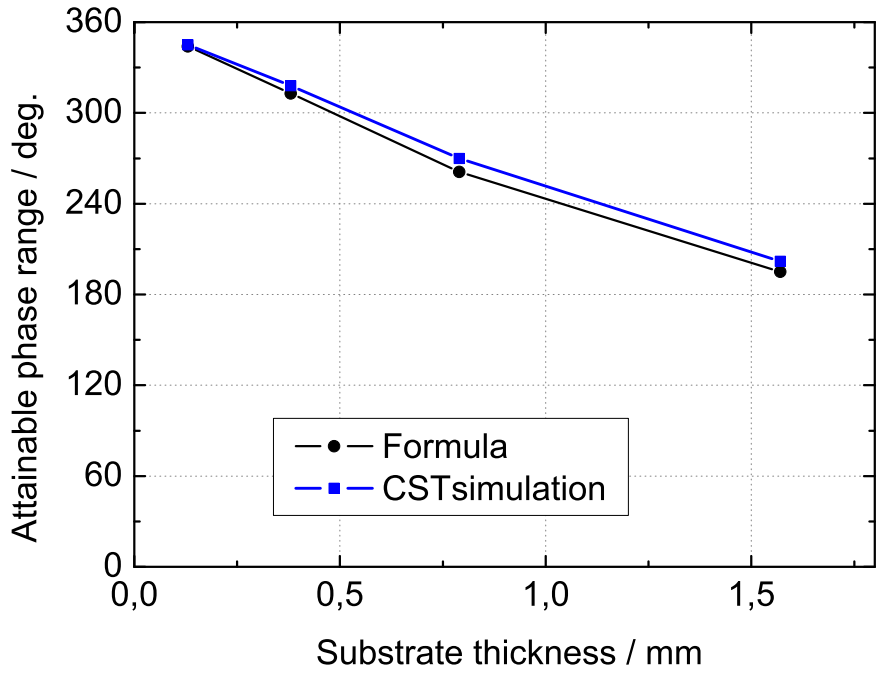

Figure 2.13: Comparison of attainable phase range for different substrate thicknesses using Eq. (2.43) and CST simulation.

[Poz93], and lots of demonstrators have been built since then, for various operating frequencies and various applications.

In [Tar94], a reflectarray with variable patches was realized at 5.3 GHz, having the same parameters as an array using patches with line stubs. The results showed similar characteristics: 27 dB gain, -20 dB SLL , $7.5° \times 7.5°$ half-power beamwidth (HPWB). The 1 dB-gain bandwidth of the reflectarray with variable sized patches was somewhat higher: 4.6% compared to 3.7%.

In [Poz97] several reflectarrays using variable sized patches as phase control mechanism, operating at various frequencies, are designed and realized as showcases. The first two arrays operate at 25 GHz, are square, with the same physical aperture (6x6 in^2) and are fed by a circular corrugated horn. The differences reside in the form, spacing and number of elements. The reflectarrays show similar characteristics, whereas the realization with the substrate of lower losses has a higher efficiency, as expected. This antenna has SLL below -20 dB, 31 dB gain, 54% efficiency and a 1 dB-gain bandwidth of about 5%.

Another reflectarray in [Poz97] has a 9 in diameter and 996 linearly polarized patches and uses a backfire feed. The SLL amounts to about -23 dB and the gain to 31.2 dB, whereas the 1 dB-gain bandwidth is about 2%. The comparison with a metallic reflector with identical diameter and feed, showed that the reflectarray is in some aspects better

than the metallic reflector (SLL, cross polarisation), even though the gain is marginally smaller due to dielectric losses and phase errors. In terms of bandwidth the reflectarray is clearly not comparable with the metallic reflector.

The last two reflectarrays presented in [Poz97] operate at 77 GHz. Actually, it is the same reflector, consisting of 5776 metallic patches printed on a RTDuroid substrate, but fed with two different feeds: a horn antenna in the focal point and a horn antenna in a Cassegrain configuration with hyperbolic subreflector. Both designs showed similar characteristics: 36 dB and 36.9 dB gain respectively, $1.5° \times 1.7°$ HPBW, 2.5% 1 dB-gain bandwidth. The SLL alone was different: -25 dB for the horn-fed reflectarray compared to -19 dB for the reflectarray with Cassegrain feeding system.

Elements with Variable Rotation Angle

Elements with variable rotation angle are another way of controlling the phase of a reflected wave, when the wave is circularly polarized. In [Hua97] it is shown, that the anti-clockwise rotation of an element with an angle ϕ causes a 2ϕ phase delay in the incident left-handed circularly polarized (LHCP) wave. If the wave is right-handed circularly polarized (RHCP), the same element rotation will cause a 2ϕ phase shift of opposite sign (a phase advance). Thus, it is possible with this technique to control the phases of the reflected wave at each element, in order to obtain a cophasal wave front in a desired direction.

In [Hua97], two reflectarrays are presented: one employs patches with line stubs of variable length to control the phase, the other uses identical patches with line stub but with variable rotation angles. The aperture of both arrays is circular, 0.5 m in diameter, consisting of 6924 elements. The design frequency is 32 GHz. The results from both arrays are similar: they both showed SLL below -22 dB, 41 dB gain 53% efficiency, low cross-polarization and a 1 dB-gain bandwidth of about 3.5%.

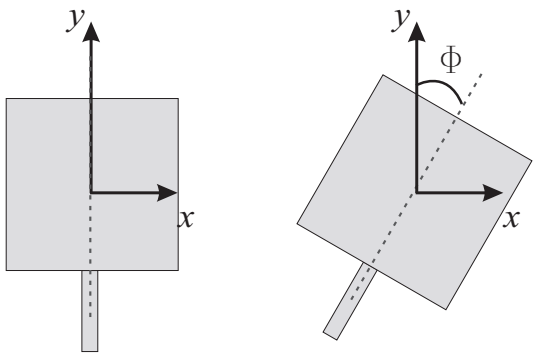

Figure 2.14: Rotation of a microstrip patch with an angle Φ.

Based on the same approach of rotating elements are the reflectarrays in [Han03] and [Str04]. However, the element is not a microstrip patch, but a microstrip ring. The reference for the rotation angle, previously given by one the attached stub-line (Fig. 2.14), is now accomplished by two diametrically opposed slots in the ring. The ring geometry has some advantages compared to the patch geometry: the line stubs are no longer needed to provide a rotation reference and there is no need for impedance matching them to the patch. The ring structure is better suited for dual-layer / dual-frequency applications, due to the enhanced "transparency" compared to the square patches [Han06b]. The reflectarray in [Han03] has 0.5 m in diameter, the design frequency is 32 GHz. It shows a HPBW of 1.3°, a cross polarization level of -40.7 dB, SLL is below -19.5 dB and the efficiency is 50%. In [Str04], a reflectarray using rotated rings working at 7.1 GHz is presented with 28.2 dB and 45.7% efficiency at 7.3 GHz, and a SLL better than 17.3 dB.

Elements with Variable Slots in the Ground Plane

The etching of a slot in the ground plane under the microstrip patch has the effect of inductively loading the patch, since the path of the currents in the ground plane is now longer, having to flow around the slot. One can tune the phase by changing the slot dimensions (mainly the length of the slot) instead of the patch dimensions (Fig. 2.15). This effect is captured in the equivalent circuit proposed in section 2.2 by a change in the value of the inductance L.

This unit cell structure is polarization dependent, since the electric field vector must be perpendicular on the slot, in order to excite it. Two crossed slots could solve this problem in case of linear polarization.

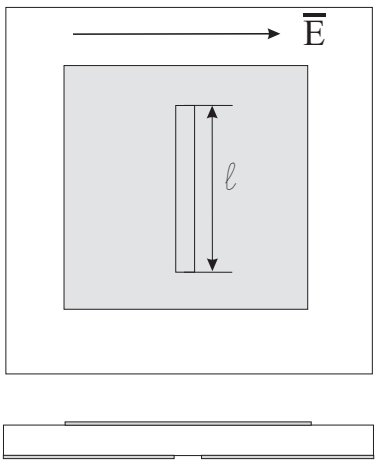

Figure 2.15: Reflectarray unit cell consisting of a square patch and a slot etched in the ground plane

Through the slots, a small part of the power can leak and radiate toward the back of the reflectarray, which is naturally undesirable. The leakage is nevertheless small, and it can be mitigated by bonding another grounded substrate behind the slotted ground.

This phase shifting mechanism was introduced in [Cha02]. In [Cha03c] several breadboards, with one, two and three dielectric layers were manufactured and compared. Each additional layer improves the electrical characteristics of the reflectarrays (see Table 2.2). Whether there is a bandwidth improvement owing to the use of crossed slots with varying arms as the authors suggest is unclear, since the main contribution to the superior bandwidth is achieved with the thicker substrate.

Table 2.2: Three reflectarrays with varying crossed slots in the ground plane from [Cha03c]: comparison of electrical properties

Nr. of diel. layers	One	Two	Three
Operating frequency	26 GHz	30 Gz	30 GHz
Measured Gain	28.65 dB	29 dB	30.5 dB
Efficiency	38%	43%	53%

Elements with Coupled Microstrip Line

The concept of an element consisting of a patch and a line coupled to it is derived from the patch with stub line . There are two possible coupling methods: proximity coupling or coupling through an aperture in the ground plane (see Fig. 2.16). The reflection phase can be adjusted just as in the case of the patch with stub line by varying the line length.

The use of these coupled structures has some advantages: the two layer configuration enables more design flexibilities, allowing for instance a better matching or enhanced bandwidth in case of proximity coupling, or separation of the radiating element from the phase shifting element by a ground plane in case of the aperture coupled line, which reduces spurious radiation. The aperture-coupled line concept can also prove advantageous in case of an electronically reconfigurable unit cell, since all the bias circuitry can be on the layer behind the ground plane, thus not interfering with the propagation of incident and reflected waves.

A microstrip reflectarray with proximity-coupled microstrip lines is presented in [Cha04]. It is designed for a center frequency of 11.6 GHz and exhibits a 3 dB-gain bandwidth of 22%. However, how much of this large bandwidth is due to the proximity coupling is

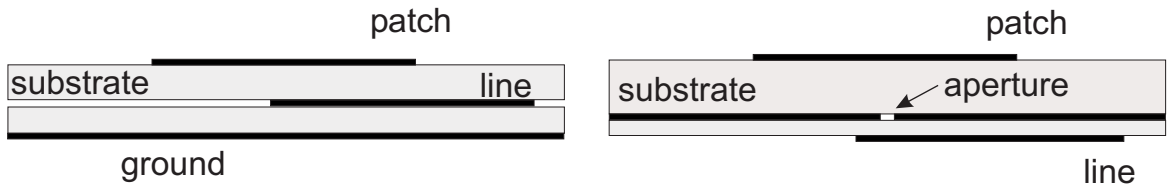

(a) Proximity coupled line (b) Aperture coupled line

Figure 2.16: Possible configurations with microstrip line of variable length coupled to the radiating element (microstrip patch)

unclear, since Pozar showed in [Poz04] that most of the bandwidth enhancement is owed to the thick substrates chosen for the realization.

A unit cell with microstrip line coupled to a patch through a slot is presented in [Car06]. The range in which the phase can be adjusted is proportional to the line length; thus, by folding the line, very wide phase range of more than four cycles ($4\times360^\circ$) can be achieved. In [Car07] the length of the coupling slot is also varied along with the line length to achieve enhanced phase linearity.

2.4 Other Types of Elements for Microstrip Reflectarrays

Up to this point, different techniques for varying the phase of a reflected wave using microstrip structures were presented. The vast majority is based on microstrip patch as reflectarray element. It is possible to use other structures besides patches for the construction of a reflectarray. In this part some of this possible structures are presented, together with their advantages and disadvantages.

The square **microstrip patch** is the most common element used for the realization of microstrip reflectarrays. This is due to the increased radiation efficiency, as well as to the better bandwidth, as compared to a **dipole** element. As shown in [Sie03], a more homogeneous field distribution under the metalization means a wider band operation, and this is achieved with a patch rather than with a dipole. The compared characteristics of the complex reflection coefficients of a square patch and dipole (Fig. 2.17) make also clear, that the patch has a wider bandwidth, derived from the gentler phase slope compared to the dipole. The wider bandwidth and the lower reflection losses make the patch preferable to the dipole in most practical reflectarrays.

A special type of reflectarray (folded planar reflector), developed at the University of Ulm uses as elements microstrip patches where both dimensions are varied independently. The depth of this reflectarray type is reduced by half through the use of a polarizing grid: the feeding horn is integrated in the reflector surface, and the polarizing

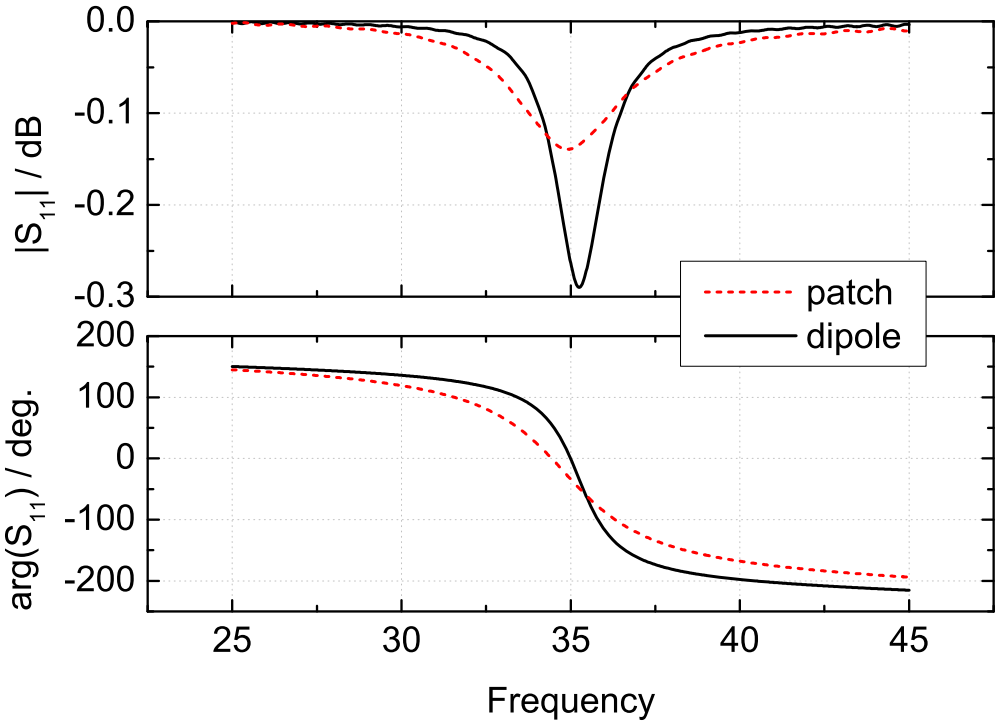

Figure 2.17: Comparison between complex reflection coefficients of square microstrip patch and microstrip dipole: above magnitude, below phase.

grid is placed in front of the reflector. The electric feed radiated by the feed is totally reflected by the polarizing grid, then captured by the microstrip elements. By independently varying both dimensions of the patch, it is possible to change the polarization of the electric field with 90° as well as to adjust its phase to collimate the beam. The re-radiated, focused field is thus able to pass the polarizing grid.

Limited bandwidth is the major drawback of microstrip reflectarray, caused by two factors: the intrinsic limited bandwidth of the microstrip element and the bandwidth limitation introduced by non-constant path delays over the surface of the flat reflector [Poz03]. However, it has been shown that the bandwidth limitation due to the narrow band element is the dominating effect [Poz03]. An element that has the benefit of significantly enhancing the bandwidth consists of two or even more **stacked patches**. It is well known that a parasitic patch over the active patch increases the bandwidth of a microstrip antenna [Cro91]. This also remains true in the case of reflectarrays, as has been extensively proven by Encinar in a series of publications [Enc96, Enc99, Enc01, Enc04].

2.5 Electronically Reconfigurable Reflectarrays

Planar printed reflectors (reflectarrays) and lenses have some advantages with respect to weight and manufacturing complexity, in comparison to other antenna classes, and are therefore particularly suitable for many applications such as space missions. A very desirable extension of their functionality would be the capability of electronic beam steering, a specific beam forming or a variable focusing (in the case of lenses). Such antennas already exist, they are however complex, large, heavy and expensive, because of the incorporation of costly phase shifters, attenuators and beam forming networks. To achieve more cost effective and more compact solutions, a lot of research has been invested in the past years in the design of electronically reconfigurable reflectarrays. The phase shifters required for beam shaping/beam steering are to be integrated in the radiating element in order to reduce cost and complexity. For this purpose a few technologies emerged as candidates: semiconductor based PIN diodes or varactor diodes, Micro-Electro-Mechanical-Systems(MEMS) [Boc02b, Hum05a, Leg05] or ferroelectric based phase shifters.

Diodes

An approach for a reconfigurable reflectarray with varactor diodes is presented in [Boc02b, Boc02a]. It is based on loading the radiating edge of a microstrip patch (as reflectarray element) with a varactor diode, as shown in Fig. 2.18(a). The varactor diode causes a tunable capacitive reactance, which enables the adjustment of the electrical length of the patch. Thus, the electrical length of the element, and consequently the phase of the reflected wave, can be adjusted via the tuning voltage of the varactor diode. The drawbacks of this approach are the reduced phase range of only 180° and the necessity of via holes in the substrate, making manufacturing more difficult. In [Boc02b, Boc02a], the authors show a prototype linear reflectarray consisting of 5 patches and operating at 10 GHz, with a main beam that can be steered between ±15° with tuning voltages of up to 11 V.

Another approach, making use of varactor diodes as well, is presented in [Hum04, Hum05a]. The phase shifting and at the same time radiating element consists here of two halves of a microstrip patch, connected together by two varactor diodes (see Fig. 2.18(b)). According to measurements performed in a waveguide simulator, a phase range of 328° can be swept at 5.25 GHz. To this purpose, tuning voltages between 0 and 20 V are applied. The losses in such an elementary cell fluctuate with the applied voltage and they are highest (4-5 dB) around the resonant electrical length of the patch, as expected [Hum04].

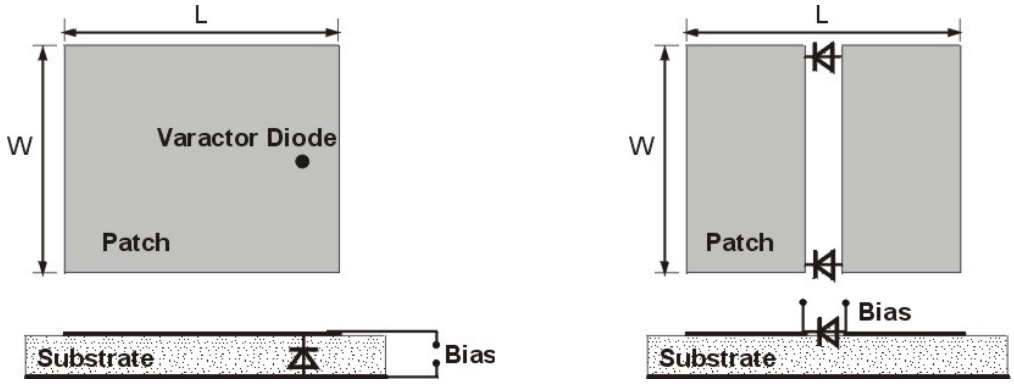

(a) Radiating edge of microstrip patch loaded with varactor diode.

(b) Two half-patches connected by varactor diodes.

Figure 2.18: Two concepts of electronically tunable reflectarray unit cells with varactor diodes.

The elements, originally designed for 5.5 GHz, worked best at 5.8 GHz, where the tunable phase range amounts to 325° and the peak losses are about 3.5 dB around resonance. Based on this element, a 7x10 reflectarray has been realized in [Hum05a], in order to demonstrate the beam steering capability. The main beam could be steered with adequate performance up to 40°.

In conclusion, both approaches are suitable for the realization of a reconfigurable reflectarray. Whereas the first approach is limited to an adjustable phase range of 180°, the second approach could theoretically achieve 360° and therefore, it is suitable for the realization of large arrays, where all phase states are required between 0° and 360°.

The advantages of tunable reflectarray elements with semiconductor diodes are the relatively simple and cost effective realization, as well as the low required tuning voltage. However, a decisive drawback is the impracticality for higher frequency application (*Ka*-Band and above), because of inappropriate performance of the semiconductor devices due to high parasitics, like series resistance or parasitic capacitances.

MEMS

A lot of research has also been dedicated in the past years to the possibility of MEMS integration in the printed reflectarray elements for the purpose of electronic beam steering. RF-MEMS are a very promising technology for realizing phase shifting in reflectarrays, due to their good electrical properties in low power applications (very high isolation, low losses), compared to semiconductor diodes or FETs.

In the following, a few concepts of reconfigurable reflectarray unit cells involving MEMS

will be briefly presented. One concept, described in [Leg03] uses MEMS to create "rotating" printed dipoles. The unit cell consists of twelve dipole halves, printed circularly on a substrate, as shown in Fig. 2.19. Two opposite dipole halves are at any given time contacted (switch *on*), while the other halves are discontinued (switch *off*). Thus, a dipole structure is created, that has a different rotation angle according to the tuning state of the MEMS. Via the rotation angle, the phase of the reflected wave can be adjusted (assuming that the wave is circularly polarized) as already shown in Section 2.3. Such elementary unit cells have been realized and measured in a waveguide simulator: the results, especially the low reflection losses of less than 1 dB are very promising. Nevertheless, to our knowledge, a complete reconfigurable reflectarrays employing this element has not been yet realized.

Other approaches to tunable MEMS unit cells for reflectarrays working in linear polarization have been proposed, for instance in [Leg05],[Men05]. The unit cell in [Leg05] consists of a printed patch with two slots, bridged in various places by MEMS switches (see Fig. 2.19 (b)). Various states of the switches correspond to various lengths of the slots, and consequently to various values of the reflection phase. With n a total number of MEMS 2^n phase states can be set. A realized reflectarray unit cell of this type shows according to measurements in the waveguide simulator reflexion losses of about 1 dB.

The approach in [Men05] aims at the separation of the radiating element from the phase shifting element: the radiating element is a microstrip patch, coupled through an aperture to a microstrip line. The line is bridged by several MEMS switches connected to ground (Fig. 2.19 (c)). At any given time, one of the MEMS switches is actuated (*on*-state), while the others are not (*off*-state). By switching a different MEMS *on*, the length of the line can be varied, and thus the phase of the reflected wave.

A considerable drawback of tunable reflectarray unit cells based on MEMS switches is their complexity. In order to achieve a high discretization that would mitigate phase errors, an accordingly high number of switches and associated bias lines would have to be integrated in the elementary cell. For reflectarrays with hundreds or even thousands

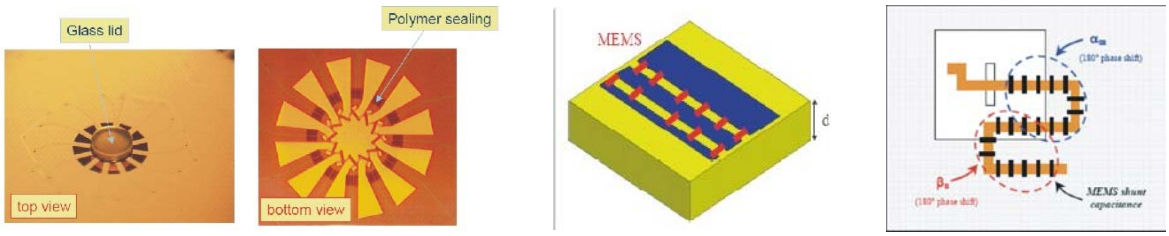

(a) From [Leg03] (b) From [Leg05] (c) From [Men05]

Figure 2.19: Different concepts of electronically tunable reflectarray unit cells with MEMS switches.

of elements, that are common in satellite communications or radar applications, this leads to a high implementation effort, and implicitly to high implementation costs.

Another drawback of the MEMS switches is that the technology is not completely mature: in order to realize MEMS with very good electrical properties, a high number of processing steps are required. If the number of process steps is reduced, as a rule the quality drops accordingly, impeding on the RF-properties of the switch. Packaging and reliability of MEMS are as well still unresolved problems that make the use of MEMS in security related or long-life applications questionable.

Ferroelectrics

Tunable phase shifters employing ferroelectric films have been studied for potential application in reflectarrays. A scanning reflectarray operating at 19 GHz was proposed by the NASA in [Rom00]. The phase shifters are based on a series of coupled microstrip lines, patterned over an approximately 400 nm thick $Ba_{0.60}Sr_{0.40}TiO_3$ film. They are terminated in an opened circuit and used in reflection mode.

The phase shift is controlled by varying the bias voltage across the coupled lines. The partial anatomy of a prototype K-band scanning reflectarray antenna incorporating 615 thin film ferroelectric phase shifters is shown in Fig 2.20. Each phase shifter is wire bonded to the microstrip patch antenna. The active array diameter (Fig. 2.20, center) is 31 cm. The 6-layer bias control board engages 615 bias pins on the backside of the reflectarray plate. The associated controller consumes 22 W. A dual-mode feed horn (not shown) illuminates the array [Rom07].

The use of ferroelectric films is critical in this configuration because of the very high dielectric constant and high losses. Indeed, the assumption made in [Rom00] for the design of the reflectarray is that a 3 dB insertion loss reflection phase shifter can be

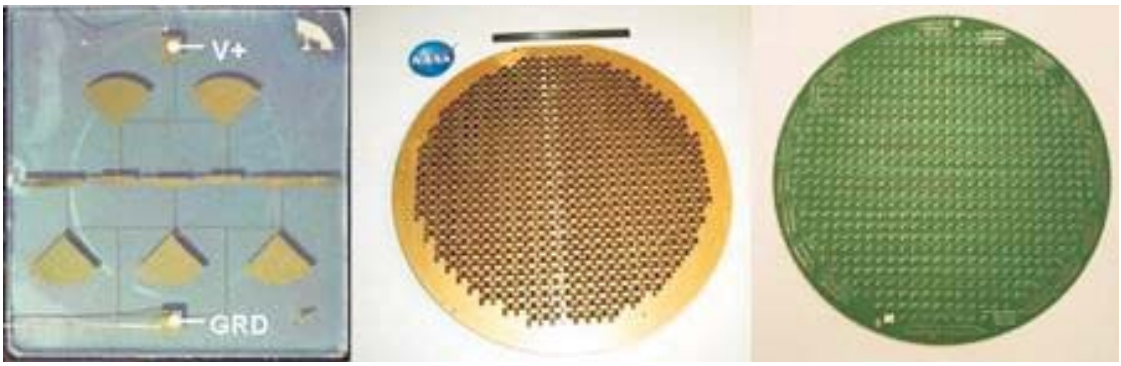

Figure 2.20: Pictures of the reflectarray with BST phase shifters (from [Rom07]).

consistently reproduced, whereas demonstrated insertion losses lie typically in the 5 dB range. A further inconvenience is represented by the high voltages needed to achieve the desired phase shift. Bias up to 350 V is applied to the sections via printed bias-tees, consisting of a quarter-wavelength radial stub in series with a very high impedance quarter-wavelength microstrip (see Fig. 2.20, left).

Alternative Approach Based on Liquid Crystals

An entirely novel approach for cost effective, reconfigurable reflectarrays, which avoids some of the aforementioned drawbacks of semiconductor diodes, MEMS switches or ferroelectric phase shifters, is in the main focus of this work. This approach is based on the use of anisotropic nematic liquid crystals as tunable materials in the microwave region of the electromagnetic spectrum (300 MHz bis 300 GHz). Instead of using lumped elements (diodes or MEMS), the microstrip structures of the reflectarrays are to be realized on a liquid crystal substrate with tunable dielectric permittivity.

The basic idea lies in the change of the relative permittivity of the liquid crystal by applying a controllable DC voltage between the ground plane and the microstrip element. The detailed architecture and functionality of such a unit cell, as well as measured results and alternative concepts, will be presented in chapter 5.

Unlike semiconductor diodes, whose functionality is limited up to about 15 GHz, liquid crystals are a much more promising solution in a frequency domain from 10 GHz up to several THz, since the material quality factor does not degrade with increasing frequency. Unlike MEMS, a liquid crystal unit cell can be continuously tuned, and therefore only one tuning voltage per unit cell is necessary. Packaging and reliability are, according to the existing experience from liquid crystal displays, not particularly problematic. These arguments suggest, that liquid crystals could be a promising technology for use in reconfigurable reflectarrays.

This approach is currently being pursued simultaneously at the Darmstadt University of Technology [Mar05, Mar06a, Mar06b, Moe06b, Moe06a, Moe07, Mar07], and at the Queens University of Belfast [Ism05a, Ism05b, Hu06].

2.6 Summary

After a brief theoretical background on reflectarrays, a lumped element equivalent circuit for microstrip reflectarray unit cells was proposed and described. The equivalent circuit allows accurate modeling and prediction of dielectric and metallic losses, based on the

physical characteristics of the unit cell (geometry, substrate and metalization properties). It is also possible to evaluate the effect of changes in the substrate permittivity on the phase and magnitude characteristic using the equivalent circuit.

Next, a classification of reflectarrays by the phase adjusting mechanism allows a review of the most important reflectarray types from the literature. A subchapter is dedicated to the overview of the different existing techniques for reconfigurable reflectarrays: based semiconductor diodes, MEMS or ferroelectric phase shifters. It was shown that each of these concepts has some drawbacks in some areas (high frequency suitability for diodes, complexity and reliability for MEMS, control voltage level and losses for ferroelectrics) so that the investigation of an alternative approach is justified.

Chapter 3

Fixed Beam Reflectarrays with Various Feeds

As a preliminary step toward the realization of liquid crystal reconfigurable reflectarrays, a number of fixed-beam (non-reconfigurable) microstrip reflectarrays have been designed, realized and investigated. In the process, special attention has been given

- to the feeding structure, as one of the most important components of a reflectarray antenna, having great impact on the overall stability and compactness of the reflectarray.
- to the problem of the bandwidth of reflectarrays, since the reduced bandwidth is one of the drawbacks inherent to any microstrip antenna, and

In this chapter, first the steps in the design of a microstrip reflectarray are described taking as example a reflectarray with single rectangular microstrip patches as elements. Then, different reflectarray realizations are presented, either with more complex elements or with different feeding structures. The primary goal is to verify different feeding concepts, whereas a bandwidth optimization is attempted for the offset fed reflectarray.

3.1 Design Procedure

The steps in the design of a fixed-beam microstrip reflectarray can be resumed as follows (see also [Poz97]):

1. Based on the desired operation frequency and bandwidth, a suitable substrate is chosen, whereas thickness, permittivity and losses play a major role.

2. A field-solver simulation is performed to obtain the complex reflection coefficient of an elementary cell in an infinite array environment (as detailed in 2.1) versus a sweep

in the geometrical dimension that controls the resonance (for instance the length in case of a microstrip patch, or the length of the line in case of a patch coupled to a microstrip line).

3. The data obtained in step 2. is interpolated to generate a look-up table, from which the dimensions of each element are derived from the phase-delay condition in Eq. (2.15).

4. The pattern of the reflectarray can be computed using array theory (according to section 2.1). The amplitude and phase of the exciting field can be derived from the radiation pattern of the feed and geometrical optics.

In order to exemplify the four steps listed above, the design process of a fixed beam microstrip reflectarray having as elements variable rectangular microstrip patches will be described in more detail.

The desired operating frequency of the reflectarray is chosen at 35 GHz. As a compromise between bandwidth and adjustable phase range a Rogers 5880 substrate with a thickness of $h = 0.79$ mm has been chosen. The phase variation over patch length is depicted in Fig. 3.1.

For this particular elementary cell, the phase variation has been computed using three different methods: one method uses an algorithm based on the method of moments

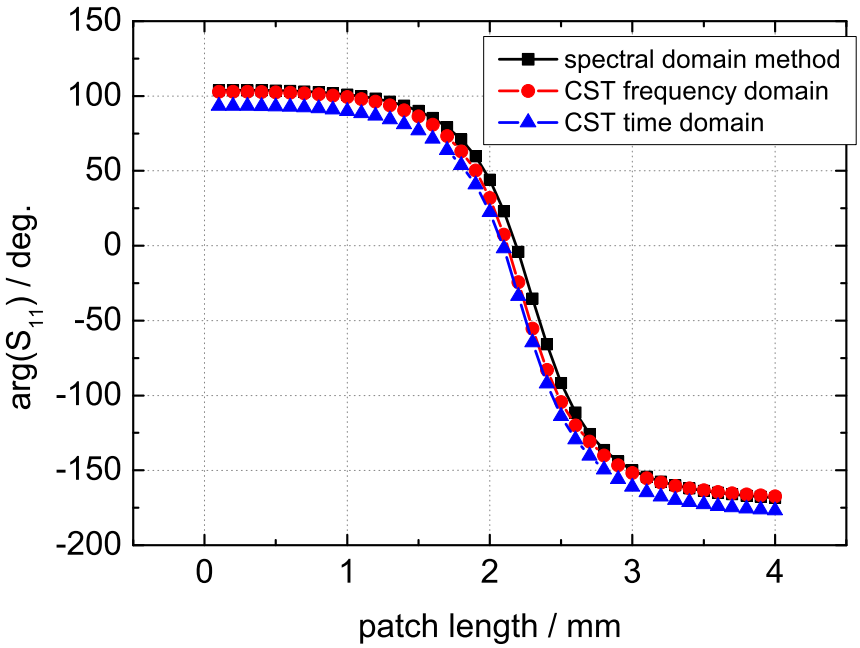

Figure 3.1: Phase variation over patch size calculated with three different methods for a reflectarray unit cell with variable length microstrip patch printed on RT DUroid 5880, h=0.79 mm.

developed at the University of Ulm [Pil99], the other two being results obtained with the commercial field solver *CST Microwave Studio*: one with the Time Domain Solver and the other with the Frequency Domain Solver. From the figure is apparent that the differences are minor: apart from a slight offset, between CST-Time Domain and MoM the difference in phase is highest near resonance, reaching about 20° and staying below 10° for the rest of the computed domain, while the phase difference between the CST-Frequency Domain and the other two methods is also small. The amplitude plot is not shown, since in the case of RF substrates with losses in the order of about $\tan\delta = 0.001$ there is no significant return loss (in the order of 0.1-0.2 dB) In this work, simulations performed with the CST-Time Domain Solver were used in step 2. of the design process.

The look-up table consisting of interpolated data of step 2. is used to generate the patch dimensions that satisfy equation 2.15. With the computed patch dimensions, a mask can be generated as shown exemplary in Fig. 3.2.

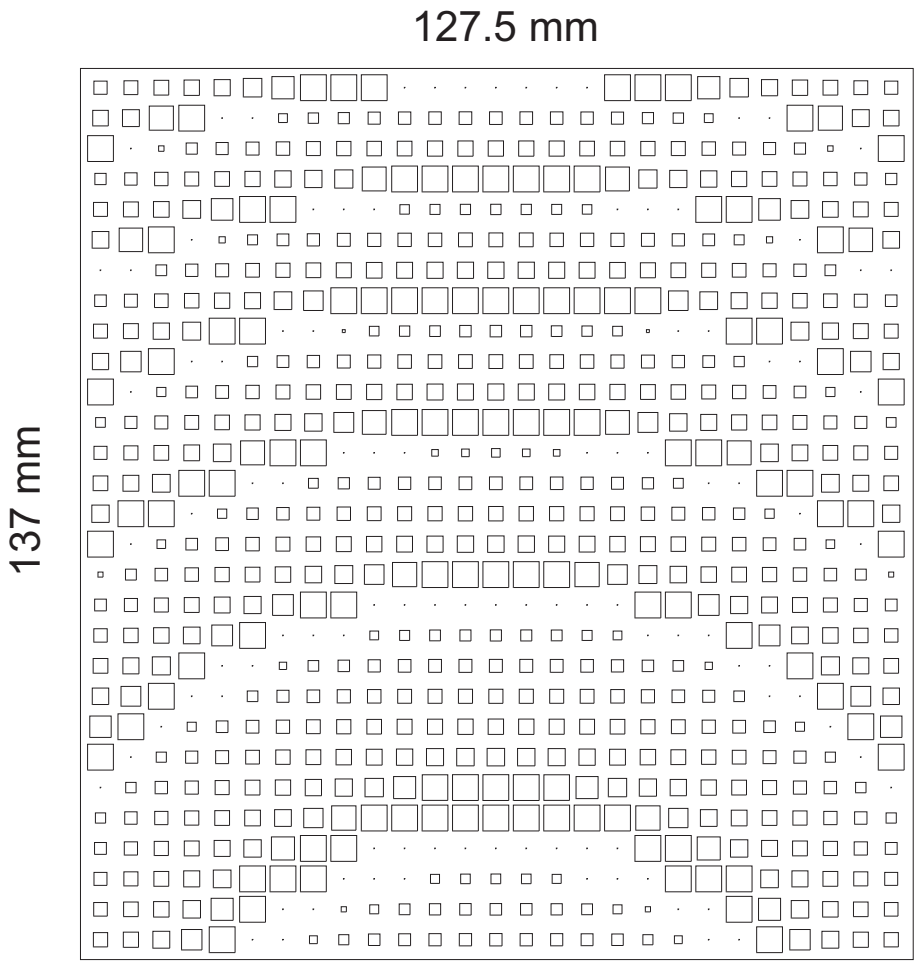

Figure 3.2: Mask layout for the single layer reflectarray with variable length microstrip patch.

3.2 Offset Fed Reflectarrays with Bandwidth Optimization

Like in a parabolic reflector, a variety of antenna configurations can be used to feed a reflectarray: center feed, Cassegrain-feed, offset feed, to name just a few. The feeding with an offset horn antenna is one of the most widespread feeding configurations. Its main advantage is that the displacement of the feed from the symmetry axis of the reflector reduces significantly the aperture blockage, thus improving the efficiency.

As shown in section 2.4, a drawback of reflectarrays is the reduced bandwidth. Therefore, an optimization of the elementary cells with regard to bandwidth was attempted. To this purpose, unit cells composed of two resonant elements were investigated: 1.) two stacked square patches and 2.) a patch with a crossed-slot etched in the ground plane. As shown in [Enc99] and [Cha02, Cha03c] respectively, these configurations are proved to improve the bandwidth of reflectarrays, when used as elementary cells.

The optimization approach of the unit cell with respect to bandwidth takes into account two degrees of freedom: the dimensions of the lower and upper patch in one case, and the patch dimension and slot length in the other case. Since there are two variable parameters, there are multiple combinations yielding the same reflection phase (according to Fig. 3.3(a)). Among these patch/slot or patch/patch combinations, a routine chooses the combination with the smoothest phase slope, since this has been shown to be an appropriate measure of the bandwidth. The following quantity is used as measure for the phase slope:

$$\nabla\phi = \sqrt{\left(\frac{\partial\phi}{\partial\ell_{patch}}\right)^2 + \left(\frac{\partial\phi}{\partial\ell_{slot}}\right)^2} \tag{3.1}$$

Moreover, care must be taken that so little power as possible is radiated toward the back of the reflectarray, through the slot. It is apparent from Fig. 3.3(b), that for some patch/slot combinations a large amount of power is lost through this mechanism, so that these combinations should be avoided. As an indicator for a suitable patch/slot (or patch/patch) pair, the following factor can be computed:

$$Q = \frac{\nabla\phi}{S_{11}} \tag{3.2}$$

A minimization of this factor ensures that a combination with smallest possible phase slope is chosen, ruling out at the same time combinations with power loss.

For the chosen substrate thickness and permittivity (RTDuroid 5880, ε_r=2.2, h=0.79 mm), a design with only one degree of freedom cannot attain a 360° phase range, whereas

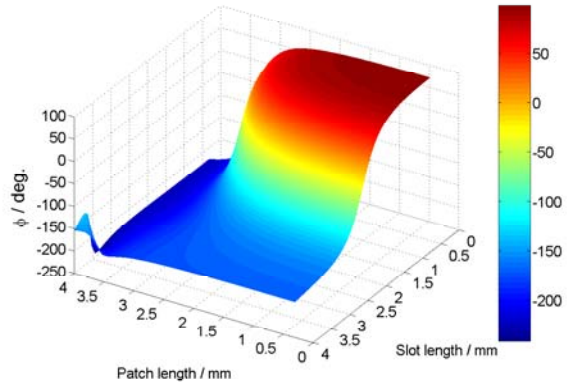

(a) Phase space of all patch/slot combinations.

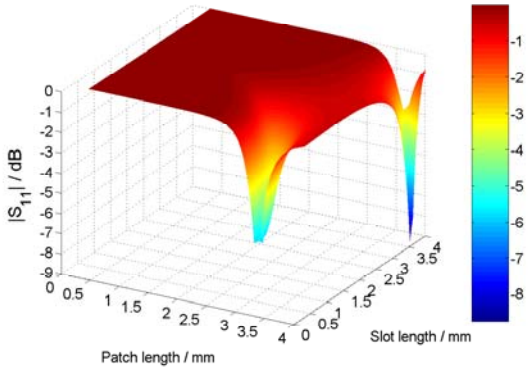

(b) Reflection loss space of all patch/slot combinations.

Figure 3.3: Phase and magnitude of the unit cell with patch and crossed slot in the ground plane for all combinations of patch length and slot length. Similar diagrams ensue for the stacked patch unit cell.

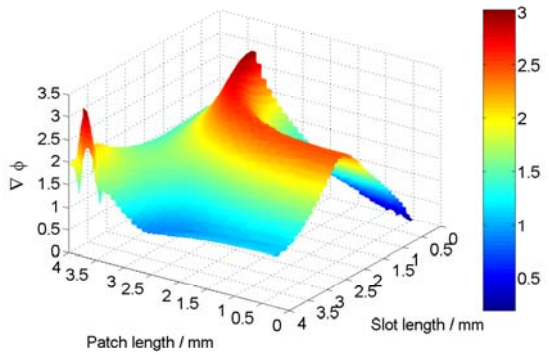

(a) $\nabla\phi$ for all patch/slot combinations.

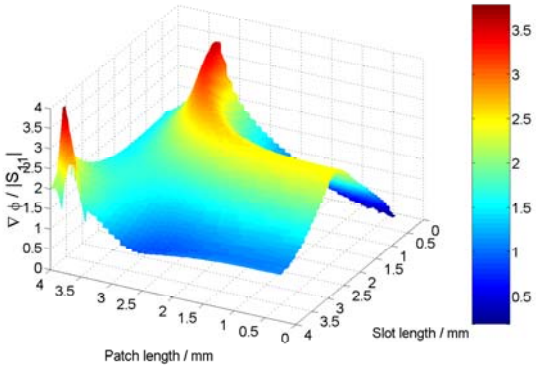

(b) $Q = \nabla\phi / |S_{11}|$ for all patch/slot combinations.

Figure 3.4: Plot of the two evaluation factors from Eq. 3.1 and Eq. 3.2 exemplary shown for the unit cell with patch and crossed slot in the ground plane for all combinations of patch length and slot length.

independent variation of patch/slot or patch/patch dimensions can provide the entire 360° range. In order to verify the assumption, that this technique would lead to increased bandwidth, two reflectarrays were realized at 35 GHz. The first array makes use of the technique of varying only patch sizes and it is used as a reference, the second of varying both patch and slot sizes.

The reflectarrays were identical in terms of size and number of elements (27x29). The elements have a grid spacing of 0.55λ, a common value for element spacing in phased arrays that avoids the appearance of grating lobes [Bal97, Kra88]. The pyramidal feeding horn was 20° offset to minimize aperture blockage, and the phase distribution over the

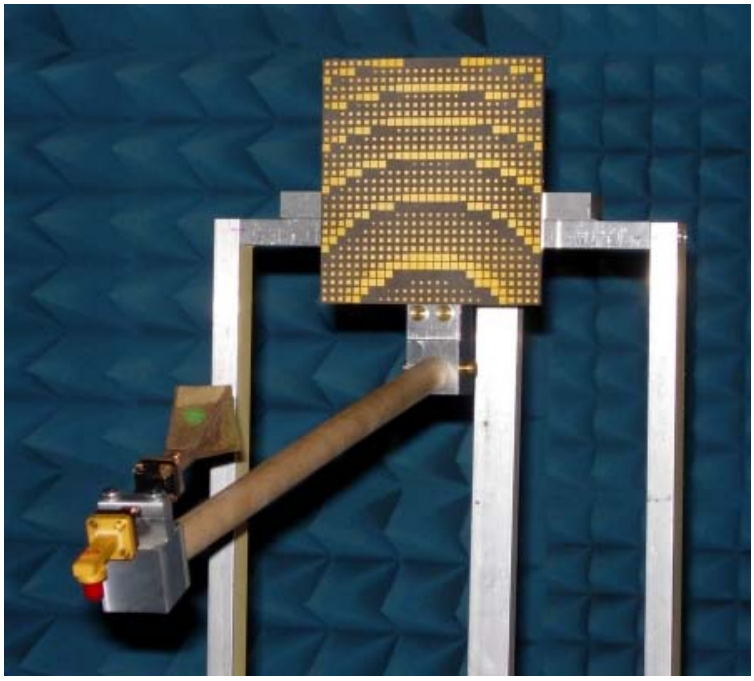

Figure 3.5: Picture of the realized stacked patch reflectarray mounted for pattern measurements

array is such chosen to direct the main beam broadside. Measurements of the two realized reflectarrays were performed in an anechoic chamber.

The element factor of the microstrip patch will only influence the array pattern for relatively large angles away from broadside (>40°), contributing to a reduction in the side lobes or to a gain reduction in the main beam, in case of a beam pointing away from broadside [Wie02].

Fig. 3.5 shows the reflectarray with variable length single patches on the measurement stand. In Fig. 3.6 and 3.7 the far-field power pattern at 35 GHz for the reflectarray with variable length single patches and for the reflectarray with patches and slots in the ground plane are shown, respectively. In both cases fair agreement is observed between the calculated and the measured results, concerning the position of the main beam and of the nulls. Mutual coupling between elements, which was not taken into consideration in the simulation, could account for the higher side lobes in the measurement.

The gain measurements revealed good agreement between calculated and measured gains for both reflectarrays. The calculated gain for the reflectarray with variable size patches was 28.57 dBi, while the measured gain amounted to 27.5 dBi. In case of the reflectarray with variable patches and slots in the ground plane, the calculated gain was 28.16 dBi, and the measured gain 26.1 dBi. The measured gain of the second reflectarray was about 1,4 dB lower probably due to additional losses caused by the slots. Both arrays reached maximum gain at about 35.7 GHz. The relative 1 dB-gain bandwidth of

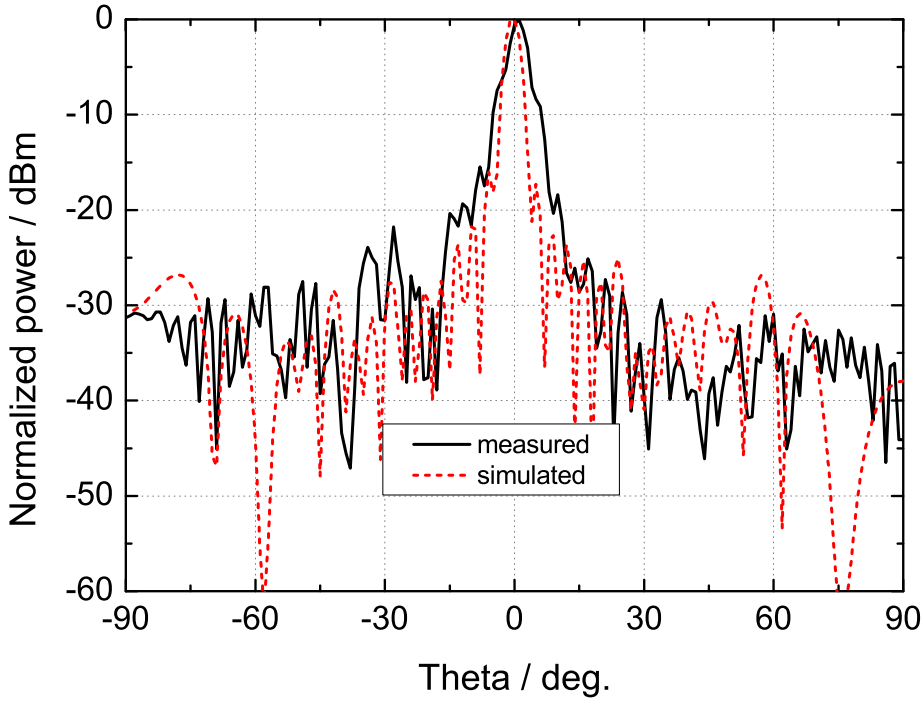

(a) E-plane

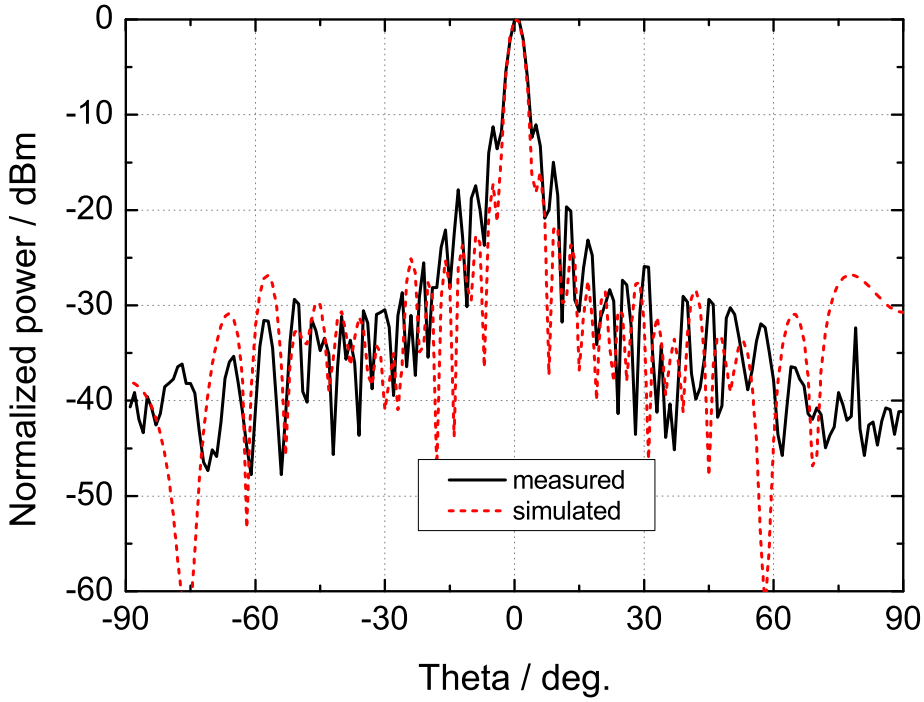

(b) H-plane

Figure 3.6: Measured far-field patterns of the reflectarray with variable single patch unit cell.

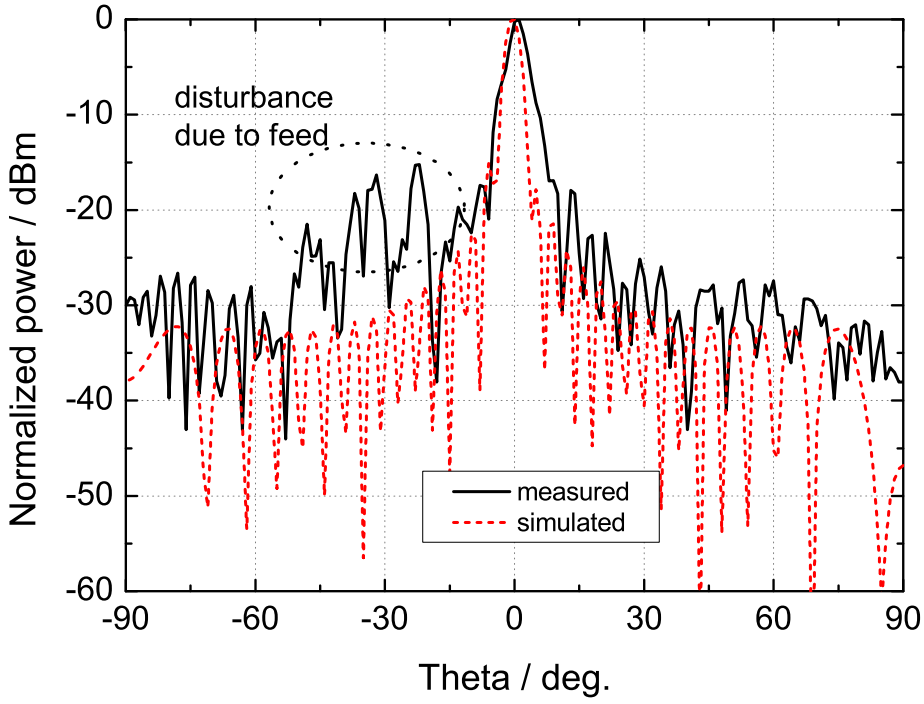

(a) E-plane

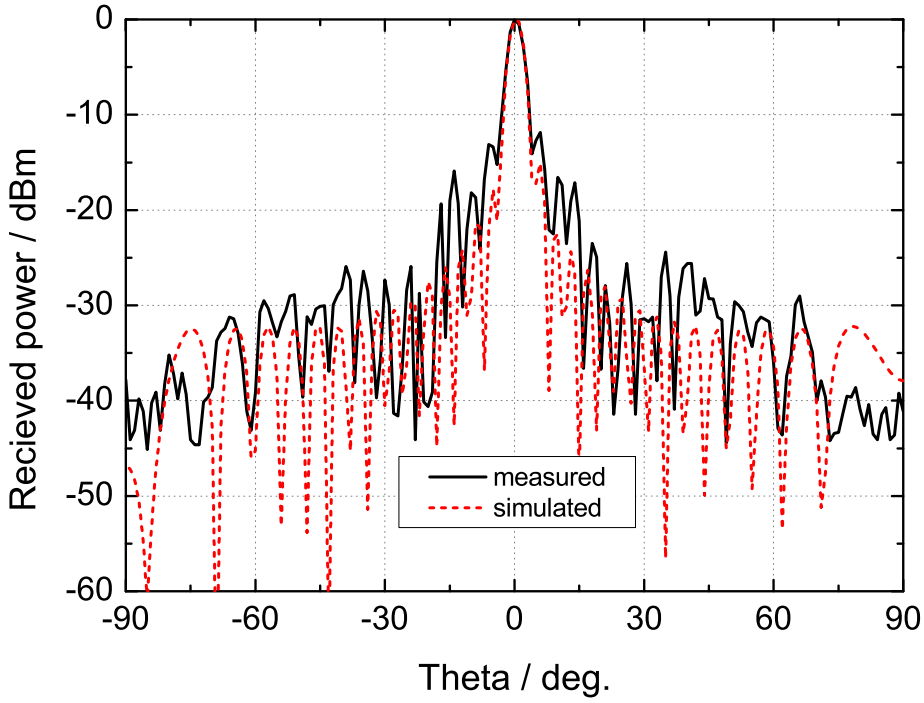

(b) H-plane

Figure 3.7: Measured far-field patterns of the reflectarray with patch/slot unit cell.

the reflectarray with optimized elements is 8.31%. It is only slightly larger than the bandwidth of the array with only variable patches with 7.68%, as it can be seen in Fig. 3.8(a). It is hence inconclusive if the optimization algorithm proposed here can achieve a significant bandwidth enhancement.

Manufacturing tolerances also contributed to the fact that the increase in bandwidth was low. Using two degrees of freedom (variable size patches loaded with variable length slots) instead of just one (variable size patches) leads to an increase in the phase range that can be achieved, from 310° to more than 360°. This suggests, that one could use a thicker substrate to increase the bandwidth, compensating the reduction in phase range by using two degrees of freedom. This has been verified by realizing a double layered reflectarray with stacked patches as elements. This reflectarray achieved a higher bandwidth than the previous two, due to the thicker substrates (both RTDuroid 5880, ε_r=2.2 and h=1.5 mm) but also due to the applied optimization routine presented previously. The measured bandwidth is shown in the Fig. 3.8(b). The relative 1 dB-gain bandwidth is also about 9.6%, whereas the relative 3 dB-gain bandwidth reaches up to 16.5%, which are good values compared to the ones in the literature.

A summary of the properties of the three realized fixed-beam reflectarrays with offset feed is presented in Table 3.1.

Table 3.1: Summary of the realized fixed-beam reflectarrays with offset feed.

Element Type	Simple square patch	Patch + slot in ground plane	Stacked patches
Substrate Type	RTDuroid 5880 ε_r=2.2 tan δ=0.0009		
Substrate Thickness	h=0.79 mm	h=0.79 mm	h_1=h_2=1.5 mm
SLL in E-Plane	-16 dB	-17 dB	-16 dB
SLL in H-Plane	-11 dB	-12 dB	-13 dB
Calculated Directivity	30.4 dB	30 dB	30.9 dB
Measured Gain	27.5 dB	26.1 dB	28.5 dB
Efficiency	51%	40.73%	57.5%
1 dB Gain Bandwidth	7.68%	8.31%	9.6%

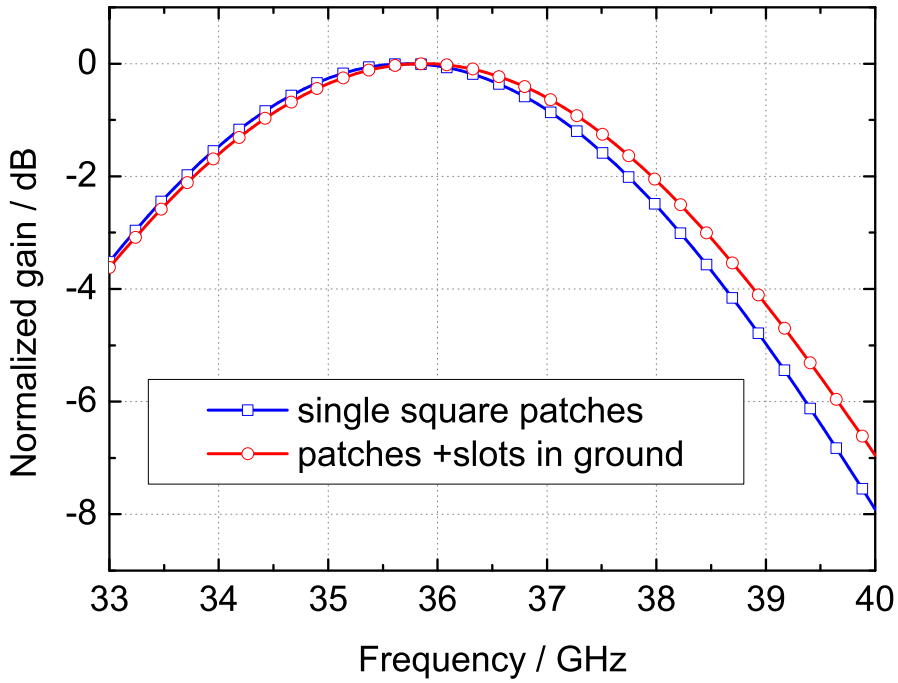

(a) Bandwidth comparison: reflectarray with single patches of variable dimension and reflectarray with variable length patches and variable length slots in the ground plane (h=0.79 mm).

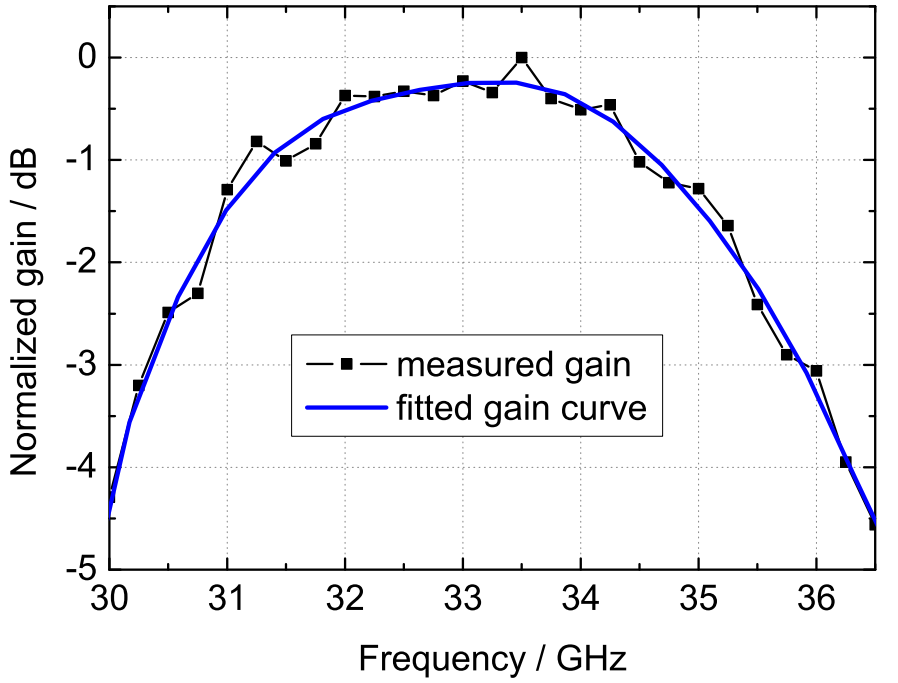

(b) Gain bandwidth of the reflectarray with variable length stacked patches and thick substrate (h=1.57 mm)

Figure 3.8: Bandwidth of the realized fixed-beam reflectarrays with offset feed.

3.3 Reflectarray with Backfire Feed

In the attempt to make the reflectarray antenna as compact as possible, the possibility of using a backfire feed (also known in the literature as a "hat feed", or a "Chinese hat feed" [Kil89, Kil97, Mol93, Yan98]) has been investigated. In this section the design and realization of such a reflectarray with backfire feed for an operating frequency of 35 GHz are presented.

3.3.1 The Feeding System

The feed consists of a shorted WR28 rectangular waveguide with two identical slots cut out in the E-walls close to the short. A subreflector consisting of two metal wings is attached at the shorted end of the waveguide to redirect the radiated fields backwards (see Fig. 3.9). This feeding system was proposed in [Lin81] and successfully employed with parabolic reflectors. It has the advantages of very simple realization, low bockage, it is simple and robust.

The feed was studied separately with respect to return loss and radiation pattern by means of simulation with *CST-Microwave Studio*. The matching and the pattern are sensitive to changes in the bending angle of the wings α. A value of $\alpha = 83^\circ$ provided satisfactory results.

Another parameter important for the design is the length of the waveguide in front of the array. Simulations with *CST Microwave Studio* showed, that the field radiated backwards toward the array elements is propagating partially using the waveguide as a kind of support. It is necessary to choose the part of the waveguide protruding in front of the reflectarray long enough for the fields to reach a quasi far field distribution, at the same time keeping it as short as possible for practical reasons regarding the compact size of the whole antenna. A length of $8.5\,\lambda_0$ at the design frequency of 35 GHz was therefore chosen.

The simulated and measured insertion losses of the feed antenna are presented in Fig. 3.10. The measured insertion loss could be improved a little with the help of a matching screw.

The reflectarray consists of 25x25 printed square microstrip patches on a dielectric substrate. The chosen substrate was RTDuroid 5880 with a thickness of h=0.79 mm and a dielectric constant $\varepsilon_r = 2.2$ [Rog07]. The employed technique for obtaining the desired phase at each element was that of varying the patch dimensions. The reflectarray was designed to emulate an existing metallic parabolic reflector; the side of the square reflectarray was thus chosen equal to the diameter of the parabolic reflector D=215 mm.

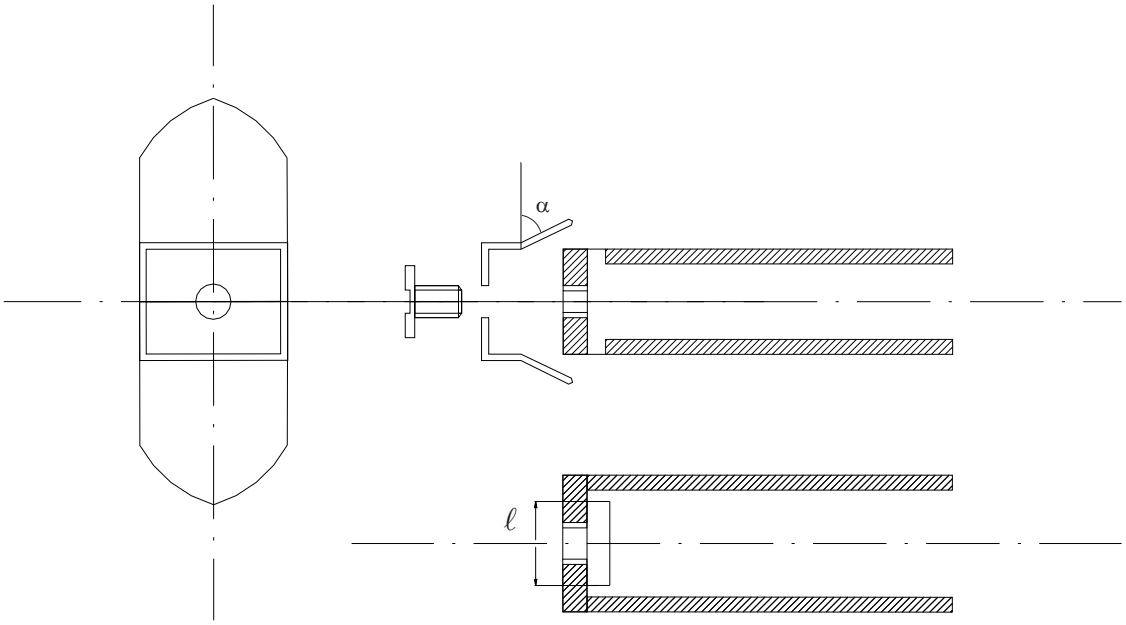

Figure 3.9: Schematic drawing of the backfire feed configuration.

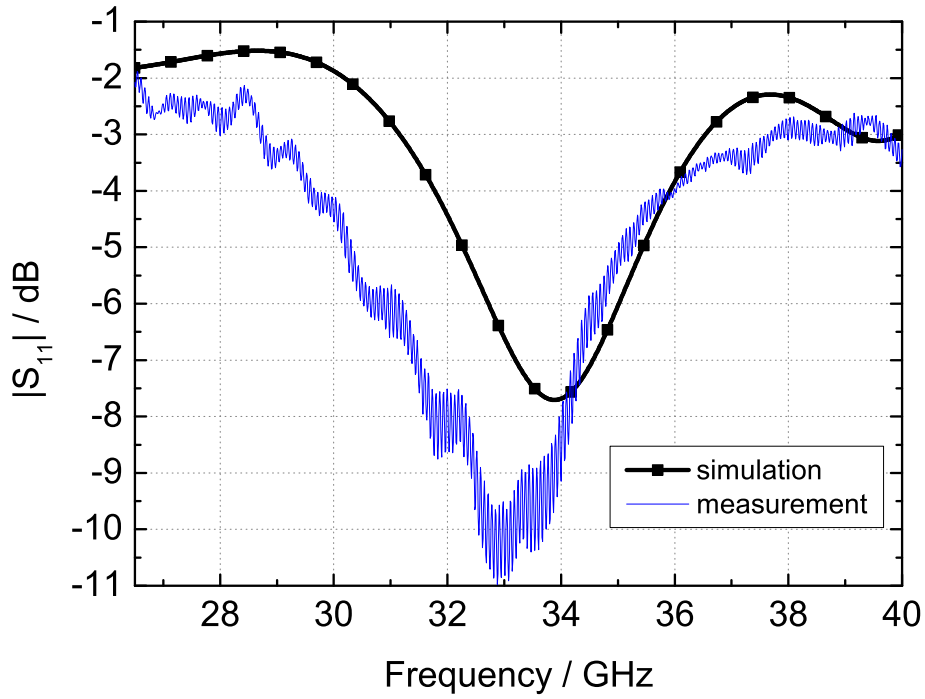

Figure 3.10: Simulated and measured insertion loss of the feed.

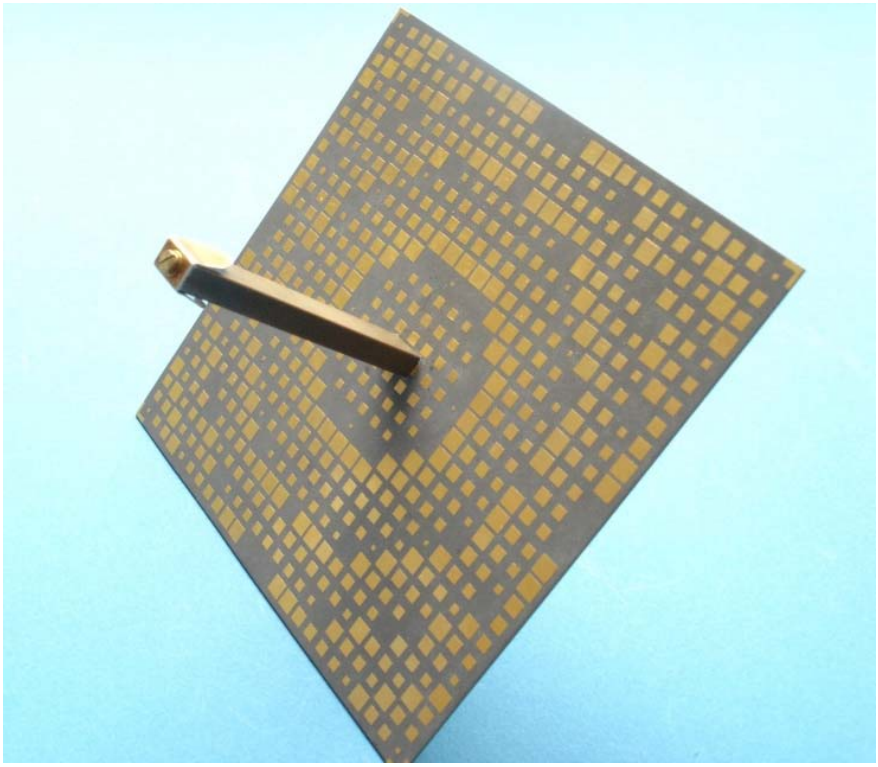

Figure 3.11: Picture of the retrodirective reflectarray.

The end of the waveguide was considered as phase center of the feed and the patches were then accordingly designed to compensate the path differences and direct the focused beam broadside. A close-up of the reflectarray with the assembled feed is shown in Fig. 3.11. The circular pattern built by the patches accounts for the compensation of the path differences in the almost spherical wave radiated backwards by the feed.

3.3.2 Measurement Results

The reflectarray was designed so that the main beam points toward broadside. Measurements were performed in the anechoic chamber. The gain-bandwidth was first measured, also in order to assess the frequency where the maximum gain occurs. The normalized gain over the frequency is shown in Fig. 3.12.

Maximum gain turned out to occur at 31 GHz, although the design frequency was 35 GHz. This could be due to factors such as an uncalibrated power source, or the narrow band matching of the feed. The reflectarray has a 2 dB bandwidth of 3 GHz centered around 32 GHz, which makes a 9% relative bandwidth.

Since the best matching of the feed was at 33 GHz we recorded the patterns at this frequency. In order to have an image about how the pattern changes over the frequency,

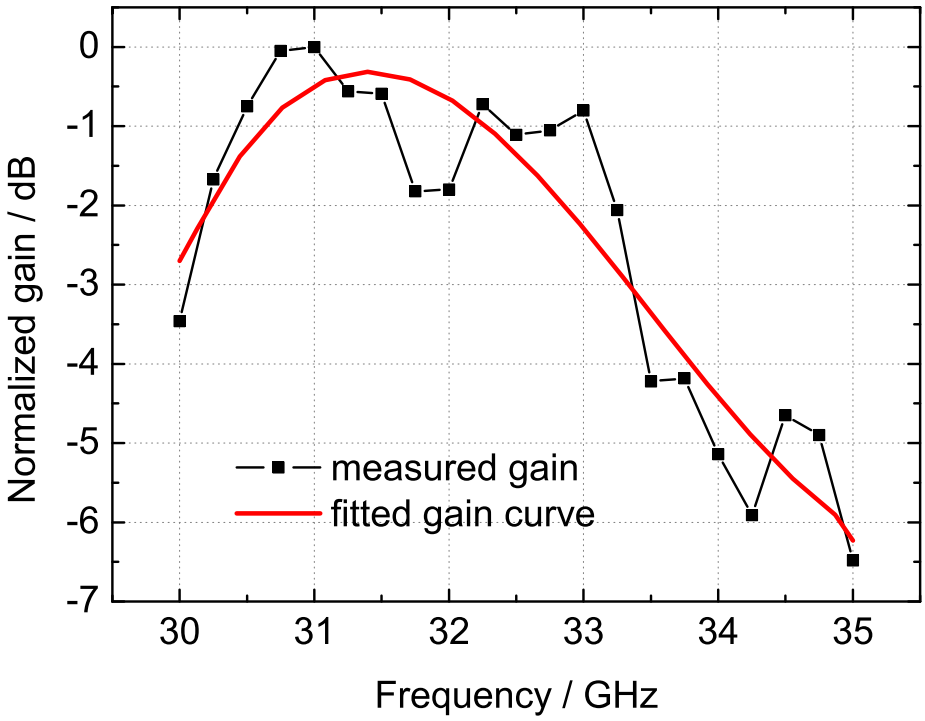

Figure 3.12: Normalized gain over the frequency for the backfire reflectarray

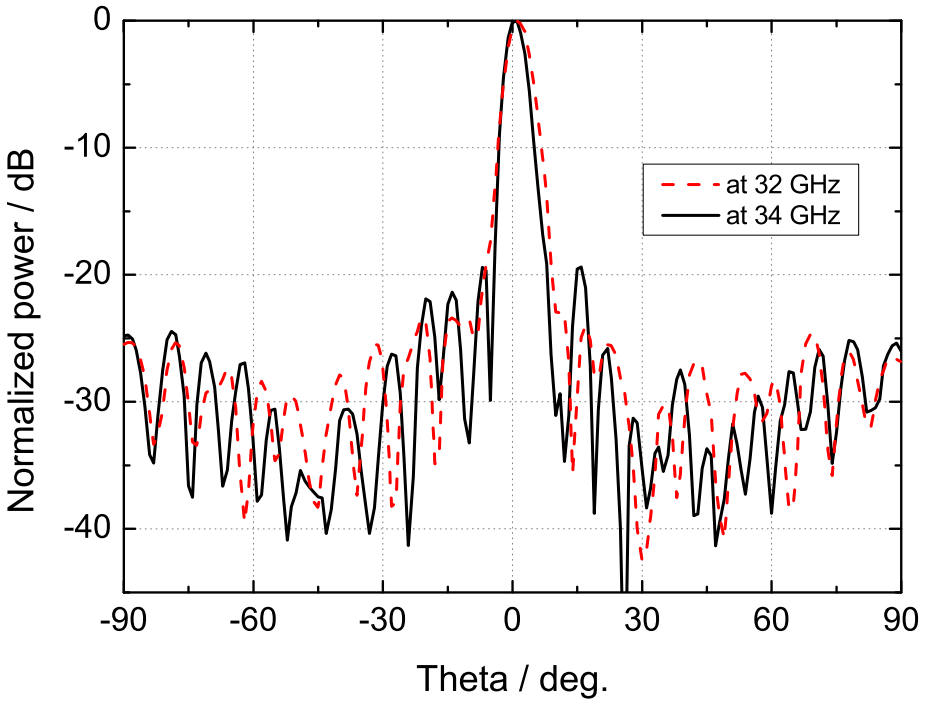

Figure 3.13: H-plane pattern of the reflectarray at 32GHz and 34 GHz.

measurements were also performed at 32 and at 34 GHz. The comparison of the two H-plane patterns is shown in Fig. 3.13. The pattern shows no significant degradation over the frequency, the side-lobe level remaining under -18 dB in both cases. Comparison between the H-and E-plane patterns of the reflectarray and of the parabolic reflector are given in Fig. 3.14.

The side-lobes of the reflectarray are in both planes considerably higher than the side-lobes of the parabolic reflector, nevertheless it has acceptable values: -16 dB in the E-plane and -18 dB in the H-plane. Reasons for this high level of the side-lobes, in comparison with the parabolic reflector could be: the couplings between the microstrip elements, which have not been taken into account in the design, the phase errors arising due to oblique incidence of the wave on the outer elements of the reflectarray (the unit cell being calculated with normal incidence), or due to inaccuracy in the choice of the feed phase center.

Table 3.2: Summary of the properties of backfire fed reflectarray

Element Type	Simple square patch
Number of elements	25×25
Substrate Type	RTDuroid 5880, h=0.79 mm, ε_r=2.2, $\tan\delta$=0.0009
SLL in E-Plane	16 dB
SLL in H-Plane	18 dB
2 dB Gain Bandwidth	9%

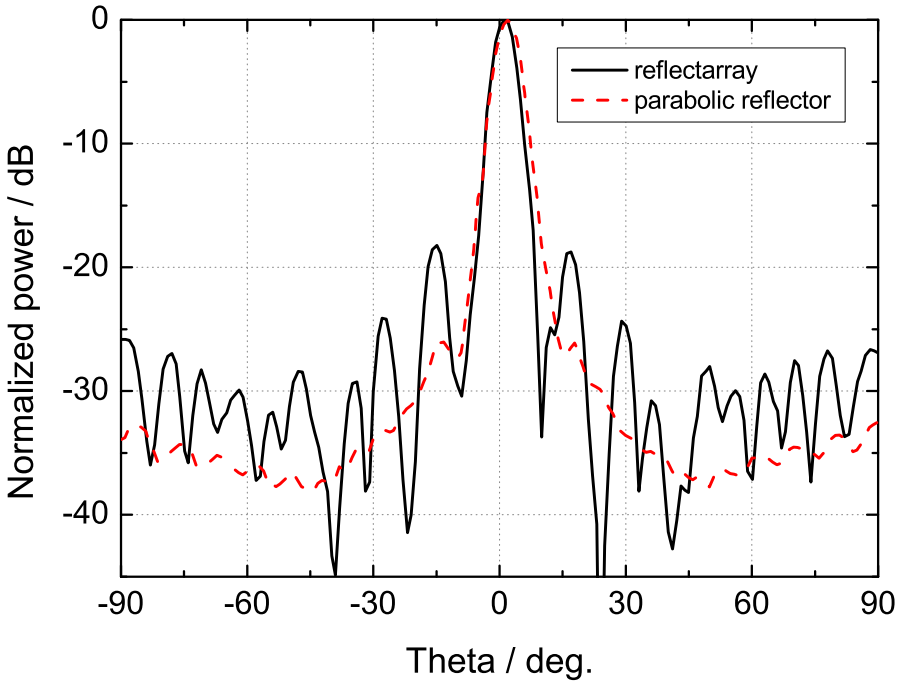

(a) H-plane

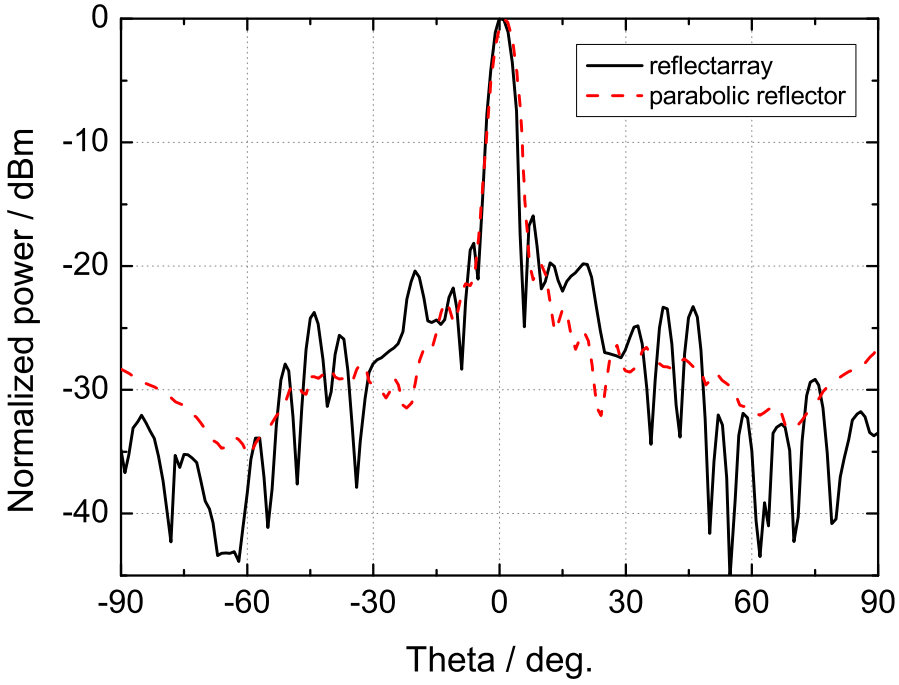

(b) E-plane

Figure 3.14: Comparison between the measured patterns of the reflectarray at 33 GHz and of the parabolic reflector at 35 GHz

3.4 Reflectarray with Slotted Waveguide Feed

3.4.1 The Feeding System

There are applications in which scanning of the main beam in only one plane is required. As it will be shown further in chapter 6, such a reflectarray, with beam scanning ability in one plane only has also been realized in the frame of this work. For such a reflectarray, a line-feed, i.e. a feed radiating a cylindrical wave front is of advantage, since the correction of the different path lengths has to be done only in the steerable plane.

Among possible feeding structures which radiate a cylindrical (or nearly cylindrical) wave front, the slotted waveguide has the advantages of being compact and relatively easy to manufacture. In this section, a fixed-beam (non-reconfigurable) reflectarray with a slotted waveguide feed is described, as a preliminary step toward a reconfigurable reflectarray with liquid crystals.

First, the type of slotted waveguide feed had to be chosen. It has long been known that a "hole" in the wall of a waveguide, when of appropriate size and in appropriate position, will "leak", allowing part of the energy to radiate. In Fig. 3.15, the possible slot configurations are depicted.

A centered longitudinal slot A in the broad wall of the waveguide will not radiate, since it has no current flow around it. But once it is displaced off center, such as slot B, it will begin to radiate. The same is valid for a slot C, tilted with respect to the longitudinal axis. Similar considerations apply in the narrow wall of the waveguide also. Slot D will not radiate, but tilting it with an angle, such as slot E, will produce radiation. In this work, slot type B has been chosen, based on the polarization properties of the radiated wave. It is obvious that for all slots the $\vec{E}$ field is polarized across the narrow dimension

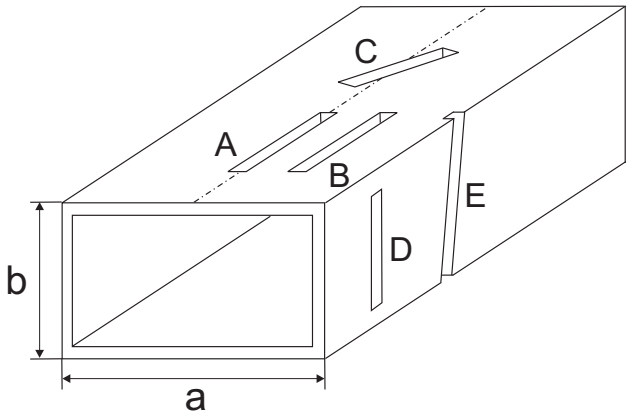

Figure 3.15: Types of slots in the waveguide walls.

of the slot. Therefore, the inclined slots have a cross-polar component relative to their inclination axis, which for reasons that will become apparent in chapter 6 we tried to avoid. Slots of type B have thus been chosen.

According to [Yee82], there are two classes of slotted waveguides: the **resonant type** slotted waveguide and the **traveling wave** slotted waveguide. The resonant type slotted waveguide is terminated in a short circuit, the result being a standing wave. The slots are spaced half a guided wavelength apart, so that voltage maxima occur simultaneously under the slots and the beam is directed at broadside. The traveling wave slotted waveguide on the other side is terminated in a matched load, so that only a forward wave is propagating. The slots are spaced less or more than half a guided wavelength apart, and therefore the beam is pointing off-broadside and its direction is frequency dependent.

A resonant type slotted waveguide has been chosen for the purpose of this work, owing to manufacturing reasons, since it is a lot easier to realize a short than a matched load. The slots have to be resonant, i.e. they have to be around $\lambda/2$ long, and also spaced $\lambda_g/2$ apart, with

$$\lambda_g = \frac{2\pi}{\beta} = \frac{\lambda}{\sqrt{1-(\lambda/2a)^2}}$$

the guided wavelength. Using these information, the design was accomplished with *CST Microwave Studio*. In the design process, the offset of the slots from the centerline, the width and length of the slots have been varied to yield a good matching of the antenna as well as a well behaved cylindrical wave front. The center frequency for the design was 35 GHz; accordingly, a WR28 waveguide with d=1 mm wall thickness was chosen.

Due to its resonant nature, a drawback of the resonant type slotted waveguide is the relatively narrow bandwidth. This will affect accordingly the bandwidth of the reflectarray. In Fig. 3.16(a) a picture of the fabricated feed is shown, as well as the simulated and measured S_{11} parameter in Fig. 3.16(b). There is fair agreement between simulation and measurement results, the slight discrepancies being most likely caused by some manufacturing inaccuracies, since the performance of the antenna is quite sensitive to the smallest variations of width, length and position of the slots. As expected, the pattern is broad in the E-plane and focused in the H-plane.

3.4.2 Measurement Results

In Fig. 3.17 the simulated radiated $\vec{E}$ field is depicted in front of the slotted waveguide. The desired cylindrical wave front is apparent. There was no possibility to measure the near field of the slotted waveguide, in order to assess the accuracy of the simulation,

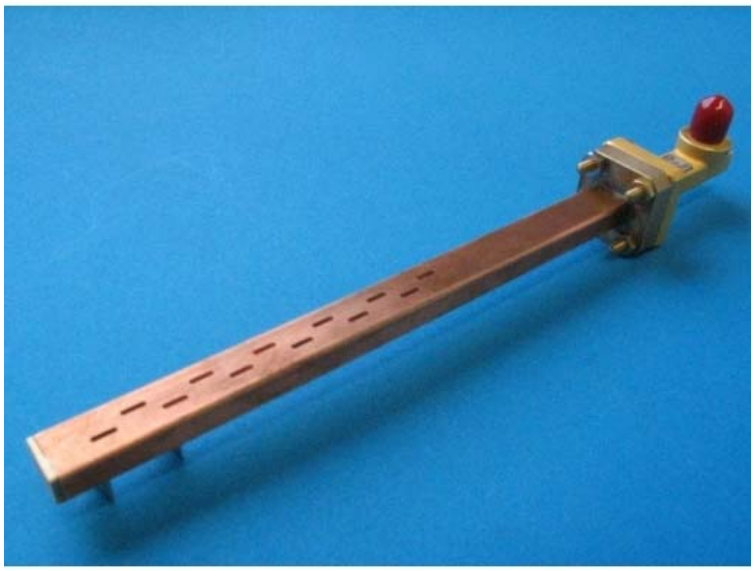

(a) Picture of the resonant type slotted waveguide array with alternating offset slots in the broad wall

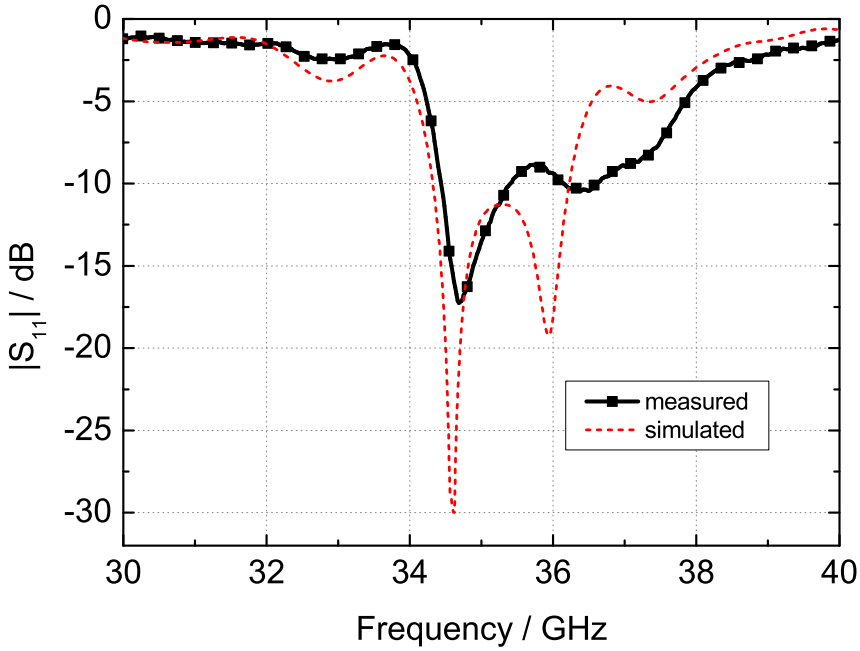

(b) Simulated (*CST Microwave Studio*) and measured input matching for the slotted waveguide array - $|S_{11}|$

Figure 3.16: The slotted waveguide feed

therefore the far field patterns have been measured. The measured patterns in the E plane as well as in the H plane agree very well with the simulations conducted with *CST Microwave Studio* (see Fig. 3.19). It is therefore legitimate to assume that the *CST Microwave Studio* simulations for the near-field are also accurate enough, so that there is a (nearly) cylindrical wave front incident on the reflectarray aperture.

Having verified the design of the feed, the fixed-beam reflectarray was designed accordingly. It consists of 16×16 patches printed on a Rogers RTDuriod 5880 substrate with a thickness h=0.50 mm. The main beam was designed to point to broadside, the phase compensation in the E-plane has been achieved by variation of the patch dimensions. A photograph of the realized reflectarray is shown in Fig. 3.18, pointing out once again its simple and compact construction. The measured far field patterns are shown in Fig. 3.20, with good agreement between simulated and measured results. A gain of 22.9 dB has been measured at 35 GHz.

The side lobe level in H plane is around -13 dB, as expected from a more or less constant amplitude distribution in that plane. In the E plane the side lobe level is somewhat lower, around -10 dB. This is due to the relatively small amplitude taper, reaching about -4 dB at the array edge. Table 3.3 summarizes the properties of the fixed beam reflectarray.

Table 3.3: Summary of the properties of reflectarray with slotted waveguide feed.

Element Type	Simple square patch
Number of elements	16×16
Substrate Type	RTDuroid 5880, h=0.79 mm, ε_r=2.2, $\tan\delta$=0.0009
SLL in E-Plane	-10 dB
SLL in H-Plane	-13 dB
Calculated Directivity	24 dB
Measured Gain	22.4 dB
Efficiency	68%

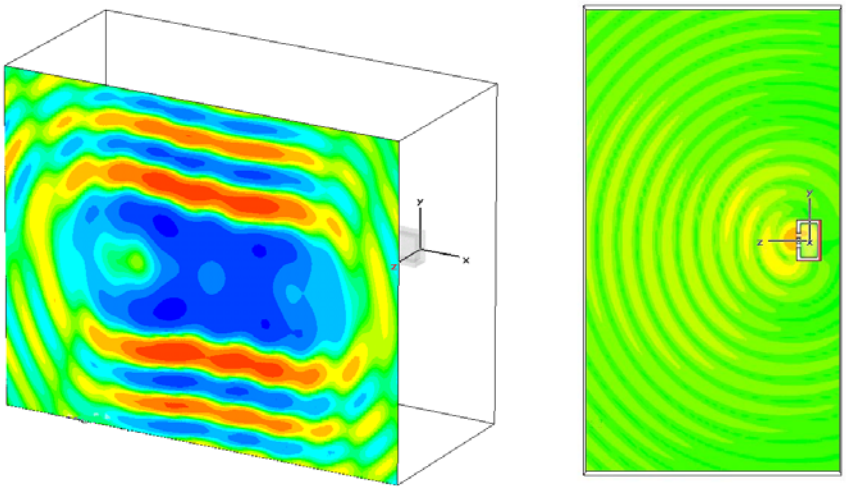

(a) Perspective field view. (b) Lateral field view.

Figure 3.17: Simulated $\vec{E}$ field in the proximity of the slotted waveguide. The cylindrical wave front radiated by a line feed can be recognized.

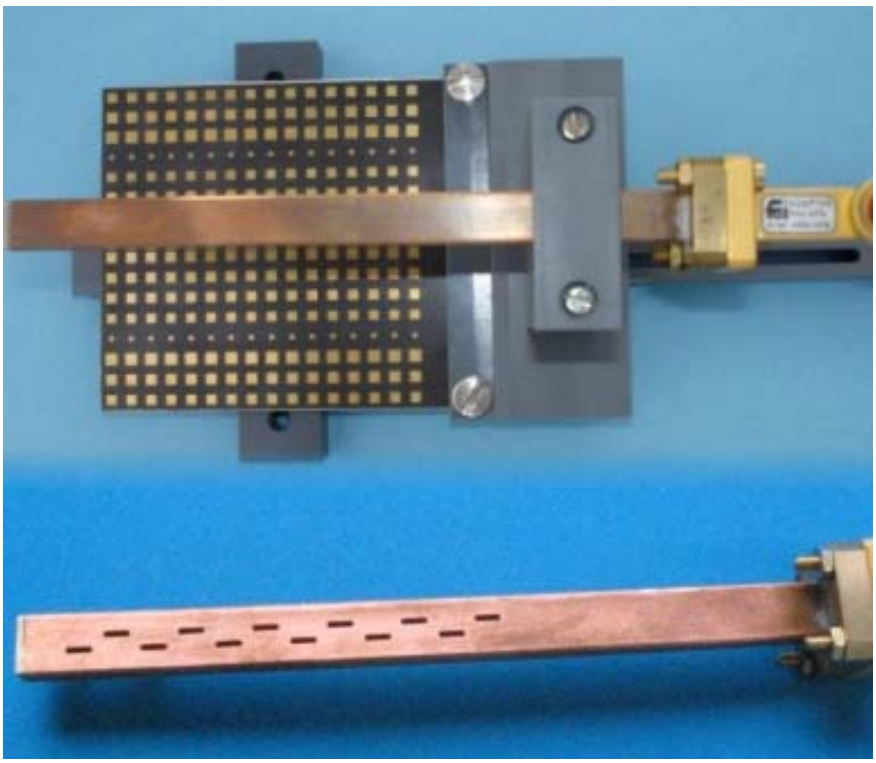

Figure 3.18: Realized fixed beam reflectarray with a slotted waveguide array as feed.

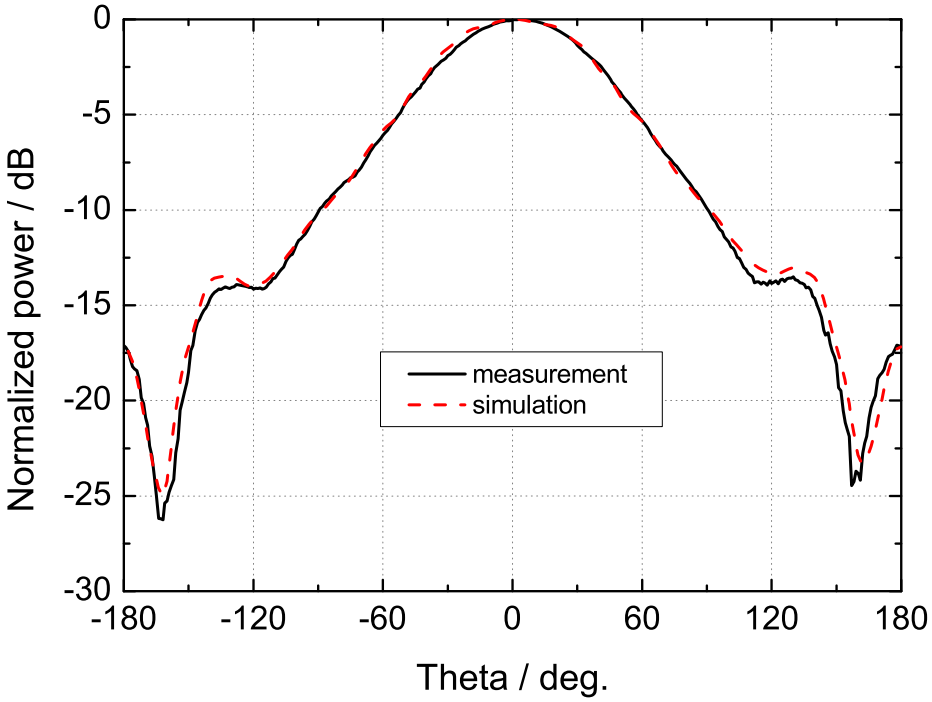

(a) Pattern E Plane

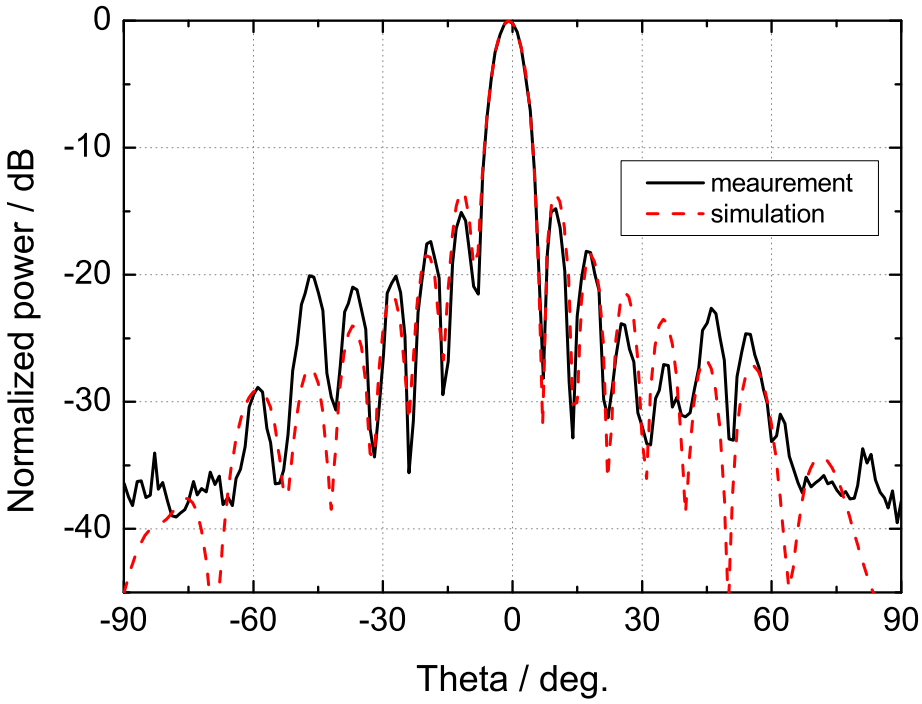

(b) Pattern H Plane

Figure 3.19: Simulated and measured patterns in the E and H planes for the slotted waveguide feed

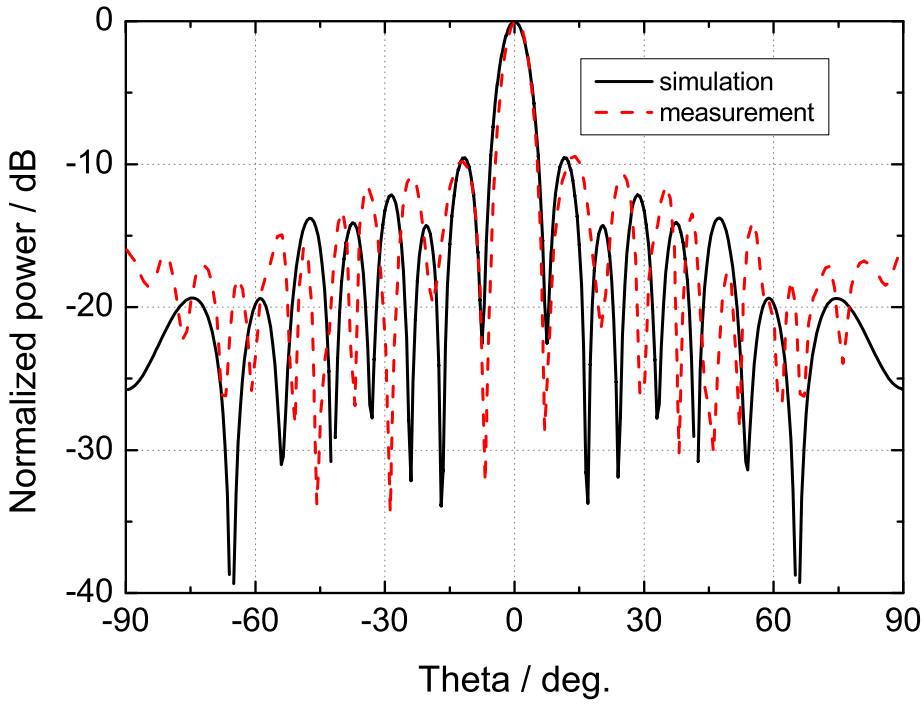

(a) Reflectarray Pattern E Plane

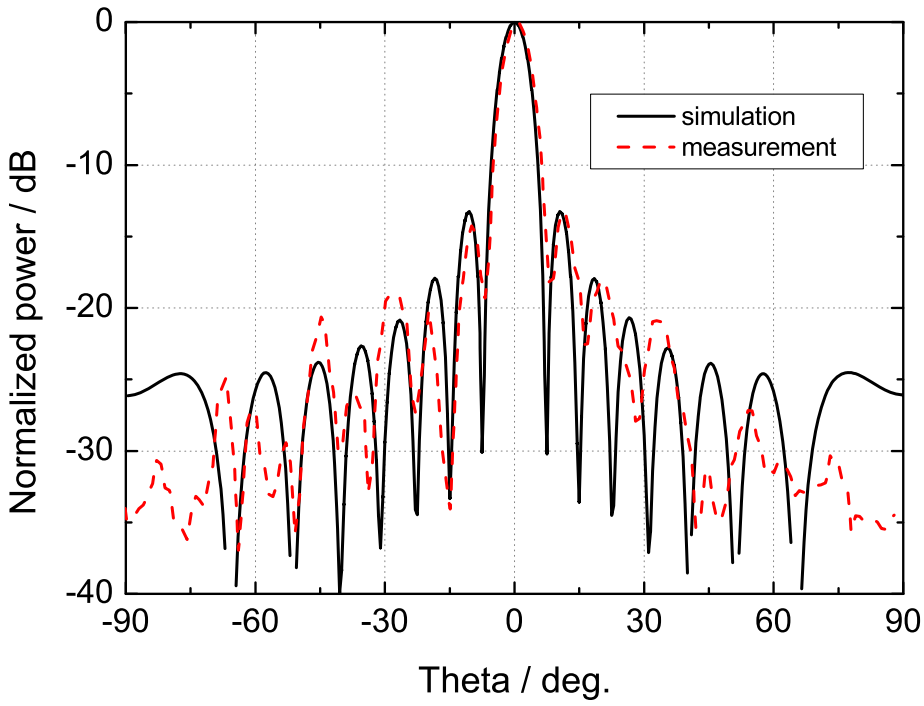

(b) Reflectarray Pattern H Plane

Figure 3.20: Simulated and measured patterns in the E and H planes for the fixed beam reflectarray employing a slotted waveguide feed

3.5 Summary

In this chapter a few non-reconfigurable (fixed-beam) reflectarrays have been presented. An optimization algorithm for bandwidth enhancement is attempted, based on simultaneous variation of two resonant structures (patch and slot in ground plane, or two stacked patches).The verification of the algorithm proved inconclusive, since the achieved bandwidth improvement was not significant.

Two feeding structures were further verified: a backfire center feed and a slotted waveguide line feed. They proved to be feasible, easy to realize feeds, suitable for achieving compact and solid reflectarray configurations.

Chapter 4

Liquid Crystals for Microwave Applications

The intention of using liquid crystal as a tunable substrate for reflectarrays has already been announced in the introductory part of this thesis. In the following chapter, the liquid crystals are introduced and their properties briefly described along with some important parameters. A central concept is in the context of this thesis the dielectric anisotropy of liquid crystals. Also very important for practical applications are techniques for orienting the liquid crystals, in order to purposefully use their dielectric anisotropy.

In the latter part of the chapter, the dielectric properties of the liquid crystals employed in this thesis are presented. The chapter closes with an overview of some previous attempts to use liquid crystals in tunable devices at microwave frequencies.

4.1 Introduction to Liquid Crystals

Liquid crystals are materials whose molecular structure, in a certain temperature domain, has an intermediate state between the crystalline and the liquid phase. Whereas in crystals the molecules are both positionally and orientationally ordered, in liquids they are not. In the solid state, the molecules are strongly bound together by attraction forces, each molecule has its well defined place in the crystal lattice (positional order) and the molecular axes are pointing in a specific direction (orientational order), the degree of order is thus very high. In the liquid state, the bounds between molecules are weak, the molecules have high freedom of movement, positionally as well as directionally, and the degree of order is very low. Characteristic for the liquid crystals is thus a degree of order somewhere in between.

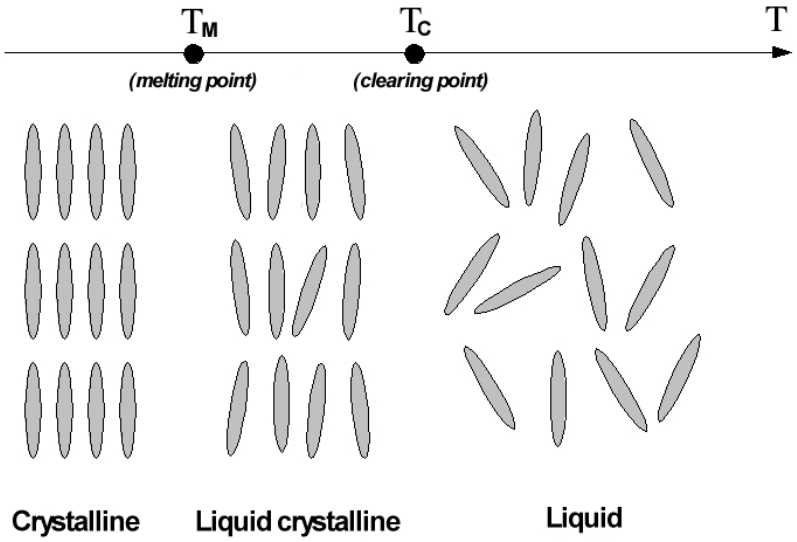

Figure 4.1: Molecular alignment for different phases of a material depending on the temperature.

By raising the temperature, the material changes from the crystalline phase into the liquid crystalline phase at the temperature T_M (*melting point*), exhibiting high viscosity and an opaque appearance. At the temperature $T_C > T_M$, the material crosses into the liquid phase, where viscosity is reduced and the opacity clears. For this reason T_C is known as the *clearing point* of a liquid crystal. At molecular level, the following happens: at the temperature T_M the molecular bonding forces break down to such an extent that the molecules have more freedom of movement as in the crystalline lattice; they remain however roughly oriented along a common reference axis (the *director*,$\vec{n}$). Then, when the temperature T_C is reached, the bonding forces between molecules are further weakened, to the extent that the degree of order lowers and the material crosses over into the liquid phase (see Fig. 4.1). The liquid crystalline phase, occurring between T_M and T_C , is also known as *mesophase* (from Greek: *mesos* = middle).

The Order Parameter and the Director

The degree of order of the molecules in a material can be quantified by defining an order parameter. The order parameter is a macroscopic quantity derived from the macroscopic properties of the molecules. It is a measure for the orientation of the molecules along the common axis, the *director*. The expression for the degree of order is obtained with a Legendre polynomial of 2^{nd} degree.

$$S = \langle P_2(\cos\theta)\rangle = \left\langle \frac{3}{2}\cos^2\theta - \frac{1}{2} \right\rangle \tag{4.1}$$

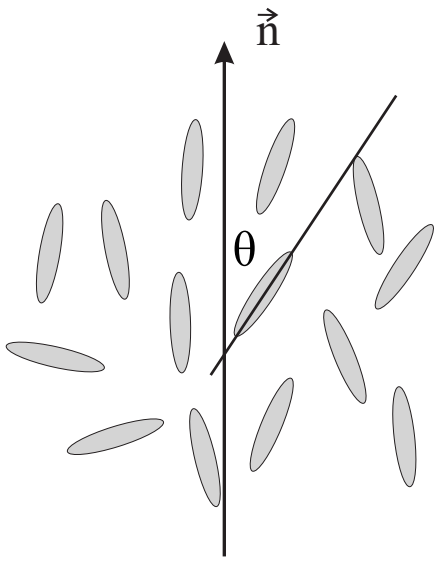

Figure 4.2: Angle θ between the main axis of a liquid crystal molecule and the director $\vec{n}$.

Here is θ the angle between a molecule and the director $\vec{n}$ (see Fig. 4.2), and $\langle\rangle$ denotes an average over many molecules at the same time, or an average over time of the same molecule [Col97]. The oder parameter can have values between 0 and 1: $S = 0$ for a system with no orientational order (i.e. molecules pointing in all directions with equal probability) and $S = 1$ for a perfectly ordered system, with all molecules pointing in exactly the same direction (as is the case in the crystalline state). In typical liquid crystals S takes values between about 0.3 and 0.8-0.9 [Col90], depending on the temperature.

The director $\vec{n}$ is a unit vector, its direction the same with the preferred direction of the molecular main axes. This means, the direction of the director is an average of the directions of the main axes of all molecules. The director orientation can be influenced by the adjoining surfaces in contact with the liquid crystal, as well as by externally applied electric and magnetic field. These mechanisms that can be used for orienting the director will be detailed in section 4.2.

Classification of Liquid Crystals

A classification by the form of the constituent molecules divides the LCs in *calamitic* and *discotic*. The calamitic LCs are made up of rod-like molecules (one molecular axis is much longer than the other two), while the discotic LCs have disk-like molecules (one molecular axis much shorter than the other two). Important for both types is that the molecule has to be rigid for at least some part in the central region, in order to maintain the elongated shape required for the anisotropy.

A typical calamitic LC molecule consists of two or more aromatic (ring) structures linked

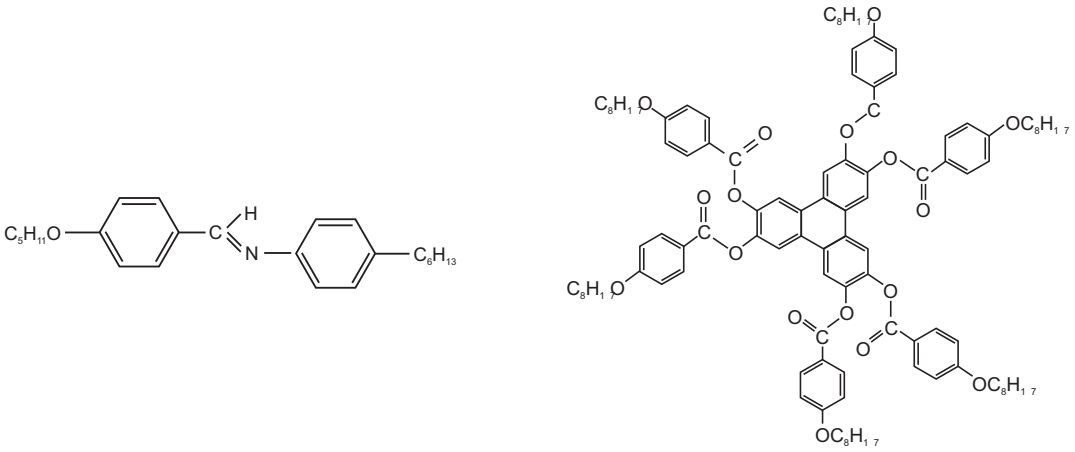

(a) Typical calamitic LC molecule. (b) Typical discotic LC molecule.

Figure 4.3: Typical chemical composition of liquid crystal molecules, from [Col97].

directly or via rigid compounds, plus hydrocarbon chains at each end (see Fig. 4.3(a)). A typical discotic LC molecule consists of a core of benzene, tryphenilene or truxene with side chains resembling a typical calamitic LC molecule (see Fig. 4.3(b)) [Col97].

Another classification of the liquid crystals sees them divided into *thermotropic* and *lyotropic*. The thermotropic LCs, who encompasses both calamitic and discotic LCs, remain in the liquid crystalline phase as long as they are in a certain temperature interval (T_M to T_C). On the other hand, the lyotropic LCs are in the liquid crystalline phase only when mixed with a suitable solvent in a well defined concentration. (A trivial example of a lyotropic liquid crystal is soap dissolved in water).

In the liquid crystalline phase, different subphases can be distinguished, depending on the degree of order of the molecules. Between T_M and T_C, a liquid crystal can cross over from one subphase in another. The most important subphases, to be shortly described further are the nematic, smectic and cholesteric phases.

The nematic phase has the lowest degree of order. Apart from the common alignment along the director, the molecules have no other positional restriction. The nematic liquid crystals are thus closest to the liquid state, in the case of a temperature raise a nematic liquid crystal crosses over directly into liquid. In the smectic phase, the degree of order grows, i.e. the liquid crystal is closer to the crystalline state. In addition to the alignment along the common director, the molecules show a tendency of arranging themselves in layers. In the cholesteric phase, the liquid crystal consists of thin layers of nematic molecules, with the director rotating from layer to layer with a small angle.

Dielectric Anisotropy

The tendency of the liquid crystals molecules, to orient themselves along a preferred direction, causes anisotropy. Anisotropy is generally speaking the non equivalence of spatial directions in a given material with respect to some properties. The properties changing with the considered spatial coordinates can be mechanic (viscosity, elastic modulus), electromagnetic (permittivity, permeability) or optical (index of refraction).

Optical anisotropy, has been exploited since a long time ago to create controllable optical devices (well known are the LC displays). The functioning principle of many everyday use LC-based optical devices can be explained with the twisted nematic cell. Such a cell consists of two polarizing filters applied on the two carriers that sandwich the nematic liquid crystal. The carrier surfaces are processed in such a way, that the LC molecules align parallel to the polarizing filter. They thus accomplish a 90° twist between the two surfaces (see Fig. 4.4). Polarized light entering one polarizing filter is "twisted" with 90° as it passes through the LC, so that it can also pass through the second polarizing filter. When an electric field is applied to the cell, as shown in Fig. 4.4 on the right, the LC molecules will align parallel to the field. The light entering the upper polarizing grid will thus not experience a polarization twist anymore and will be reflected by the second polarizing grid. Hence, by simply applying a voltage, the twisted nematic cell can switch between a bright and a dark state.

Dielectric anisotropy is closely related to the polarization that occurs in a liquid crystal in the presence of an electric field. An external electric field $\vec{E}$ causes a dipole moment per unit volume (due to charge separation on the molecules). This dipole moment per unit volume is called polarization $\vec{P}$ and is composed of summation of elementary dipole

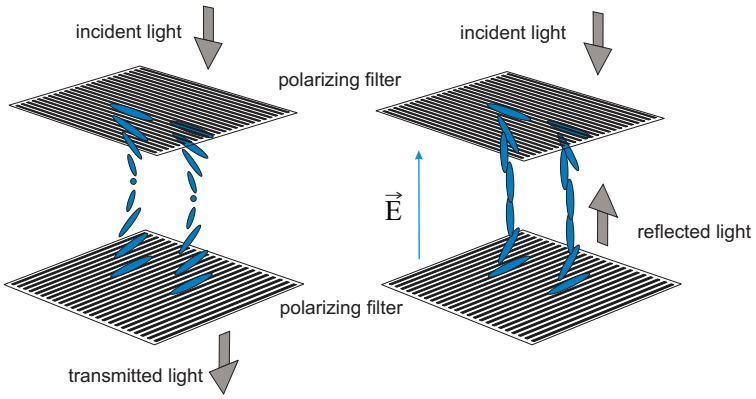

Figure 4.4: Functional principle of optical LC devices illustrated with a twisted nematic cell.

moments of each molecule[Wei03a].

$$\vec{P} = \frac{\partial \vec{p}}{\partial V} = \sum_i \vec{p}_i \tag{4.2}$$

Generally the polarization is not proportional to the intensity of the electric field. For relatively weak intensities however, the assumption can be made that there is a linear relation between the polarization and the electric field [Leh96]. The constant of proportionality is called the electric susceptibility of the material χ_e.

Assuming the director $\vec{n}$ is along the z-axis of the coordinate system, if the polarizing electric field is parallel to the director one obtains a value $\chi_\parallel$ for the electric susceptibility:

$$P_z = \varepsilon_0 \chi_\parallel E_z$$

Is the polarizing electric field along the x or y directions, the electric susceptibility is in both cases $\chi_\perp$ (since the directions are equivalent with regard to the director).

$$P_x = \varepsilon_0 \chi_\perp E_x \qquad\qquad P_y = \varepsilon_0 \chi_\perp E_y$$

with $\varepsilon_0 \approx 8.854\,10^{-12}\,\mathrm{F/m}$ the vacuum permittivity.

Thus, the polarization can be written:

$$\begin{pmatrix} P_x \\ P_y \\ P_z \end{pmatrix} = \varepsilon_0 \begin{pmatrix} \chi_\perp & 0 & 0 \\ 0 & \chi_\perp & 0 \\ 0 & 0 & \chi_\parallel \end{pmatrix} \begin{pmatrix} E_x \\ E_y \\ E_z \end{pmatrix} \qquad \text{or} \qquad \vec{P} = \varepsilon_0 \overleftrightarrow{\chi_e}\ \vec{E} \tag{4.3}$$

with $\overleftrightarrow{\chi}$ the electric susceptibility tensor.

The electric displacement $\vec{D}$ is then defined as [Ell03]:

$$\vec{D} = \varepsilon_0 \vec{E} + \vec{P} = \varepsilon_0 \vec{E} + \varepsilon_0 \overleftrightarrow{\chi_e}\ \vec{E}$$

$$\vec{D} = \varepsilon_0 \left(\overleftrightarrow{1} + \overleftrightarrow{\chi_e}\right) \vec{E} = \varepsilon_0 \overleftrightarrow{\varepsilon_r}\ \vec{E} = \overleftrightarrow{\varepsilon}\ \vec{E} \tag{4.4}$$

with $\overleftrightarrow{1}$ the unit tensor, $\overleftrightarrow{\varepsilon_r} = \overleftrightarrow{1} + \overleftrightarrow{\chi_e}$ the relative permittivity (or dielectric constant) of the material and $\overleftrightarrow{\varepsilon} = \varepsilon_0 \overleftrightarrow{\varepsilon_r}$ the permittivity of the material. The permittivity as well as the dielectric constant of liquid crystals are also tensor quantities, since they derive directly from the electric susceptibility. The liquid crystal permittivity can thus be expressed in

dependence of the three orthogonal spatial coordinates as:

$$\overleftrightarrow{\varepsilon}_{LC} = \begin{pmatrix} \underline{\varepsilon}_x & 0 & 0 \\ 0 & \underline{\varepsilon}_y & 0 \\ 0 & 0 & \underline{\varepsilon}_z \end{pmatrix} \tag{4.5}$$

or, if once again the z-axis is chosen parallel to the director:

$$\overleftrightarrow{\varepsilon}_{LC} = \begin{pmatrix} \underline{\varepsilon}_\perp & 0 & 0 \\ 0 & \underline{\varepsilon}_\perp & 0 \\ 0 & 0 & \underline{\varepsilon}_\parallel \end{pmatrix} \tag{4.6}$$

The dielectric anisotropy is defined as:

$$\Delta\varepsilon = \varepsilon_\parallel - \varepsilon_\perp \tag{4.7}$$

and, analogously for the relative permittivity:

$$\Delta\varepsilon_r = \varepsilon_{r,\parallel} - \varepsilon_{r,\perp} \tag{4.8}$$

The anisotropy can be positive or negative. All nematic liquid crystals used in this work exhibit positive anisotropy.

A useful quantity to characterize liquid crystals with respect to how much anisotropy they possess is the tunability. Tunability is a common parameter in association to tunable materials or devices and it is defined as:

$$\tau = \frac{\varepsilon_{r,\parallel} - \varepsilon_{r,\perp}}{\varepsilon_{r,\parallel}} \tag{4.9}$$

For an arbitrary angle between director and coordinate system axes, the permittivity tensor can be expressed as a function of director, of the permittivity $\varepsilon_\perp$ and of the dielectric anisotropy ([Mue07]):

$$\overleftrightarrow{\varepsilon}_{x,y,z} = \varepsilon_\perp \overleftrightarrow{1} + \Delta\varepsilon\ (\vec{n} \otimes \vec{n}) = \varepsilon_\perp \cdot \begin{pmatrix} 1 & 0 & 0 \\ 0 & 1 & 0 \\ 0 & 0 & 1 \end{pmatrix} + \Delta\varepsilon \begin{pmatrix} n_x^2 & n_x n_y & n_x n_z \\ n_y n_x & n_y^2 & n_y n_z \\ n_z n_x & n_z n_y & n_z^2 \end{pmatrix} \tag{4.10}$$

4.2 Orienting the Liquid Crystals

In order to be able to effectively use the liquid crystal anisotropy for microwave applications, a well defined orientation of the director has to be enforced. This orientation can be in principle achieved in three ways:

- with a magnetostatic field
- with an electric field
- with an orientation layer

A simple way to describe the mechanism of director orientation when applying an external field, be it magnetic or electric, is by means of the continuum theory and the free Gibbs energy [Sta99]. In a nematic LC a free energy per unit volume w_f and a total free energy W_f can be defined, according to:

$$w_f = \underbrace{w_{f,splay} + w_{f,twist} + w_{f,bend}}_{volume\ terms} + \underbrace{w_{f,surface}}_{surface\ term} - \underbrace{(w_{f,el} + w_{f,mag})}_{external\ fields} \tag{4.11}$$

and

$$W_f = \int_V w_f \, dV \tag{4.12}$$

It is assumed that the equilibrium state is the state in which the director orientation does not vary inside the volume. Also, in this state the free energy reaches a minimum.

The volume terms in Eq. 4.11 represent increases in the free energy caused by deviations of the director in certain parts of the volume from the preferred global direction, due to three types of distortions in the director (denoted *splay*, *twist* and *bend*). The free energy is further increased due to interactions at the contact surface between the LC and the adjoining material, conveyed by the surface term.

The energy per unit volume caused by an electric field is [Leh96]:

$$w_{el} = \frac{1}{2}\vec{E}\,\vec{D}^* = \frac{1}{2}\vec{E} \overset{\leftrightarrow}{\varepsilon} \vec{E}^* \tag{4.13}$$

Using the expression in Eq. (4.10) for the permittivity tensor, the electric energy per unit volume can be written as:

$$w_{el} = \varepsilon_\perp |E|^2 + \Delta\varepsilon \left(\vec{n}\,\vec{E}\right) \tag{4.14}$$

For the energy stored in magnetic field applies:

$$w_{mag} = \frac{1}{2}\vec{H}\,\vec{B}^* = \frac{1}{2}\vec{H}\ \overleftrightarrow{\mu}\ \vec{H}^* \tag{4.15}$$

and, analog to (4.14):

$$w_{mag} = \mu_\perp |H|^2 + \Delta\mu \left(\vec{n}\,\vec{H}\right) \tag{4.16}$$

The last term in Eq. (4.14) and (4.16) depends on the orientation of the field vector relative to the director $\vec{n}$. Since the terms related to the external fields in Eq. (4.11) ($w_{f,el}$ and $w_{f,mag}$) have a negative sign, the system will tend to maximize them, in order to minimize the overall energy per unit volume. The minimum of w_f is thus achieved when the field vectors ($\vec{E}$ and $\vec{H}$ respectively) are aligned with the director $\vec{n}$.

Orientation with a Magnetic Field

Is an external magnetic field applied to a liquid crystal volume, in the light of the presented energy considerations, the director will tend to rotate and align as much as possible with the field lines, minimizing the overall free energy of the system.

Orientation with a magnetic field is practical for experimental purposes, when the realization of metallic electrodes to apply an electric field for the orientation is not always possible or impairs the RF properties of the DUT. In this case the DUT containing the liquid crystal can be inserted between the pole shoes of an electromagnet, for operation with $\varepsilon_{r,\perp}$ for instance, and then either the pole shoes or the DUT can be rotated with 90° to obtain operation with $\varepsilon_{r,\parallel}$. For a functional device however, the usage of bulky permanent magnets or electromagnets is not reasonable because of size and weight, and solutions must be sought to control the director orientation with an electric field.

Orientation with an Electric Field

Based on the same energy considerations, when an external electric field is applied to the liquid crystal, the molecules will rotate as well until the director is parallel with the electric field lines.

The reorientation of the LC molecules in an electrostatic field is also known under the name *Fréedericksz-effect*. The reorientation begins as soon as a threshold voltage is exceeded (*Fréedericksz-transition*). For the case of an LC volume enclosed between two

parallel electrodes, the threshold voltage can be expressed with the formula:

$$U_{th} = \frac{E_{th}}{d} = \pi\sqrt{\frac{K}{\Delta\varepsilon}}\,, \tag{4.17}$$

with E_{th} the threshold electric field intensity, d the distance between the electrodes and K an LC specific elastic constant. Is the voltage increased above the threshold, the molecules will start to rotate from their initial state. Eventually a saturation state is reached, when they are parallel to the electric field lines. The orientation with electric field is schematically presented in Fig. 4.5 for the case of a parallel plate capacitor.

The reorientation with an electric field is naturally the preferred choice for practical applications. In the case of microstrip reflectarrays this reorientation method is very suitable, since the topology of a microstrip reflectarray unit cell resembles that of a parallel plate capacitor. The ground will provide a common potential, and suitable voltages will have to be provided to the microstrip elements, under the assumption that the substrate between them is replaced by liquid crystal. The only problem that has to be carefully taken into consideration is the interference caused by the voltage control lines to the RF field radiated by the cell.

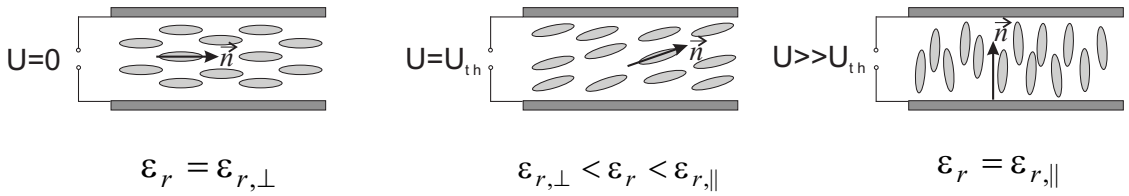

Figure 4.5: Orientation of the liquid crystal molecules by applying an electric field. The relative permittivity seen by a RF wave propagating through the LC changes continuously.

Orientation with an Orientation Layer

When a nematic LC is in contact with another phase, an *interface* is created. At this interface, the nematic order is disturbed and the orientation of the LC molecules is determined by the adjoining surface and its properties. This phenomenon is called *surface anchoring* [Pen00].

Depending on the tilt angle α (the angle between the director and boundary surface) the alignment of nematic LC can be categorized as follows:

(a) $\alpha = 0°$ - planar (parallel) alignment: director parallel to the boundary surface

(b) $\alpha = 90°$ - homeotropic (perpendicular) alignment: director perpendicular to the

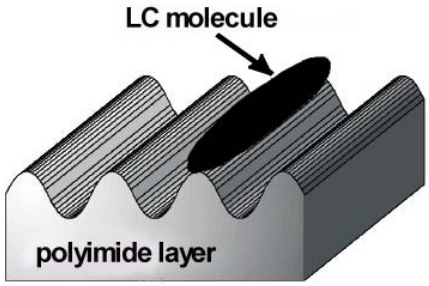

Figure 4.6: Illustrative orientation of a rod-like liquid crystal molecule by use of a polyimide layer with corrugations.

boundary surface

(c) $0° < \alpha < 90°$ - tilted alignment

Surface treatments can further be divided into two major groups: mechanical treatment and deposition of substances that assist the alignment. In this work mechanical treatment has been used, owing to the relatively simple processing and also to the existing know how in our group.

Rubbing the boundary surface in one direction to obtain homogeneous alignment of the molecules is one of the most widely used techniques, in research laboratories as well as in the industry. First, a very thin polyimide layer (with typical thickness between 100-300 nm) is deposited by spin coating on the surface and cured by backing in two steps. The technological details are given in Appendix A2. Fine, parallel corrugations are applied into this layer through mechanical rubbing in one direction (for instance with a textile material). These corrugations, together with the chemical interaction between polyimide and the LC molecules will cause the orientation of the director $\vec{n}$ along the rubbing direction, with an angle of approximately $0°$ with respect to the surfaces, as illustrated in Fig. 4.6.

Switching times

A drawback of liquid crystals for applications where speed is a requirement are the switching times. Switching times are a measure for the time interval characterizing the transition from one equilibrium state to another, when external fields are applied or removed. For instance, using the example of the parallel plate capacitor from the previous subsection, one can define two switching times, a Δt_{on} for the transition from $\varepsilon_{r,\perp}$ to $\varepsilon_{r,\parallel}$ when the DC electric field is applied, and a Δt_{off} for the inverse transition when the electric field is removed.

For these switching times following formulas are valid [Tar92]:

$$\Delta t_{on} \propto \frac{\gamma\, d^2}{\Delta\varepsilon\ \left(U_c^2 - U_{th}^2\right)} \qquad \Delta t_{off} \propto \frac{\gamma\, d^2}{\Delta\varepsilon\, U_{th}^2} \tag{4.18}$$

with γ the rotational viscosity of the LC molecules, U_c the control voltage, U_{th} the Fréedericksz threshold voltage and d the distance between the electrodes.

The rotational viscosity and the dielectric anisotropy are material dependent, therefore only an optimization of LCs with respect to these two parameters could improve the switching times. However, the switching times are directly proportional with the square of the liquid crystal layer thickness, which means that they could be reduced by designing devices with LC layers that are as thin as possible.

In [Mue05a] switching times of a finline phase shifter with a LC layer thickness of d=127 μm were measured. For Δt_{on} the values were in the order of 10^{-2} s, whereas for Δt_{off} the values were in the range 5-15 s. These values have to be dramatically improved for time-sensitive applications.

4.3 Properties of Employed Liquid Crystals

The microwave dielectric anisotropy of liquid crystal, unlike the optical anisotropy, began to be investigated in conjunction with potential applications relatively recently. First publications date back to [Lim93, Dol93] and they present first proof-of-concepts for electronically controllable microwave phase shifters, in waveguide and microstrip technology respectively.

Until then, electromagnetic properties of liquid crystals were known either at very low frequencies (DC up to a few MHz) or at very high frequencies (infrared, visible and ultraviolet). More recently, characterization of various liquid crystals has been undertaken at frequencies covering most of the microwave spectrum [Wei03a, Mue05b, Mue05a, Mue06, Mue07, Pen04, Pen06].

In this work several liquid crystals have been employed, whose relevant properties will be shortly presented in this chapter. There is a distinction between commercially available LCs and experimental LC mixtures: unlike the first ones, the experimental mixtures can be synthesized only in limited quantities in the laboratory, at the moment. That is why their availability for the devices presented in this work was not self-evident.

The commercially available liquid crystal 5CB (known also as K15) is a typical liquid crystal for displays. It is therefore usually used as a benchmark against which newly developed mixtures are evaluated. This LC has a nematic phase at room temperature,

between 18°C and 35°C. Dielectric properties of K15 at 38 GHz versus the temperature, are presented in Fig. 4.7. They are extracted with the cavity perturbation method [Pen04, Mue07].

Another commercially available liquid crystal is BL006. It has roughly the same dielectric properties as K15 (only slightly larger $\Delta\varepsilon_r$ and similar $\tan\delta$), but with the advantage of a wider temperature range of the nematic phase (from around -10°C to more than 100°C). Its dielectric properties at 38 GHz over temperature are shown in Fig. 4.8.

MDA-05-893 is the internal name given to a liquid crystal mixture specially developed for microwave applications by Merck KGaA. It has similar dielectric properties to BL006 over a quite large temperature range of nematic phase, as seen from Fig. 4.9.

Finally, the mixture designated MDA-03-2844, was also synthesized by Merck KGaA to achieve increased anisotropy and low loss at microwave frequencies. However, its availability was very limited. Fig. 4.10 gives its dielectric properties over temperature at 9 GHz. Measurements at 38 GHz have not been conducted yet.

Table 4.1 gives an overview of the properties of the four presented liquid crystals at room temperature. From the table it is obvious that for the first three LCs the tunability τ increases slowly, but at the same time the losses are increasing as well (mainly $\tan\delta_\perp$). The last LC mixture, however, exhibits almost twice the tunability of the best of the remaining LCs (28.8% compared to 15.47%) with no increase in losses.

Table 4.1: Properties of the used liquid crystals at room temperature (20°C).

LC Type	f	$\varepsilon_{r,\|\|}$	$\varepsilon_{r,\perp}$	τ	$\tan\delta_{\|\|}$	$\tan\delta_\perp$
K15	35 GHz	2.57	2.3	10.5%	0.0048	0.02
BL006		3.03	2.62	13.53%	0.01	0.022
MDA-05-893		2.65	2.24	15.47%	0.01	0.025
MDA-03-2844	9 GHz	3.4	2.42	28.8%	0.007	0.02

4.4 Applications of Liquid Crystals at Microwaves

The dielectric anisotropy of liquid crystal is very suitable for phase shifting purposes, since the change in permittivity is associated with a corresponding change in the phase of a wave propagating through the liquid crystal. Therefore, the most investigated applications for liquid crystals at microwave frequencies were phase shifter devices.

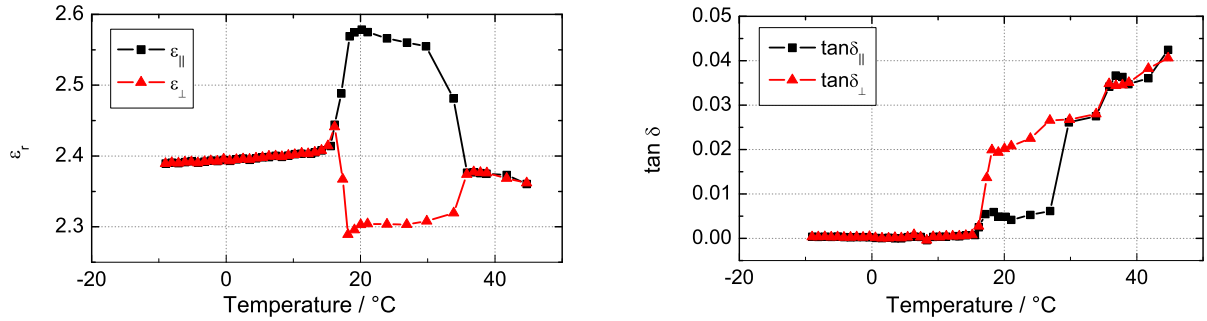

(a) Relative permittivity ε_r (b) Loss angle $\tan\delta$

Figure 4.7: Dielectric properties of K15 over temperature at 38 GHz

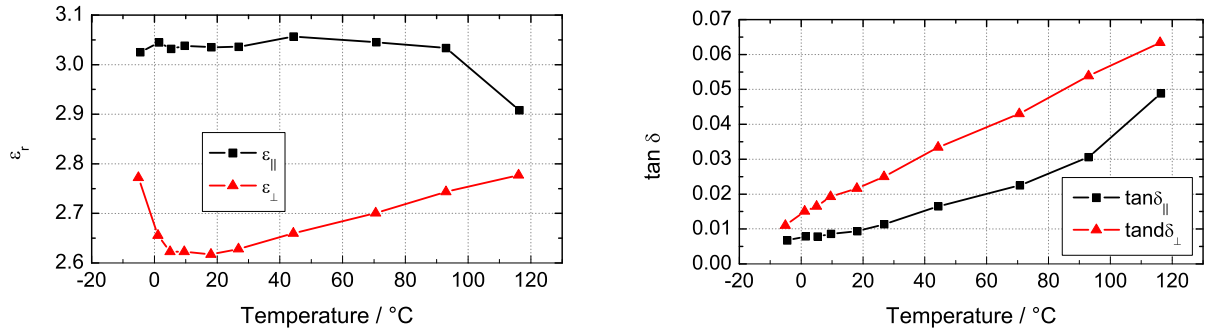

(a) Relative permittivity ε_r (b) Loss angle $\tan\delta$

Figure 4.8: Dielectric properties of BL006 over temperature at 38 GHz

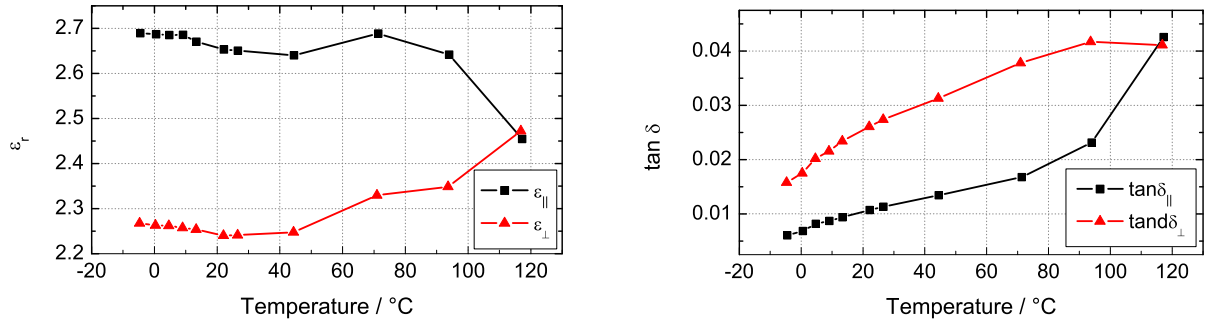

(a) Relative permittivity ε_r (b) Loss angle $\tan\delta$

Figure 4.9: Dielectric properties of MDA-05-893 over temperature at 38 GHz

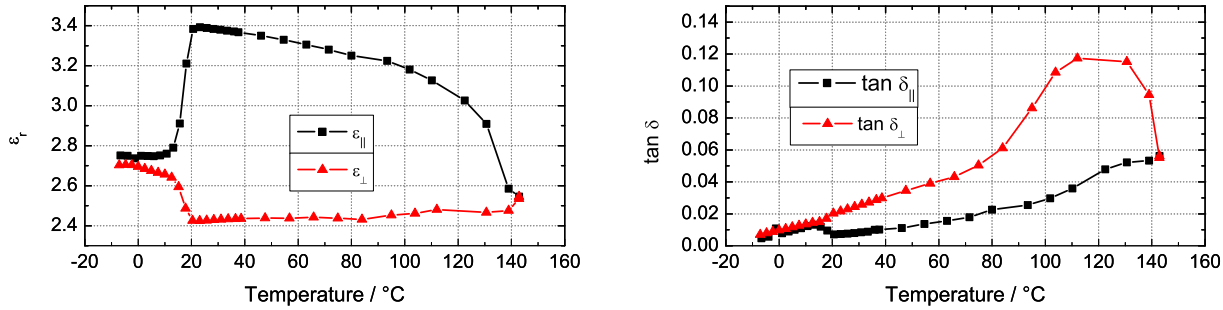

(a) Relative permittivity ε_r

(b) Loss angle $\tan\delta$

Figure 4.10: Dielectric properties of MDA-03-2844 over temperature at 9 GHz

A very important quantity for phase shifters is the figure of merit, defined as:

$$\text{Figure of Merit} = \frac{\text{Differential Phase Shift}}{\text{Insertion Loss}} \quad [^\circ/\text{dB}] \tag{4.19}$$

The figure of merit of a phase shifter is material and device dependent.

A phase shifter in inverted-microstrip technology was presented in [Wei02]. Inverted-microstrip topology is quite convenient for a LC phase shifter, since it provides the cavity needed for the LC and, owing to the propagating microstrip mode, most of the electric field is dominantly guided through the LC, therefore using its dielectric anisotropy very effectively. The phase shifter in [Wei02] was filled with K15, and it was measured between 8 and 18 GHz. A differential phase shift of 53° was measured at 18 GHz with a line length of 49 mm. The FoM was constant over the frequency range, with values of about 8 and 12°/dB for bias voltages of 0 V and 40 V respectively.

In [Mue04], using the same phase shifter type in inverted-microstrip technology, a comparison was made by filling the cavity with K15 and with the highly anisotropic novel mixture. The measurements were performed between 1 and 35 GHz. Compared to a FoM of only 21°/dB for the K15 phase shifter, the phase shifter with the novel mixture exhibited a FoM of 111°/dB. The tendency of increased FoM with higher frequency could also be observed in the considered frequency range.

A finline based phase shifter device is presented in [Mue05a]. The transmission line is an antipodal finline integrated in a Ka-Band rectangular waveguide, with liquid crystal inserted between the overlapping conductors. Differential phase shifts of 75° and 303° were measured at 40 GHz for K15 and the highly anisotropic novel mixture respectively. The resulting FoM was 9°/dB for K15 and 62°/dB for the novel mixture.

In [Mar03] the authors propose a frequency-agile patch antenna with liquid crystal. The patch, designed to operate around 5 GHz, was printed on a 500 μm foam substrate. A

cavity was generated in the foam under the patch, where the LC is filled. Using K15 as liquid crystal, a relative resonance frequency shift of 2.95% was achieved when the bias voltage was changed from 0 to 20 V.

A liquid crystal based millimeter-wave beam former is presented in [Kam04]. It consists of 100μm-thick layers of LC alternately stacked with 10μm metallic electrodes for the application of bias voltage. The millimeter-wave signal is spatially fed to the LC layers, leaving the stack at the opposite side after its phase has been electronically adjusted in each LC layer individually. The device can hence be operated also as a millimeter-wave lens to focus or defocus the beam. Electronic beam steering of $\pm 13^{\circ}$ and lens operation were successfully demonstrated with this device between 50 and 75 GHz.

It is possible to use liquid crystal for realizing tunable frequency selective surfaces (FSS) as shown in [Hu07a]. The FSS presented in this publication uses the dielectric anisotropy of the LC to generate an electronically tunable bandpass filter response at D-band (110-170 GHz). The FSS consists of two printed arrays of slot elements, separated by a 130 μm thick layer of liquid crystals. A 3% shift in the filter passband could be demonstrated by applying a control signal of 10 V.

4.5 Summary

This chapter gave a brief introduction to liquid crystals, highlighting some of their most important and for this work relevant characteristics. Some typical notions like order parameter and director were introduced and explained, followed by classifications of liquid crystals.

Dielectric anisotropy was introduced next, as the central characteristic of liquid crystals for this work. Then, the methods for controlling the dielectric anisotropy were presented: orienting the liquid crystal molecules by means of external fields or processed surfaces. A section was dedicated to the presentation of the dielectric properties of the liquid crystals employed in the present thesis. The chapter closed with a brief overview of existing applications of liquid crystals for tunable microwave devices.

Chapter 5

Tunable Elementary Cells for Reflectarrays using Liquid Crystal

As already presented in chapter 2, there are numerous topologies available for the design of a reflectarray unit cell, each one exhibiting particular properties. One needs therefore to chose the most promising ones for the purpose of tuning with LC. First, the unit cell structure has to be optimized in order to make best use of the dielectric anisotropy of liquid crystals. It has been shown in [Mue07], that the tunability of MIM (Metal-Insulator-Metal) structures exceeds that of slot structures (Fig. 5.1). It is therefore reasonable to focus the investigation efforts on unit cells in MIM geometries.

Furthermore, attention is dedicated to optimizing the electrical properties of the unit cells (tunable phase range, reflection loss). Mechanical properties are not neglected in the process, in order to be able to realize the structures with the available technology and to allow for a robust construction.

The microwave design is constrained by specific restrictions imposed by the use of liquid crystal such as the thickness of the LC layer or the limited amount of available LC. The height of the LC cavity should not exceed a few hundreds of micrometers in order to allow alignment with polyimide layers [Dol93]. Furthermore, it has been shown that

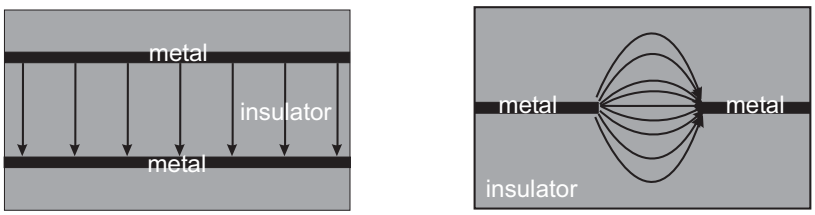

Figure 5.1: Exemplary MIM structure and slot structure with schematic distribution of the electric field lines.

there is a strong dependency of the switching times on the LC layer thickness.

Operating frequencies of 35 GHz and 77 GHz have been chosen for LC unit cells because of potential applications of reflectarrays in space missions and long-range automotive radar. In addition, this frequency bands offer a good compromise: the restrictions mentioned above can be held, whereas the resulting dimensions of the structures still allow the use of a simple etching technology (see Appendix A3 for details of the etching process). Therefore, a first group of LC tunable unit cells has thus been designed and measured in the *Ka*-band. Since it has been shown that liquid crystals are more promising for higher operating frequency, a second group of unit cells has been designed at 77 GHz.

5.1 Functional Principle

Printed microstrip patch

Taking the elementary cells presented in section 2.3 as a starting point, different structures can be imagined that can serve as LC-tunable reflectarray unit cells. One possible configuration is that of a metallic patch over a ground plane, with a LC layer sandwiched in between. Fig.5.2 presents a cross section of such a LC-tunable reflectarray unit cell.

The principle is the same as illustrated in section 4.2 on the basis of the LC orientation in a parallel plate capacitor. The two electrodes of the capacitor are now replaced by the patch and the ground plane. The liquid crystal molecules are initially aligned parallel to the patch and ground as shown in Fig. 5.2 (a). The alignment is enforced with the aid of the polyimide layer, as explained in section 4.2. The RF-field ($\vec{E}_{RF}$), given by the microstrip patch fundamental mode of resonance TM_{010}, is mainly confined in the LC-volume and is essentially perpendicular to the director orientation. Thus, the RF-field will "perceive" an $\varepsilon_{r,LC,eff} \approx \varepsilon_{\perp}$. Applying an increasing control voltage, the molecules will begin to rotate as soon as the voltage exceeds the threshold voltage V_{th} (see Fig. 5.2 (b)). Is the control dc voltage increased even further, the LC molecules will tend to align with the DC field lines, until eventually they are (almost) completely aligned and a further increase of the control voltage will have no effect. In this state, the main axis of the molecules becomes parallel to the RF-field $\vec{E}_{RF}$, and the experienced permittivity becomes $\varepsilon_{r,LC,eff} \approx \varepsilon_{\parallel}$, as depicted in Fig. 5.2 (c).

By being able to continuously tune the effective relative permittivity, the electrical length of the patch is continuously varied as well. Therefore, the patch physical size can now be kept constant for all reflectarray elements (identical patches, instead of variable patches as in chapter 3), while the phase adjustment is realized electronically. A further ad-

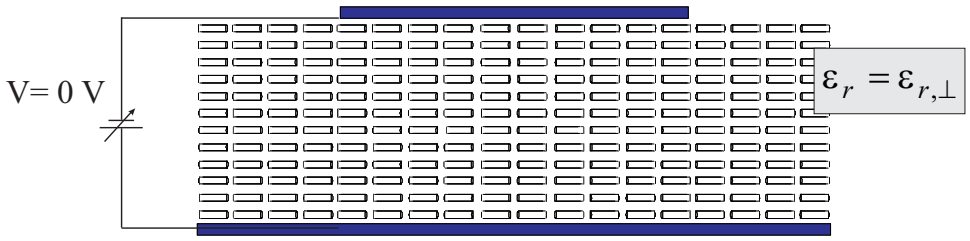

(a) Director is parallel to patch and ground plane, due to prealignment with polyimide film.

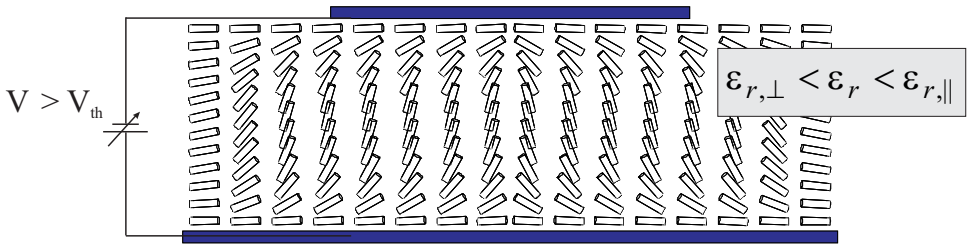

(b) Director reorients itself according to the spatial distribution of field lines and the field intensity.

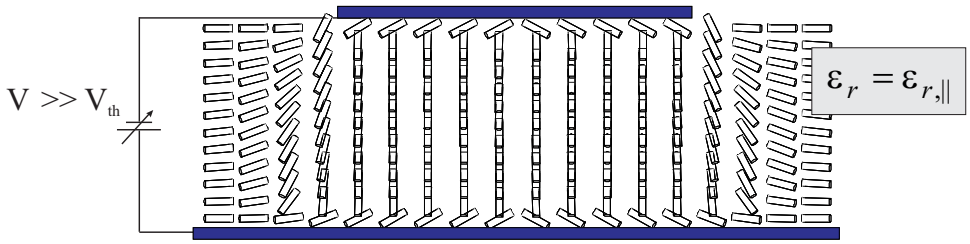

(c) Director is totally oriented along the field lines, except for the anchoring layer adjacent to the polyimide film.

Figure 5.2: Functioning principle of the LC-tunable reflectarray unit cell with single microstrip patch.

vantage is that the tuning can be accomplished dynamically during operation of the reflectarray.

Line coupled to patch

Another possible configuration of a LC-tunable reflectarray unit cell is that consisting of a patch coupled to a line through an aperture in the ground plane, as described in section 2.3. Instead of varying the line length, as in the case of fixed beam reflectarrays, the liquid crystal will be enclosed between line and ground plane. The principle is the same as described above, except that now the electric length of the line is changed, instead of the electric length of the patch, according to the equation:

$$\Delta\varphi = \Delta\beta\,\ell = \Delta\left(\frac{2\,\pi}{\lambda_g}\right)\cdot\ell = 2\,\pi\frac{\ell}{\lambda_0}\left(\sqrt{\varepsilon_{eff,\perp}} - \sqrt{\varepsilon_{eff,\parallel}}\right) \tag{5.1}$$

where β is the phase constant, ℓ the physical length of the line, $\lambda_g = \lambda_0 / \sqrt{\varepsilon_r}$ the guided wavelength and ε_{eff} the effective dielectric constant of the microstrip line.

From these two basic configurations other structures can be derived, trading off simplicity for other convenient electrical features. A stacked patch configuration is for instance conceivable: the additional degree of freedom offered by the dimensions of the upper patch allows to compensate for a slight loss of tunability, since now less field is confined in the liquid crystal, between the lower patch and ground. The aperture coupled line can be as well replaced by a microstrip filter, the complexity of the structure and the additional loss being compensated for by other desirable features like for instance a steeper phase curve that allows enhanced tunable phase range.

Illustration of phase shift principle and associated problems

Considering the unit cells employed in chapter 3 for the realization of the fixed beam reflectarrays - a single patch printed on a metalized substrate -, let us now suppose that the substrate has a tunable permittivity from $\varepsilon_{r1} = 2.3$ to $\varepsilon_{r1} = 2.6$. This yields a tunability of about 12%, a typical value for commercially available LCs (see Table 4.1). The simulated phase curves show the typical characteristics presented in Fig. 5.3. It is apparent that by tuning the relative permittivity of the substrate the phase curve shifts, allowing at a given frequency, e.g. 35 GHz, the adjustment of the phase in a certain range.

From Fig. 5.3 two problems can be recognized:

1. As long as the losses of the substrate are low, in the range of $\tan\delta \approx 10^{-3...4}$, the attenuation of the reflected wave is almost negligible, as shown in Fig. 5.3 (a). Liquid crystals, however, exhibit losses in the magnitude of $\tan\delta \approx 10^{-2}$, which causes significant attenuation, as seen in Fig. 5.3 (b). Moreover, the attenuation is not constant, but for different adjusted phase values the attenuation varies as well: for instance between -1 dB and -1.5 dB at 35 GHz in the presented case.

2. Ideally, the entire phase range of 360° is required; if one allows some phase errors, 300° could also be sufficient for a functional reflectarray [Tsa03a]. This hypothetical structure can however only provide a tunable phase range, between the two extreme values of the permittivity, of about 100° at 35 GHz. A larger tunable phase range can be achieved either by using specially designed LC mixtures with higher tunability, or / and by designing the structure in such a way to enhance its phase shifting properties.

In order to enhance the tunable phase range, the phase characteristic should be steeper. This can be achieved for instance with a thinner substrate, as already shown in section 2.3. However, a steeper phase characteristic means a stronger resonant behavior, which

leads to higher reflection attenuation, as shown in Fig. 5.4. By using a thinner substrate, the tunable phase range is indeed increased to around 250°, on the other hand the peak reflection losses also reach -6 dB.

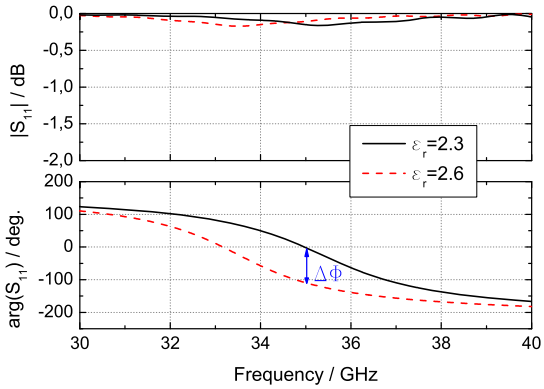

(a) Patch on substrate with h=0.38 mm, variable ε_r and tan δ=0.001

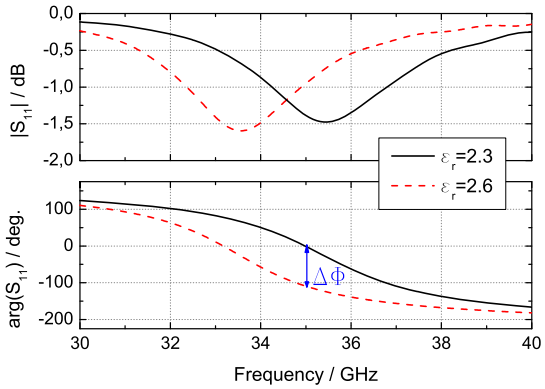

(b) Patch on substrate with h=0.38 mm, variable ε_r and tan δ=0.01

Figure 5.3: Magnitude and phase vs. frequency: tuning of the reflection phase by means of permittivity variation. The peak reflection losses increase as an effect of the lossy substrate.

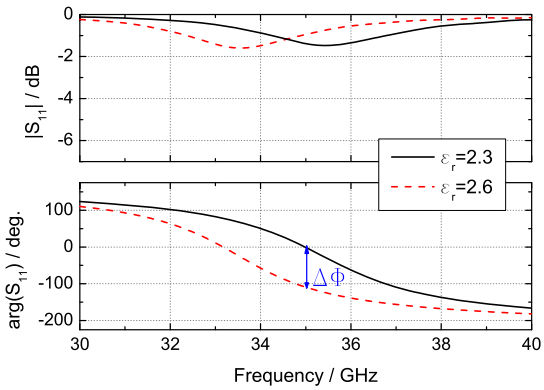

(a) Patch on substrate with h=0.38 mm, variable ε_r and tan δ=0.01

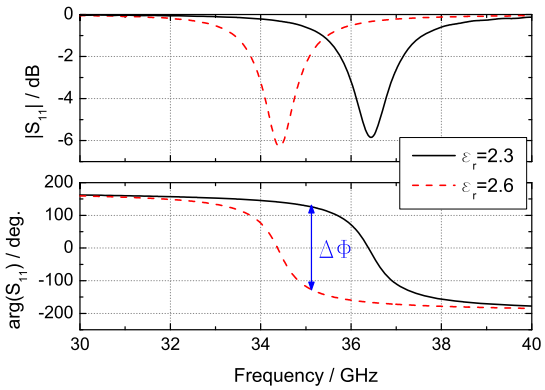

(b) Patch on substrate with h=0.12 mm, variable ε_r and tan δ=0.01

Figure 5.4: Illustration of the trade-off governing the reflectarray unit cells with single patch and lossy substrate: a steeper phase characteristic implies larger tunable phase range but also higher reflection losses.

Therefore, it is important to investigate the dependency of the tunable phase range and that of the associated peak losses on different parameters, such as dielectric loss angle tan δ, metallic conductivity σ or substrate thickness h. By using the lumped element equivalent circuit presented in section 2.2, such an analysis can be conducted very fast.

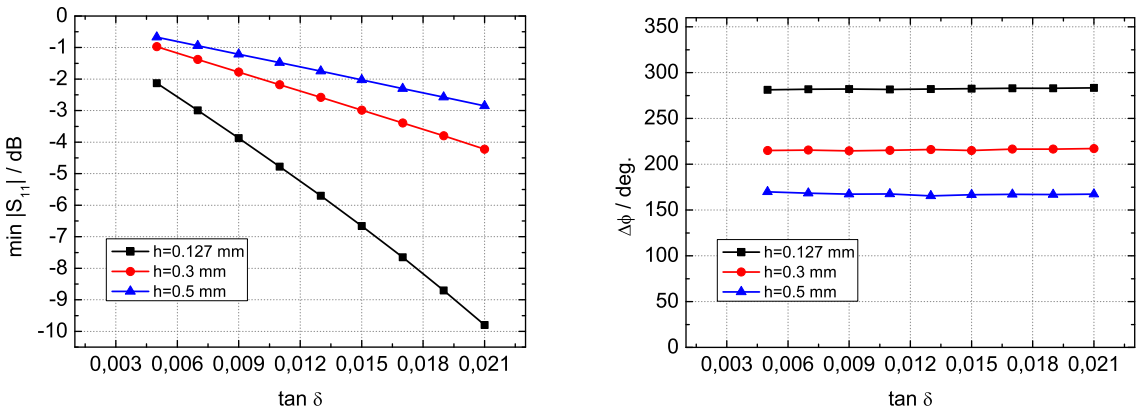

(a) Peak reflection loss $|S_{11}|$ vs. $\tan\delta$.

(b) Phase range at 35 GHz vs. $\tan\delta$.

Figure 5.5: Peak losses and tunable phase range at 35 GHz with a permittivity variation of the substrate between $\varepsilon_{r,1} = 2.2$ to $\varepsilon_{r,2} = 2.8$, for different substrate thicknesses.

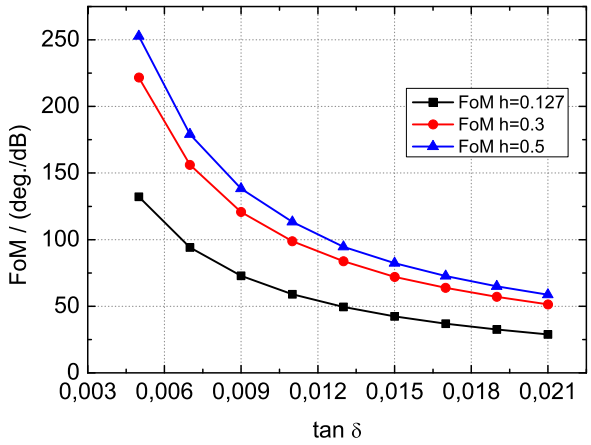

Figure 5.6: FoM vs. $\tan\delta$.

Fig. 5.5 presents the dependency of phase range and peak losses on the substrate loss angle for a 35 GHz reflectarray unit cell, when the substrate permittivity is varied from $\varepsilon_{r,1} = 2.2$ to $\varepsilon_{r,2} = 2.8$. As expected, the peak losses increase with the increase of the loss angle. Furthermore, the thinner the substrate, the more pronounced is the increase ratio of the losses as shown in Fig. 5.5 (a). The phase range that can be tuned at a certain frequency is independent of the substrate loss angle, but strongly dependent on the substrate thickness, as demonstrated in Fig. 5.5 (b).

In order to capture the existing trade-off, a figure of merit can be defined, that puts the tunable phase range in relation to the peak losses:

$$FoM = \frac{\Delta\varphi}{-|S_{11}|} \left[\frac{\text{deg.}}{\text{dB}}\right] \tag{5.2}$$

The plot of this figure of merit versus the loss angle in Fig. 5.6 indicates that a thicker substrate (300...500 μm) would be more suitable, representing the best compromise between phase range and reflection losses. On the other hand, the plot in Fig. 5.5 (b) indicates that a thinner substrate (≈100 μm) is mandatory in order to approach a phase range of at least 300°.

Similarly, characteristics can be derived for a variation of the metallic conductivity σ for different substrate thicknesses h. As expected, the conductivity of the microstrip element as well as the substrate thickness have both a strong impact on the value of the peak losses, exhibited in Fig. 5.7 (a). On the other hand, the phase range achievable with a certain dielectric anisotropy (here $\Delta\varepsilon_r$=2.8-2.2=0.6) is independent of σ but strongly dependent on the substrate thickness h, as indicated in Fig. 5.7 (b).

The plot of the FoM versus σ in Fig 5.8 yields a very similar characteristic as the plot of FOM versus $\tan\delta$: the FoM degrades with the reduction of the conductivity, and the best results in terms of FoM are achieved with thicker substrates (300...500 μm) according to Fig 5.8. It would therefore be interesting to see how the figure of merit depends of the substrate thickness. For this purpose, the loss angle and the patch conductivity have been fixed to typical values ($\tan\delta = 0.01$ and $\sigma = 5 \cdot 10^6\,\text{S/m}$), while the substrate

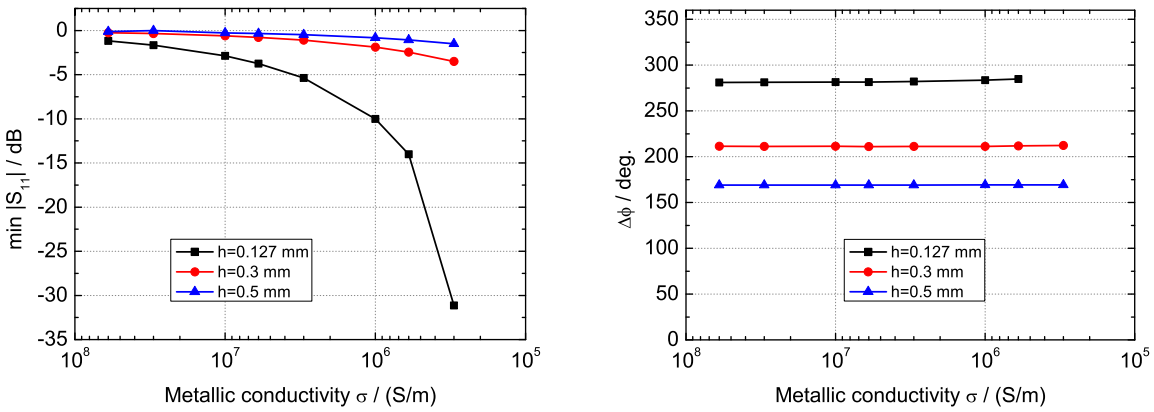

(a) Peak reflection loss $|S_{11}|$ vs. σ.

(b) Phase range at 35 GHz vs. σ.

Figure 5.7: Peak losses and tunable phase range at 35 GHz with a permittivity variation of the substrate between $\varepsilon_{r,1} = 2.2$ to $\varepsilon_{r,2} = 2.8$, for different substrate thicknesses.

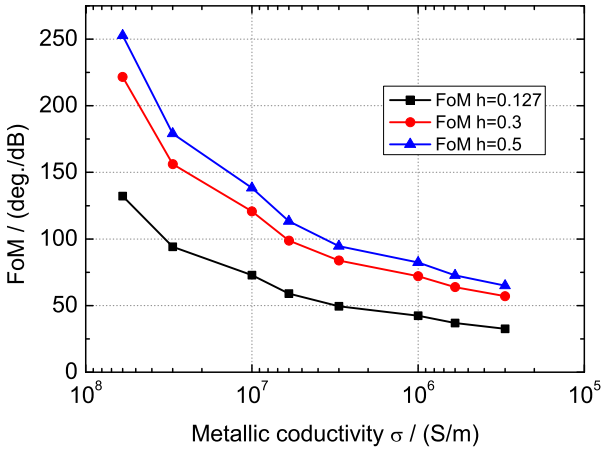

Figure 5.8: FoM vs. σ.

thickness has been varied. Now, one can extract the characteristics of peak loss, tunable phase range and FoM versus substrate thickness h, which are shown in Fig. 5.9.

The adjustable phase range diminishes with the increase of the substrate height, an expected result, already discussed in section 2.3. On the other hand, the reflection losses ($|S_{11}|$) also diminish with the increase of the substrate height. The plot of the FoM versus h confirms that thicker substrates yield better FoM, however the FoM improvement is underproportional to the increase in substrate height.

Although the presented results of FoM indicate that the choice of a thicker substrate is preferable, there are other considerations, of a more practical nature, that require the

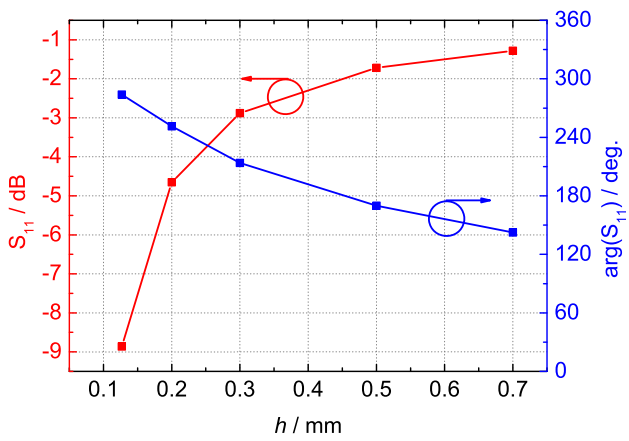

(a) Peak losses (here: $|S_{11}|$) and phase range versus substrate height h.

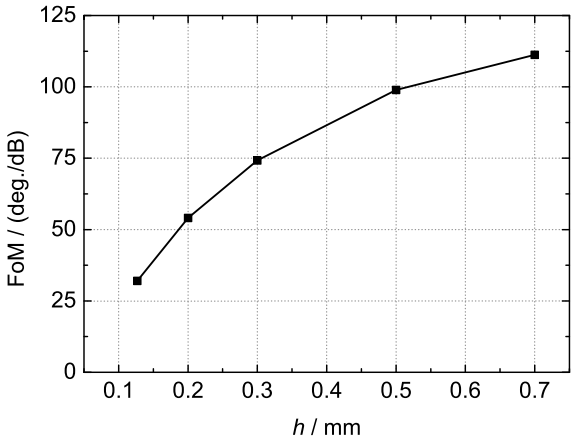

(b) FoM versus substrate height h.

Figure 5.9: Dependency of peak losses, phase range and FoM on the substrate height h.

opposite. First, an LC layer thicker than about 300 μm would reduce the effectiveness of the polyimide layer, making it impossible to prealign the director parallel to patch and ground plane throughout the entire layer. Second, a thicker LC layer would increase the maximum voltage necessary for complete director reorientation. Third, the switching times, which are anyway very long (see Section 4.2), would become even longer, according to the formulas 4.18. For these reasons, the thickness of the LC layer was kept in this work as low as possible: 127 μm at 35 GHz and 50 μm at 77 GHz. However, as a trade-off, relatively large peak losses have to be accepted.

Another analysis reveals the dependency between the dielectric anisotropy $\Delta\varepsilon$ (or tunability τ) of the liquid crystal, and the amount of tunable phase range at the operation frequency. The plots for a 35 GHz design are presented in Fig.5.10. Based on these plots, following observations can be made: as expected, the amount of tunable phase range increases with the tunability of the used liquid crystal. However, as the tunability increases, the additional gain in phase range is less and less. This saturation effect is best seen for the thin layer with $h = 127\,\mu$m.

This is an important insight, allowing a better formulation of the requirements that should be met by liquid crystals for use in reflectarrays. While tunability is by all means not unimportant, it was shown that it makes little difference whether the used LC has a tunability of 25% or of 35%, since the gain in phase range is comparatively small. On the other hand, it makes a lot of difference whether the dielectric loss angle of the liquid crystal is 0.01 or 0.02, since this has a critical effect on the peak reflection losses, according to Fig. 5.5 (a).

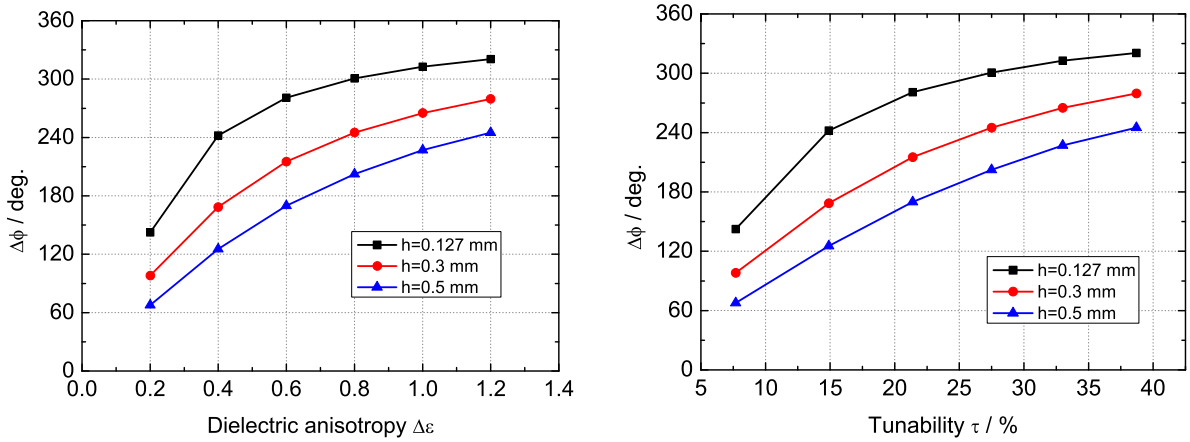

(a) Phase range at 35 GHz versus dielectric anisotropy $\Delta\varepsilon$.

(b) Phase range versus tunability τ.

Figure 5.10: Achievable phase range at 35 GHz versus dielectric anisotropy $\Delta\varepsilon$ and tunability τ for different substrate heights.

5.2 Simulation and Characterization Setup

In order to assess the reflection properties of the LC unit cells, the same simulation environment is used as for non-tunable unit cells. Suitable boundary conditions are chosen: two of the cell boundaries are perfect electric conductors (PEC), the other two are perfect magnetic conductors (PMC), as shown in Fig. 5.11. One can thus simulate with little computational effort a plane wave impinging at normal incidence on an infinite array with identical elements. The simulation tool used throughout the work is the FIT solver *CST-Microwave Studio* [cst07]. The port is set at a convenient distance from the cell (about 1.5 to 2λ) to allow some propagating space, without however making the computation domain unnecessarily large. The reflection coefficient is recorded at the surface of the cell, simply by setting the reference plane of the port accordingly.

Whereas E-walls (PEC boundaries) can be quite accurately represented by metallic walls, in reality it is very difficult to emulate H-walls (PMC boundaries): it is possible, using artificial surfaces, but with limited accuracy and in a narrow frequency band.

Therefore, for the characterization of the realized unit cells a *waveguide simulator* has been used, which is well known from the literature ([Han65, Sto05]). It consists of a rectangular waveguide terminated with a pair of unit cells. The boundary conditions are different than in the simulation: four E-walls instead of two H-walls and two E-walls. The PEC walls act like periodic boundary conditions around the elements. This causes the enclosed microstrip elements to behave as though they are in an infinite array of identical elements. Currents on the microstrip patches are imaged on the waveguide walls, where image currents simulate the presence of an infinite array of patches, accounting for all mutual coupling among elements [Sto05].

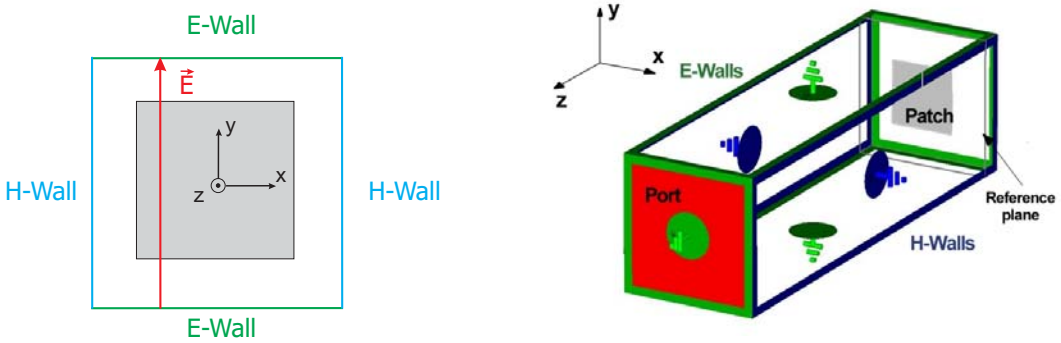

(a) Schematic of the cell boundaries and polarization of incident electric field.

(b) Simulation setup in CST Microwave Studio.

Figure 5.11: Boundaries for the simulation environment of a LC-tunable reflectarray unit cell: two parallel E-walls (PEC) and two parallel H-walls (PMC).

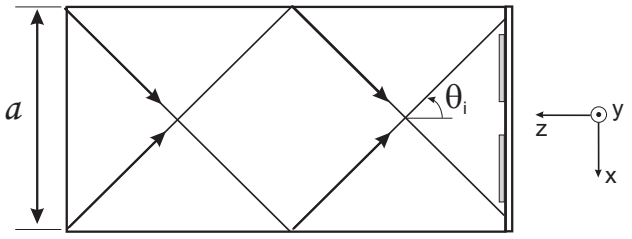

Figure 5.12: Schematic of the plane wave decomposition in a rectangular waveguide.

According to Fig. 5.12, the fundamental TE_{10} mode, which is propagating in the waveguide in z-direction as imposed by the boundary conditions, is composed by the superposition of two plane waves, making an angle of

$$\theta_i = \arcsin\left(\frac{\lambda_0}{\lambda_c}\right) \tag{5.3}$$

with the plane containing the unit cells (λ_0: free-space wavelength, λ_c: cut-off wavelength). With $\lambda_c = 2\,a$ for the fundamental mode, the expression for the incident angle becomes:

$$\theta_i = \arcsin\left(\frac{\lambda_0}{2\,a}\right) \tag{5.4}$$

For the *Ka*-band waveguide simulator this angle varies between 31.8° at 40 GHz and 52.6° at 26.5 GHz (the band edges), and it amounts to 37° at 35 GHz, the frequency of interest. In Fig. 5.13 it is shown, that the superposition of two plane waves making an angle of θ=37° with the propagation direction, yields a distribution of the field with $\vec{E}$ field nulls along parallel planes. The distance between the walls equals exactly the large dimension of the WR28 waveguide a=7.12 mm. Metallic (waveguide) walls can be thus inserted along these lines without interfering with the field pattern.

Since the phase response of the unit cell is dependent of the incidence angle, slight differences between simulation and measurement results are likely to occur. However it has been shown that this differences are not very severe up to an incidence angle of about 40° [Tar94], and thus the setup can be seen as adequate for the purpose of testing in principle the functionality of LC-tunable unit cells.

In Fig. 5.14 the schematic of the measurement setup and a picture of the employed waveguide simulator with the two terminating unit cells are presented. The waveguide has been manufactured by milling, out of two brass blocks. The milled blocks are screwed together to form the WR28 waveguide. In order not to disturb the currents flowing in the waveguide walls, the two halves are separated precisely at the center of E-plane (in the coordinate plane y-z).

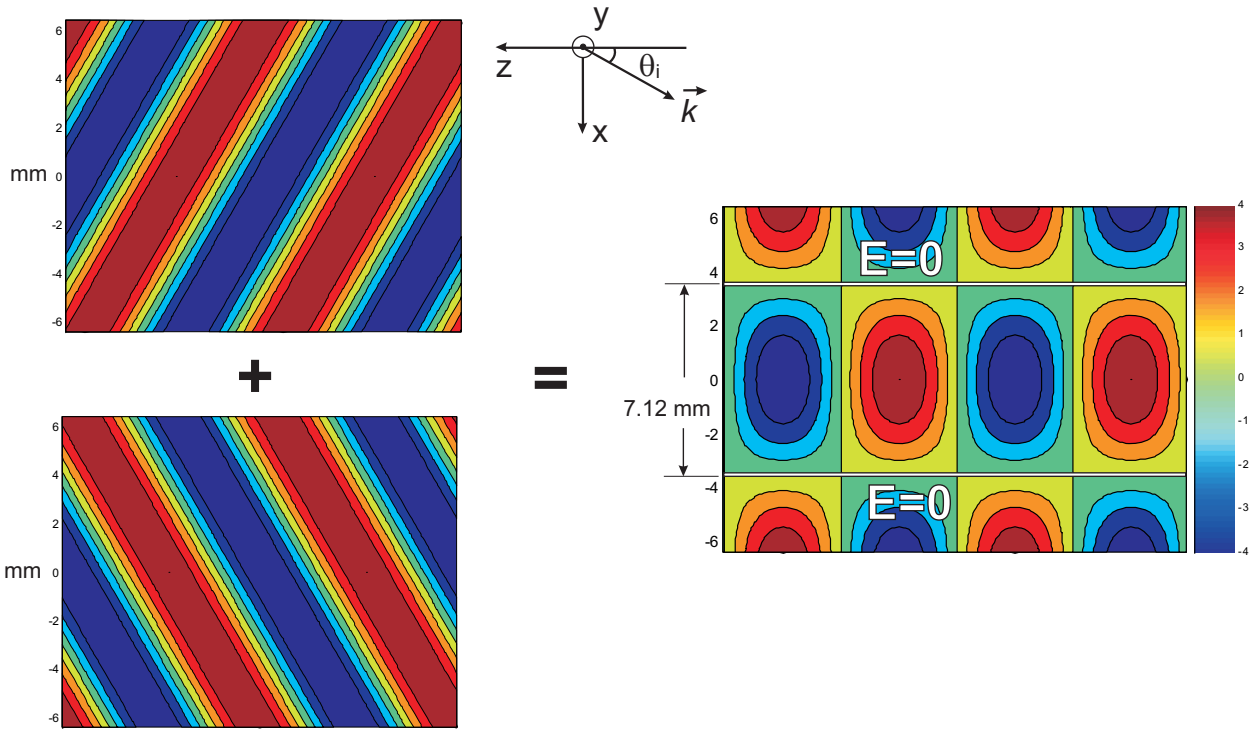

Figure 5.13: Superposition of two plane waves, each making an angle θ=37° with the propagation direction (f=35 GHz).

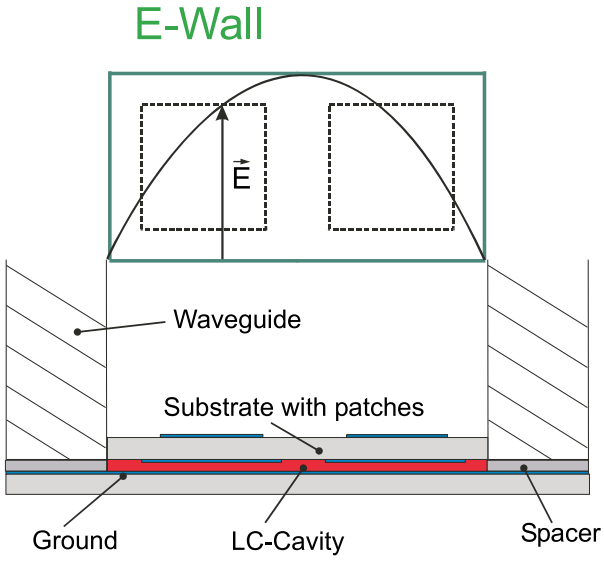

(a) Schematic of the unit cell pair terminating the waveguide simulator.

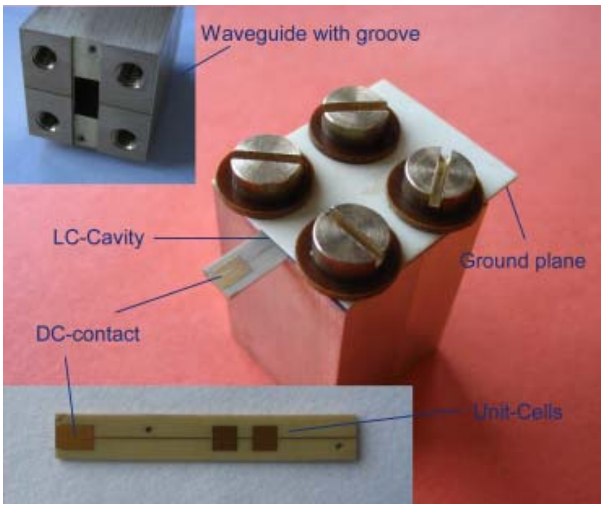

(b) Picture of the used waveguide simulator and of the two unit cells.

Figure 5.14: Measurement setup for the extraction of the complex reflection coefficient S_{11} of LC reflectarray unit cells.

A groove is also milled at one end in order to accommodate the unit cell pair. The groove allows at the same time to prolong the substrate carrying the unit cell pair past the edge of the waveguide block, thus providing easy access to the DC control line. The DC bias line connects to the side of both patches that make up the unit cell pair. It is perpendicular to the electric field that excites the patches, so that the patch side to which it connects will not be an active side. Thus, the DC bias line has no noticeable effect on the measurement.

The waveguide is connected to the Port 1 of the Anritsu 37397C Vector Network Analyser, by means of a waveguide to coaxial cable transition. A SSL (Short - offset Short - Load) waveguide calibration technique with sliding load is employed. The calibration plane is the contact plane between the coax-waveguide transition and the waveguide simulator, as shown in Fig. 5.15.

The measured phase and magnitude of the complex reflection coefficient S_{11} are then extracted. In a further step, the delay introduced by the length of the waveguide simulator is finally deembedded from the results, to obtain the phase of the reflection coefficient at the reference plane (see Fig. 5.15). The deembeded phase is calculated according to the following relation:

$$arg(S_{11})|_{ref.plane} = arg(S_{11})|_{cal.plane} + 2\,\beta_g\,\ell \tag{5.5}$$

where $arg(S_{11})|_{ref.plane}$ is the phase of the reflection coefficient at the reference plane, $arg(S_{11})|_{cal.plane}$ is the measured phase of the reflection coefficient, at the calibration

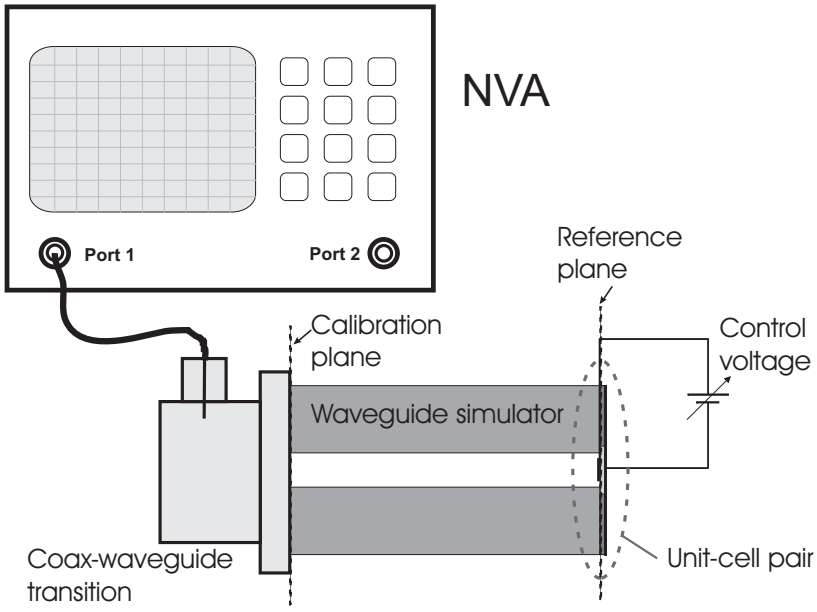

Figure 5.15: Measurement setup with the waveguide simulator connected to Port 1 of the VNA by means of a coaxial-to-waveguide transition.

plane, β_g is the guided phase constant in the waveguide simulator and ℓ=30 mm is the length of the waveguide simulator.

For the guided wavelength holds [Wei99]:

$$\beta_g = \frac{2\pi}{\lambda_g} = \frac{2\pi}{\lambda_0}\sqrt{1-\left(\frac{\lambda_0}{\lambda_c}\right)^2}) = 2\pi\sqrt{\left(\frac{1}{\lambda_0}\right)^2-\left(\frac{1}{\lambda_c}\right)^2} = 2\pi\sqrt{\left(\frac{1}{\lambda_0}\right)^2-\left(\frac{1}{2\,a}\right)^2} \quad (5.6)$$

with

$$\lambda_g = \frac{\lambda_0}{\sqrt{1-\left(\frac{\lambda_0}{\lambda_c}\right)^2}} \quad (5.7)$$

the guided wavelength.

5.3 Investigated Unit Cells and Measurement Results at 35 GHz

In this section the investigated unit cell topologies for use with LC at 35 GHz will be discussed. For each topology brief schematic and specification of the used materials are presented, followed by the presentation and discussion of the measured results.

5.3.1 Single Patch

The most straightforward topology of a LC unit cell for reflectarrays is that of a microstrip patch over the LC cavity. It was chosen for its simplicity, as the use of liquid crystal introduces errors and uncertainties anyway, so that a structure as simple as possible was desired in a first step. The change in LC permittivity shifts the resonance frequency of the patch, thus allowing control of the phase.

To create a cavity for the liquid crystal, a superstrate is needed, which is also used to carry the patch metalization, as shown in Fig. 5.16. The patch is printed on 0.50 mm thick TMM3 Rogers carrier substrate, since this ceramic substrate provides a relatively low dielectric constant ($\varepsilon_{TMM3} \approx 3.27$ [Rog07]) and also the mechanical rigidity and flatness required to form the LC cavity. The ground plane consists as well of TMM3 ceramic, completely metalized on one side.

This type of cell has been filled with several liquid crystal mixtures: two commercially available LCs known under the names K15 and BL006, and the highly anisotropic mix-

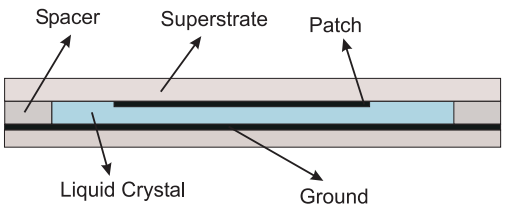

(a) Schematic of the unit cell with single patch.

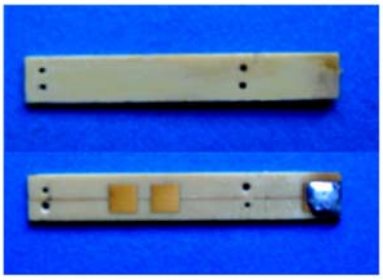

(b) Realisation of the unit cell with simple patch - front and backside view.

Figure 5.16: Unit cell with simple patch

ture specially developed by Merck, known as MDA-03-2844 (see also chapter 4). The control voltage was swept during the first measurements between 0 and 40 V, but it was soon observed that a complete resonance frequency shift is achieved at 20 V.

The measurement results are organized as follows: the phase and magnitude of the reflection coefficient versus frequency are shown for each measurement for all the applied bias voltages. For clarity reasons, and in order to suggest the displacement of the curves as the bias voltage is increased, only a few curves are highlighted and labeled with the respective voltages. Next, a vertical cut is made at the frequency where the maximal phase shift is achieved – designated as the operation frequency of the unit cell – and the phase and magnitude dependence on the bias voltage are recorded in a single plot.

Fig. 5.17 shows the phase and magnitude of the reflection coefficient for the cell filled with K15. There is a very pronounced resonance notch in the magnitude characteristic, varying from about -14 dB for 0 V to -10 dB for 20 V. The variation can be explained with the variation of $\tan\delta$ from $\tan\delta_{\perp} = 0.02$ to $\tan\delta_{\parallel} = 0.0048$.

The resonance frequency can be tuned between about 32.5 to 34 GHz. The maximal phase shift is achieved at 33 GHz, which represents an error of about 6% with respect to the desired operating frequency of 35 GHz. This can be regarded as a reasonable deviation, considering some factors that caused it:

- The cell has been designed for permittivities of $\varepsilon_{r,\perp} = 2.3$ and $\varepsilon_{r,\parallel} = 2.6$, there are however uncertainties of the measured values of $\varepsilon_{r,K15}$ as high as 4%, as reported in [Mue07].

- There are inevitable etching errors, alignment errors of the cell in the waveguide simulator, errors regarding the cavity height, since the used spacer was a soft substrate prone to compression.

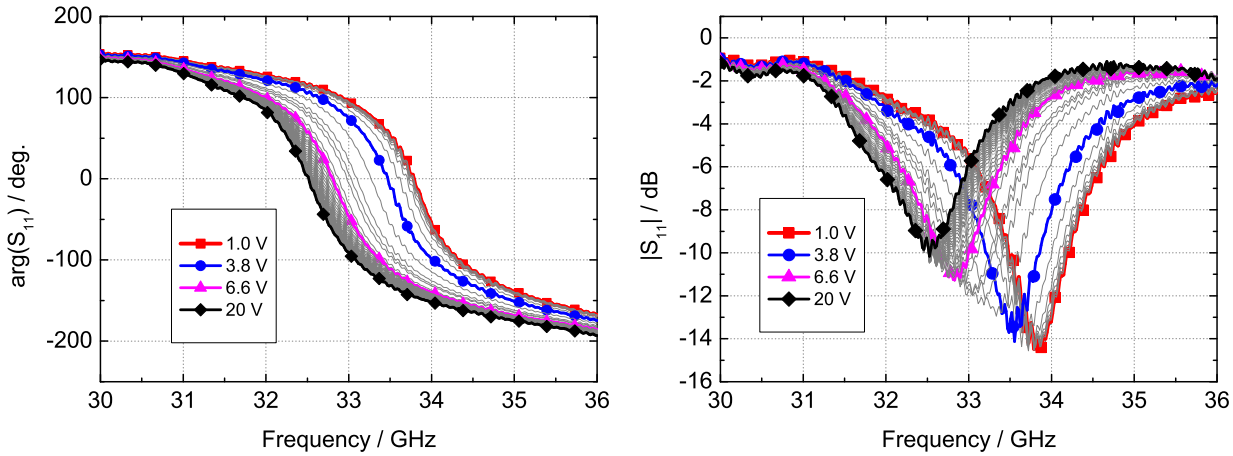

(a) Phase of the reflection coefficient

(b) Magnitude of the reflection coefficient

Figure 5.17: Measured results of the unit cell pair with single patches filled with K15

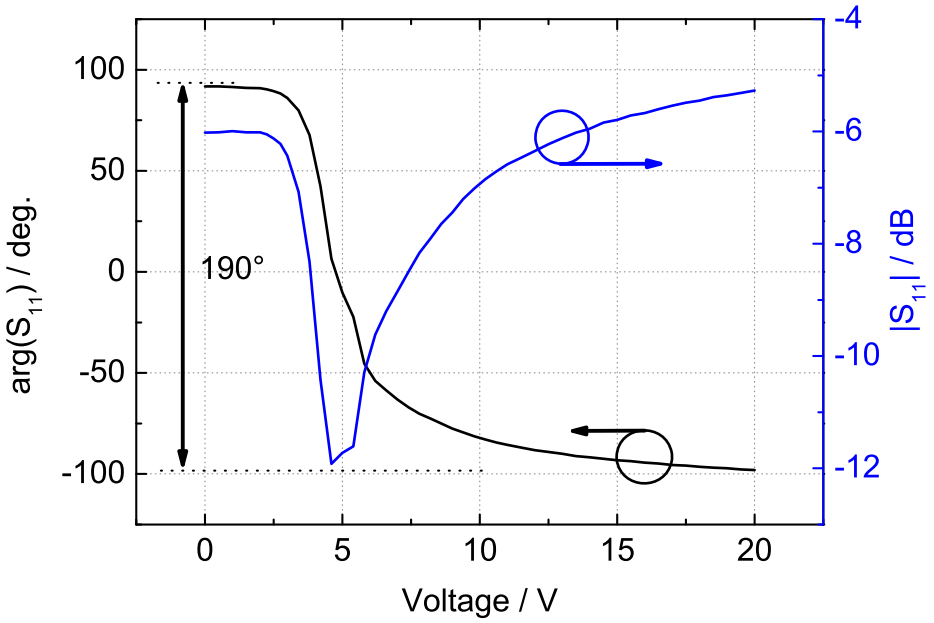

Figure 5.18: Phase and magnitude of the complex reflection coefficient $\underline{S}_{11}$ versus the control voltage at 33 GHz - unit cell filled with K15.

Fig. 5.18 reveals that only about 190° tunable phase range can be achieved with this unit cell, which is far too little, compared with the at least 300° needed.

The measured results of the unit cell with single microstrip patch filled with BL006 are shown in Fig. 5.19. The resonance notch in the magnitude plot can now be tuned between 31.5 GHz and 34 GHz, which is 1 GHz more than with the K15 unit cell, or an improvement of 60% in relative terms. The peak return loss is also slightly reduced, it varies between -13 dB and -8 dB compared to -14 dB to -10 dB. The performance improvement,

especially the wider tuning of the resonance, is expected because of the better tunability of BL006 compared to K15.

As a consequence, the tunable phase range at 33 GHz increases to about 250°, as can be observed in Fig. 5.20. At this frequency, the maximal return loss is slightly under -10 dB. The actual operating frequency is also deviating from the design operating frequency for the same reasons highlighted previously.

As expected, the best result is obtained by filling the unit cell with the highly anisotropic

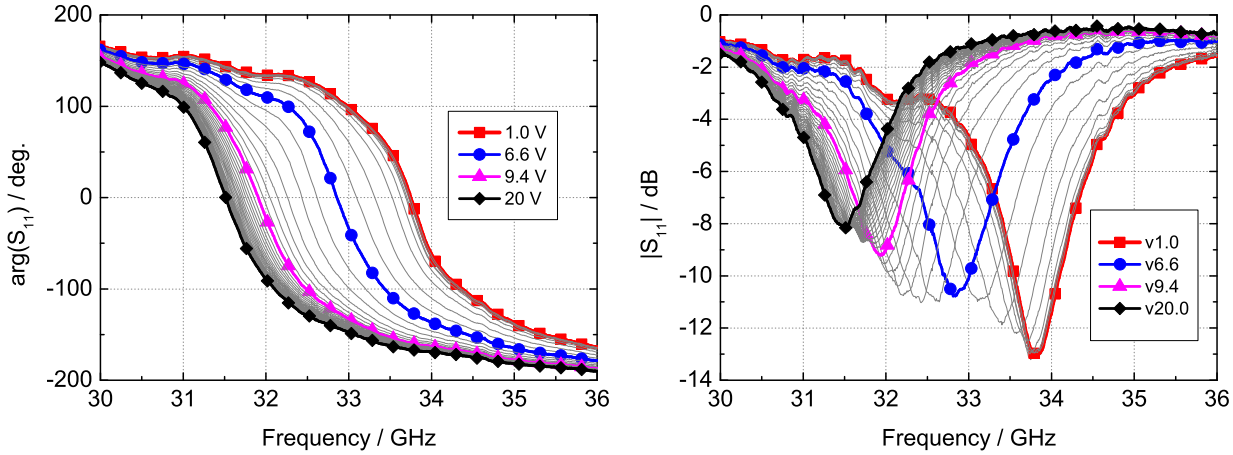

(a) Phase of the reflection coefficient

(b) Magnitude of the reflection coefficient

Figure 5.19: Measured results of the unit cell pair with single patches filled with BL006

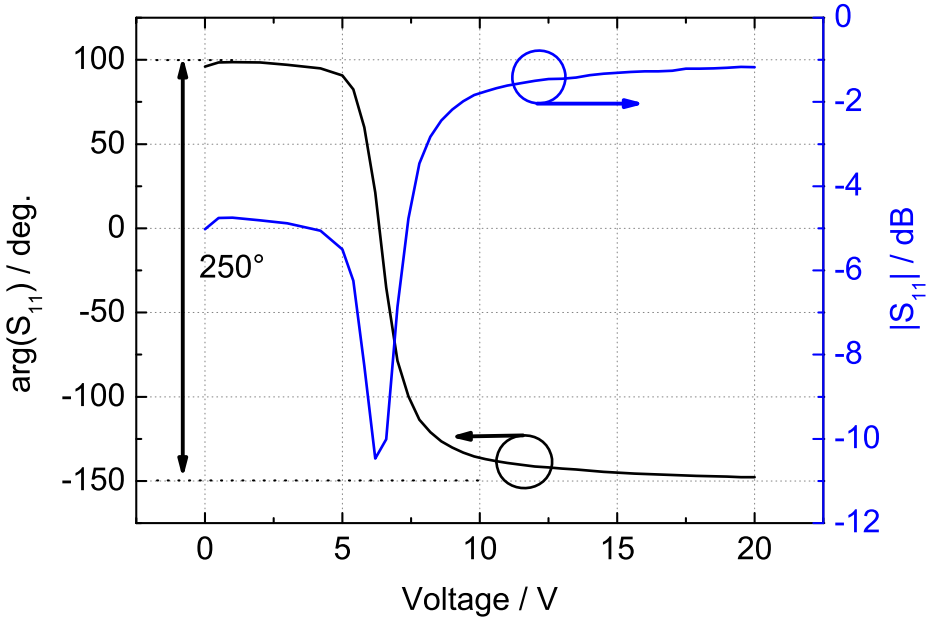

Figure 5.20: Phase and magnitude of the complex reflection coefficient $\underline{S}_{11}$ versus the control voltage at 33 GHz - unit cell filled with BL006.

mixture MDA-03-2844. Fig. 5.21(b) shows that the resonant notch of the magnitude can be tuned between 33 and 37 GHz, i.e. in a 4 GHz-span compared to 2.5 GHz with BL006 and 1.5 GHz with K15. The return loss remains roughly constant at around -8 dB. The fact that the return loss does not diminish with the increase of the bias voltage, as it was the case with the previous two unit cells filled with K15 and BL006, can be explained with the help of the lumped element equivalent circuit in section 2.2. As the value of

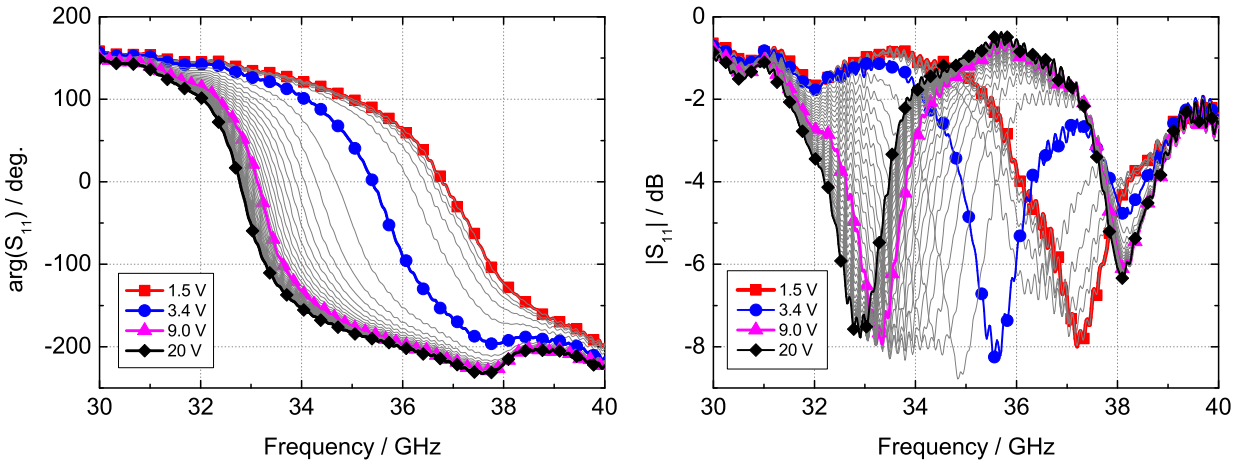

(a) Phase of the reflection coefficient

(b) Magnitude of the reflection coefficient

Figure 5.21: Measured results of the unit cell pair with single patches filled with the special mixture MDA-03-2844.

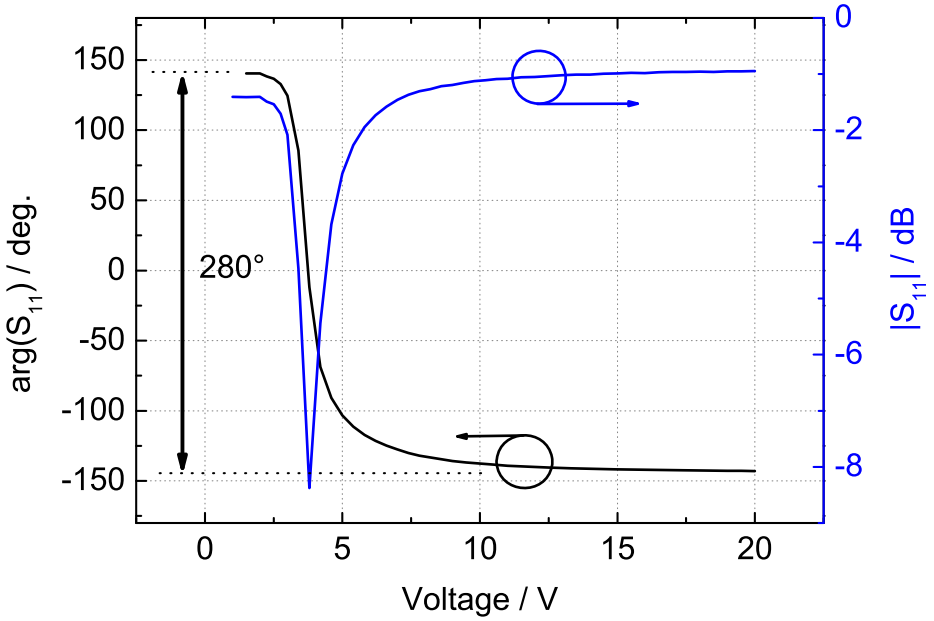

Figure 5.22: Phase and magnitude of the complex reflection coefficient $\underline{S}_{11}$ versus the control voltage at 35 GHz - unit cell filled with MDA-03-2844.

the relative permittivity is changed from $\varepsilon_{r,\perp} = 2.4$ to $\varepsilon_{r,\parallel} = 3.4$, the capacitance C in the equivalent circuit (capacitance between patch and ground) is increased. This makes the value of the impedance of the unit cell Z_{cell} approach the value of the free space impedance η_0, which results into a steeper phase curve and higher return loss. This effect is counterbalanced by the simultaneous reduction of the loss factor of the liquid crystal $\tan\delta$ as the voltage increases, from $\tan\delta_{r,\perp} = 0.02$ to $\tan\delta_{r,\parallel} = 0.007$.

As shown in Fig 5.22, at 35 GHz the phase can be now adjusted in a 280° range, which is close to the aim of 300°, the desired value that would allow realization of a large reflectarray without significant loss of performance. The reflection losses are between -1 dB and -8 dB. The peak losses are still very high. However, on a large reflectarray, the losses will be distributed between -1 and -8 dB in accordance with the phase distribution of the elements. Thus, the average loss of power will be considerably lower than the peak losses of a unit cell.

The properties of the measured unit cells with single patches are synthesized in Table 5.1. A *tuning bandwidth* is here defined as the frequency interval swept by the resonant magnitude notch when the control voltage is varied:

$$BW_{tun} = |f_{res,U=0} - f_{res,U=max}| \ . \tag{5.8}$$

It should not be confused with the operating bandwidth. A tunable unit cell can usually be operated in a much narrower band than the tuning bandwidth. It is however a good measure for the tunability of the unit cell. A relative tuning bandwidth can be readily calculated with:

$$BW_{tun,rel} = \frac{|f_{res,U=0} - f_{res,U=max}|}{f_0} \tag{5.9}$$

with f_0 the operating frequency.

Table 5.1: Overview: measurements of unit cells with single patches.

Liquid Crystal	Frequency	Phase range	Losses	BW_{tun}	Rel. BW_{tun}
K15	33 GHz	190°	-12 dB	1.5 GHz	4.2%
BL006	33 GHz	250°	-10 dB	2.5 GHz	7.5%
MDA-03-2844	35 GHz	280°	-8 dB	4 GHz	11.4%

5.3.2 Stacked Patches

The single patch configuration can be easily transformed into a stacked patch configuration, by printing an additional patch on the outer side of the superstrate, as shown in Fig. 5.23. The manufacturing process is not being complicated, since the etching takes place in a single step.

The presence of the upper patch introduces a second resonance, which can be used as an additional degree of freedom. By varying the dimensions of both patches independently, the positions of the two resonances can be adjusted to enable a design optimized either for maximum phase range at a given frequency or for maximum bandwidth, as in section 3.2. The advantage of a second resonance is nevertheless limited by a diminution of the tuning efficiency, caused by the fact that a part of the electric field is confined between the two patches, thus reducing the fraction of the total field that is affected by the anisotropy of the liquid crystal.

The carrier substrate is the same as before, a 0.50 mm thick TMM3 Rogers high frequency ceramic. The spacers are also from the same 127 μm RTDuroid material as in the previous section.

Fig. 5.24 presents the results of a unit cell with stacked patches filled with BL006. The phase characteristics exhibit distortions around the design frequency of 35 GHz, so the cell is not usable around this frequency. It is apparent from the magnitude plot, that the phase distortions appear in conjunction with very high losses. The mechanism underlying those phase distortions will be explained in more detail at the end of the chapter.

In Fig 5.25 two cuts at different frequencies are presented, to illustrate the existing tradeoff between tunable phase range and return loss. At 34 GHz the phase can be adjusted in an interval of about 190° with peak losses of about -6 dB, whereas at 34.5 GHz the

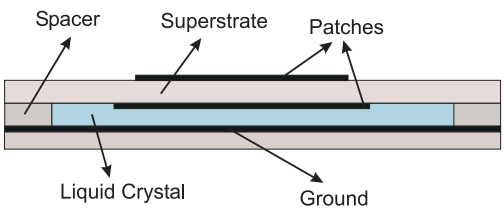

(a) Schematic of the unit cell with stacked patches.

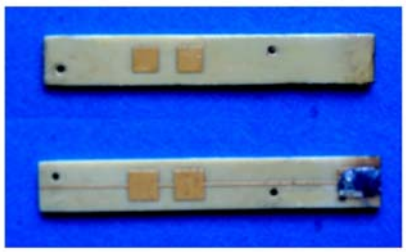

(b) Realisation of the unit cell with stacked patches - front and backside view.

Figure 5.23: Unit cell with stacked patches

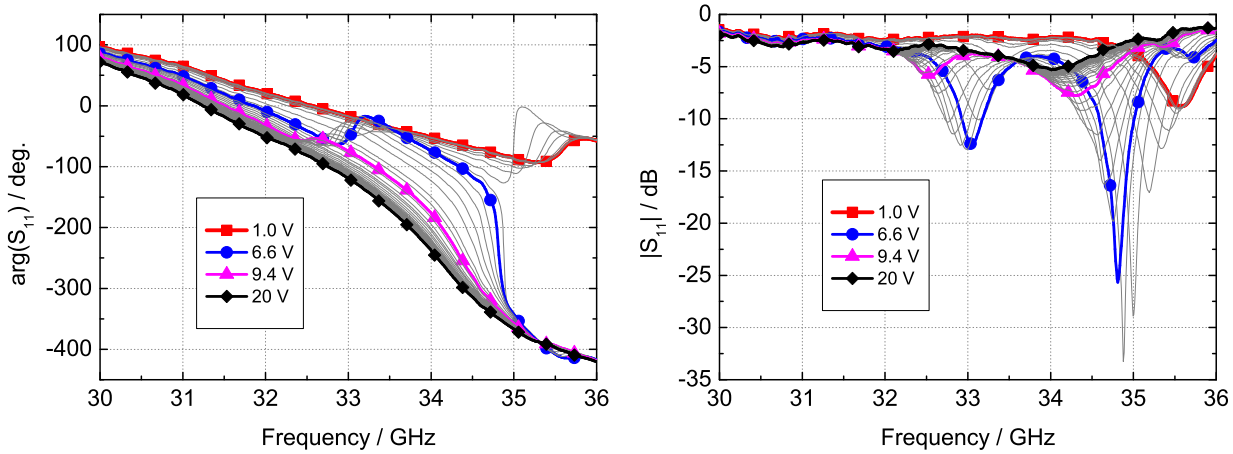

(a) Phase of the reflection coefficient for different tuning voltages.

(b) Magnitude of the reflection coefficient for different tuning voltages.

Figure 5.24: Measured results of a unit cell with stacked patches filled with BL006.

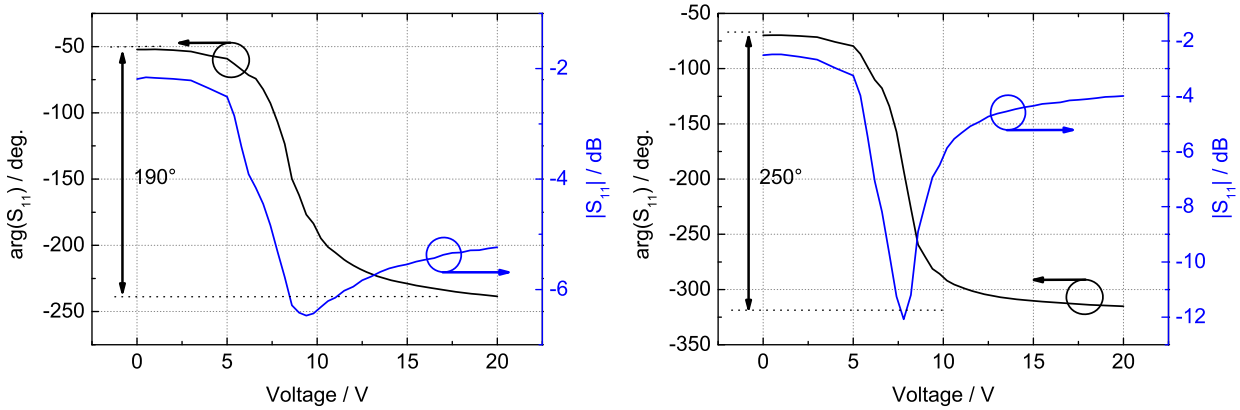

(a) Phase and magnitude of the complex reflection coefficient S_{11} versus the control voltage at 34 GHz

(b) Phase and magnitude of the complex reflection coefficient S_{11} over the control voltage at 34.5 GHz

Figure 5.25: Unit cell with stacked patches filled with BL006.

tunable phase range increases to 250° but the return losses also deteriorate to -12 dB.

In order to exemplify the possibility of adjusting the patch dimensions to enhance a desired characteristic, like the tunable phase range or the operating bandwidth, three structures have been realized with stacked patches: the first one (structure 1) aims at maximum adjustable phase range at the design frequency of 35 GHz, the second (structure 2) aims at maximizing the operating bandwidth around the design frequency, and the third (structure 3) represents a compromise between phase range and bandwidth. All three structures have been filled with the highly anisotropic mixture MDA-03-2844.

The measured results for structure 1 are presented in Fig. 5.26. The maximum tun-

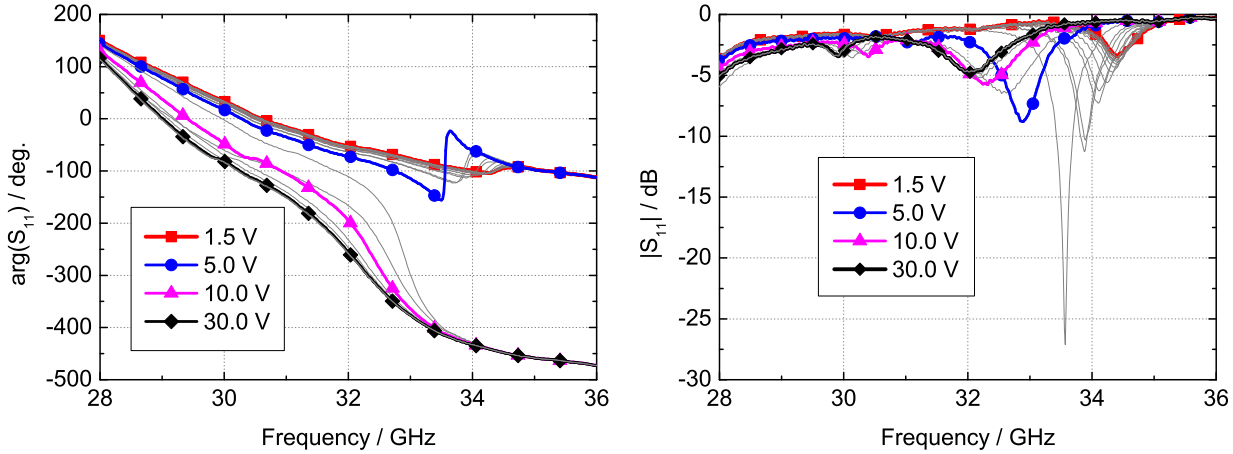

(a) Phase of the reflection coefficient for different tuning voltages.

(b) Magnitude of the reflection coefficient for different tuning voltages.

Figure 5.26: Measured results of a unit cell with stacked patches filled with MDA-03-2844. The dimensions of the patches are optimized for maximum tunable phase range at the operating frequency.

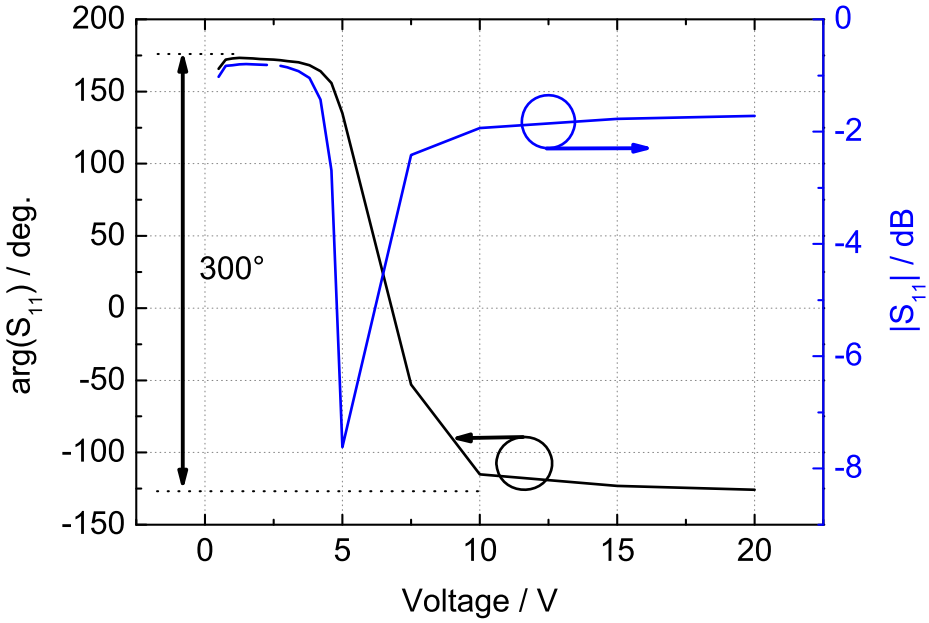

Figure 5.27: Phase and magnitude of the complex reflection coefficient S_{11} versus the control voltage at 33 GHz for a unit cell filled with MDA-03-2844.

able phase range occurs at 33 GHz, whereas from about 33.5 GHz the phase distortions mentioned earlier appear. In Fig. 5.27 the phase and magnitude behavior versus bias voltage is shown at 33 GHz. The phase can be adjusted in a 300° range, with peak losses reaching -8 dB. However, this high adjustable phase range is achieved at the expense of bandwidth: the patch dimensions are chosen such that the resonance behavior at the

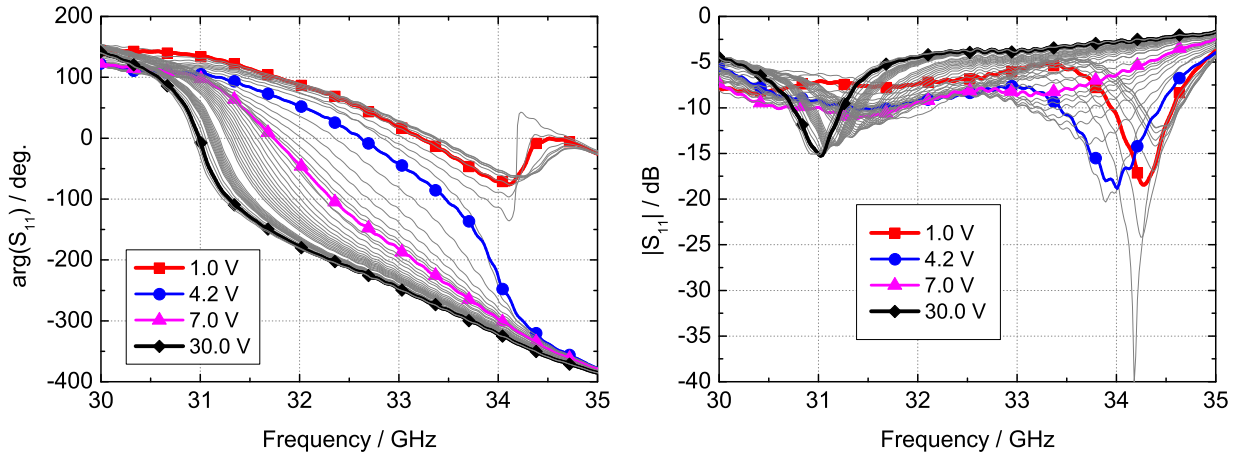

(a) Phase of the reflection coefficient for different tuning voltages.

(b) Magnitude of the reflection coefficient for different tuning voltages.

Figure 5.28: Measured results of a unit cell with stacked patches filled with MDA-03-2844. The dimensions of the patches are optimized for maximum operating bandwidth around the operating frequency.

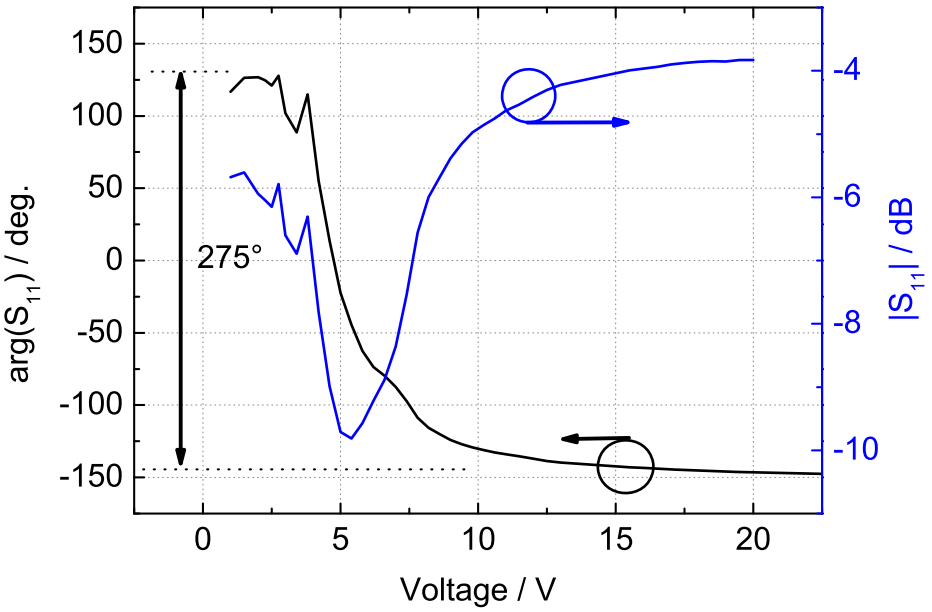

Figure 5.29: Phase and magnitude of the complex reflection coefficient S_{11} over the control voltage at 33 GHz for a unit cell filled with MDA-03-2844.

desired frequency is enhanced. This leads to very steep phase curves and relatively high losses, leaving a very narrow usable band.

For structure 2, the measured results are presented in Fig. 5.28. One can observe the large frequency band (31.5 to 34 GHz) where the phase can be tuned in a roughly constant range (around 270°). This gives about 7.5% relative operating bandwidth, a figure that

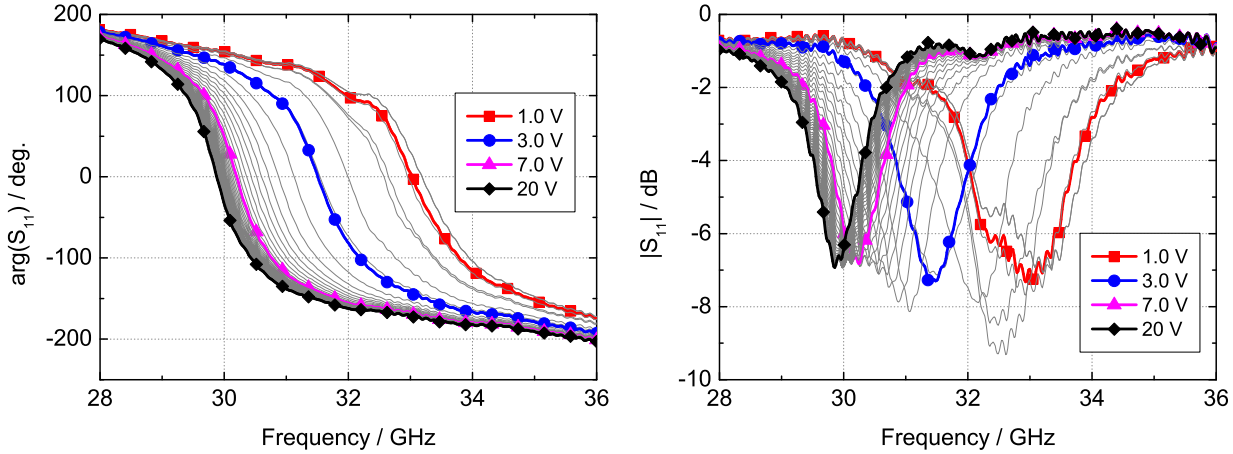

(a) Phase of the reflection coefficient for different tuning voltages.

(b) Magnitude of the reflection coefficient for different tuning voltages.

Figure 5.30: Measured results of a unit cell with stacked patches filled with MDA-03-2844. The dimensions of the patches are chosen to achieve a compromise between tunable phase range and operating bandwidth.

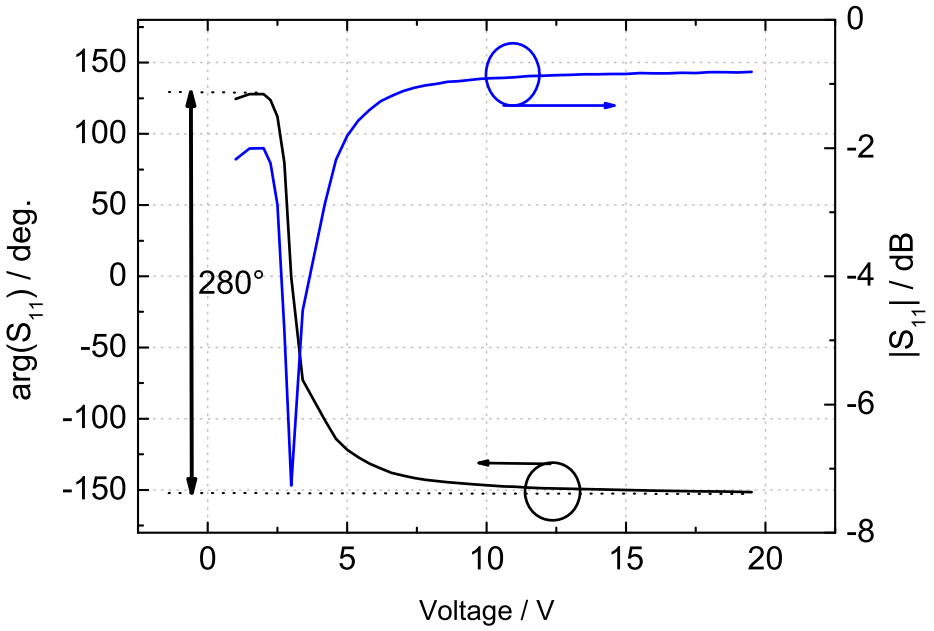

Figure 5.31: Phase and magnitude of the complex reflection coefficient S_{11} versus the control voltage at 31.5 GHz for a unit cell filled with MDA-03-2844.

might appear small, but that is actually quite acceptable for such a highly resonant structure. For low voltages the distortions in phase curve are again visible, though outside the usable frequency band.

As already mentioned the third stacked patch structure represents a compromise between phase range and operating bandwidth. At the same time special attention has

been devoted to avoiding the unwanted phase distortions that apear at low voltages. The measured results are shown in Fig. 5.30. Phase distortions are no longer present, and the maximal tunable phase range of 280° is achieved at 31.5 GHz. From Fig. 5.31 can be seen that the losses at 31.5 GHz are between -1 and -7 dB depending on the bias voltage.

To give an overview of the three presented unit cells with stacked patches, their properties have been summarized in Table 5.2.

Table 5.2: Unit cells with stacked patches

Struct. nr.	Optimized for	Upper / Lower	Operation frequency	Phase range	Peak losses	BW_{tun}	$BW_{tun,rel}$
1.	phase range	2.284 mm / 2.294 mm	33 GHz	300°	-8 dB	1.5 GHz	4.5%
2.	bandwidth	2.2 mm / 2.3 mm	33 GHz	275°	-10 dB	3.3 GHz	10%
3.	compromise	1.38 mm / 2.2 mm	32 GHz	280°	-7 dB	3 GHz	9.3%

5.3.3 Aperture coupled line

According to Eq. 5.1, the phase shift is proportional to the physical length of the microstrip line coupled to the patch. Therefore, it would be possible to increase the tunable phase range of a unit cell by simply making the line longer. This could compensate for a liquid crystal with insufficient anisotropy. However, it is naturally not possible to make the line arbitrarily long, since the line corresponding to each patch has to also fit in the area reserved for one unit cell.

A unit cell consisting of a microstrip patch aperture coupled to a line has also been manufactured and measured. RTDuroid 5880 with 0.5 mm thickness was employed as a substrate, with the printed patches on one side and the apertures in the ground plane on the other side (see Fig. 5.32). The lines were printed on 0.5 mm thick TMM3, whereas 0.127 mm thick RTDuroid 5880 was used as spacer.

As it is apparent from Fig. 5.32, the line has been folded to a U-shape in order to maximize the tunable phase range. Owing to the manufacturing errors and probably also to some alignment errors by the positioning of the line with respect to the aperture in the ground plane, the results are not as good as with the previous two structures. Moreover, the line is terminated with an "open", which is far from ideal.

The plots presented in Fig. 5.33 show the shift of the phase and magnitude versus the frequency when the control voltage is swept between 0 and 20 V. It can be observed that the resonant frequency is slightly shifted, to 36 GHz. At this frequency, the phase is adjustable over only 240°. More concerning, however, is the poor performance in terms of reflection loss, which is between -5 and -16 dB (see Fig. 5.34). The fact that there is high return loss even outside the resonance suggests that a large part of the power is being radiated. The assumption is at hand that some of the power is radiated by the open ended line, and part of it is lost through the bias line, although simulations were used to minimize the influence of the bias line.

Phase Distortions

It has been mentioned that in some of the tuning states, corresponding mostly to low applied voltages, the phase characteristics show distortions from the expected S-shaped characteristic (see Fig. 5.24, Fig. 5.26, Fig. 5.28). This induced the misleading assumption that the low voltage values are the cause, due to not being able to overcome inherent molecular torque [Hu06].

However, the lumped element equivalent circuit presented in section 2.2 helps to understand the mechanism underlying the phase distortions. Indeed, most of the phase distortions that occurred in the measurements were observed at the low-voltage end of the tuning interval. Nevertheless, the real cause for the distortions is the higher loss angle usually associated with this low-voltage states (see Tab. 4.1).

In Fig. 5.35 phase and magnitude plots are shown for three tuning states of a unit cell filled with the novel mixture MDA-03-2844. To better understand the phenomenon, let

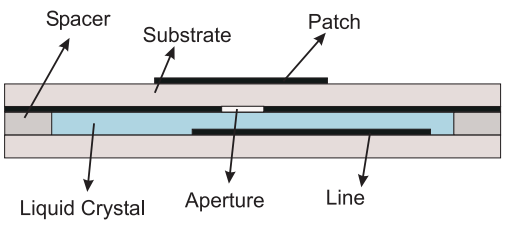

(a) Schematic of the unit cell with patch aperture coupled to a line.

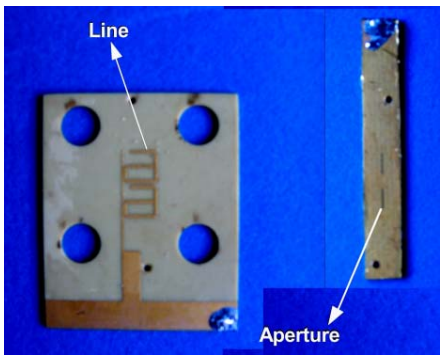

(b) Realisation of the unit cell with patch aperture coupled to a line - front and backside view.

Figure 5.32: Unit cell with microstrip patch aperture coupled to a line.

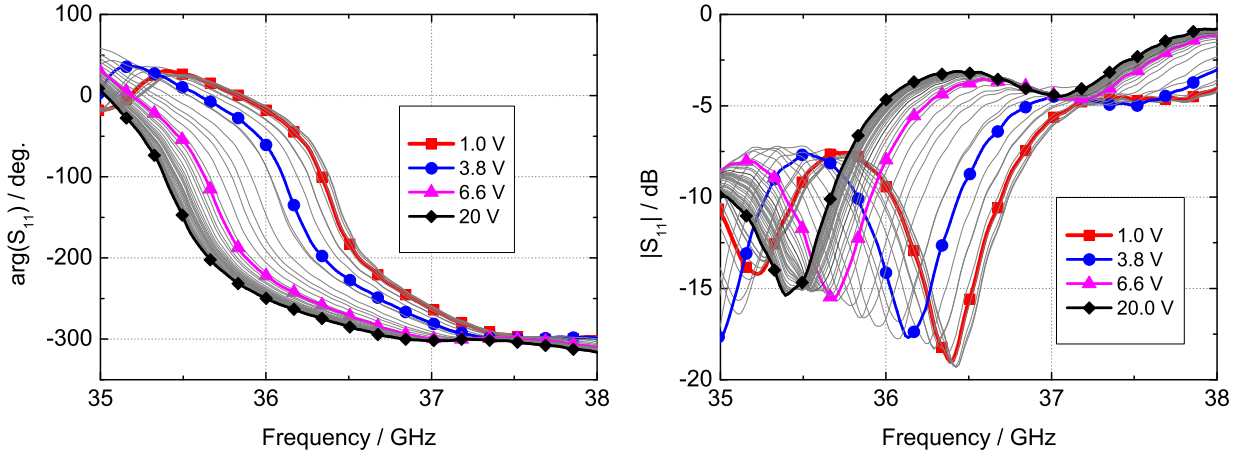

(a) Phase of the reflection coefficient for different tuning voltages.

(b) Magnitude of the reflection coefficient for different tuning voltages.

Figure 5.33: Unit cell with aperture coupled line filled with MDA-03-2844: measured results.

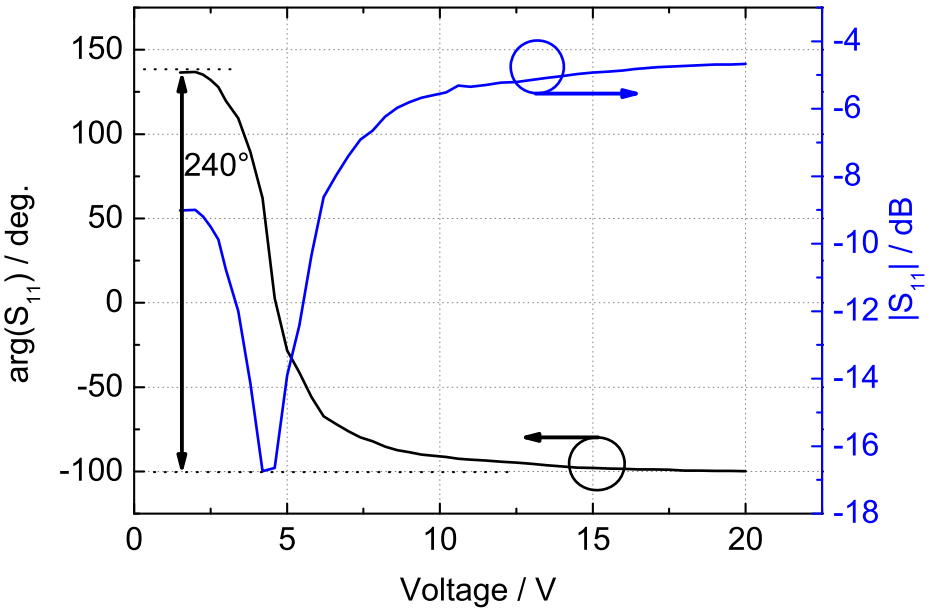

Figure 5.34: Phase and magnitude of the complex reflection coefficient S_{11} versus the control voltage at 36 GHz - unit cell filled with MDA-03-2844.

us suppose the unit cell is first in the state 1, when no phase distortions are present. The value of the relative permittivity $\varepsilon_{LC,1}$ for this state is achieved with the control voltage V_1. If the voltage is now lowered to V_2, the relative permittivity changes to $\varepsilon_{LC,2}$, shifting the resonance to higher frequencies, but at the same time the loss angle increases $\tan\delta_1 > \tan\delta_2$. This increase in the loss angle is modeled in the proposed lumped element equivalent circuit by a decrease in the value of R_C, according to the

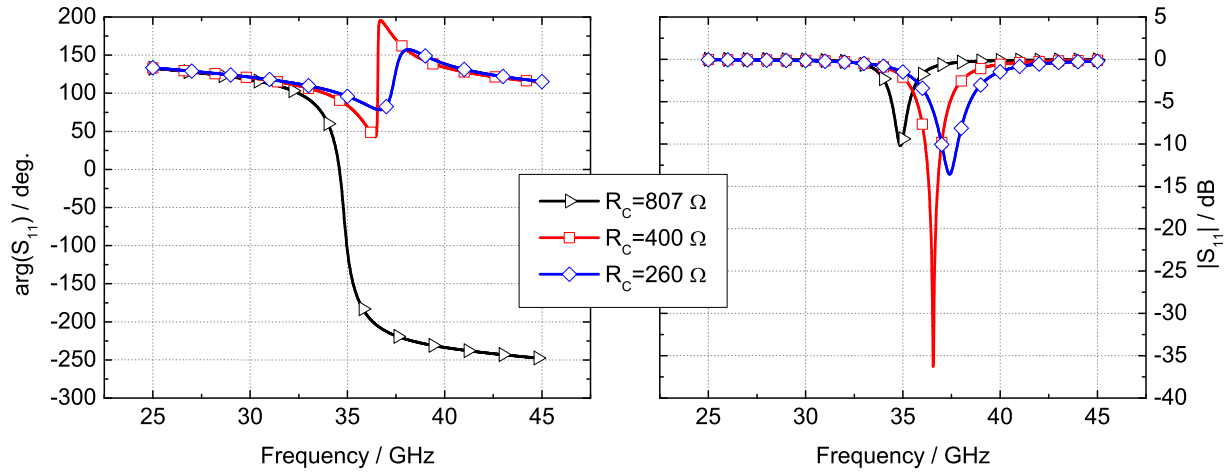

Figure 5.35: Phase Distortions

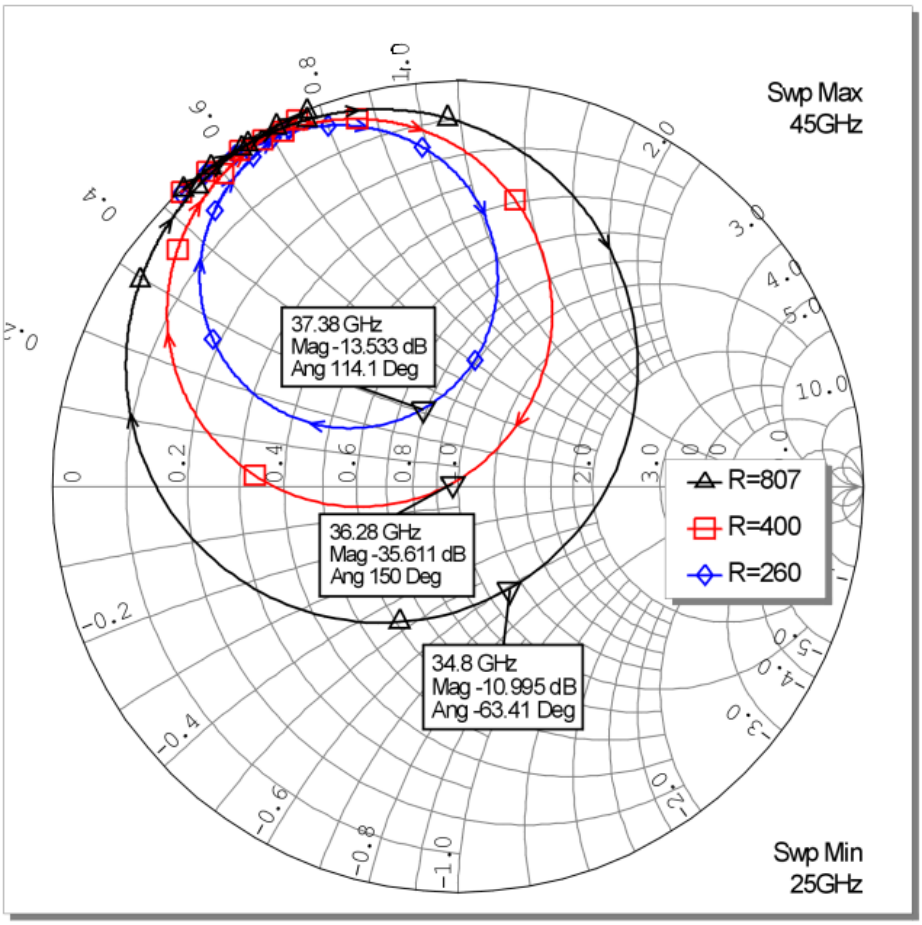

Figure 5.36: Smith Chart illustrating the shift in the $\underline{S}_{11}$ curve as the dielectric losses increase (R_C decreases).

relation 2.37.

The increase in loss angle and the shift in the capacitance C cause a shifting of the $\underline{S}_{11}$ curve in the Smith chart, as shown in Fig. 5.36. The unit cell is now almost perfectly matched at the resonance frequency, which has shifted from 34.8 GHz to 36.3 GHz. If loss angle increases even further, the $\underline{S}_{11}$ curve in the Smith chart, which describes a circular shape, will shrink even further leaving the Smith chart origin (the (1,0) point) outside. Thus, in state 3, the $\vec{S}_{11}$ phasor will not rotate the whole 360°. Instead, the phase curve exhibits two inflexion points, corresponding to the points where the phasor is tangent to the S_{11} curve in the Smith chart.

A similar effect takes place when the metallic losses are considered instead of the dielectric losses. By reducing the metallic conductivity, the $\underline{S}_{11}$ curve in the Smith chart is shifted toward the (1,0) point. It is thus proximate to assume that the phase distortions that were observed in the previous section are due to the cumulative effects of dielectric and metallic losses.

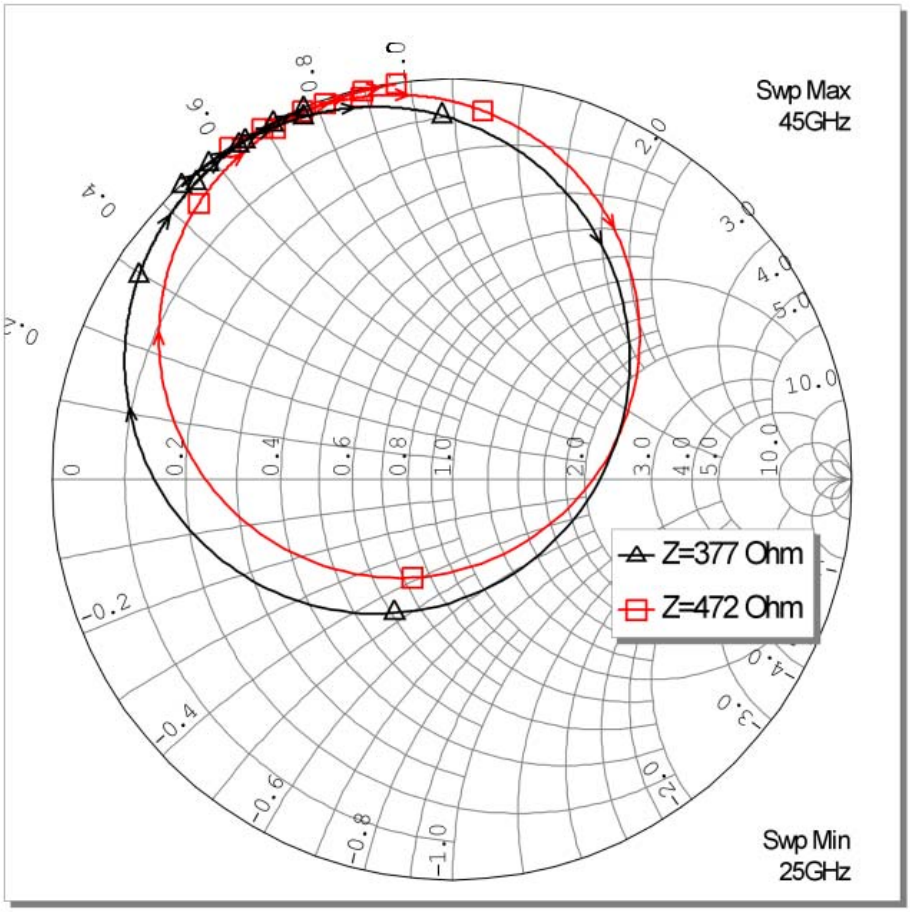

Figure 5.37: Smith Chart illustrating the shift in the $\underline{S}_{11}$ curve as the wave impedance Z increases.

Besides the losses (dielectric and metallic), another parameter can slightly influence the phase characteristic and can contribute to the occurrence of phase distortions. Considering again the lumped element equivalent circuit, the impedance of the line section that stands for the wave propagation before incidence on the unit cell can change. The wave impedance in the waveguide Z_{wg}, for a TE mode, is different from the free space impedance $\eta_0 = 377\,\Omega$, namely according to the formula [Wei99]:

$$Z_{wg} = \eta_0 \frac{1}{\sqrt{1 - \left(\frac{\lambda_0}{\lambda_c}\right)^2}} \tag{5.10}$$

with λ_0 the free space wavelength and $\lambda_c = 2\,a$ the cut-off wavelength for the considered mode, in this case TE_{10}. Moreover, as the voltage is lowered, the resonance shifts toward higher frequencies, to which correspond lower values for λ_0 and accordingly higher values for Z_{wg}. Fig. 5.37 shows the influence of a change in the wave impedance on the characteristic in the Smith chart. Combined with an increase in dielectric losses, an increase of the wave impedance favors the appearance of phase distortions, since the characteristic moves closer to the (1,0) point.

5.4 Investigated Unit Cells and Measurement Results at 77 GHz

After investigating the unit cells at 35 GHz and obtaining a proof of concept for their phase shifting with LC, the leap to higher frequencies has been made. The reasons are multiple:

- As already discussed in section 4.3, liquid crystals show a tendency of performance improvement with increasing frequency, a behavior untypical for most materials
- The increased frequency allows the reduction of the cavity height, without degradation of the bandwidth. This, in turn, leads to shorter switching times, according to the Eq. 4.18 in section 4.2.
- Assuming a doubling of the frequency and a halving of the cavity height, the volume of the cavity will reduce eight times, which enables the realization of larger reflectarrays, given the already mentioned small LC quantities available.

The operating frequency of the unit cells has been chosen at 77 GHz, because this is a commercially used band for automotive long-range radar systems. Several unit cells with different topologies have been realized. The unit cell element was either a single square patch, or two stacked patches of different dimensions. For the LC-cavity thick-

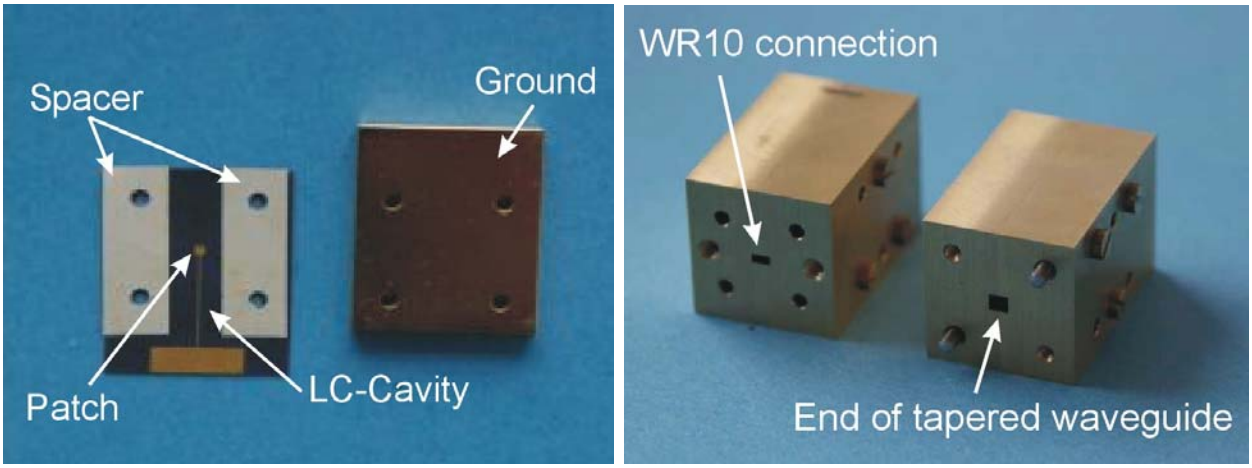

(a) Components of a 77 GHz tunable reflectarray unit cell prior to the cell assembly. The unit cell with the bias line is visible, as well as the spacer sheets.

(b) Picture of the waveguide simulator with WR10 connection at one end and taper at the other end.

Figure 5.38: Realization of 77 GHz unit cells and waveguide simulator.

ness, two values have been simulated and realized: 127 μm and 50 μm, corresponding to the thicknesses of available spacers: RT Duroid 5880 and R/flex 3000, respectively [Rog07]. The ground plane is provided by a 5 mm thick metallic plate, which gives mechanical stability to the assembly. After the polyimide layer is applied on both substrate and on one side of the metallic plate, the parts are glued together, separated by stripes of the spacer material (see Fig. 5.38),thus forming the desired cavity. LC is filled in the cavity by means of capillary attraction, and afterward the cell is sealed using epoxy glue. Care is taken to apply the epoxy based glue only in regions with no electric field, since it has a rather high loss angle.

Two different liquid crystals were used for the measurements: the commercially available liquid crystal BL006 and the novel mixture with improved properties in the microwave region, MDA-03-2844.

Different combinations of printed element (single patch or stacked patches), cavity thickness and liquid crystal have been simulated using *CST Microwave Studio*. The most promising were realized and the measured results are discussed in section 5.4.2.

5.4.1 Measurement Setup

In order to practically demonstrate the phase shifting capability of the unit cells, a *waveguide simulator* has been employed, as in the case of the 35 GHz unit cells. It consists of a split block waveguide having a WR10 connection at one end, to be attached at the ex-

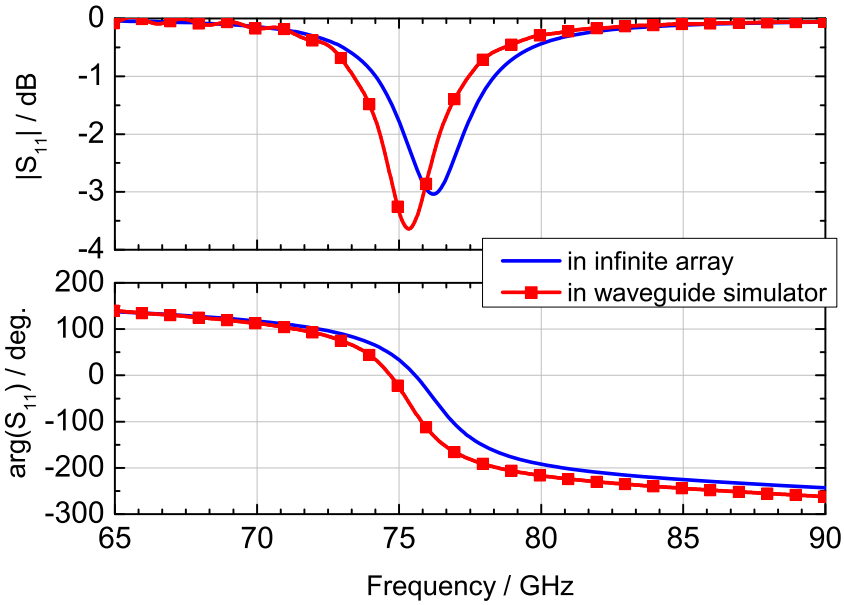

Figure 5.39: Simulated characteristics of a unit cell with $\varepsilon_r = 2.7$ and $\tan\delta = 0.01$, in an infinite array environment with the *CST Microwave Studio* model and in the waveguide simulator.

ternal mixers of the network analyzer. However, in this case the unit cell dimensions of $0.55\,\lambda$ are larger than the height of the WR10 waveguide (2.14 mm compared to 1.27 mm). In order to be able to accommodate the unit cell at the end of the waveguide, the latter has been linearly tapered in the E-plane to an almost square (2.3 mm x 2.54 mm) aperture at the other end, as seen in Fig. 5.38 (b).

The complex reflection coefficient of the unit cell is measured with the Anritsu 37397C network analyzer, using the frequency extension modules in the range 65-110 GHz. A reference measurement with the waveguide terminated with a short circuit is used for deembedding.

The field distribution incident on the unit cell is that of the TE_{10}-Mode of the waveguide and it is only an approximation of the plane wave simulated in CST Microwave Studio. Figure 5.39 shows the simulated reflection coefficient of a unit cell for two cases: once placed in the waveguide simulator and once in the infinite array environment. The simulated characteristics are quite similar, except for a frequency shift due to the different wavelength in the waveguide with respect to the free space wavelength, and a small deviation in the magnitude of S_{11} due to the different field distribution. Thus, there are slight differences expected between the simulated and the measured results, but the setup is nevertheless suitable for verifying the tunability of the unit cell in principle.

In the square section of the waveguide simulator, due to the specific dimensions, the

propagation of an unwanted mode (TE_{01}) is possible starting at 62 GHz (in the frequency range of interest). This mode is nevertheless perpendicular to the TE_{10} mode that is excited in the WR10 section of the waveguide simulator, and simulations with *CST Microwave Studio* have shown, that its excitation in the last section of the waveguide simulator is improbable. Other higher order modes are excited starting with 88 GHz (cut-off frequency of the TE_{11} mode) and are therefore outside the observed frequency range.

5.4.2 Measurement Results and Discussion

Phase and magnitude of the reflection coefficient for a unit cell with stacked patches and 127 μm cavity height, filled with the highly anisotropic mixture MDA-03-2844 are plotted in Fig. 5.40. The maximal tunable phase range is achieved at 75 GHz, which means the actual operating frequency is shifted with only 2 GHz compared to the designed operating frequency of 77 GHz, or a relative deviation of 2.6%. Taking into consideration manufacturing and alignment tolerances, this is quite acceptable. The reflection losses are between -2 dB and -8 dB at 75 GHz (see Fig. 5.41).

Due to the smoothness of the RT Duroid 5880 carrier substrate and consequent lack of adhesion during the spinning process, it proved impossible to apply the thin polyimide layer on the upper side of the cavity. The initial alignment of the LC molecules parallel to the cavity walls was enforced only by the polyimide on the ground plane, which was a suboptimal. This accounts for the somewhat reduced phase range of only 210 ° for this unit cell.

An additional magnetic field has been applied, in order to compensate for the lack of the polyimide layer on one side of the cavity. The tunable phase range can be thus enhanced by around 30 °, resulting in a total tunable phase range of 240°.

Unit cells with single patch and a cavity height of 50 μm have also been realized and filled with the liquid crystals BL006 and MDA-03-2844. Phase and magnitude plots versus the frequency when the control voltage is swept are shown in Fig. 5.42 and Fig. 5.44 respectively.

The unit cell filled with BL006 shows a tunable phase range of 280°, and maximum losses of about -16 dB at an operating frequency of 71 GHz (see Fig. 5.43). The resonant magnitude notch can be tuned over a bandwidth of 4.5 GHz, yielding a relative tuning bandwidth of about 6.3%.

As expected, the best results are achieved with the highly anisotropic liquid crystal mixture MDA-03-2844: a maximum of tunable phase range of 280° with corresponding peak losses of -6.7 dB at an operating frequency of 77 GHz (Fig. 5.45). The magnitude

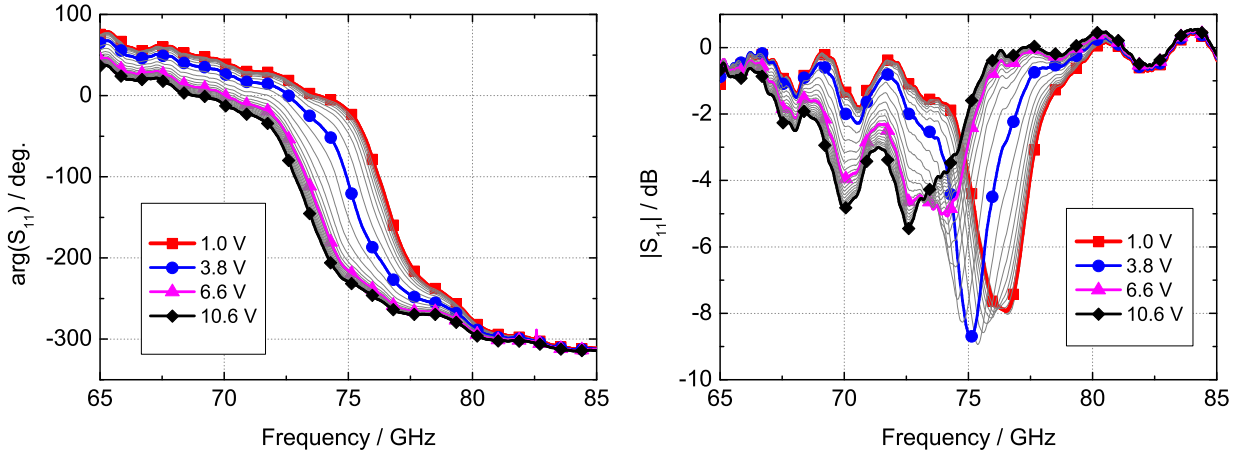

(a) Phase of the reflection coefficient for different tuning voltages.

(b) Magnitude of the reflection coefficient for different tuning voltages.

Figure 5.40: Measured results of a unit cell with stacked patches and h=100 μm filled with MDA-03-2844. The results are with no additional magnetic field applied to enforce the initial director orientation.

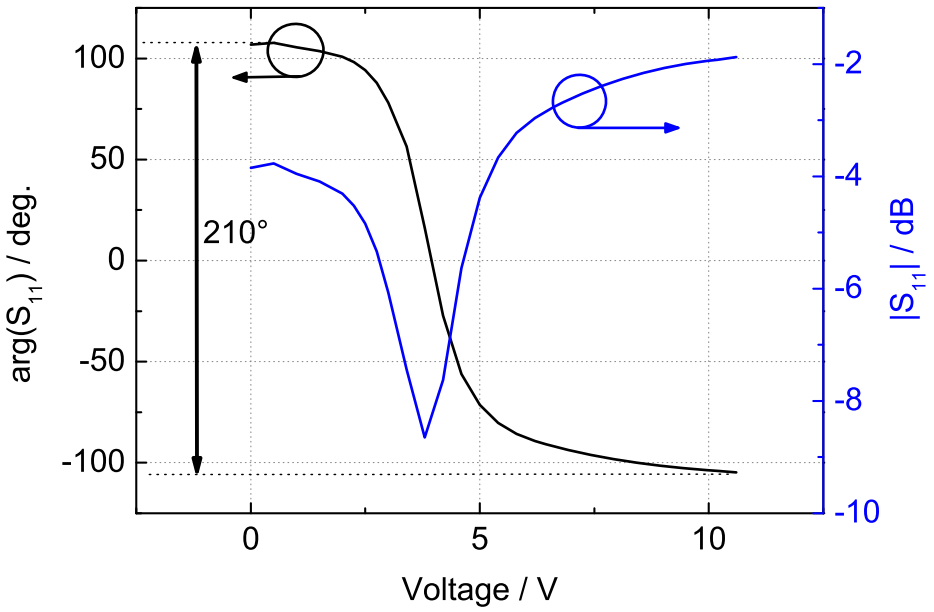

Figure 5.41: Phase and magnitude of the complex reflection coefficient S_{11} over the control voltage at 75 GHz for a unit cell filled with MDA-03-2844.

resonance shifts in a frequency range of 9 GHz, from 72 GHz to 81 GHz. This translates according to the definition given in the previous section into a relative tuning bandwidth of 11.7%.

A common characteristic of the measurements is, that the magnitude values stay below -2 dB or even -4 dB for the whole measured frequency band, i.e. outside resonance

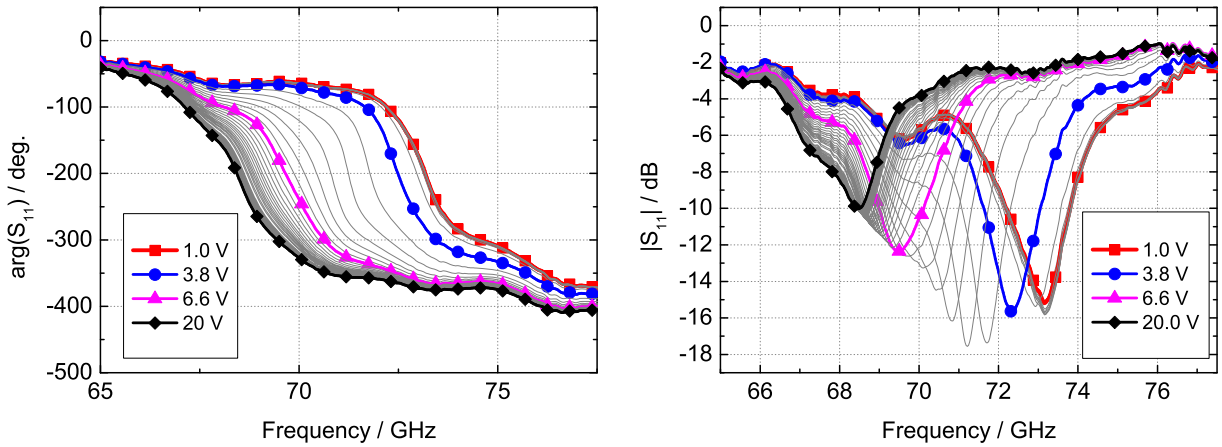

(a) Phase of the reflection coefficient for different tuning voltages.

(b) Magnitude of the reflection coefficient for different tuning voltages.

Figure 5.42: Measured results of a unit cell with single patch and h=50 μm filled with BL006 mixture.

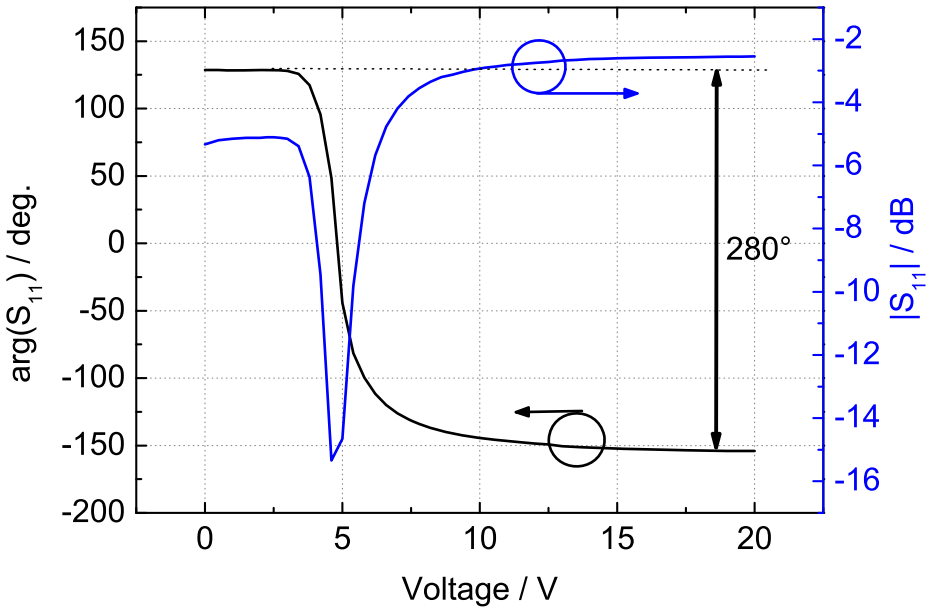

Figure 5.43: Phase and magnitude of the complex reflection coefficient S_{11} over the control voltage at 71 GHz for a unit cell filled with BL006.

as well. This leads to the assumption, that part of the power is lost to leakage due to mechanical mismatch of the setup (see Fig. 5.46). This assumption, together with the simulated S_{11} magnitudes (Fig. 5.39), from which it is apparent that outside the resonance the entire power is reflected, indicates that the actual peak losses in a cell filled with the novel mixture could actually be considerably lower than -6.7 dB.

For the unit cells with 50 μm cavity height no additional tuning was observable when

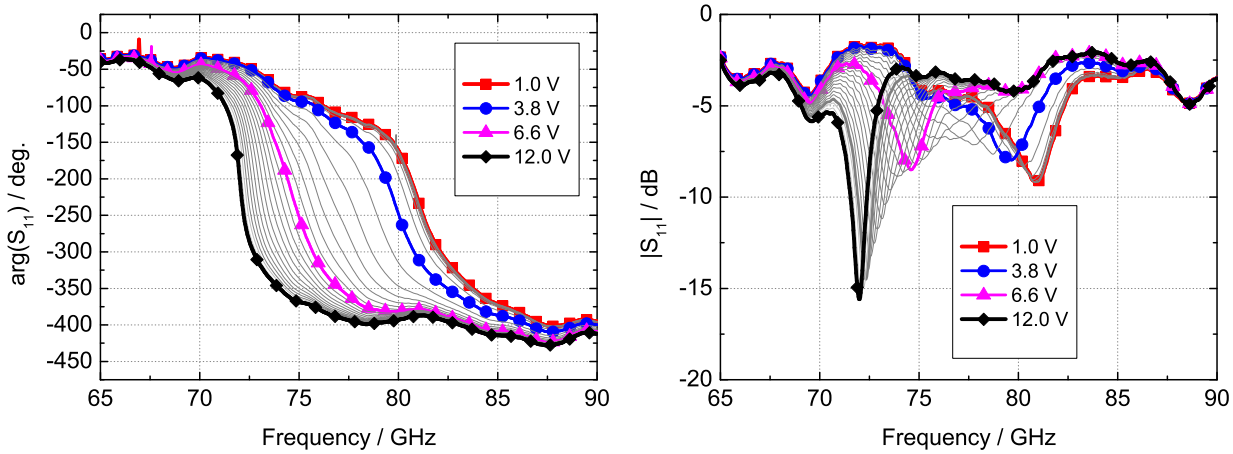

(a) Phase of the reflection coefficient for different tuning voltages.

(b) Magnitude of the reflection coefficient for different tuning voltages.

Figure 5.44: Measured results of a unit cell with single patch and h=50 μm filled with MDA-03-2844.

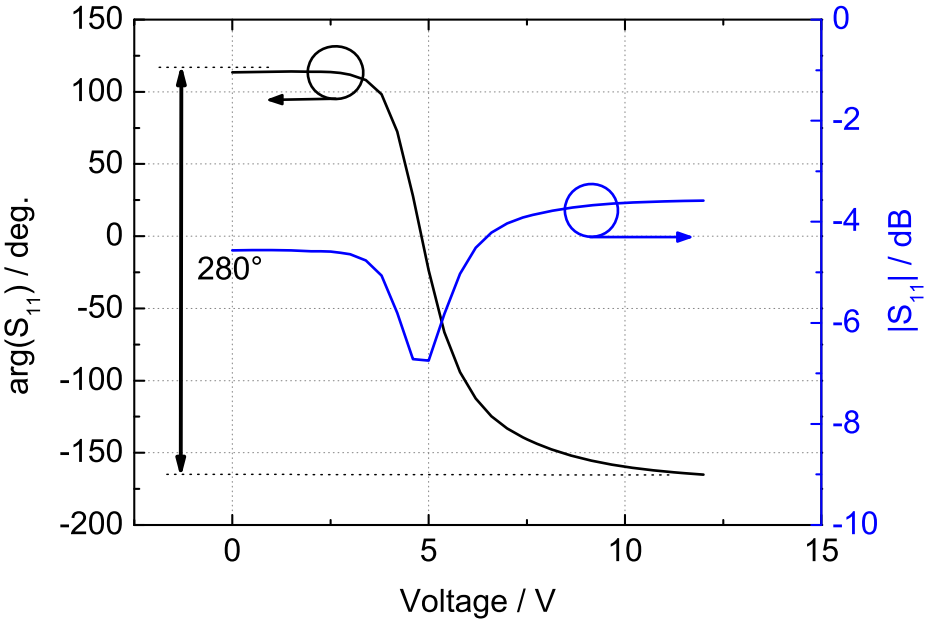

Figure 5.45: Phase and magnitude of the complex reflection coefficient S_{11} versus the control voltage at 75 GHz for a unit cell filled with MDA-03-2844.

the magnetic field was applied. Thus, for a cavity of 50 μm or less, a polyimide layer on only one side of the cavity appears to be sufficient for complete initial alignment.

It is also interesting to observe that for the unit cells with 50 μm cavity a lower voltage (about 12 V) is sufficient for complete reorientation of the molecules, instead of 15-20 V as needed for the thicker cavity.

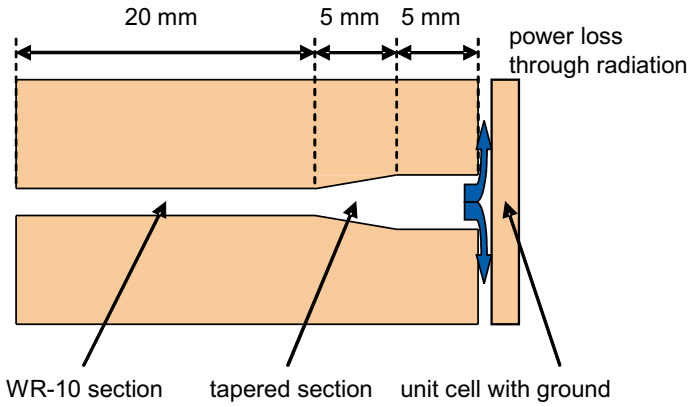

Figure 5.46: Possible power loss mechanism in the tapered waveguide due to gap.

The measured results of the 77 GHz unit cells are resumed in Table 5.3. Although there is no exhaustive investigation, the unit cells with 50 μm cavity seem to exhibit superior performance, which together with the advantages mentioned above (polyimide on just one side, lower tuning voltage, faster switching times) makes them ideal candidate for a full scale reflectarray demonstrator.

Table 5.3: Summarized results of the measured unit cells.

LC	Printed element	Cavity thickness	Phase range	Maximum loss
BL006	single patch	50 μm	280°	16 dB
Mixture	single patch	50 μm	280°	6.7 dB
Mixture	stacked patches	127 μm	210°	8.5 dB

5.5 Summary

In this chapter, first, the functioning principle of LC-tunable reflectarray unit cells was described. Using the lumped element equivalent circuit presented in section 2.2, investigations were conducted to evaluate the effect of dielectric losses, metallic conductivity and LC cavity height on the unit cell performance. This helped anticipate a serious problem associated with the high dielectric losses of the liquid crystals and metallic losses inherent to thin substrates: the tuning of the phase is related to large variations in amplitude.

Next, measurement setups for the investigations of LC-tunable reflectarray unit cells

at 35 GHz and 77 GHz and the results thereof were presented. Waveguide simulators adapted for each frequency were realized and shown to provide accurate enough results for a testing of the unit cell tunablity in principle. The measurement results confirm the possibility of phase adjustment with voltages of up to 20 V.

Different unit cell topologies (aperture coupled line, single patch, stacked patches) have been realized and measured at 35 GHz, with different liquid crystals. The aperture coupled line showed the poorest results, although presumably this structure deserves further attention: more accurate realization and improved design could bring drastic performance improvement. Structures with only a single patch printed on the top side of the LC cavity delivered good results; the improvement in the cell performance is considerable when LCs with better dielectric properties are used. With the unit cells using two stacked patches it was shown to be possible to optimize the patch dimensions for either maximal phase shift, maximal bandwidth or a compromise between the two. However, the stacked patches proved to me more sensitive to manufacturing tolerances than the single patch structures.

At 77 GHz the realization of LC-tunable reflectarray unit cells has been demonstrated with RF substrates, using a common etching technology. The higher design frequency allows the reduction of the LC cavity height without degrading the unit cell performance, neither in terms of bandwidth, nor of tunable reflection phase or reflection losses.

The reasons for the phase distortions observed in some of the measurements were explained, showing that the high reflection losses are the main cause, and that changes in the wave impedance of the wave incident on the unit cell also play a role.

Chapter 6

Reconfigurable Reflectarray Demonstrators

In the previous chapter, different investigated tunable reflectarray unit cells based on liquid crystals were successfully demonstrated. The natural subsequent step was to design and fabricate fully assembled liquid crystal reconfigurable reflectarrays.

First, a compromise has to be achieved regarding the size of the reflectarray. A larger size reflectarray (for instance 30×30 elements, or even more) would be preferable because of its higher directivity, which is desirable for many applications and which, in our case, also increases the dynamic range of the measurement system. Moreover, as shown previously, the unit cell is investigated in an infinite array environment, a situation that can be emulated by the elements in the center of the array, but not for those near the edges. For example, considering that the elements on the outer two rows and columns do not fulfill the infinite array assumption, in a 10×10 reflectarray there would be 64% such elements, whereas in a 30×30 reflectarray there would be only 25% such elements.

Unfortunately, a large size implies increased manufacturing difficulties. Tolerance requirements are harder to meet: for instance it is more difficult to keep the height of the LC cavity in an acceptable tolerance range for a $150\times150\,\mathrm{mm}^2$ cavity area than for a $80\times80\,\mathrm{mm}^2$ cavity area. After the realization, the filling of the cavity with liquid crystal is also a size dependent issue: the capillary forces that help fill the cavity are much more difficult to control in the case of a large area cavity than in the case of a smaller one, increasing the probability of air bubbles being trapped in the liquid crystal. Finally, another impediment of large sized reflectarrays is the already mentioned limited amount of liquid crystal available for experiments.

A 16×16 elements reflectarray, with the elements placed $0.55\,\lambda$ appart has been considered to represent a good compromise to the issues discussed above.

A further challenge in the realization of a LC-tunable reflectarray is the biasing of each element individually. Providing 256 independently controllable voltages for each element of the reflectarray would have been a very difficult technological task. For instance, the challenges here are the connection of the DC voltage to each microstrip element without significant disturbance to the RF-field, or the implementation of a suitable calibration technique for simultaneous tuning of 256 voltage values to achieve a desired pattern. For these reasons, in a first development step, a demonstrator has been designed with beam steering capability in one plane only (so called 1D-reconfigurable reflectarray). In a further step, the first challenge was tackled by designing and realizing a bias network able to address each element individually (2D) with minimal interference with the RF field.

6.1 Reflectarray with Beam Steering in One Plane

6.1.1 Realization

Based on the measured results of LC-tunable unit cells, presented in chapter 5, elementary cells with single printed patch have been selected for the realization of the reflectarrays. It can be observed that, even though stacked patch elementary cells are more versatile, allowing additional optimization with respect to phase range or bandwidth, they are also more sensitive to etching tolerances, tolerances in the cavity height, or uncertainties in the values used for the dielectric properties of the LCs. Since the phase curve yielded by a stacked patch structure is based on the superposition of two resonances, a shift of one of the resonances could dramatically change the phase characteristic, for instance by inducing phase distortions. On the other side, the single patches are more robust: manufacturing inaccuracies and uncertainties about material properties will maybe cause a shift of the operating frequency, but the probability that the phase distortions occur is lower.

The cavity for the liquid crystal was formed just as in the case of the unit cells by two carrier substrates. The difference is that the carrier substrates are much larger, since all 256 unit cells share the same liquid crystal cavity (see Fig. 6.1). One of the carrier substrates is completely metalized on one side (ground plane in Fig. 6.1), therefore the dielectric properties of the substrate material are of no importance. Its mechanical characteristics are however important: it has to exhibit an even, planar surface and provide mechanical stability to the assembly. RO4003 from Rogers Corporation was used [Rog07], with one side of the metalization gold plated.

The other carrier substrate supports the printed microstrip elements - in this particular

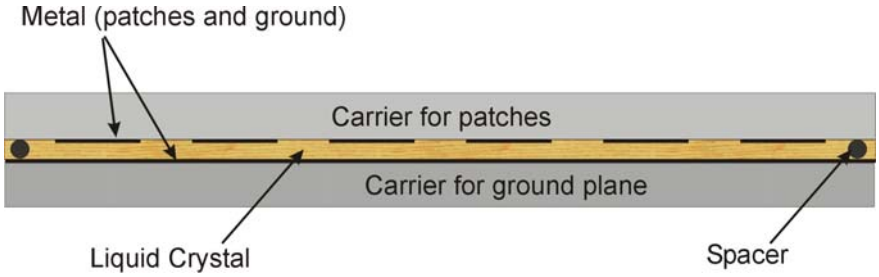

Figure 6.1: Schematic of the array.

case square patches - and acts as a radome at the same time. TMM3 from Rogers with a thickness $h = 0.51\,\text{mm}$ and dielectric properties $\varepsilon_r = 3.27$ and $tan\delta = 0.002$ (@ 10 GHz) was chosen as material for the superstrate, since it is a readily available material with a relative permittivity in the desired range ($\varepsilon_r \approx 2\ldots4$) and exhibiting desired planarity and rigidity due to its ceramic powder content. All metalic patches have the same dimension, $l_{patch} = 2.36\,\text{mm}$.

RTDuroid 5880 with a thickness $h = 127\,\mu\text{m}$ was used as spacer, as shown in Fig. 6.2. Apart from the outer frame, which besides the spacer role also contributes to the sealing of the LC cavity, three more small pieces of RTDuroid (about $1 \times 1\,\text{mm}$) were placed inside the array, in between the microstrip patches, at regular intervals. They have the role to prevent a "hanging" of the superstrate and thus a non-uniform height of the cavity.

From Fig. 6.2 (a) it is also apparent that all patches in a row have been connected with a very thin line. This means, that all patches in a row will tune identically and will ideally reflect the incoming wave with the same phase shift. A steering of the main beam is thus only possible in the plane perpendicular to the rows.

Consequently, the feed will also have to be polarized perpendicularly to the thin connecting lines, so that the lines are connected to the non-radiating edges of the patches and do not affect the RF field. The slotted waveguide array described in detail in section 3.4, radiating a cylindrical wave, has been employed as a linearly polarized line feed. Thus, this reflectarray design works only in linear polarization and allows only steering in the E-plane (1D steering).

Polyimide film is spin coated on the patches and on the ground plane, then backed according to the procedure described in section 4.2 and finally mechanically rubbed to produce the micro-grooves that enforce the LC alignment. The process parameters are those listed in Appendix A1. The framing spacers are glued, and then the small spacers are placed inside the array at equal intervals, care being taken that they are in between patches, so that the RF-field is not affected. The two parts, substrate and superstrate are then glued together under a custom made press. Once again, glue based on epoxy resin

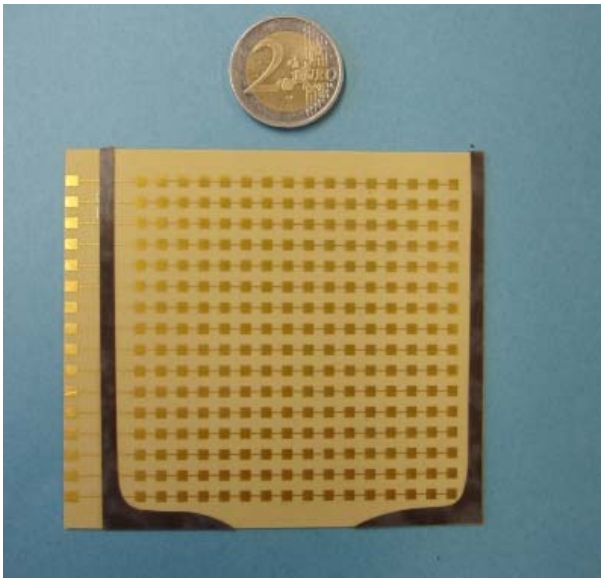

(a) Picture of the array with the two spacer cut out of RTDuroid 5880 (black stripes) before assembly of the ground plane.

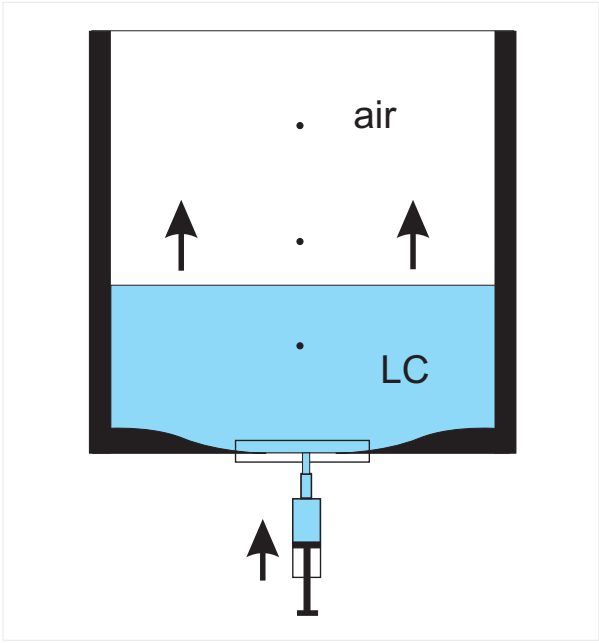

(b) Filling the array by injection from bottom to top in order to avoid formation of air bubbles.

Figure 6.2: Liquid crystal reflectarray with one dimensional steering capability.

is used. It is applied only on the spacer frames, far from the electromagnetically active regions (the patch edges), so that its high dielectric losses do not affect the reflectarray performance.

Filling of the cavity

After the realization of the reflectarray liquid crystal has to be filled into the cavity. The intransparent substrates do not allow visualization of the filling status, which makes the task even more difficult. The biggest problem is the possibility that air bubbles get trapped inside the liquid crystal. Especially if the cavity height is not perfectly uniform over the entire cavity surface, there would also be different capillary forces at work along the LC/air front, and thus different velocities for the propagation of LC inside the cavity. This can favor the occurrence of such air bubbles. Needless to say, one or more air bubbles under the patches would greatly impair the performance of the reflectarray.

Numerous trials were conducted using glass plates instead of substrates and colored ink as a substitute for LC in order to determine the best filling method. First, the glass plates were placed horizontally and ink was placed at one opening. It was drawn inside the cavity by the capillary forces, but the LC/air front advanced quickly and irregularly, due to the already mentioned variations in cavity height. This provoked the formation of air

bubbles.

In order to slow down the LC advance, trials were conducted with the glass plates in vertical position, immersed with the bottom opening in an ink receptacle. The LC/air interface did indeed advance slower and more uniformly, but unfortunately the capillary forces were not sufficient to completely overcome the gravity and fill the entire array, but only about three quarters.

Finally, with the glass plates in vertical position, gentle pressure was added from underneath, to help overcome the gravitational force, by injecting the colored liquid through a custom filling tube. Several trials have proven this method as reliable, providing a complete and bubble-free filling of the cavity. Consequently, this method was used to fill the reflectarray with liquid crystal, as depicted in Fig. 6.2 (b).

Two prototypes of the 1D steerable reflectarray have been manufactured and filled with the two commercially available liquid crystals K15 and BL006, whose microwave dielectric properties have been presented in section 4.3. A picture of such a reflectarray, fully assembled and filled, is shown in Fig. 6.3. The slotted waveguide feed, the bias lines providing the control voltages as well as the filling tube are also visible.

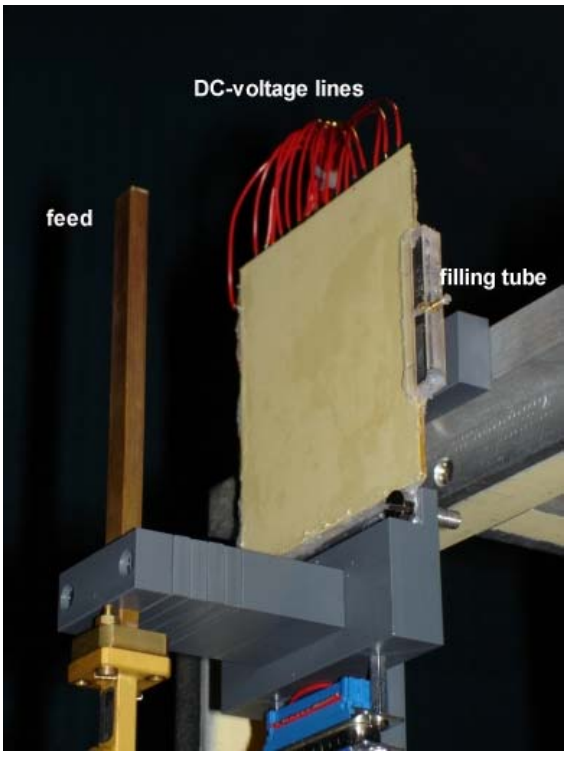

Figure 6.3: Picture of the assembled LC-reflectarray with feed mounted for measurements. Control voltage lines are also visible.

6.1.2 Experimental results

Since the material used as spacer (RTDuroid 5880) is a soft material prone to compressions when pressed, and in the middle of the cavity few support points have been used, there was concern regarding the accuracy of the realized cavity height. The first performed measurement was thus before the filling of the array: capacitance values of each row over the common ground have been measured. The measurements have been performed using an Agilent 4279A 1MHz C-V Meter, by connecting a row and the ground plane to the terminals at a time. This method is only approximate, since height deviations along the row of patches are not detectable and are averaged in the row capacitance. It provides nevertheless a rough estimate of the height of the LC cavity in the direction perpendicular to the rows of patches.

The results in Fig. 6.4 are for the reflectarray with K15. A gradient in the capacity from the 1st to the 16th row is evident, which translates into an unwanted slope in the cavity thickness. Moreover, the cavity height is between 120 μm and 70 μm, i.e. always lower than the 127 μm nominal spacer thickness. This can be attributed to causes like asymmetric compression of the soft substrate used as spacer, different thicknesses of the glue layers used to bond the parts together.

Fig. 6.5 presents the results for the second manufactured array, which was filled with BL006. The slope in the cavity thickness is also present, but not as severe as previously. The thickness decreases from 140 μm to 100 μm, being on average closer to the nominal value of 127 μm.

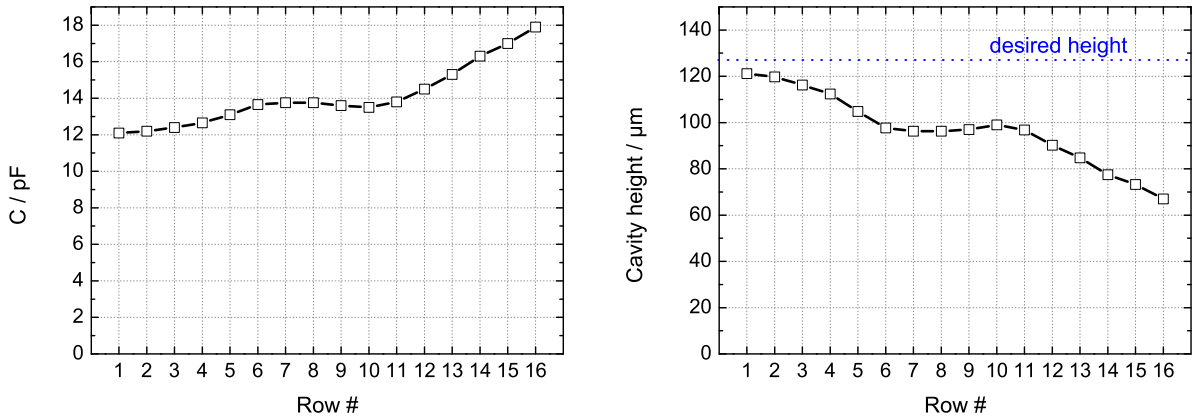

(a) Measurement of capacitance of each row of patches.

(b) Cavity height derived from measured capacitance.

Figure 6.4: Capacitance measurement for the estimation of the cavity height for the 1D reflectarray filled with K15.

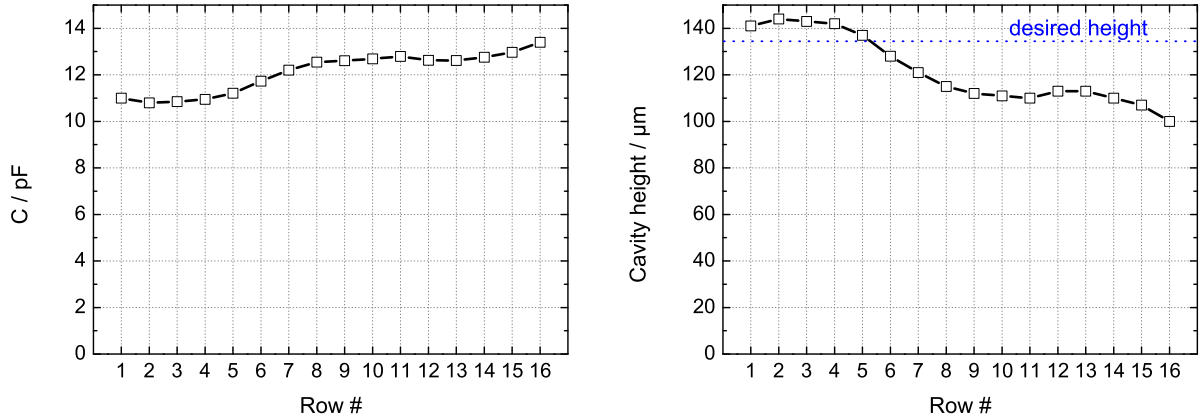

(a) Measurement of capacitance of each row of patches.

(b) Cavity height derived from measured capacitance.

Figure 6.5: Capacitance measurement for the estimation of the cavity height for the 1D reflectarray filled with BL006.

Next, the far-field radiation patterns of the reflectarrays have been measured in the anechoic chamber. A circuitry commanded in *Matlab* sets the desired 16 element voltage-array on the 16 rows. Fig. 6.6 shows a schematic of the measurement setup. The electronic consists of a I/O-unit, providing a voltage up to 5 V. An operational amplifier delivers 15 V to a 1-to-16 multiplexer, whose output is controlled by 4 bits set from the computer via the same I/O unit. The 15 V are enough to tune the phase over more than 95% of the achievable phase range, as it appears from the results presented in section 5.3.

The *phase-voltage*-characteristic of a unit cell measured in the waveguide setup cannot be translated to the unit cells that make up the array. There are multiple reasons for this:

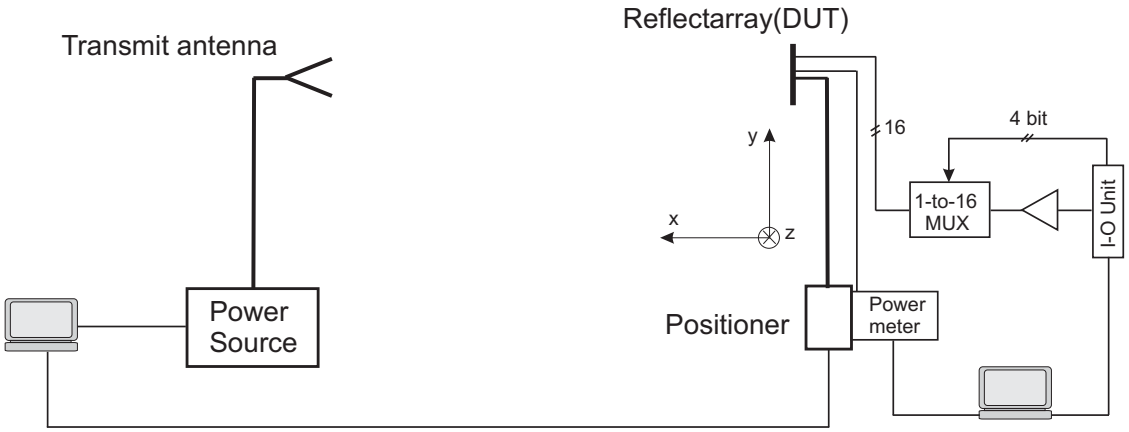

Figure 6.6: The measurement system for calibration of the antenna and pattern measurements

• The **manufacturing accuracy**, and especially the accuracy with which the height of the LC-cavity can be controlled is much higher in the case of the two unit cells measured in the waveguide simulator as in the case of the full-scale reflectarray. The aspect ratio *height/surface* for the two cavities are approximately $2.8 \cdot 10^{-3}$ in case of the unit cells in waveguide and $22.3 \cdot 10^{-6}$ for the full-scale reflectarray.

• The spinning of the thin **polyimide film** on both sides of the cavity does not assure a perfectly uniform thickness of the film. Furthermore, the mechanical rubbing of the film surface is not perfectly uniform over the entire surface as well. Thus, the alignment forces produced by the polyimide film are presumably also not uniform, differing from cell to cell. This affects consequently the *phase-voltage* characteristic of the cells.

• In the waveguide setup the waveguide walls assure an **infinite periodicity condition** that is not existent on the reflectarray. This condition is approximately satisfied for the unit cells in the middle of the array, but is obviously violated for the elements which are close to the edge.

• The wave radiated by the feed falls under **various incidence angles** on the reflectarray elements, depending on their position, whereas the measurement in the waveguide simulator emulates incidence of a plane wave under a certain angle and the simulation environment accounts only for normal incidence.

Given these reasons, it was impossible to compute in advance a certain voltage set for a desired pattern (steering angle) from the characteristics measured in the waveguide (or from the simulated results). Thus, a calibration of the reflectarray is necessary for each pointing direction of the main beam.

Due to the high amplitude modulation owing to the losses, a phase only calibration algorithm is not possible. A very complicated calibration is also prohibitive owing to the slow switching time of the liquid crystal (see Section 4.2). Therefore, a straightforward algorithm (also mentioned in [Sie03]) for focusing the beam in a desired direction has been employed. The control voltages are kept constant at a given value (e.g. 15 V) on all rows except on one. On this row, the voltage is swept, and the setting yielding maximum received power is stored. The procedure is repeated for the next row. When the control voltages on all rows have been swept a new iteration can start (see Fig. 6.7).

Different values have been tested as a start value for the voltage, but the best results were achieved with all row voltages set at 15 V. The duration of one iteration is in the range of 1.5. . .2 hours.

At first a broadside beam pointing has been chosen. By letting the above mentioned algorithm perform, a distinct focusing of the beam can be observed. This is apparent in Fig. 6.8(a) and Fig. 6.9(a), where a comparison of two patterns is shown: one obtained

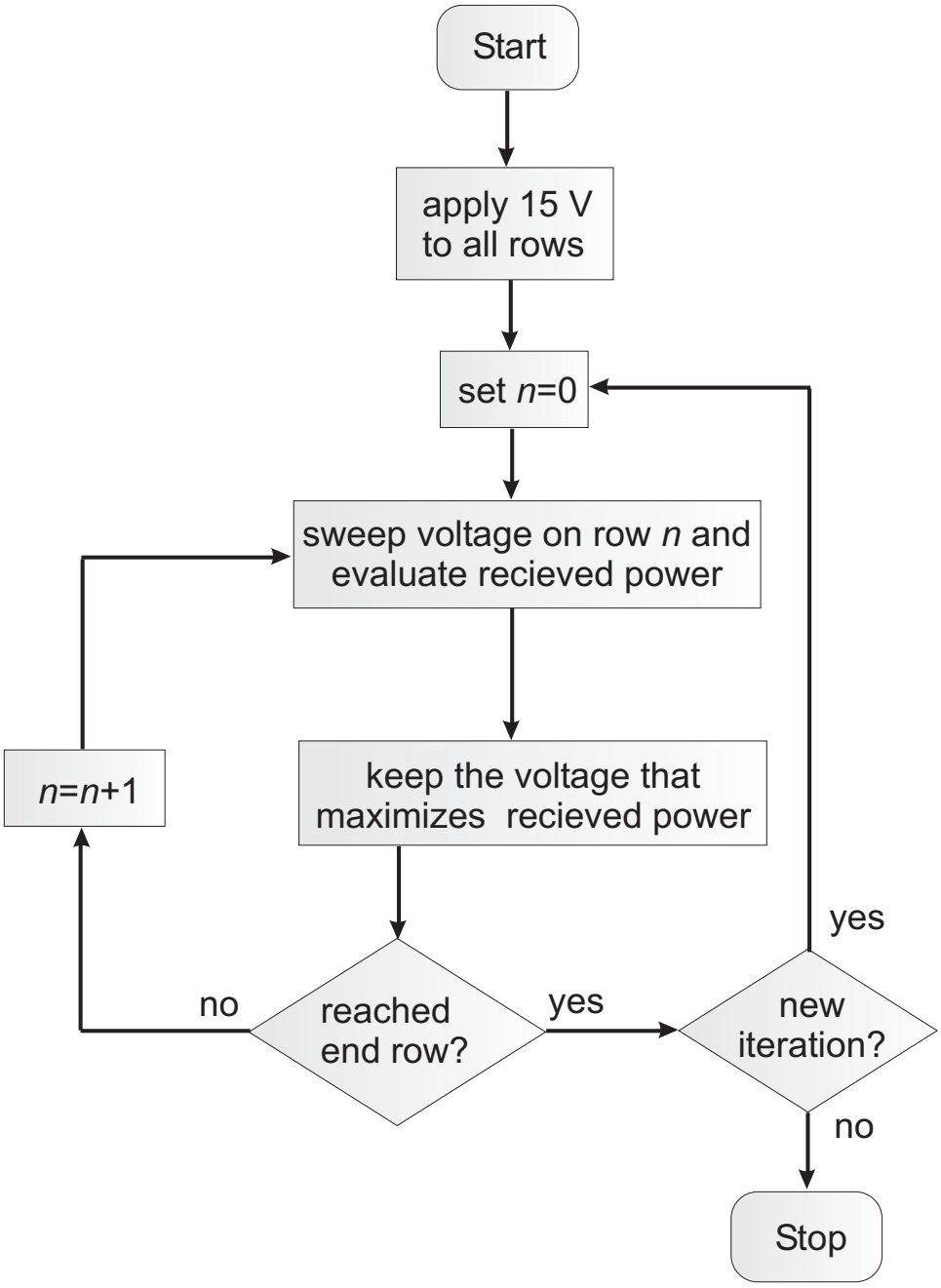

Figure 6.7: Flowchart of the employed algorithm for focusing the beam in a desired direction.

when all voltages are set to 15 V and the other one obtained with a set of voltages maximizing power to broadside.

By positioning the reflectarray to point toward different angles and running the power maximization routine each time, different patterns can be recorded, showing the beam steering ability of the reflectarray in the E-plane. Fig. 6.8(b) shows the results for the first demonstrator filled with K15: four E-plane far-field patterns with the main beam directed toward -20°, -10°, 0° and +10° respectively. At each position a distinct focusing

of the main beam is achieved. The side lobe level is around -5 dB for all patterns.

The results for the second demonstrator filled with BL006 are presented in Fig. 6.9(b). Here, three far-field patterns with main beams toward -20°, 0° and +15° are shown. The side lobe level is -6 dB for the pattern with the main beam at broadside and deteriorates

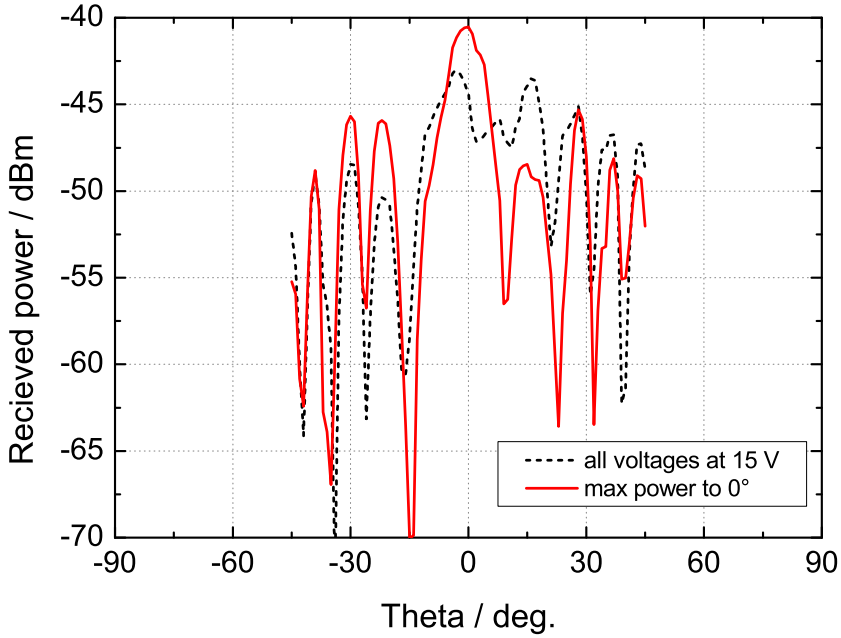

(a) Focusing of the beam.

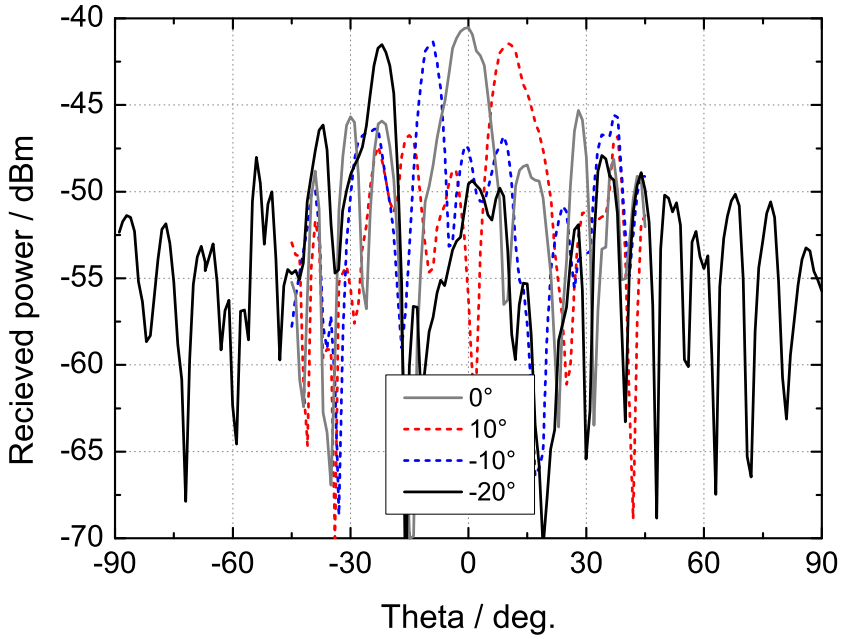

(b) Beam pointing to different steering angles.

Figure 6.8: Far-field pattern measurements of the 1D reflectarray filled with K15

to about -4.5...-5 dB for the scanned patterns.

The patterns of the reflectarray filled with BL006 look generally better than those obtained with the K15 demonstrator (smoother characteristic, constant beam width), presumably owing to slightly better dielectric properties of BL006 and also to the better

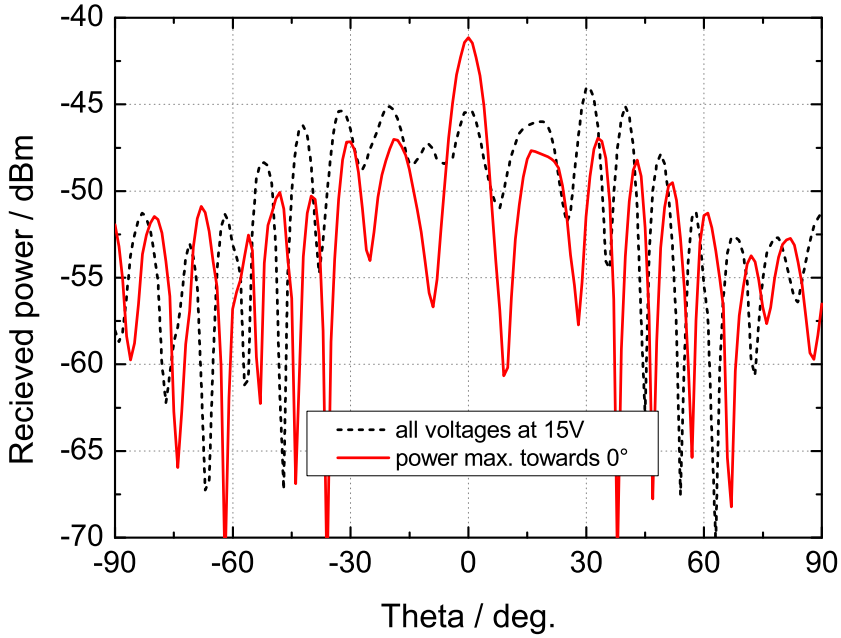

(a) Focussing of the beam.

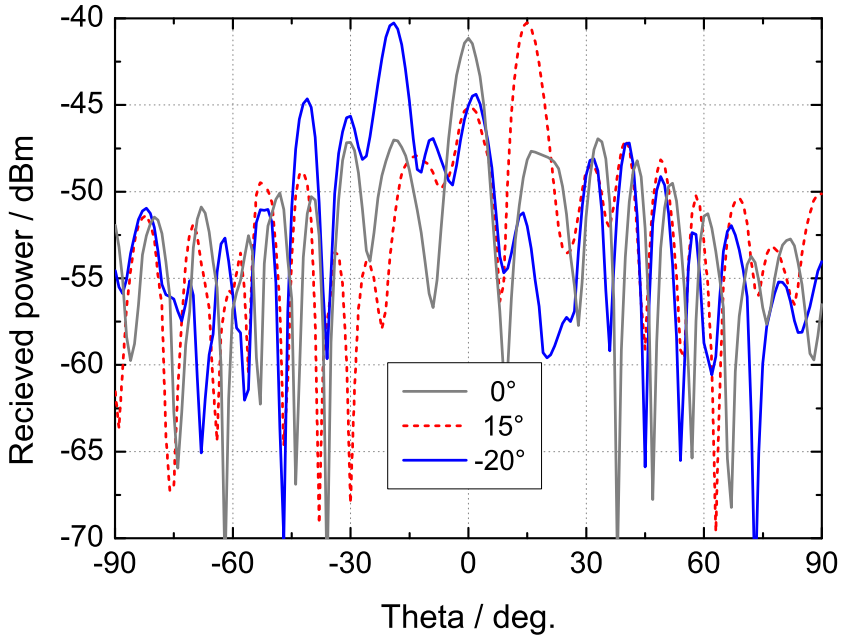

(b) Beam pointing to different steering angles.

Figure 6.9: Far-field pattern measurements of the 1D reflectarray filled with BL006

realization of the LC-cavity.

Although the calibration times for the focusing of the power to a certain angle is in the range of 1.5...2 hours, once the sets of voltages needed to point the beam to particular angles are known, the switching of the beam between two states takes about 10...20 seconds. This is of course a far to long time for certain applications, nevertheless there are other applications (for instance in-orbit beam reconfiguration for a satellite antenna) that can cope with such long switching times. Certainly, there is obvious need for further research to improve the switching times.

The very high side lobes for both realized reflectarrays can be explained by several factors:

- The severe fluctuations of the reflected wave amplitude in dependence of the control voltage.
- The occurring phase errors, owing to an adjustable phase range of only around 240°. This can cause phase errors as high as 60°.
- The significant aperture blockage produced by the centrally placed feed, especially when the beam is pointing to broadside.
- The fact that the calibration procedure optimizes the received power and not the pattern/side lobe level.
- The taper of the incident field at the array edges is only about -3...-4 dB; with a stronger taper (-10 dB) the SLL could be improved.

Furthermore, the algorithm for finding the voltage set delivering maximum power in a desired direction does not necessarily find a global optimum. It can very well be trapped in a local optimum, since it only evaluates a very limited amount of states from the vast space of possible states. To have an idea about the magnitude of the problem, let us suppose that the voltage is discretized in 30 steps. There would hence be 30^{16} possible voltage combinations (voltage sets) that can be applied to the 16 rows. The employed algorithm evaluates in the first iteration only 30×16 thereof, of course, not randomly chosen, but made to converge toward a maximum in received power. There is however no guarantee that this is a global maximum.

An indication that the voltage finding algorithm is suboptimal is for instance the set of patterns in Fig. 6.9 (b). The power recorded with the main beam pointing to 0° is lower than the power values recorded in the steered state. This is contrary to what is normally expected: the power recorded in steered states should be lower, due to reduction of the effective aperture with the factor $\cos\theta$ and also due to the element factor. It is only presumable, that in the 0° case the voltage finding algorithm did bot found the best set of voltages.

For the reflectarray filled with BL006 the pattern has also been recorded in the non-steerable H-plane, with the beam focused to broadside. It is presented in Fig. 6.10. It is a well-behaved pattern, with side lobes around -14 dB. This value of the side lobes validates the assumption that a nearly cylindrical wave, with constant amplitude distribution in H-plane is incident on the array. The side lobe level is marginally better than the theoretical value of -13.2 dB due to a slight tapering of the amplitude distribution toward the edges of the array in the H-plane, as can be observed in Fig. 3.17(b) (Section 3.4).

The measured gain of the antenna is 19.5 dBi and from two 360°-cuts, one in the H-plane and one in the E-plane with the main beam pointing toward 0°, a directivity of about 24 dBi is evaluated. This corresponds to an antenna efficiency of 35,4%. The overall loss of the reflector thus amounts to 4.5 dB, which is less than the peak loss of -10.5 dB of one unit cell (Fig. 5.20 in section 5.3.1). This fact verifies the assumption that the losses are distributed over the array aperture according to the tuning state of the cells, between -1 and -10.5 dB.

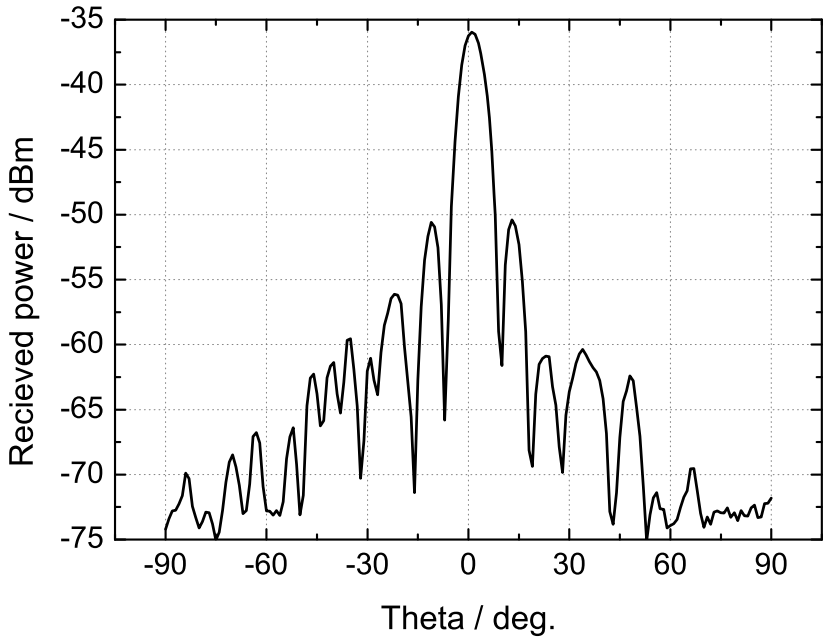

Figure 6.10: H-plane pattern for the BL006 reflectarray, with main beam focused toward broadside.

6.2 Reflectarray with Two Dimensional Control Capability

In this section, the possibility of individually addressing each element of the reflectarray with a control voltage, thus enabling focusing and steering of the main beam in an arbitrary plane, is explored. The challenge lies in the structuring of the bias network in such a way, as to minimize interference with the RF radiation of the array elements. The printing of thin metallic bias lines from each element toward the edge of the array is prohibitive even for reflectarrays of small dimensions, therefore an alternative solution had to be sought.

6.2.1 Realization

The idea pursued here is that of etching a very fine grid in the ground plane, thus providing each microstrip element with a separate "ground". Via holes are then drilled in each thus originated "ground" plates, and are plated through in order to take the potential to the backside of the array for easy access (see Fig. 6.11). Care must be taken that the via holes are completely closed, so that liquid crystal cannot leak from the cavity after the filling.

The effect of the grid etched in the ground plane has been analyzed with *CST Microwave Studio*. As long as the gap is small (<200μm) there is hardly any difference between the results with gap and those without gap. This is expected, since the high operation frequency together with the high capacity between adjacent "ground" pads leads to very low RF impedances.

Fig. 6.12 shows a photograph of the ground plane with the etched grid and the plated vias. The grid lines have a width of 100 μm, and the vias are 500 μm in diameter. On the right side of the picture the back side of the ground plane is shown, where connectors have been soldered to the vias to facilitate the access to each voltage control line.

The patches are connected as in the previous section, with thin printed lines joining all the patches in a column. These lines are then connected together at the edge of the array,

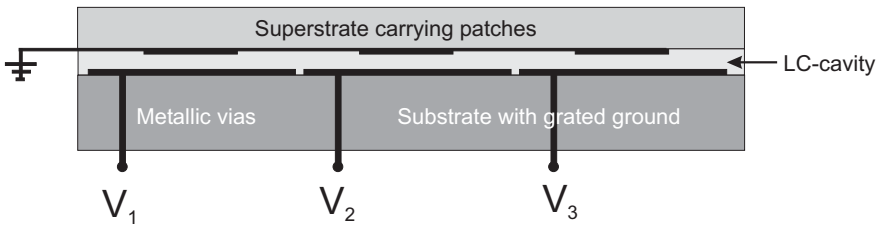

Figure 6.11: Schematic illustration of the bias network using plated vias for individual adressing of each element.

thus bringing all patches to a common potential. This reflectarray works therefore, as the previous two, only in linear polarization.

A further novelty in the realization of this demonstrator, compared with the one presented in the previous chapter is the use of SU8 structured spacers. As already pointed out in the previous section, the use of soft RF substrates as spacers is not practical, since it makes it very difficult to accurately control the cavity height. SU 8 is an epoxy resin that can be spin coated on a substrate to very precise layer heights, than cured and structured with photolithographic techniques. Technological details are given in Appendix A4.

The SU8 was structured on the TMM3 substrate supporting the patches (see Fig. 6.13). Columns with a diameter of 4 mm were disposed circularly and placed at the edge of the LC cavity. Thinner columns, of only 1 mm in diameter were uniformly distributed inside the LC cavity, in between the patches, in order to keep the cavity height as uniform as possible.

The choice of the spacer arrangement has been influenced by the need to subsequently spin the polyimide film. Hence, columns have been preferred to a continuous frame in order to prevent the accumulation of the polyimide at the edges in the spinning process.

The design height of the SU8 columns was $110\mu m$. After the structuring process, the spacer height was acquired with a surface profiler. The average height was $116\mu m$ with fluctuations of $\pm 14\mu m$. The bonding of the two parts was made by placing small glue drops on the 4 mm SU8 columns and then pressing the two component substrates together under a custom-made press.

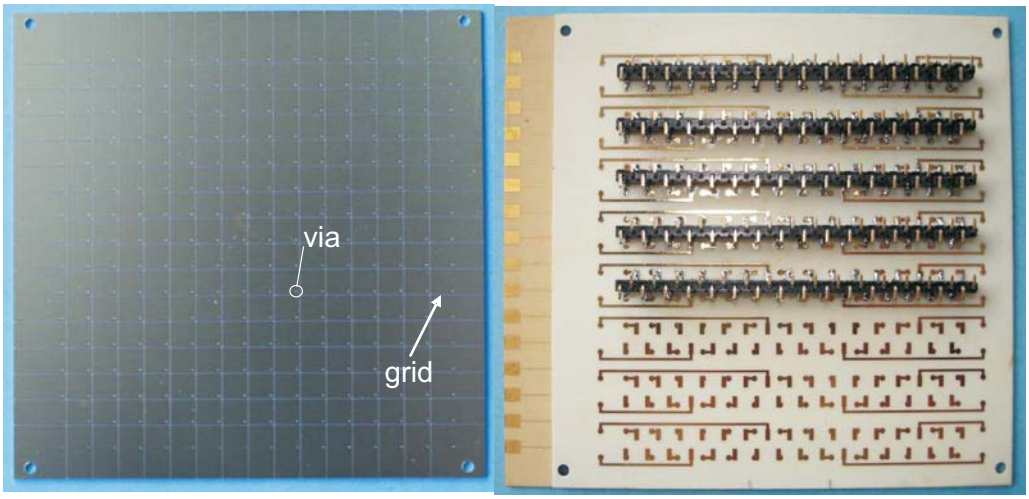

Figure 6.12: Photograph of the ground plane with etched grid for two dimensional voltage adressing. On the right, the back side of the ground plane is shown, with connectors for applying the control voltage.

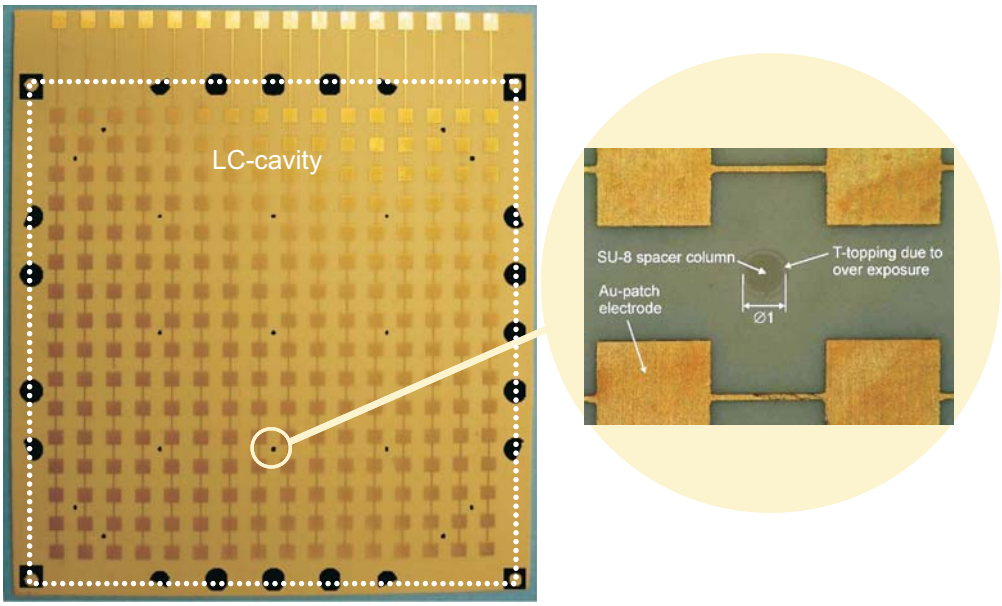

Figure 6.13: Photograph of the SU 8 spacers structured on the TMM3 substrate.

6.2.2 Experimental Results

With this demonstrator, capacitance measurements were conducted as well, in order to estimate the height of the LC cavity (Fig. 6.14). The measured capacitance values and by extension the derived cavity height show once again a decreasing slope from the first to the last row. The outlier at row 14 must be a measurement inaccuracy, since such a large height variation ($\approx 60\,\mu m$) between adjacent rows is improbable.

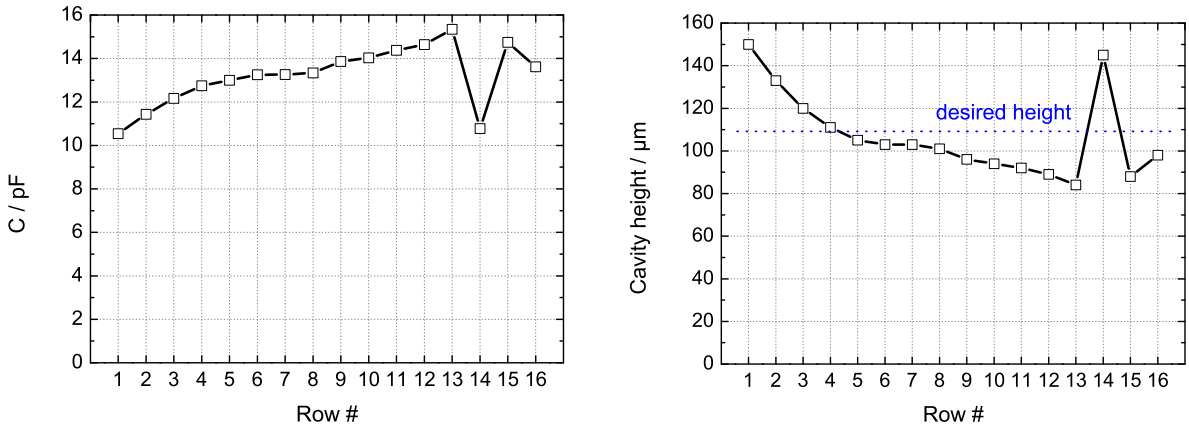

(a) Measurement of capacitance of each row of patches.

(b) Cavity height derived from measured capacitance.

Figure 6.14: Capacitance measurement for the estimation of the cavity height for the reflectarray with 2D control capability filled with MDA-05-893.

Next, the cavity was filled with the liquid crystal MDA-05-893 with the dielectric properties presented in section 4.3. In the anechoic chamber the reflectarray has been measured following the same procedure as for the previous one. Practical issues, such as the large calibration time or the very small change in recorded power when only one element

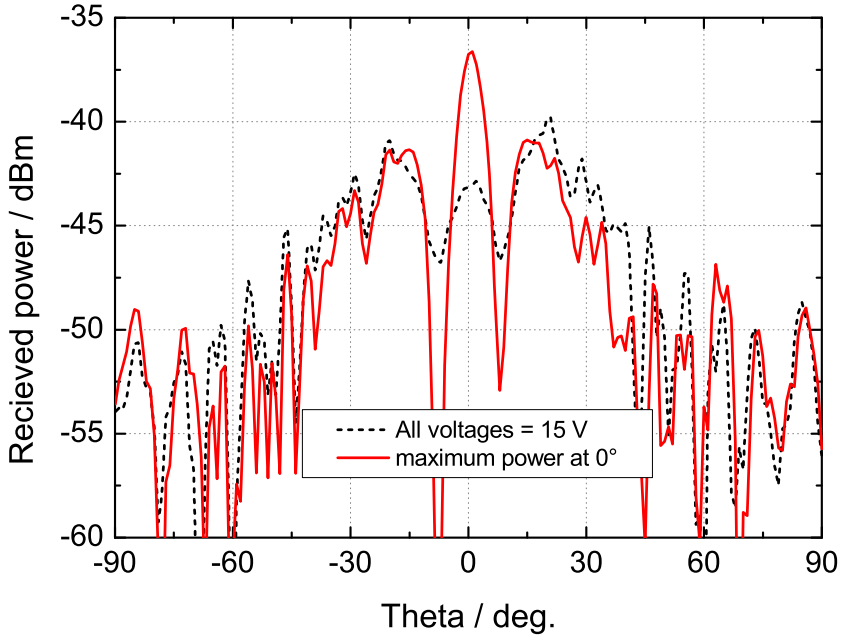

(a) Focussing of the beam.

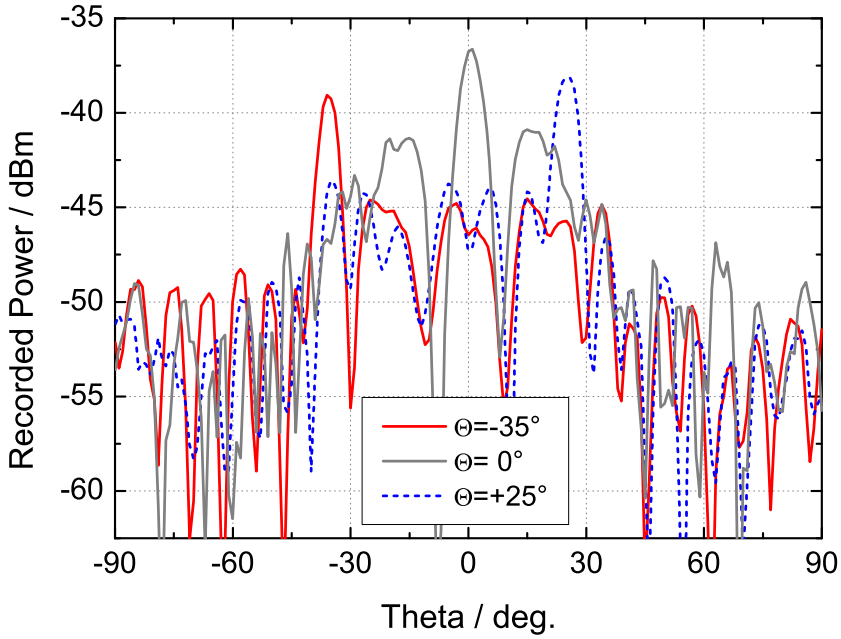

(b) Beam pointing to different steering angles.

Figure 6.15: Pattern measurements

is driven, did not allow the verification of the beam steering both planes (2D control). Therefore, the pins visible in Fig. 6.12 at the back side of the ground plane were connected together for each row, reducing the functionality of the reflectarray to steering in one plane, like in the previous section.

In Fig. 6.15(a), a comparison is shown between the patterns recorded with all rows connected to 15 V and the voltage configuration that maximized power toward 0°. One can observe the distinct focusing of the beam, but a SLL of only 4.2 dB could be achieved. In Fig. 6.15(b), two more patterns are shown, corresponding to voltage configurations that maximize power toward -35° and 25° respectively. For these steered cases the SLL improves to about 6 dB. The relatively poor SLL is attributed to the same reasons as in the case of the 1D demonstrators: high amplitude variations, randomly distributed across the aperture, high phase errors, low taper of the feed pattern at the edges, the calibration algorithm, yielding maximum power in a direction but not necessarily the best SLL.

A gain of about 20.3 dBi was measured for this reflectarray, with the beam pointing at 0°. From the two 360°-cuts, one in the E-plane and one in the H-plane with the main beam pointing toward 0°, an approximate directivity of about 24 dBi is calculated. This yields an antenna efficiency of 42,6%. Despite the very high peak losses of the cells, the overall loss on the reflectarray is thus only about 4 dB. This is due to the calibration trying to maximize the reflected power, thus preferring states with lower losses but higher phase errors.

Properties of the 1D reflectarray filled with BL006 and of the 2D reflectarray filled with MDA-05-893 are compared in Table 6.1. It can be concluded that their performance is relatively similar, with a slightly higher gain for the 2D reflectarray, which can be attributed to a better realization of the cavity with SU 8 spacers.

Table 6.1: Summary of the realized LC-reflectarrays with beam steering capability

Electronic steering	in E-plane only	possible in both planes
Liquid Crystal	BL006	MDA-05-893
Spacer type	RT Duroid 5880 h=127 μm	SU8 columns h=110 μm
SLL in E-Plane	-4.5 dB to -6 dB	-4.2 dB to -6 dB
SLL in H-Plane	-14 dB	-14 dB
Directivity	24 dB	24 dB
Measured Gain	19.5 dB	20.3 dB
Efficiency	35.4%	42.6%

6.3 Summary

In this chapter three demonstrators of beam steering reflectarrays with liquid crystal have been presented.

The impossibility to determine the characteristics (phase-voltage and amplitude-voltage) of each unit cell in the reflectarray environment, lead to the solution of finding the voltage combination that maximizes power in a certain direction via a calibration procedure.

Despite using a suboptimal calibration algorithm, and even though the losses of the unit cells composing the reflectarrays (metallic + dielectric losses) are quite high, a distinct beam focusing could be achieved in all cases, as well as beam steering with large steering angles. One of the demonstrators has a construction that allows application of bias voltage to each cell independently. However, only beam steering in one plane has been verified, owing to impracticably high calibration times for a 2D control and to the almost undetectable change in recorded power when just one element is biased.

Difficulties were encountered with the construction of the reflectarray, i.e. mainly the realization of a very large cavity with a uniform height (aspect ratio *height / surface* $\approx 22 \cdot 10^{-6}$) , but also bubble-free filling the liquid crystal into the cavity and sealing the assembly. First steps were undertaken for the achievement of more accurate control of the cavity height by using SU-8 structured spacers.

Chapter 7

Conclusions and Outlook

7.1 Contributions of the Thesis

The main contribution of this thesis resides in the introduction of a novel concept for reflectarrays with beam steering/reconfiguration capability. The novelty consists in the integration of a liquid crystal layer in the reflectarray, and in controlling the reflection phase at each elementary cell by making use of the bias voltage dependent permittivity of the liquid crystal.

Preliminary work has been conducted with fixed beam reflectarrays. Different feeding configurations were proposed and tested: the well-known and widely used offset feed with a horn antenna, retrodirective (or backfire) feed and a line feed consisting of a slotted waveguide array. The retrodirective feed and the slotted waveguide array line feed proved to be viable alternatives, yielding simple, stable and compact constructions.

To demonstrate the concept of liquid crystal steerable reflectarrays with reduced effort and cost, at first LC-tunable reflectarray unit cells have been designed, manufactured and characterized. The functional principle of the cells, the simulation environment, the measurement setup as well as the obtained results are discussed. The LC-tunable unit cells presented in this work are the worldwide first demonstrated LC-reconfigurable reflectarray unit cells.

At first, unit cells with an operating frequency of 35 GHz were investigated. Next, the designs of the unit cells and of the measurement setup were adapted for an operating frequency of 77 GHz to prove the viability of the concept at higher frequencies as well. Different microstrip configurations were investigated: single microstrip patch, stacked patches and patch with aperture coupled line. In the focus were the phase shifting properties and the attenuation of the unit cells.

The patch with aperture coupled line, despite the relatively poor results obtained in this work - mainly due to manufacturing inaccuracies - remains a promising alternative that deserves further investigation. With the single patch and stacked patch configurations better results were achieved: tunable phase ranges of up to 300° with peak losses of -8 dB could be shown by using a highly anisotropic LC mixture. Moreover, since the choice of the LC-layer thickness is very limited, the additional degree of freedom provided by the stacked patches allows choices in the design of the unit cells: for instance unit cells aimed at maximal tunable phase range or unit cells aimed highest possible bandwidth.

The stacked patch configuration proved on the other side to be quite sensitive to manufacturing inaccuracies, a small etching or alignment error being able to cause large deviations from the designed phase response. Therefore, the simplest and most robust configuration, the single microstrip patch, has been chosen to serve as unit cell for the full scale reflectarrays that were built as proof-of-concept.

First worldwide realizations of electronically steerable reflectarrays based on LCs are presented in this work. The design of the reflectarrays, the problems encountered at the manufacturing, the measurement setup with its calibration algorithm and the obtained results are in the focus. Among the manufacturing problems that had to be solved were the bubble free filling with LC of the very large cavity, as well as the realization of a precise, uniform cavity height. Two of the reflectarrays have beam steering capability in one plane, in order to simplify the bias circuitry. They were filled with K15 and BL006 and showed the possibility of focusing the beam towards a desired direction, with steering angles of at least $\pm 20°$.

The third reflectarray was designed for beam steering capability in both azimuth and elevation; to this purpose a solution with a very fine grid etched in the ground plane has been proposed. This design also allows the bias voltage to be taken to the back of the array by means of plated via holes, which provides very easy access without interference with the RF part. This reflectarray has been filled with the mixture MDA-05-893, the measurement results showing also distinct focusing of the beam and beam steering in the E-plane between at least $\pm 40°$. The high side lobe levels of all three reflectarrays, around -5 to-6 dB, are due to the high attenuation in the unit cells, because of dielectric and metallic losses, as well as to the suboptimal calibration algorithm.

The overall conclusion that can be drawn from both the measurements of the unit cells and of the reflectarrays is that the quality of the employed liquid crystal (losses and tunability) is crucial for the achievement of appropriate performance. The fact that the presented performance of the three reflectarray demonstrators could be achieved with commercially available liquid crystals, with average performance with respect to tunability and losses, allows the presumption that significant improvement would be possible with the use of a highly anisotropic, low-loss mixture.

7.2 Directions for Future Research

At the moment the first promising steps are made in the development of liquid crystal reflectarrays. The achieved results encourage further research efforts for performance improvement.

To allow a calculation in advance of the bias voltages necessary to achieve a beam pointing toward a certain direction, and thus eliminate the need for a long and cumbersome calibration procedure, knowledge of the characteristics of each unit cell in the array environment is mandatory. For the extraction of the magnitude-voltage and phase-voltage characteristics, a near-field probe that scans all unit cells sequentially could be a solution. The knowledge of the characteristic of each cell would further allow more complex beam forming besides steering of the main beam, such as forming of sector beams or nulling at desired angles.

It has been shown, that the severe fluctuations in amplitude are an important problem, seriously diminishing the performance of the reflectarrays in terms of efficiency and side lobe level. They are caused primarily by high losses in dielectric and metal, but are also enhanced by the resonant behavior of the unit cell. The high attenuations could thus be alleviated by using more complex structures with a flatter magnitude response and a more linear phase, but at the same time capable of providing the required phase shift. Candidates are for instance appropriately designed bandpass filters.

In a further step, even higher frequency of operation can be targeted, in the sub-mm wave region. This will bring advantages that were already mentioned across the thesis: the thinner LC layers would enable faster tuning with lower control voltages, and at the same time the manufacturing of electrically large arrays would be simplified. Moreover, liquid crystals are thought to have superior performance in this region in comparison to semiconductor or ferroelectric based phase shifters.

The use of RF-"transparent" electrodes, consisting of highly resistive films (e.g. Indium Tin Oxide, also used for control of LC displays), would simplify the design of the control circuitry, since one does not have to worry any more about the interference of the electrodes with the RF-field. A control circuitry similar to that currently used in LCDs is conceivable. Thus, for a $n \times n$ reflectarray, only $2\,n$ control lines, $n \times n$ transistors for the cell selection and $n \times n$ capacitors to hold the voltage until the next refresh cycle are required, instead of applying $n \times n$ bias voltages simultaneously.

List of Symbols and Abbreviations

β	phase constant
χ	electric susceptibility
$\Delta\varepsilon$	dielectric anisotropy
ϵ	(antenna) efficiency
η_0	wave impedance of free space
Γ	complex reflection coefficient
λ	wavelength
μ_0	permeability of vacuum, $\mu_0 \approx 4\,\pi\,10^{-7}\,\mathrm{H/m}$
ω	angular frequency
σ	metallic conductivity
$\tan\delta$	loss angle of a dielectric material
τ	tunability
$\underline{Z}$	complex impedance
ε_0	permittivity of vacuum, $\varepsilon_0 \approx 8.854\,10^{-12}\,\mathrm{F/m}$
ε_r	relative permittivity
φ, $\Delta\varphi$	phase, phase shift
$\vec{E}$	electric field vector
$\vec{H}$	magnetic field vector
$\vec{n}$	director
$\vec{P}$	(electric) polarization
A	physical aperture
f	frequency
I	current intensity
Q	quality factor of a resonator
S_{ij}	element ij of the scattering matrix
U	electric voltage
C	capacitance
h	substrate thickness
k	wavenumber
L	inductance

R	resistance
S	order parameter
ACC	Adaptive Cruise Control
BST	Barium Strontium Titanate
CDMA	Code-Division Multiple Acces
CST	Computer Simulation Technology
DUT	Device Under Test
FDMA	Frequency-Division Multiple Acces
FIT	Finite Integration Technique
FoM	Figure of Merit
FSS	Frequency Selective Surface
HPBW	Half Power Beamwidth
LC	Liquid Crystal
LHCP	Left Handed Circular Polarization
MEMS	Micro-Electro-Mechanical Systems
MIM	Metal Insulator Metal
MoM	Method of Moments
NASA	National Aeronautics and Space Administration
PEC	Perfect Electric Conductor
PGMEA	Propylene Glycol Methyl Ether Acetate
PMC	Perfect Magnetic Conductor
RF	Radio Frequency
RHCP	Right Handed Circular Polarization
SDMA	Space-Division Multiple Acces
SSL	Short - offset Short - Load
TDMA	Time-Division Multiple Acces
TFT	Thin Film Transistor
VNA	Vector Network Analyzer

APPENDIX

A1: Calculation of metallic loss in the microstrip element

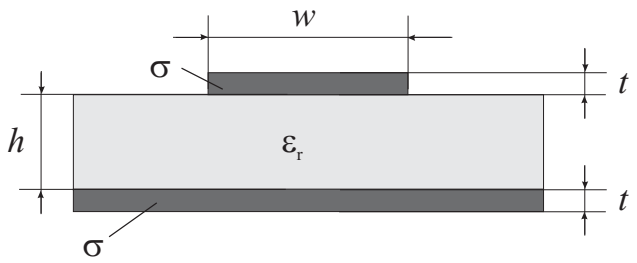

Figure 7.1: Cross-section of a microstrip line.

The calculation of the metallic losses in the reflectarray unit cell, to be used in the lumped element equivalent model as resistance R_L, is based on formulas given in [Sch01] for metallic losses in a microstrip line:

For a zero thickness line, without substrate, the characteristic impedance is given by:

$$Z_{L0} = \frac{\eta_0}{2\,\pi} \cdot \ln\left\{ \frac{F_1\,h}{w} + \sqrt{1 + \left(\frac{2\,h}{w}\right)^2} \right\} \tag{A-1}$$

with

$$F_1 = 6 + (2\,\pi - 6) \cdot \exp\left\{ - \left(30.666 \cdot \frac{h}{w}\right)^{0.7528} \right\}$$

and

$$\eta_0 = \sqrt{\frac{\mu_0}{\varepsilon_0}}\,.$$

Including a dielectric substrate with $\varepsilon_r > 1$, the effective relative permittivity of the line

is:

$$\varepsilon_{r,eff,0} = \frac{\varepsilon_r + 1}{2} + \frac{\varepsilon_r - 1}{2} \cdot \left(1 + \frac{10\,h}{w}\right)^{-a\,b} \tag{A-2}$$

with

$$a = 1 + \frac{1}{49} \cdot \ln\left\{\frac{\left(\frac{w}{h}\right)^4 + \left(\frac{w}{52\,h}\right)^2}{\left(\frac{w}{h}\right)^4 + 0.432}\right\} + \frac{1}{18.7} \cdot \ln\left\{1 + \left(\frac{w}{18.1\,h}\right)^3\right\}$$

and

$$b = 0.564\,\left(\frac{\varepsilon_r - 0.9}{\varepsilon_r + 3}\right)^{0.053}$$

The equivalent conductor width, without and with dielectric is given by:

$$w_{eq0} = w + \frac{t}{\pi} \cdot \ln\left\{1 + \frac{4 \cdot \exp(1)}{\frac{t}{h} \cdot \coth^2\left(\sqrt{6.517\,\frac{w}{h}}\right)}\right\} \tag{A-3}$$

and

$$w_{eqZ} = w + \frac{w_{eq0} - w}{2} \cdot \left(1 + \frac{1}{\cosh\left(\sqrt{\varepsilon_r - 1}\right)}\right) \tag{A-4}$$

respectively. Based on (A-1)-(A-4), characteristic impedance and relative permittivity of the lossless microstrip, for $\varepsilon_r > 1$ and $t > 0$ are:

$$Z_L = \frac{Z_{L0}(w_{eqZ})}{\sqrt{\varepsilon_{r,eff,0}(w_{eqZ})}} \tag{A-5}$$

$$\varepsilon_{r,eff} = \varepsilon_{r,eff,0}(w_{eqZ}) \cdot \left[\frac{Z_{L0}(w_{eq0})}{Z_{L0}(w_{eqZ})}\right]^2 \tag{A-6}$$

The line resistance per unit length can now be written:

$$R_L^{'} = 2\,Z_L\,\alpha(f) \tag{A-7}$$

with

$$\alpha(f) = 0.1589 \cdot A \cdot \frac{R_S(f)}{h\,Z_L} \cdot \frac{32 - \left(\frac{w_{eq0}}{h}\right)^2}{32 + \left(\frac{w_{eq0}}{h}\right)^2} \quad \text{for} \quad \frac{w}{h} \leq 1$$

or

$$\alpha(f) = 7.0229 \cdot 10^{-6} \cdot A \cdot \frac{R_S(f)\,Z_L\,\varepsilon_{r,eff}}{h} \cdot \left[\frac{w_{eq}}{h} + \frac{0.667\frac{w_{eq}}{h}}{\frac{w_{eq}}{h} + 1.444}\right] \quad \text{for} \quad \frac{w}{h} \geq 1$$

and

$$A = 1 + \frac{h}{w_{eq0}}\left[1 + \frac{1.25}{\pi}\ln\left(\frac{2\,h}{t}\right)\right]$$

$$R_S(f) = \sqrt{\frac{\pi\,f\,\mu_0}{\sigma}}$$

A2: Processing of the Polyimide Film

Polyimide	AL-3046	Mix in volume ratio 1:1
Solvent	ACT-600	

Process-Step	**Parameters**		**Observations**
Spincoating	2000 rot / min.	40 s	target thickness: 300 nm
Prebacking	100°C	60 s	on hot plate
Postbacking	180°C	90 min.	in convection oven

A3: The Etching Process Parameters

	Process step	**Substances and parameters**
1.	Photoresist spincoating	positive resist AZ PL 177; 2000 rot / min. ($\approx 5\,\mu m$)
2.	Photolitography	scattered light
3.	Photoresist developing	NaOH process for positive resist
4.	Wet etching	$FeCl_3$ spray etching

A4: Spacer structuring with SU 8

The processing of the SU-8 has been conducted by Dipl.-Ing. Dirk Eicher at the Laboratory of Microtechnology and Electromechanical Systems (Fachgebiet Mikrotechnik und Elektromechanische Systeme).

Process-Step	**Parameters**		**Observations**
Spincoating	2500 rot / min.		5 ml SU8
Softbacking	95°C	45 min	on hot plate
Exposure	broadband UV		
Postbacking	95°C	20 min.	on hot plate
Development	immersion in PGMEA		

A5: IEEE Frequency Band Designations

Band	Waveguide	GHz	Comment
L	WR-650	1.1-1.7	**L**ong Wave
R	WR-430	1.7-2.6	
S	WR-284	2.6-3.95	**S**hort Wave
H (G)	WR-187	3.95-5.85	
C	WR-147	5.85-8.2	**C**omprise between S and X
W (H)	WR-112	7.05-10	
X	WR-90	8.2-12.45	
K_u	WR-62	12.4-18	**K**urz **u**nder
K	WR-42	18-26.5	**K**urz
K_a	WR-28	26.5-40	**K**urz **a**bove
Q	WR-22	33-50	
U	WR-19	40-60	
V	WR-15	50-75	
E	WR-12	60-90	
W	WR-10	75-110	
F	WR-8	90-140	
D	WR-6.5	110-170	
G	WR-5.1	140-240	

References

[Arr06] Arrebola, M., Encinar, J., Alvarez, Y. and Las-Heras, F. Design and Evaluation of a Three-Beam LMDS Central Station Antenna Using Reflectarrays. In *Electrotechnical Conference, 2006. MELECON 2006. IEEE Mediterranean*, pages 328–331. 16-19 May 2006.

[Bal97] Balanis, C. A. *Antenna Theory*. John Wiley & Sons, Inc., second edition edition. 1997.

[Ber63] Berry, D., Malech, R. and Kennedy, W. The reflectarray antenna. *Antennas and Propagation, IEEE Transactions on [legacy, pre - 1988]*, 11(6):pages 645–651. Nov 1963.

[Boc02a] Boccia, L., Venneri, F., Amendola, G. and Di Massa, G. Application of varactor diodes for reflectarray phase control. In *Antennas and Propagation Society International Symposium, 2002. IEEE*, volume 3. June 2002.

[Boc02b] Boccia, L., Venneri, F., Amendola, G. and Di Massa, G. Experimental investigation of a varactor loaded reflectarray antenna. In *Microwave Symposium Digest, 2002 IEEE MTT-S International*, volume 1, pages 69–71. 2-7 June 2002.

[Boz04a] Bozzi, M., Germani, S. and Perregrini, L. A Figure of Merit for Losses in Printed Reflectarray Elements. *IEEE Antennas and Wireless propagation Letters*, 3:pages 257–260. 2004.

[Boz04b] Bozzi, M., Germani, S. and Perregrini, L. Modeling of losses in printed reflectarray elements. In *Microwave Conference, 2004. 34th European*, volume 3, pages 1393–1396. 11-15 Oct. 2004.

[Car06] Carrasco, E., Barba, M. and Encinar, J. Aperture-coupled reflectarray element with wide range of phase delay. *Electronics Letters*, 42(12):pages 1–2. 08 June 2006.

[Car07] Carrasco, E., Barba, M. and Encinar, J. Reflectarray Element Based on Aperture-Coupled Patches With Slots and Lines of Variable Length. *Antennas and Propagation, IEEE Transactions on*, 55(3):pages 820–825. March 2007.

[Cha92] Chang, D.-C. and Huang, M.-C. Microstrip reflectarray antenna with offset feed. In *Electronics Letters*, volume 28, pages 1489–1491. 30 July 1992.

[Cha02] Chaharmir, M., Shaker, J., Cuhaci, M. and Sebak, A. Circularly polarised reflectarray with cross-slot of varying arms on ground plane. In *Electronics Letters*, volume 38, pages 1492–1493. 21 Nov. 2002.

[Cha03c] Chaharmir, M., Shaker, J., Cuhaci, M. and Sebak, A. Reflectarray with variable slots on ground plane. In *Microwaves, Antennas and Propagation, IEE Proceedings -*, volume 150, pages 436–439. Dec 2003.

[Cha04] Chang, T. N. and Wei, Y. C. Proximity-coupled microstrip reflectarray. *Antennas and Propagation, IEEE Transactions on*, 52(2):pages 631–635. Feb. 2004.

[Col90] Collings, P. *LIQUID CRYSTALS Nature s Delicate Phase of Matter*. Princeton University Press. 1990.

[Col97] Collings, P. J. and Hird, M. *Introduction to Liquid Crystals*. Taylor&Francis. 1997.

[Cro91] Croq, F. and Pozar, D. M. Millimeter-Wave Design of Wide-Band Aperture-Coupled Stacked Microstrip Antennas. *IEEE Transactions on Antennas and Propagation*, 39(12):pages 1770–1776. Dec. 1991.

[cst07] *CST Microwave Studio*. `www.cst.com`. 2007.

[Dol93] Dolfi, D., Labeyrie, M., Joffre, P. and Huignard, J. P. Liquid Crystal Microwave Phase Shifter. *Electronics Letters*, 29:pages 926–928. May 1993.

[Ell03] Elliot, R. S. *Antenna Theory and Design*. IEEE Press Wiley-Interscience, revised edition edition. 2003.

[Enc96] Encinar, J. Design of a dual frequency reflectarray using microstrip stacked patches of variable size. In *Electronics Letters*, volume 32, pages 1049–1050. 6 June 1996.

[Enc99] Encinar, J. Design of two-layer printed reflectarrays for bandwidth enhancement. In *Antennas and Propagation Society International Symposium, 1999. IEEE*, volume 2, pages 1164–1167vol.2. 11-16 July 1999.

[Enc01] Encinar, J. Design of two-layer printed reflectarrays using patches of variable size. *Antennas and Propagation, IEEE Transactions on*, 49(10):pages 1403–1410. Oct. 2001.

[Enc04] Encinar, J. and Zornoza, J. Three-layer printed reflectarrays for contoured beam space applications. *Antennas and Propagation, IEEE Transactions on*, 52(5):pages 1138–1148. May 2004.

[Han65] Hannan, P. and Balfour, M. Simulation of a phased-array antenna in waveguide. *Antennas and Propagation, IEEE Transactions on [legacy, pre - 1988]*, 13(3):pages 342–353. May 1965.

[Han03] Han, C. and Chang, K. Ka-band reflectarray using ring elements. In *Electronics Letters*, volume 39, pages 491–493. 20 Mar 2003.

[Han06b] Han, C. M. *Dual-Band Reflectarrays Using Microstrip Ring Elements and their Aapplications with Various Feeding Arrangements*. Ph.D. thesis, Texas A&M University. Aug. 2006.

[Har02] Hartzstein, C. 76 GHz Radar Sensor for Second Generation ACC. In *11th International Symposium ATA EL 2002 Ûİ New Technologies for Advanced Driver Assistance Systems, Siena, Italy*. Oct. 2002.

[Hu06] Hu, W., Ismail, M., Cahill, R., Gamble, H., Dickie, R., Fusco, V., Linton, D., Rea, S. and Grant, N. Tunable liquid crystal reflectarray patch element. In *Electronics Letters*, volume 42, pages 509–511. 27 April 2006.

[Hu07a] Hu, W., Dickie, R., Cahill, R., Gamble, H., Ismail, Y., Fusco, V., Linton, D., Grant, N. and Rea, S. Liquid Crystal Tunable mm Wave Frequency Selective Surface. *IEEE Microwave and Wireless Components Letters*, 17(9):pages 667–669. Sept. 2007.

[Hu07b] Hu, W., Zhang, D., Lancaster, M. J., Button, T. W. and Su, B. Investigation of Ferroelectric Thick-Film Varactors for Microwave Phase Shifters. *IEEE Transactions on Microwave Theory and Techniques*, 55(2):pages 418–424. Feb. 2007.

[Hua91] Huang, J. Microstrip reflectarray. In *Antennas and Propagation Society International Symposium, 1991. AP-S. Digest*, pages 612–615vol.2. 24-28 June 1991.

[Hua97] Huang, J. and Pogorzelski, R. Microstrip reflectarray with elements having variable rotation angles. In *Antennas and Propagation Society International Symposium, 1997. IEEE., 1997 Digest*, volume 2, pages 1280–1283vol.2. 13-18 July 1997.

[Hua99] Huang, J. and Feria, A. Inflatable microstrip reflectarray antennas at X and Ka-band frequencies. In *Antennas and Propagation Society International Symposium, 1999. IEEE*, volume 3, pages 1670–1673vol.3. 11-16 July 1999.

[Hua00] Huang, J., Feria, A. and Lou, M. The development of inflatable array antennas. In *Aerospace Conference Proceedings, 2000 IEEE*, volume 5, pages 59–65vol.5. 18-25 March 2000.

[Hua01a] Huang, J. The development of inflatable array antennas. *Antennas and Propagation Magazine, IEEE*, 43(4):pages 44–50. Aug. 2001.

[Hua01b] Huang, J., Feria, V. and Fang, H. Improvement of the three-meter Ka-band inflatable reflectarray antenna. In *Antennas and Propagation Society International Symposium, 2001. IEEE*, volume 1, pages 122–125vol.1. 8-13 July 2001.

[Hum04] Hum, S. and Okoniewski, M. An electronically tunable reflectarray using varactor diode-tuned elements. In *Antennas and Propagation Society International Symposium, 2004. IEEE*, volume 2, pages 1827–1830Vol.2. 20-25 June 2004.

[Hum05a] Hum, S., Okoniewski, M. and Davies, R. Realizing an electronically tunable reflectarray using varactor diode-tuned elements. *Microwave and Wireless Components Letters, IEEE [see also IEEE Microwave and Guided Wave Letters]*, 15(6):pages 422–424. June 2005.

[Hum05b] Hum, S. V., Okoniewski, M. and Davies, R. J. An equivalent circuit model for reflectarray elements. In *Proceedings of the 2005 IEEE Antennas and Propgation Society International Symposium*. July 2005.

[Hum07] Hum, S. V., M., O. and J., D. R. Modelling and Design of Electronically Tunable Reflectarrays. *IEEE Transactions on Antennas and Propagation*, 55(8). Aug. 2007.

[Ism05a] Ismail, M. and Cahill, R. Application of liquid crystal technology for electronically scanned reflectarrays. In *Applied Electromagnetics, 2005. APACE 2005. Asia-Pacific Conference on*, page 4pp. 20-21 Dec. 2005.

[Ism05b] Ismail, M. and Cahill, R. Beam steering reflectarrays using liquid crystal substrate. In *High Frequency Postgraduate Student Colloquium, 2005*, pages 62–65. 5-6 Sept. 2005.

[Jav95] Javor, R., Wu, X.-D. and Chang, K. Design and performance of a microstrip reflectarray antenna. *Antennas and Propagation, IEEE Transactions on*, 43(9):pages 932–939. Sept. 1995.

[Ji04] Ji, T. *A Four Element Phased Array Antenna System Monolithically Implemented on Silicon*. Ph.D. thesis, Pennsylvania State University. 2004.

[Kam04] Kamoda, H., Kuki, T., Fujikake, H. and Nomoto, T. Millimeter-wave beam former using liquid crystal. In *Microwave Conference, 2004. 34th European*, volume 3, pages 1141–1144. 11-15 Oct. 2004.

[Kil89] Kildal, P.-S. and Jensen, T. Efficient small reflector with hat feed. In *Antennas and Propagation, 1989. ICAP 89., Sixth International Conference on (Conf. Publ. No.301)*, pages 154–157vol.1. 4-7 Apr 1989.

[Kil97] Kildal, P.-S. and Yang, J. FDTD optimizations of the bandwidth of the hat feed for MM-wave reflector antennas. In *Antennas and Propagation Society International Symposium, 1997. IEEE., 1997 Digest*, volume 3, pages 1638–1641vol.3. 13-18 July 1997.

[Kra88] Kraus, J. D. *Antennas*. Mc-Graw Hill Series in Electrical Engineering. Mc-Graw Hill, Inc., second edition edition. 1988.

[Leg03] Legay, H., Pinte, B., Charrier, M., Ziaei, A., Girard, E. and Gillard, R. A steerable reflectarray antenna with MEMS controls. In *Phased Array Systems and Technology, 2003. IEEE International Symposium on*, pages 494–499. 14-17 Oct. 2003.

[Leg05] Legay, H., Caille, G., Girard, E., Pons, P., Calmon, P., Perret, E., Aubert, H., Laisne, A., Gillard, R. and van der Vorst, M. MEMS controlled phase-shift elements for a linear polarized reflectarray. In *28th ESA Antenna Workshop*. June 2005.

[Leh96] Lehner, G. *Elektromagnetische Feldtheorie für Ingenieure und Physiker*. Springer Verlag, Berlin / Heidelberg. 1996.

[Lim93] Lim, K. C., Margerum, J. D. and Lackner, A. M. Liquid crystal milimeter wave electronic phase shifter. *Applied Physics Letters*, 62:pages 1065–1067. Mar. 1993.

[Lin81] Lindenberger, B. and Mojdeh, M. H. *Messtechnische Untersuchung von 35 GHz Antennen*. Student research project St 1192, Technische Hochschule Darmstadt. Oct. 1981.

[Mar03] Martin, N., Laurent, P., Person, C., Gelin, P. and Huret, F. Patch Antenna Adjustable in Frequency Using Liquid Crystal. In *33rd European Microwave Conference, Proceedings of*, pages 699 – 702. Oct. 2003.

[Mar05] Marin, R., Mossinger, A., Freese, J., Muller, S. and Jakoby, R. Basic investigations of 35 GHz reflectarrays and tunable unit-cells for beam steering applications. In *2005 European Microwave Conference*, volume 3, page 4pp. 4-6 Oct. 2005.

[Mar06a] Marin, R., Mossinger, A., Freese, J., Manabe, A. and Jakoby, R. Realization of 35 GHz Steerable Reflectarray using Highly Anisotropic Liquid Crystal. In *Antennas and Propagation Society International Symposium 2006, IEEE*, pages 4307–4310. 9-14 July 2006.

[Men99] Menzel, W., Pilz, D. and Leberer, R. A 77-GHz FM/CW radar front-end with a low-profile low-loss printed antenna. *Microwave Theory and Techniques, IEEE Transactions on*, 47(12):pages 2237–2241. Dec. 1999.

[Men03] Menzel, W., Al-Tikriti, M. and Leberer, R. Compact Folded MM-Wave Reflectarray Antennas. 3rd ESA Workshop on Millimetre Wave Technology and Application. In *3rd ESA Workshop on Millimetre Wave Technology and Application, Espoo, Finland*, pages 101–106. May 2003.

[Men05] Mencagli, B., Gatti, R., Marcaccioli, L. and Sorrentino, R. Design of large mm-wave beam-scanning reflectarrays. In *2005 European Microwave Conference*, volume 3, page 4pp. 4-6 Oct. 2005.

[Moe06b] Moessinger, A., Marin, R., Mueller, S., Freese, J. and Jakoby, R. Electronically reconfigurable reflectarrays with nematic liquid crystals. In *Electronics Letters*, volume 42, pages 899–900. August 3, 2006.

[Mol93] Moldsvor, A., Raberger, M. and Kildal, P.-S. An efficient rectangular hat feed for linear polarization and low sidelobes. In *Antennas and Propagation Society International Symposium, 1993. AP-S. Digest*, pages 270–273vol.1. 28 June-2 July 1993.

[Mue04] Mueller, S., Scheele, P., Weil, C., Wittek, M., Hock, C. and Jakoby, R. Tunable passive phase shifter for microwave applications using highly anisotropic liquid crystals. In *Microwave Symposium Digest, 2004 IEEE MTT-S International*, volume 2, pages 1153–1156Vol.2. 6-11 June 2004.

[Mue05a] Mueller, S., Felber, C., Scheele, P., Wittek, M., Hock, C. and Jakoby, R. Passive tunable liquid crystal finline phase shifter for millimeter waves. In *2005 European Microwave Conference*, volume 1, page 4pp. 4-6 Oct. 2005.

[Mue05b] Mueller, S., Penirschke, A., Damm, C., Scheele, P., Wittek, M., Weil, C. and Jakoby, R. Broad-band microwave characterization of liquid crystals using a temperature-controlled coaxial transmission line. *Microwave Theory and Techniques, IEEE Transactions on*, 53(6):pages 1937–1945. June 2005.

[Mue06] Mueller, S., Goelden, F., Scheele, P., Wittek, M., Hock, C. and Jakoby, R. Passive Phase Shifter for W-Band Applications using Liquid Crystals. In *36th European Microwave Conference (EuMC)*. Sept. 2006.

[Mue07] Mueller, S. *Grundlegende Untersuchungen steuerbarer passiver Flüssigkristall-Komponenten für die Mikrowellentechnik*. Ph.D. thesis, Darmstadt University of Technology. 2007.

[Pen00] Peng, B. *Liquid Crystal Polymer Brushes and their Application as Alignment Layers in Liquid Crystal Cells*. Ph.D. thesis, Johannes Gutenberg-Universität Mainz. 2000.

[Pen04] Penirschke, A., Muller, S., Scheele, P., Weil, C., Wittek, M., Hock, C. and Jakoby, R. Cavity perturbation method for characterization of liquid crystals up to 35 GHz. In *Microwave Conference, 2004. 34th European*, volume 2, pages 545–548. 13 Oct. 2004.

[Pen06] Penirschke, A., Mueller, S., Goelden, F., Lapanik, A., Lapanik, V., Bezborodov, V., Haase, W. and Jakoby, R. Cavity Perturbation Method for Temperature Controlled Characterization of Liquid Crystals at 38 GHz. In *GeMiC 2006 German Microwave Conference*. Mar. 2006.

[Pil99] Pilz, D. *Periodische und quasi-periodische Strukturen zur Realisierung von gedruckten Antennen und Polarisatoren*. Ph.D. thesis, Universität Ulm. 1999.

[Poz93] Pozar, D. and Metzler, T. Analysis of a Reflectarray Antenna Using Microstrip Patches of Variable Size. *Electronics Letters*, 29:pages 657–658. April 1993.

[Poz97] Pozar, D., Targonski, S. and Syrigos, H. Design of millimeter wave microstrip reflectarrays. *Antennas and Propagation, IEEE Transactions on*, 45(2):pages 287–296. Feb. 1997.

[Poz99] Pozar, D., Targonski, S. and Pokuls, R. A shaped-beam microstrip patch reflectarray. *Antennas and Propagation, IEEE Transactions on*, 47(7):pages 1167–1173. July 1999.

[Poz03] Pozar, D. Bandwidth of reflectarrays. *Electronics Letters*, 39:pages 1490–1491. 16 Oct. 2003.

[Poz04] Pozar, D. M. Comments on "Proximity-Coupled Microstrip Reflectarray". *IEEE Transactions on Anatennas and Propagation*, 52(12). Dec. 2004.

[Poz05] Pozar, D. M. *MIcrowave Engineering*. John Wiley & Sons, Inc. 2005.

[Qur07] Qureshi, J., Kim, S., Buisman, K., Huang, C., Pelk, M., Akhnoukh, A., Larson, L., Nanver, L. and de Vreede, L. A Low-Loss Compact Linear Varactor Based Phase-Shifter. In *Radio Frequency Integrated Circuits (RFIC) Symposium, 2007 IEEE*, pages 453 –456. June 2007.

[Reb03] Rebeiz, G. M. *RF MEMS Theory, Design, and Technology*. John Wiley & Sons. 2003.

[Rog07] RogersCorporation. High Frequency Laminates. www.rogerscorporation.com. 2007.

[Rom00] Romanofsky, R., Bernhard, J., van Keuls, F., Miranda, F., Washington, G. and Canedy, C. K-band phased array antennas based on Ba.60Sr.40 TiO thin-film phase shifters. *Microwave Theory and Techniques, IEEE Transactions on*, 48(12):pages 2504–2510. Dec. 2000.

[Rom07] Romanofski, R. SCDS Antenna Technologies - Ferroelectric Reflectarray. http://sulu.lerc.nasa.gov/organization/branches/amosb/RCA_SCDS/SCDS_reflectarray.htm. Nov. 2007.

[Sch01] Schnieder, F. and Heinrich, W. Model of Thin-Film Microstrip Line for Circuit Design. *IEEE Transactions on Microwave Theory and Techniques*, 49:pages 104–110. 2001.

[Sch02] Schneider, M. Smart Antennas and their Relevance for Car Radar Sensors. In *IMS 2002, IEEE MTT-S International Microwave Symposium, Seattle, Washington*, Workshop Notes & Short Courses. June 2002.

[Sch04] Scheele, P., Mueller, S., Weil, C. and Jakoby, R. Phase-shifting coplanar stubline-filter on ferroelectric-thick film. *Proceedings of the 34th European Microwave Conference*, 3:pages 1501–1504. Oct. 2004.

[Sie99] Sievenpiper, D. *High Impedance Electromagnetic Surfaces*. Ph.D. thesis, University of California, Los Angeles. 1999.

[Sie03] Sievenpiper, D., Schaffner, J., Song, H., Loo, R. and Tangonan, G. Two-dimensional beam steering using an electrically tunable impedance surface. *Antennas and Propagation, IEEE Transactions on*, 51(10):pages 2713–2722. Oct. 2003.

[Sta99] Stark, H. *Physics of Inhomogeneous Nematic Liquid Crystals: Colloidal Dispersions and Multiple Scattering of Light*. Ph.D. thesis, Universität Stuttgart. 1999.

[Sto05] Stockmann, J. and Hodges, R. The use of waveguide simulators to measure the resonant frequency of Ku-band microstrip arrays. In *Antennas and Propagation Society International Symposium, 2005 IEEE*, volume 1A, pages 417–420Vol.1A. 3-8 July 2005.

[Str04] Strassner, B., Han, C. and Chang, K. Circularly polarized reflectarray with microstrip ring elements having variable rotation angles. *Antennas and Propagation, IEEE Transactions on*, 52(4):pages 1122–1125. April 2004.

[Sze99b] Sze, K. and Shafai, L. Substrate thickness in a microstrip reflectarray. In *Microwave Conference, 1999 Asia Pacific*, volume 1, pages 146–149vol.1. 30 Nov.-3 Dec. 1999.

[Tar92] Tarumi, K., Finkenzeller, U. and Schuler, B. Dynamic behaviour of twisted nematic liquid crystals. *Japanese Journal of Applied Physics*, 31:pages 2829–2836. Sept. 1992.

[Tar94] Targonski, S. and Pozar, D. Analysis and design of a microstrip reflectarray using patches of variable size. In *Antennas and Propagation Society International Symposium, 1994. AP-S. Digest*, volume 3, pages 1820–1823vol.3. 20-24 June 1994.

[Tsa03a] Tsai, F.-C. and Bialkowski, M. Designing a 161-element Ku-band microstrip reflectarray of variable size patches using an equivalent unit cell waveguide approach. *Antennas and Propagation, IEEE Transactions on*, 51(10):pages 2953–2962. Oct. 2003.

[Wei99] Weiland, T. *Skriptum zur klassischen Feldtheorie*. Technische Universität Darmstadt. 1998/1999.

[Wei02] Weil, C., Luessem, G. and Jakoby, R. Tunable inverted-microstrip phase shifter device using nematic liquid crystals. In *Microwave Symposium Digest, 2002 IEEE MTT-S International*, volume 1, pages 367–370. 2-7 June 2002.

[Wei03a] Weil, C. *Passiv steuerbare Mikrowellenphasenschieber auf der Basis nichtlinearer Dielektrika*. Ph.D. thesis, Darmstadt University of Technology. Nov. 2003.

[Wen05] Wenger, J. Automotive Radar Ű Status and Perspectives. *Proc. of the CSIC 2005, IEEE Compound Semiconductor Integrated Circuit Symposium*, pages 21–24. 2005.

[Wie02] Wiesbeck, W. *Antennen und Antennensysteme - Skriptum zur Vorlesung*. Universität Karlsruhe - Fakultät für Elektrotechnik. 2002.

[Yan98] Yang, J. and Kildal, P.-S. FDTD design of a Chinese hat feed for shallow mm-wave reflector antennas. In *Antennas and Propagation Society International Symposium, 1998. IEEE*, volume 4, pages 2046–2049vol.4. 21-26 June 1998.

[Yee82] Yee, H. Y. and Richardson, P. N. Slotted Waveguide Antenna Arrays. *IEE Antennas and Propagation Society Newsletter*, 24:pages 5–8. 1982.

[Zor03a] Zornoza, A., Encinar, J. and Bialkowski, M. A double-layer microstrip reflectarray design to obtain Australia and New Zealand footprint. In *Antennas*

and Propagation Society International Symposium, 2003. IEEE, volume 3, pages 310–313vol.3. 22-27 June 2003.

Own Publications

[Mar04] Marin, R., SchüSSler, M., Freese, J. and Jakoby, R. Compact Cross Coupled Bandpass Filter with Improved Stop-Band Characteristics. *Frequenz*, 58:pages 211–213. 9-10 2004.

[Mar05] Marin, R., Mössinger, A., Freese, J., Müller, S. and Jakoby, R. Basic Investigations of 35 GHz Reflectarrays and Tunable Unit-Cell for Beamsteering Applications. In *IEEE European Microwave Week, EuMW2005*. Paris, France. Oct. 2005.

[Mar06a] Marin, R., Mössinger, A., Freese, J. and Jakoby, R. Characterisation of 35 GHz Tunable Reflectarray Unit Cells Using Highly Anisotropic Liquid Crystal. In *GeMiC 2006 German Microwave Conference,*. Karlsruhe, Germany. March 2006.

[Mar06b] Marin, R., Mössinger, A., Freese, J., Manabe, A. and Jakoby, R. Realization of 35 GHz Steerable Reflectarray Using Highly Anisotropic Liquid Crystal. In *2006 IEEE APS/URSI Symp. on Antennas and Propagation*. Albuquerque, New Mexico, USA. July 2006.

[Mar07] Marin, R., Moessinger, A., Goelden, F., Mueller, S. and Jakoby, R. 77 GHz Reconfigurable Reflectarray with Nematic Liquid Crystal. In *2nd European Conference on Antennas and Propagation*. Edinburgh, UK. Nov. 2007.

[Moe06a] Moessinger, A., Marin, R., Freese, J., Mueller, S., Manabe, A. and Jakoby, R. Investigations on 77 GHz Tunable Reflectarray Unit Cells with Liquid Crystal. In *1st European Conference on Antennas and Propagation*. nice, France. Nov. 2006.

[Moe06b] Moessinger, A., Marin, R., Mueller, S., Freese, J. and Jakoby, R. Electronically reconfigurable reflectarrays with nematic liquid crystals. *Electronics Letters*, 42(16):pages 899–900. August 3, 2006.

[Moe07] Moessinger, A., Marin, R., Eicher, D., Jakoby, R. and Schlaak, H. Liquid Crystal Reflectarray with Electronic 2D-Reconfiguration Capability. In *29th ESA Antenna Workshop on Multiple Beams and Reconfigurable Antennas*. Nordwijk, The Netherlands. April 2007.

[Mue07] Mueller, S., Moessinger, A., Marin, R., Goelden, F., Lapanik, A., Haase, W. and Jakoby, R. Liquid Crystals Ű Microwave Characterization and Tunable Devices. *Frequenz*, 61:pages 217–223. Sept.-Oct. 2007.

Supervised Student Research Projects and Diploma Thesis

[Ben04] Benoit, G. O. *Design und Realisierung eines Messaufbaus für Grundlegende Untersuchung von Steuerbaren Microstrip-Arrays auf Basis Nematischer Flüssigkristalle* / Design and Realization of a Measurement Setup for Basic Investigations of Tunable Microstrip Arrays based on Nematic Liquid Crystals. Student research project St2072, Darmstadt University of Technology. 2004.

[Fel04] Felber, C. *Flüssigkristall-Finlinephasenschieber für Mikro- und Millimeterwellenanwendungen* / Liquid Crystal Finline Phase-Shifter for Microwaves and mm-Waves Applications. Diploma ThesisD2072, Darmstadt University of Technology. 2004.

[Mös04] Mössinger, A. *Design und Realisierung eines Reflectarrays unter Berücksichtigung verschiedenerFeedstrukturen* / Design and Realization of a Reflectarray under Consideration of Various Feed Structures. Diploma Thesis D2076, Darmstadt University of Technology. 2004.

[Pon06] Pondrom, P. *Entwurf und Untersuchung von Einheitszellen für elektronisch rekonfigurierbare Reflectarrays in mm-Wellen Bereich* / Design and Investigation of Unit-Cells for Electronically Reconfigurable Reflectarrays for mm-Waves. Student research project St2094, Darmstadt University of Technology. 2006.

Curriculum Vitae

Personal Information

Name:	Radu Marin
Birth date:	27.01.1979
Birth place:	Bucharest, Romania
Citizenship:	romanian
Marital status:	single

Education

1993-1997:	High school at "Colegiul National *Sf. Sava*" Bukarest
june 1997:	High school diploma
1997-2003:	University Politehnica Bukarest - Economical Engineering
may-aug. 2003:	Diploma thesis at Darmstadt University of Technology with a DAAD scholarship

Professional Activity

2003-2007:	assistant at the Department for Wireless Communications Darmstadt University of Technology

Darmstadt, 11.12.2007

Radu Marin

Lebenslauf

Persönliche Daten

Name:	Radu Marin
Geburtsdatum:	27.01.1979
Geburtsort:	Bukarest, Rumänien
Staatsbürgerschaft:	rumänisch
Familienstand:	ledig

Ausbildung

1993-1997:	Gymnasium "Colegiul National *Sf. Sava*" Bukarest
Juni 1997:	Abitur
1997-2003:	Universität Politehnica Bukarest Sudium der Wirtschaftsingenieurwesen
Mai-Aug. 2003:	Diplomarbeit an der TU Darmstadt in Rahmen eines DAAD Stipendiums
Sep. 2003	Diplom

Berufstätigkeit

2003-2007:	Wissenschaftlicher Mitarbeiter am Fachgebiet Funkkommunikation, TU Darmstadt

Darmstadt, den 11.12.2007

Radu Marin